Universidad de Jaén
Escuela de Doctorado

UNIVERSIDAD DE JAÉN

ESCUELA POLITÉCNICA
SUPERIOR DE JAÉN

DEPARTAMENTO DE INGENIERÍA
MECÁNICA Y MINERA

TESIS DOCTORAL

ANÁLISIS Y DISEÑO DE DISPOSITIVOS PARA LA MEJORA AERODINÁMICA DE CUERPOS ROMOS

PRESENTADA POR:
MANUEL LORITE DÍEZ

DIRIGIDA POR:
PROF. CARLOS MARTÍNEZ BAZÁN
DR. D. JOSÉ IGNACIO JIMÉNEZ GONZÁLEZ
DR. D. CÁNDIDO GUTIÉRREZ MONTES

JAÉN, JULIO 2019

Universidad de Jaén

Analysis and design of devices for bluff bodies aerodynamics improvement

Tesis Doctoral

Autor
Manuel Lorite Díez

Directores
Prof. Carlos Martínez Bazán
Dr. José Ignacio Jiménez González
Dr. Cándido Gutiérrez Montes

Jaén, Julio 2019

DEPARTAMENTO DE INGENIERÍA MECÁNICA Y MINERA
Escuela Politécnica Superior

Analysis and design of devices for bluff bodies aerodynamics improvement

Análisis y diseño de dispositivos para la mejora aerodinámica de cuerpos romos

Autor
Manuel Lorite Díez

Directores de Tesis
Prof. Carlos Martínez Bazán
Dr. José Ignacio Jiménez González
Dr. Cándido Gutiérrez Montes

Jaén, Julio 2019

A mi familia, con la que naces y la que vas encontrando.

Quien pregunta es ignorante durante 5 minutos, el que no lo hace, lo es toda la vida.

TESIS DOCTORAL

ANALYSIS AND DESIGN OF DEVICES FOR BLUFF BODIES AERODYNAMICS IMPROVEMENT

Autor: Manuel Lorite Díez

Directores de Tesis:
Prof. Carlos Martínez Bazán
Dr. José Ignacio Jiménez González
Dr. Cándido Gutiérrez Montes

Firma del Tribunal Calificador:

Firma

Presidente: Dr. Ramiro Godoy Diana
Vocal: Dr. Luis Parras Anguita
Secretario: Dr. Francisco Huera Huarte
Suplente: Dr. Alejandro Sevilla Santiago
Suplente: Dr. Soledad Le Clainche Martínez

Calificación:

Jaén, de Septiembre de 2019

Agradecimientos

Tengo la sensación de que una etapa importante se cierra y pienso que es momento de dar las gracias a las personas sin las que esta tesis no hubiese sido posible. Para empezar, querría dar las gracias a mis directores de tesis. A José Ignacio, por haber compartido incontables horas conmigo durante estos años, sin importar el día, la hora o el país. Gran parte de esta tesis es gracias a su enorme dedicación, su ánimo por crecer y por qué no decirlo, la presión que nos contagia a todos los que trabajamos con él. Me gustaría también dar las gracias a Carlos, por ser siempre un modelo a seguir tanto en la academia como en la forma de hacer las cosas, siempre esforzándote, queriendo dar continuamente lo mejor de ti sin importarte lo demás. Por último, agradecer a Cándido no haberme asustado demasiado durante mi primera toma de contacto con la Mecánica de Fluidos, así como por convencerme para trabajar en el Grupo de Mecánica de Fluidos de Jaén.

En dicho grupo, hay personas cuyo papel ha sido importantísimo durante la realización de esta tesis. Inicialmente, quisiera dar las gracias a mi compañero de fatigas y despacho, Javi, el cual he tomado como ejemplo de paciencia, constancia y ética de trabajo. Durante estos años, me gustaría destacar el papel de Rocío, la cual siempre intenta ayudar, alegrar y sumar con su brillante punto de vista. También quería recordar los breves pero intensos dos años de Mariano con nosotros, la vida en el despacho nunca fue tan divertida y molesta al mismo tiempo. No sé si darte las gracias o no por haber generado en mí un trastorno importante en cuanto a las figuras. No quiero olvidarme tampoco de José Carlos que tuvo el valor de compartir conmigo mis primeros días en el laboratorio, con todo lo que ello conlleva. Por último, me gustaría dar las gracias a los técnicos de laboratorio que han intentado en todo momento ayudar a resolver los galimatías que les planteamos, gracias a Mario, Alejandro y Cosme.

During these last four years, I spent nine months at ENSTA where I met two really important people for my academic development. Luc, from the very first day, you were tremendously helpful and motivating. I would also like to thank Olivier for his interest on my work, forcing me to do my best in our collaboration, it is an incredible pleasure to learn from you.

En el plano personal, quiero agradecer profundamente a mis padres y hermanos su ayuda, apoyo y confianza depositada en mí desde mucho antes que decidiese hacer el doctorado. En especial, me gustaría destacar a Laura, sin la cual no sería quien soy ahora y por la que me siento afortunado cada día, ya que es la mejor hermana-amiga que pudiese imaginar. También dar las gracias a mi abuela María, la gran experta familiar en esta tesis, a la que por fin le voy a poder decir que ya he acabado la tesis sobre los camiones.

Según mi experiencia, la tesis no es sólo una época importante debido al tremendo desarrollo académico y profesional que se experimenta. Para mí, también, ha supuesto el comienzo de mi vida adulta en la que han seguido junto a mi mis amigos de siempre además de las personas geniales que he ido conocociendo, las cuales me han enseñado muy diversas formas de ver la vida y afrontar la carrera investigadora. Destacar entre ellos a los que estaban haciendo también un doctorado, ya que siempre es de agradecer las miradas de compresión y mantener conversaciones que parecen salidas de una terapia de grupo.

Finalmente, nunca podré dar las gracias lo suficiente y lo que se merece a Macarena. Ella es la principal responsable de gran parte de esta tesis, su apoyo constante, sus ganas de animarme en los malos momentos, su paciencia, amor, comprensión y ternura desinteresados han sido fundamentales durante estos años.

Resumen

Las cada vez más restrictivas políticas encaminadas a la reducción de emisiones globales de gases de efecto invernadero unidas al creciente intercambio comercial entre países y regiones obligan a la industria del transporte, especialmente al terrestre, a llevar a cabo planes encaminados a la reducción de emisiones de CO_2 en sus flotas.

Parte de la energía obtenida por el consumo de combustible en vehículos terrestres tiene como objetivo vencer la resistencia aerodinámica o la fuerza de oposición que ejerce el aire de alrededor al avance de un vehículo. Dicho consumo energético es especialmente elevado en el caso de los vehículos pesados como tráileres o autobuses. Para este tipo de vehículos, la parte trasera del vehículo es responsable de un cuarto de la resistencia aerodinámica total, debido a la región de baja presión que se genera en la parte posterior o base del vehículo al desprenderse la corriente de aire que fluye alrededor del mismo lo que genera la aparición de una estela trasera.

En la literatura, numerosos trabajos se han dedicado a estudiar el flujo alrededor de cuerpos romos ya que su geometría se asemeja a la de los vehículos pesados. Ambos tipos de geometrías comparten la separación trasera masiva de la capa límite y la creación de una estela que se extiende tras el cuerpo. Esto se traduce en una importante fuerza de arrastre actuando sobre los mismos. El principal objetivo de estos estudios, además de caracterizar la naturaleza temporal y espacial de la estela, es la de controlarla y ser capaces de reducir la resistencia aerodinámica asociada a ella. Para ello, diversos dispositivos de muy diferentes caracteristicas se han propuesto a lo largo de los años, en concreto, la presente Tesis se centra en dos de ellos.

Por un lado, hemos estudiado las cavidades traseras como sistema de control pasivo de estelas, los cuales no necesitan aporte de energía externa para funcionar. Cuando éstas se incorporan en la parte trasera de los distintos cuerpos romos, son capaces de reducir en gran medida la resistencia aerodinámica, aumentando la presión en la base del cuerpo y además, reducen las fuertes oscilaciones de la estela. Sin embargo, estas cavidades tienen su eficiencia fuertemente ligada a su profundidad, lo cual limita su aplicabilidad. Por ello, la primera parte de la presente Tesis comienza con la obtención de una forma optimizada de dicho tipo de cavidad con una profundidad fija. La optimización se ha realizado para un cuerpo romo bidimensional de cabeza redondeada, el cual incluye en su parte posterior una cavidad clásica recta. Para la obtención de dicha forma optimizada, se ha planteado un problema de optimización empleando el método adjunto, la sensibilidad de la resistencia aerodinámica a perturbaciones localizadas y algoritmos de optimización topológica.

La forma obtenida para la cavidad se ha analizado bajo diversas condiciones de cara a estudiar su viabilidad en términos de reducción de resistencia aerodinámica al implementarla en situaciones reales. En particular, esta cavidad mejorada se ha evaluado mediante simulaciones turbulentas tridimensionales para distintas condiciones del flujo, validando el estudio de optimización. Además, las distintas geometrías traseras tales como cuerpo romo, cavidad recta y optimizada se han comparado en flujos transitorios mediante medidas experimentales y simulaciones numéricas. En ambos casos, la forma obtenida en el proceso de optimización ha presentado una excelente respuesta en términos de reducción de la resistencia aerodinámica como de control de la estela cercana si la comparamos con las otras geometrías.

Teniendo en cuenta estos prometedores resultados, dicha cavidad mejorada se ha adaptado para cuerpos romos tridimensionales que se asemejan en mayor grado a los vehículos terrestres. De nuevo, los resultados experimentales muestran una reducción de la resistencia aerodinámica mayor que la de la cavidad recta original. Además, se ha obtenido una mejor respuesta en términos aerodinámicos cuando el modelo empleado y la corriente de aire incidente no están alineados.

Sin embargo, las reducciones obtenidas en el caso de cuerpos tridimensionales son menores a las de la geometría bidimensional. Por otro lado, parte del potencial de reducción de la resistencia aerodinámica capaz de obtener la cavidad mejorada se pierde debido a las características completamente tridimensionales del flujo, con lo que un sistema de control adicional podría utilizarse para mejorar su eficiencia.

Por ello, y debido a que existen muy pocos estudios que estudien el efecto del soplado de base perimétrico en la estela biestable de dichos modelos tridimensionales de sección rectangular, la presente Tesis analiza también el efecto de soplar de manera estacionaria en la base de dichos cuerpos empleando distintas disposiciones de soplado. El estudio llevado a cabo, revela cómo dependiendo de localización de la inyección de aire, la topología de la estela cambia de manera muy significativa. Por un lado, el soplado es capaz de aumentar inicialmente la longitud de la zona recirculación, incrementando la presión de la base y reduciendo la resistencia aerodinámica. En cambio, para caudales de soplados más elevados, la burbuja de recirculación se retrae y aumenta la fuerza de arrastre. En dicho estudio, se han analizado la transición entre ambos regímenes y sus características: ya sea su relación con la localización, masa y cantidad de movimiento asociados al soplado, los cambios experimentados en la estela durante ambos como los mecanismos físicos involucrados.

Finalmente, se ha estudiado el efecto de cambiar la densidad del gas introducido en la estela medianto soplado perimétrico estacionario. Los experimentos realizados han mostrado una mayor reducción de la resistencia aerodinámica cuando se emplea un soplado ligero, ya que su menor densidad permite introducir el soplado con una mayor velocidad en la estela. Dicho efecto consigue aumentar en mayor medida la longitud de la región de recirculación así como la velocidad con la que el flujo es dirigido hacia la base del cuerpo con respecto a un soplado de aire, lo que se traduce en un aumento adicional de la presión en dicha parte trasera.

Los resultados presentados en este documento corresponden a las siguientes publicaciones:

- **Lorite-Díez, M.**, Jiménez-González, J. I., Gutiérrez-Montes, C. & Martínez-Bazán, C. (2017) Drag reduction of slender blunt-based bodies using optimized rear cavities. *Journal of Fluids and Structures*, 74, 158-177.
- **Lorite-Díez, M.**, Jiménez-González, J. I., Gutiérrez-Montes, C. & Martínez-Bazán, C. (2018) Effects of rear cavities on the wake behind an accelerating D-shaped bluff body. *Physics of Fluids*, 30(4), 044103.
- **Lorite-Díez, M.**, Jiménez-González, J. I., Pastur, L., Cadot, O. & Martínez-Bazán, C. (2019) Effect of the shape of rear cavities on the drag reduction of a three-dimensional blunt body at different yaw angles. *Enviado a Journal of Wind Engineering and Industrial Aerodynamics.*
- **Lorite-Díez, M.**, Jiménez-González, J. I., Pastur, L., Martínez-Bazán, C. & Cadot, O. (2019) Sensitivity of 3D wake modes to local base blowing. *Enviado a Journal of Fluid Mechanics.*
- **Lorite-Díez, M.**, Jiménez-González, J. I., Pastur, L., Cadot, O. & Martínez-Bazán, C. (2019) On the role of base blowing density on the drag reduction of three-dimensional blunt bodies. *Enviado a Physical Review Fluids.*

Palabras clave: reducción resistencia aerodinámica, estelas tras cuerpos romos, control de estelas, cuerpo Ahmed, cavidades traseras, sensibilidad de la resistencia aerodinámica, optimización topológica, soplado perimétrico estacionario, soplado ligero, inestabilidad.

Abstract

The current restrictive environmental policies devoted to reduce the green-house gases emissions, along with the growing commercial exchange between regions and countries, are forcing the transport industry to develop strategies to reduce the CO_2 emissions, especially for ground transportation industry. One of the main contributions to the energy expenses related to fuel consumption in ground vehicles is the aerodynamic drag, i.e. the resisting force acting on the vehicle motion applied by the surrounding air. The drag is significantly notable in the case of heavy vehicles as trucks, lorries or buses. In particular, the rear blunt base of such vehicles is responsible for a 25% of the total aerodynamic drag due to the appearance of a low pressure region in the near wake, created by the massive flow separation behind the vehicle.

Many scientific works have been traditionally carried out to improve the aerodynamics of heavy vehicles. Most of the studies have focused on the analysis of wakes behind simplified bluff bodies, due to their simpler geometry. However, although these models are different from the real vehicles, they share most of the flow aerodynamic features, such as the boundary layer massive separation at the rear end, and the appearance of a wide wake, that entails a large drag force acting on the body. The main goals of such studies, aside from the characterization of the flow properties, are the wake control and the drag reduction, what has generated numerous control strategies and devices of different nature. Among them, rear cavities and base blowing systems have been proven to be simple and efficient control mechanisms, although their potential for drag reduction can be still improved, what will be the goal of the present thesis.

More precisely, rear cavities, which are passive devices (no external energy is required), manage to reduce the drag coefficient when implemented on bluff bodies, by increasing the base pressure and weakening the wake fluctuations. However, their efficiency is strongly linked to their depth, which is a limitation in terms of applicability. Thus, the first part of the present Thesis is devoted to the design of an optimal rear cavity shape of reduced depth. The optimization has been performed for a two-dimensional D-shaped body, which initially implements a straight rear cavity. The modification of such straight cavity has been performed by using linear adjoint sensitivity and shape optimization approaches, to give a curved cavity with an improved performance.

The resulting optimized shape has been analyzed and employed under several flow conditions to evaluate its applicability in terms of drag reduction in more realistic and practical applications. In particular, the performance of the improved cavity on the wake behind the D-shaped body has been satisfactorily proven by means of three-dimensional turbulent numerical simulations at high Reynolds numbers. Moreover, transient situations under several accelerating conditions have been also analyzed for the same D-shaped body with three different rear ends, namely, a blunt base, a straight cavity and the optimized geometry. Experimental measurements and numerical simulations show a great response of the optimized cavity for both drag reduction and near wake control in comparison with the two other geometries.

In view of these promising results, the optimized cavity has been adapted to be implemented in a three-dimensional, square-back Ahmed body, as a simplified model of heavy vehicles, to test it experimentally under more realistic conditions. Again, the experimental results show a greater drag reduction for the optimized, curved cavity than for a straight cavity with the same depth. Moreover, such cavities have been shown to mitigate the bistable dynamics of the wake behind the square-back model, which consists in a long-time random switching of the wake between two horizontal mirrored deflected states, that induces sudden reversal of lateral forces and induced drag. Furthermore, when yawed flow incident conditions are imposed, the drag reduction provided by the optimal cavity response is even more efficient.

On the other hand, a steady perimetric base blowing has been also analyzed as an active strategy, to control the bistable dynamics of the wake behind the square-back Ahmed body. Thus, several blowing configurations have been employed, revealing the existence of preferred blowing distributions in terms of wake topology manipulation. In general, low blowing flow rates are able to enlarge the recirculating region, thus increasing the base pressure and reducing the drag. Conversely, for high blowing flow rates, the recirculation bubble is deflated by the blowing, what increases the drag. These two behaviors, denoted respectively as mass and momentum regimes, have been deeply characterized in terms of wake topology changes and the associated physical mechanisms.

Finally, the effect of the blowing density has been also analyzed, by using air, helium and carbon dioxide as blowing gases. The experiments reveal a larger drag reduction when a light gas is employed, what is related to fact that a larger blowing velocity can be injected on the recirculation bubble before the transition to the momentum regime takes place. Therefore, the light base bleed allows to elongate the recirculation region and increase the backflow velocities on the near wake more than when homogeneous or dense blowing are used, thus giving rise to a greater base pressure recovery.

The results presented in this dissertation are comprised in part or totally in the following publications:

- **Lorite-Díez, M.**, Jiménez-González, J. I., Gutiérrez-Montes, C. & Martínez-Bazán, C. (2017) Drag reduction of slender blunt-based bodies using optimized rear cavities. *Journal of Fluids and Structures*, 74, 158-177.

- **Lorite-Díez, M.**, Jiménez-González, J. I., Gutiérrez-Montes, C. & Martínez-Bazán, C. (2018) Effects of rear cavities on the wake behind an accelerating D-shaped bluff body. *Physics of Fluids*, 30(4), 044103.

- **Lorite-Díez, M.**, Jiménez-González, J. I., Pastur, L., Cadot, O. & Martínez-Bazán, C. (2019) Effect of the shape of rear cavities on the drag reduction of a three-dimensional blunt body at different yaw angles. *Submitted to Journal of Wind Engineering and Industrial Aerodynamics.*

- **Lorite-Díez, M.**, Jiménez-González, J. I., Pastur, L., Martínez-Bazán, C. & Cadot, O. (2019) Sensitivity of 3D wake modes to local base blowing. *Submitted to Journal of Fluid Mechanics.*

- **Lorite-Díez, M.**, Jiménez-González, J. I., Pastur, L., Cadot, O. & Martínez-Bazán, C. (2019) On the role of base blowing density on the drag reduction of three-dimensional blunt bodies. *Submitted to Physical Review Fluids.*

Keywords: drag reduction, bluff body wakes, wake control, Ahmed body, base cavities, drag sensitivity, shape optimization, steady perimetric blowing, light base bleed, instability.

Contents

List of Tables

List of Figures

CHAPTER

ONE

Introduction

1.1 Industrial motivation and general context

The current severe economical and environmental restrictions on fuel consumption are contributing to important changes in the transport industry, which is being encouraged to reduce their energetic expenses in the coming years. In particular, the contribution of road transportation to the global greenhouse gas emissions is about a 20% (Dekker et al., 2012; Palmer, 2007), although such ratio is increasing yearly due to the growing commercial exchange between different countries. In this regard, the European Union is imposing limitations on the CO_2 emissions for road vehicles manufacturers. More precisely, a new limit is established for 2021, that enforces a reduction of 30% of CO_2 emissions with respect to the current regulated limit. In addition, a new approval cycle called *Woldwide harmonized Light vehicles Test Procedure* (WLTP) will set new conditions for the evaluation of vehicle emissions, including a set of more realistic conditions during the certification process as a moving ground on wind tunnel tests or wide yaw conditions (Bonnavion, 2018).

In order to reach these goals, different improvements on engine technology, transmissions, mass diminution and aerodynamics are needed. In fact, the *aerodynamic drag* is the resisting force acting on the vehicle motion applied by the surrounding air. To get an idea, more than 50% of the total tractive power expense of a passenger car in a highway is invested to overcome the aerodynamic drag (Hucho and Sovran, 1993), being such ratio even larger in the case of trucks or buses. Moreover, this percentage increases quadratically with the cruising velocity (Wood and Bauer, 2003). The drag force is mainly determined by the vehicle shape and it is usually expressed in non-dimensional form by means of the drag coefficient, C_d. A significant part of the drag comes from the pressure difference between front and rear part of the vehicle (see Fig. 1.1a). Over the last century, the drag force has been reduced over a 70% (Hucho, 1998) due to the optimization of the vehicle shape. However, aerodynamic improvements are commonly subject to constraints related to functional, economic and aesthetic aspects. Therefore, all cars have a very similar shape, since the constraints and goals are the same for all vehicle manufacturers.

Nonetheless, trucks, buses or lorries still have room for improvement of their aerodynamic performance due to its simpler and blunt shape (Choi et al., 2014). In this regard,

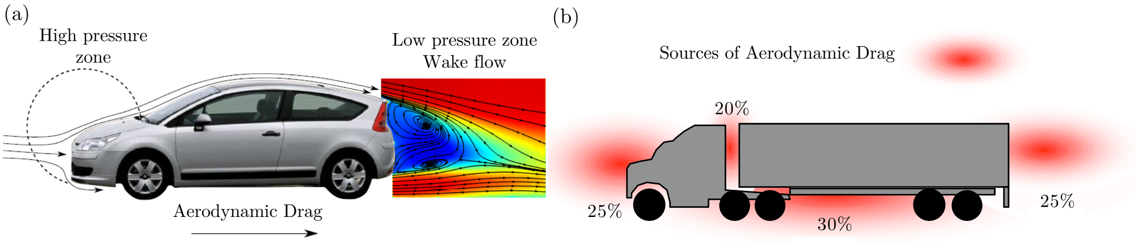

Figure 1.1: Aerodynamic drag on real vehicles. (a) Drag production due to front and rear pressure difference on real vehicle geometry from (Barros, 2015). (b) Sources of aerodynamic drag on a truck model adapted from (Wood, 2006).

.

their blunt-based geometry, conceived to maximize the loading capacity, provokes a massive flow detachment at the rear edge, leading to the development of a large recirculating zone. Such separation configures the *wake* flow, which is characterized by a general velocity deficit, with backflow and eddies in the vicinity of the base, that give rise to low pressure values in such region. The aforementioned difference between front (high pressure zone) and rear (low pressure zone) vehicle surfaces, results in the *pressure drag.* In particular, the rear low pressure region is responsible of approximately the 25% of the total aerodynamic drag on a real truck (Wood, 2006) (see Fig. 1.1b). Apart from the pressure drag, there is another contribution to the aerodynamic resistance which is the *friction drag*, that comes from the contact between vehicle' surface and air in relative motion due to the fluid viscosity. In particular, for *streamlined bodies*, such as airfoils, aircrafts or ships, the drag is mainly created by friction (Li, 2017). However, when the flow separate massively, the pressure drag becomes dominant, which is a feature shared by *bluff bodies*, such as cars, trucks, spheres or cylinders.

Given the environmental and economical impact of the road transportation and heavy vehicles, the reduction of the aerodynamic drag of bluff bodies has been a major goal of plenty of classical and recent investigations. More precisely, most of drag reduction strategies have been focused on the control of flow separation around rear edges of bluff bodies and the modifications of the near wake properties, aiming at efficiently increase the base pressure. Within this frame, this Thesis is devoted to the design of efficient passive control strategies implemented on different bluff bodies, focusing on the analysis of their effect on the wake features and the aerodynamic resistance. The design of such strategies can be only based on the profound knowledge of the near wake topology and dynamics for different geometries, which will be discussed in detail in the next Sect. 1.2, before presenting a general classification of traditional control strategies in Sect. 1.3.

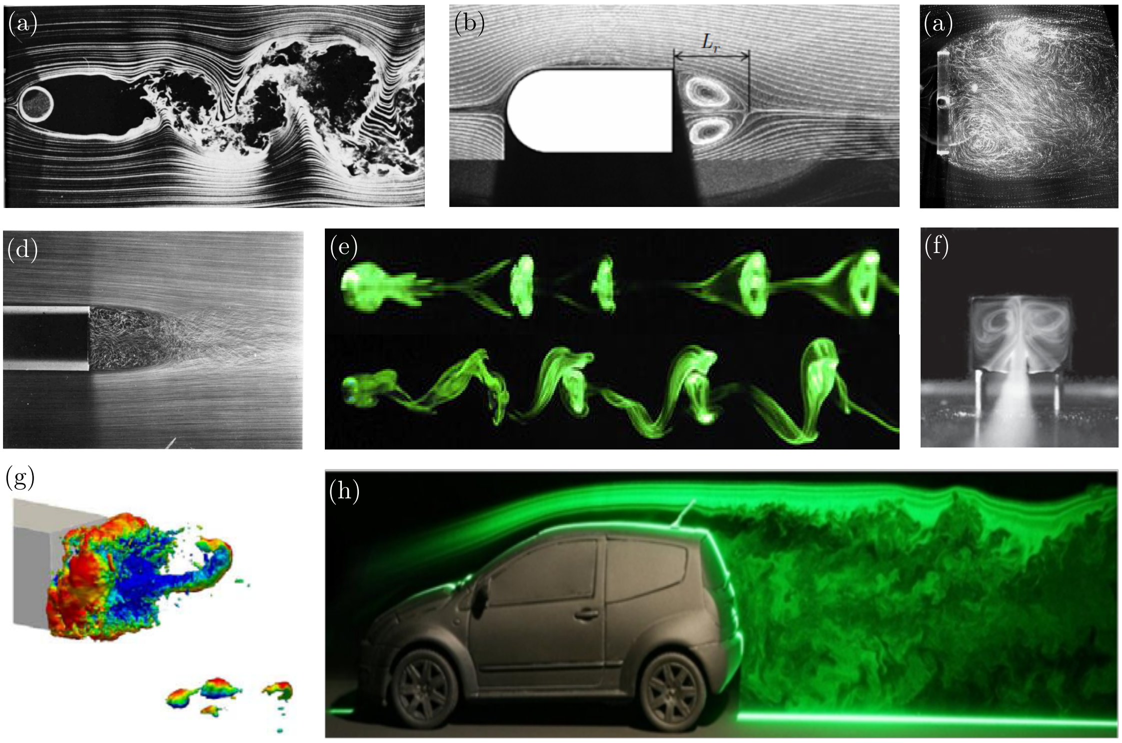

Figure 1.2: Wakes behind different bluff bodies. (a) Circular cylinder in cross-flow at $Re = 1 \times 10^4$ (Van Dyke, 1982). (b) Averaged streamlines for the recirculation region behind a D-shaped body at $Re = 1.3 \times 10^4$ (Parezanović and Cadot, 2012). (c) Visualizations behind a fixed plate at $Re = 2.64 \times 10^5$ (Cadot, 2016). (d) Axisymmetric time-averaged wake flow past a body of revolution (Van Dyke, 1982). (e) Dye-visualizations of the wake behind a rolling sphere at $Re = 190$ (top) and $Re = 230$ (bottom) adapted from Bolnot et al. (2011). (f) Steady and symmetric laminar wake behind an Ahmed body at $Re = 310$. (g) Isocontour of pressure coloured by velocity in a wake of square-back Ahmed body at $Re = 2 \times 10^4$ (Dalla Longa et al., 2019). (h) Wake flow visualization behind a modern real car (Grandemange, 2013).

1.2 General features of bluff body wakes

We will now describe some of the salient features of wakes behind bluff bodies and how they are related to the generation of aerodynamic loads. In that sense, Fig. 1.2 shows some examples of wakes behind bluff bodies, which illustrate the massive flow separation occurring due to the bluffness of geometries, which leads to the flow unsteadiness and an important induced pressure drag on the body (Roshko, 1993). As observed, the *boundary layers*, which develop along the body surfaces, separate at the rear ends due to adverse pressure gradient produced by the abrupt geometry changes characterizing such bodies. For the particular case of blunt-based bodies, with sharp rear edges, the separation point is fixed. The sudden detachment of the flow gives rise to the development of *shear layer instabilities* as the well-known *Kelvin-Helmholtz instability* (Drazin and Reid, 2004), which is responsible for the coherent vortex shedding at the wake behind bluff bodies. In particular, such wakes exhibit a strong intrinsic dynamics, characterized by the periodic detachment of coherent structures and the consequent *vortex shedding*, which typically occurs at a dominant frequency, ϖ. Such shedding is the result of the absolute unstable nature of the recirculation region formed behind the body, which behaves as an *oscillator* (Huerre and Monkewitz, 1990), insensitive to external noise of low amplitude.

As detailed by Gerrard (1966), the interaction between opposite shear layer configures a massive separated region which is characterized by the equilibrium of mass fluxes filling and emptying the recirculating region. The mass equilibrium is set when the entrainment along the generated free shear layer and the downstream vortex shedding are compensated by the recirculating flow, that generates an intense low pressure region close to body base which is characterized by their length, L_r (see Fig. 1.2b) and their bluffness, H_r. In general, the extension of the recirculating flow surrounded by free shear layers, and the dynamics of the periodic vortex shedding, depends strongly on the Reynolds number Re, which is defined as $Re = U_\infty l/\nu$, where l is a characteristic bluff body length, U_∞ the free-stream velocity and ν the kinematic viscosity of the surrounding fluid. Similarly, the dominant shedding frequency can be characterized by means of the non-dimensional Strouhal number, $St = \varpi l/U_\infty$.

Although the complex wake features are well-identified in the literature and their strong connection to aerodynamic drag is clear, the exact relation between both remains a challenge. Starting from D'Alembert paradox and Kirchhoff (1869) hypothesis, the connection between wake flow and aerodynamic drag theory was deeply analyzed by Roshko (1993). His model, based on a the analysis of a control volume defined about the time-averaged recirculation bubble, consists of a balance of the averaged forces on the recirculation region, which allows to estimate the pressure force over the body base. Roshko (1993) stated that, on average, the base pressure is balanced by the pressure, and the normal and shear Reynolds stresses acting on the separatrix (see red dashed line in Fig. 1.3). Then, for

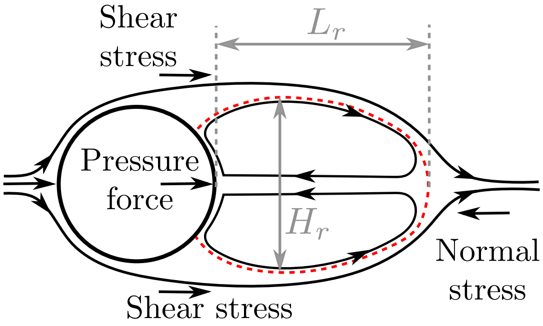

Figure 1.3: Sketch of a circular cylinder averaged wake adapted from Grandemange (2013) and Brackston (2017).

a bluff body, the drag is strongly linked to the dissipation of turbulent structures in the wake, or their vorticity. Therefore, a wake presenting significant unsteadiness will presumably have a high drag, since the dampening of these fluctuations will reduce the Reynolds stresses (Brackston, 2017). Moreover, the base pressure is also related to the shape of the separated region. Thus, a short recirculation bubble is associated to high values of drag since the sharp separatrix curvature implies a low pressure distribution over the boundary of the separated region. In addition, Roshko (1955) experimentally concluded that the base pressure is recovered when wake bluffness, H_r, is reduced. Additionally, any asymmetry on the flow will induce lateral forces, which are shown to contribute as well to the generation of drag (Grandemange et al., 2015).

The previously described features are shared by bluff body wakes, although depending on the body geometry, there may exist some specific characteristic which need to be analyzed separately. In fact, Fig. 1.2 presents a wide range of geometries that will be classified into three main groups for the following analysis, namely: two-dimensional bodies (e.g. cylinders or prisms), axisymmetric bodies (e.g. spheres, disks or slender revolution blunt bodies) and three-dimensional blunt-based bodies (e.g. as simplified models of real vehicles).

1.2.1 Two-dimensional geometries

In this Section, some common features of two-dimensional long bluff bodies will be described, highlighting also the eventual differences between body geometries. In particular, the wake behind circular cylinders represents one of the most studied flows in the literature (see e.g. Williamson, 1996), and is characterized by the interaction of two shear layers of opposite vorticity sign, which leads to the development of a wide vortex street behind the body. The same type of dynamics is found for wakes behind rectangular or D-shaped prisms, which are also commonly referred to as cylinders in the literature. The differences between geometries, which will be subsequently discussed, stem from the boundary layer

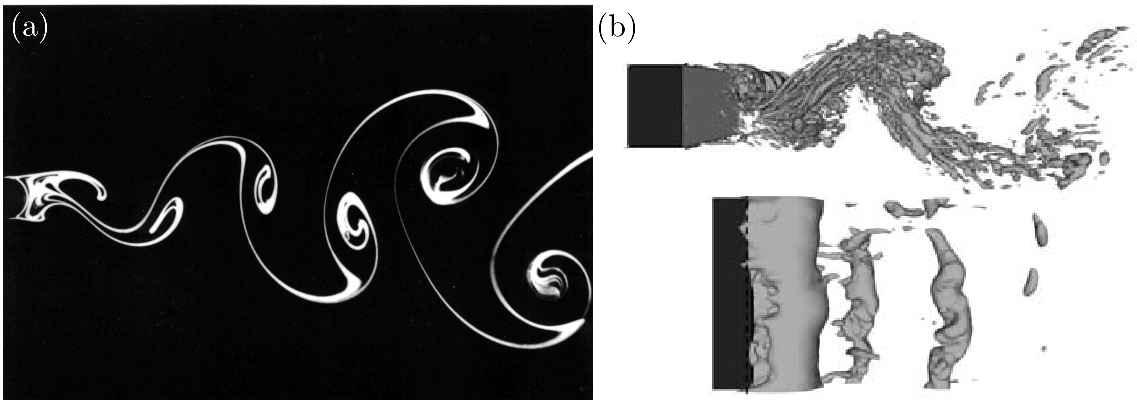

Figure 1.4: Flow topologies of wakes behind two-dimensional bodies. (a) Bénard-von-Kármán street behind a circular cylinder at $Re = 140$ (Van Dyke, 1982). (b) Instantaneous vortical structures in the wake of a D-shaped body at $Re = 4200$ (Park et al., 2006).

separation, which for the case of circular cylinders do not have a fixed detachment point, whereas for blunt-based bodies the separation occurs always at the rear trailing edges.

Different wake regimes behind cylinders are observed as the Reynolds number increases. At very low Re, the flow remains attached to the cylinder and does not produce any recirculating region ($Re < 5$). Once such recirculation region is formed, it becomes unsteady over a certain critical Reynolds number ($Re = 47$) and the periodic shedding of vortices starts, forming the Bénard-von-Kármán street, as depicted in Fig. 1.4(a). The flow unsteadiness occurs through the amplification of flow perturbations on the separated shear layers whose interaction generates the periodicity by means of a Hopf bifurcation (Provansal et al., 1987). When Re is further increased ($Re > 190$), the wake becomes three-dimensional (Roshko, 1993), and different modes of instability are present at the flow. Within the turbulent regime, secondary shear layer instabilities occur leading to the appearance of numerous time and length scales on the wake. Finally, for $Re > 10^5$, the separation point is modified, giving rise to the drag crisis, where the wake bluffness is strongly reduced (Williamson, 1996). The intense periodic vortex shedding is also a major feature of wakes behind D-shaped cylinders (see e.g. Fig. 1.4b), although such geometries do not undergo any drag crisis, due to the fact that the separation point remains fixed at the rear edges regardless of the Reynolds number. Besides, the characteristic vortex shedding frequency remains almost constant for a wide range of the Reynolds number, being it approximately $St \sim 0.2$. Such value, however, is slightly larger for blunt-based cylinders (Bearman, 1965).

Additionally, such intense vortices are related to low pressure cores, in such a way that their formation in the near wake dramatically affects the base pressure and the aerodynamic forces. Moreover, the associated velocity fluctuations at the wake play a significant role on the generation of Reynolds stresses, which, as it has been previously discussed, are also related to important drag variations. Thus, for such type of flows, the

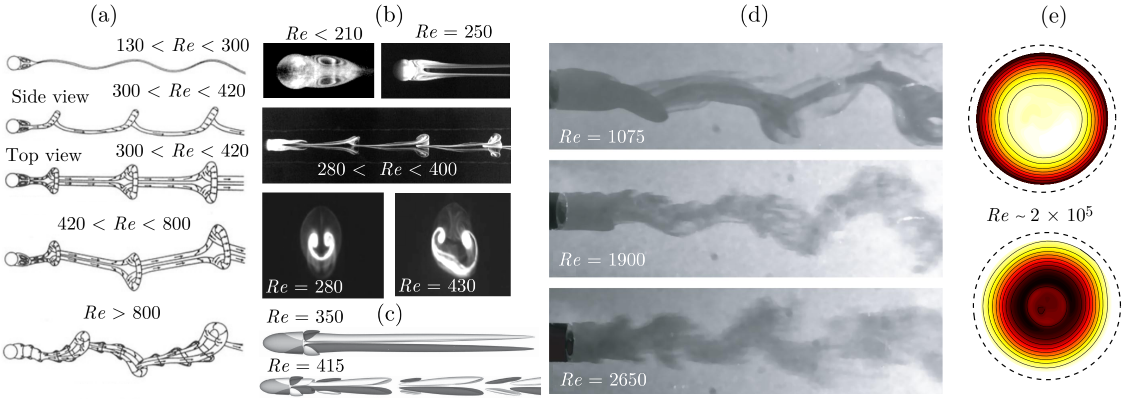

Figure 1.5: Wakes behind axisymmetric bodies. (a) Flow regimes at the wake behind a sphere (Sakamoto and Haniu, 1990). (b) Dye visualizations of sphere wake flow at different Re numbers (Nakamura, 1976; Thompson et al., 2001; Chrust et al., 2013). (c) Contours of constant streamwise vorticity behind a slender blunt-based axisymmetric body (Jiménez-González, 2013). (d) Visualizations of the wake behind a slender blunt body for several values of the Reynolds number (Sevilla and Martínez-Bazán, 2004). (e) Base pressure distribution for a turbulent axisymmetric wake: mean (top) and root-mean-square of the fluctuating component (bottom) topologies (Rigas et al., 2014).

Bénard-von-Kármán street dominates the dynamics and its control is relevant when drag reduction needs to be achieved.

1.2.2 Axisymmetric bodies

The wakes behind axisymmetric bodies are more complex than those previously described for two-dimensional geometries. For instant, the wake behind a sphere, which represents a classical flow, exhibits a rich and complex wake dynamics in spite of its simple geometry. In particular, such wake undergoes several bifurcations as Re grows (see Fig. 1.5a), in the route towards a fully turbulent flow (Ruelle and Takens, 1971; Sakamoto and Haniu, 1990). In this regard, as seen in Fig. 1.5(b), the wake remains axisymmetric until $Re = 210$ approximately, where a steady pitchfork bifurcation takes place (Fabre et al., 2008), giving rise to a wake featuring two steady and counter-rotating streamwise vortices which are symmetric with respect to an axial plane (see Fig. 1.5b). Secondly, a Hopf bifurcation renders the wake unsteady at $Re = 272$, leading to the shedding of vortex loops which preserve the previous symmetry plane, as shown in Fig. 1.5(b) (Tomboulides and Orszag, 2000). When the Reynolds number increases above $Re = 380$, a new wake regimes emerges, where the symmetry plane is no longer fixed and the azimuthal orientation of the shedding starts to oscillates randomly (Chrust et al., 2013).

Similarly, axisymmetric blunt-based bodies follow an analogous pattern of bifurcations and sequence of regimes as the Reynolds number increases, as it is displayed in Fig. 1.5(c). However, as the length-to-diameter aspect ratio increases, the wake is stabilized, and laminar transitions occurs at higher Reynolds number than for the sphere (Bohórquez et al.,

Figure 1.6: Simplified heavy vehicle models: slanted Ahmed body (top) and square-back Ahmed body (bottom), adapted from Choi et al. (2014).

2011; Bury and Jardin, 2012; Rigas et al., 2017). As shown by Bohórquez et al. (2011), the thicker profile of the boundary layer prior to separation point stabilizes the flow and elongates the recirculating region, thus delaying the transitions and reducing body drag (Mariotti et al., 2015). At moderate Reynolds numbers, the existence of high frequency instabilities in the mixing layers turns into large turbulent vortex loops shedding from the recirculation region, that preserve a coherent helical structure, as seen in Fig. 1.5(d) (Sevilla and Martínez-Bazán, 2004). Besides, at turbulent regimes with high values of Re, the wake is characterized by the random, azimuthal oscillation of the vortex detachment location, as studied recently by Grandemange et al. (2012b) and Rigas et al. (2014). The random nature of such long-time dynamics is manifested when the mean base pressure distribution and corresponding root-mean-square of the fluctuating component are computed, as in Fig. 1.5(e). Such axisymmetric distributions allow to infer that the loci of low pressure associated to the detachment of vortices, explore with the same probability the whole azimuth, when the time is sufficiently long. Finally, in addition to vortex shedding and the wake azimuthal random oscillations, several studies have highlighted another key feature for such wake flows, which is related to the existence of a long-time pulsation of the recirculating bubble, which leads to some unsteadiness of the near wake with a lower frequency than that characterizing the vortex shedding (Berger et al., 1990; Rigas et al., 2014).

1.2.3 Simplified models of road vehicles

The complex shape and the variety of length scales involved in real ground vehicles make it difficult their use in experiments or numerical simulations. Concerning wind tunnel tests, only a few facilities around the world allows to fit a real vehicle inside them without experiencing blockage problems. Thus, most of the studies related to the aerodynamics of real ground vehicles employ simplified and scaled models which mostly retain the main geometrical and flow features.

Numerous scientific works have been performed to study this kind of geometries and their characteristic, as detailed by Sovran (2012). In particular, one of the most investigated models was proposed originally by Ahmed et al. (1984), whose geometry is presented in Fig. 1.6. More precisely, there are two versions of the original Ahmed bodies, featuring, respectively: a slanted rear surface, which allows to study the influence of the slant angle (α); and a square-back, blunt-based, where the separation point is fixed. There has been a large number of studies devoted to analyze the flow around Ahmed-like models, both numerically (Krajnović and Davidson, 2005; Verzicco et al., 2002; Minguez et al., 2008; Guilmineau, 2008; Guilmineau et al., 2011; Lucas et al., 2017; Dalla Longa et al., 2019) and experimentally (Ahmed et al., 1984; Thacker et al., 2012; Rossitto et al., 2016; Grandemange, 2013; Barros, 2015; Li, 2017; Bonnavion, 2018). Such studies have helped to shed light on the flow topology behind the models, and how such features contribute to the aerodynamic forces. For instance, in the case of rear slanted surface model, the generation of a pair of streamwise counter-rotating vortices at the top edge of the slanted surface, leads to the large values of induced drag, so that their control is required to achieve efficient drag reductions (Ahmed et al., 1984; Hucho, 1998). Conversely, the square-back model does not present such vortical structures, although the associated drag is also important. Note that the work included at present Thesis will only consider the square-back Ahmed body as simplified three-dimensional model for real vehicles, so that in the following only such geometry will be analyzed.

As said before, for square-back models, the flow separation takes place always at the rear edges, however, the upstream boundary layer profile plays a significant role on the wake formation and recirculation length. In that sense, it should be noted that the frontal shape of such model may vary among the different studies, what sometimes leads to the flow detachment on the front (Barros, 2015; Bonnavion, 2018). Besides, most of the studies are performed with ground to replicate realistic flow conditions for road vehicles. The ground presence renders the wake asymmetric in the vertical plane and introduces another significant variable for the problem, namely the *ground clearance* or distance from the body to the floor. Therefore, the wake topology may be considerably affected by the ground clearance, thus modifying the associated lift force. Similarly, the model supports may modify the underbody flow, and consequently, alter the near wake topology.

As in the case of axisymmetric bodies, the flow behind the Ahmed body undergoes a similar pattern of bifurcations at laminar regime. Thus, as reported by Grandemange et al. (2012a) and Evstafyeva et al. (2017), the flow is initially steady for low values of Re, featuring a reflectional symmetry with respect to a vertical plane, while it is slightly asymmetric in the vertical direction on account of the ground effect. Then, a Hopf bifurcation takes places at $Re = 415$ approximately ($Re = 365$, experimentally), setting the unsteadi-

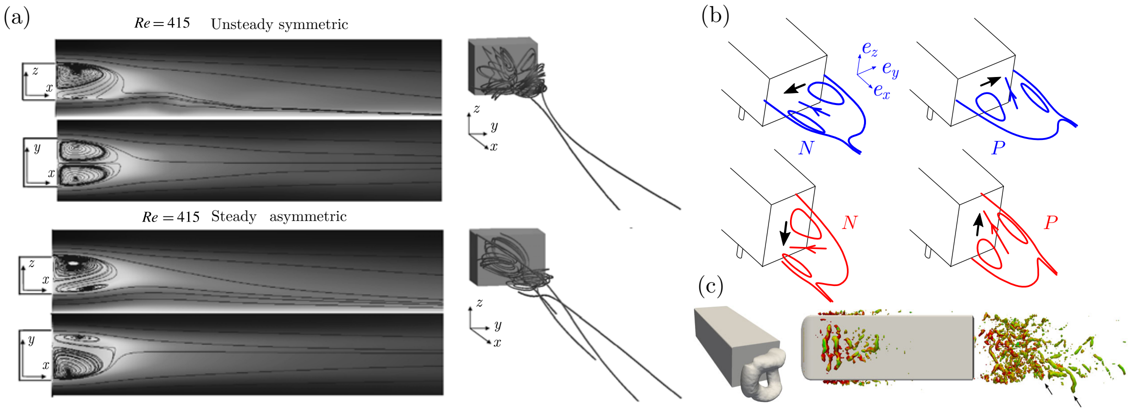

Figure 1.7: Wake behind square-back Ahmed bodies. (a) Laminar wake topology at $Re = 415$ from Evstafyeva et al. (2017). (b) Sketches of the recirculating bubbles for horizontal (top) and vertical (bottom) steady asymmetric instabilities, displaying P and N wake states (Bonnavion, 2018). (c) N wake state topology in turbulent regime obtained through numerical simulations (Lucas et al., 2017).

ness while keeping the planar symmetry of the wake. However, such regime is unstable, and after some time, the wake becomes steady again and a new asymmetric state appears at this Reynolds number (see Fig. 1.7a). Such regime is associated to the destabilization of *reflectional symmetry breaking* modes (RSB), and therefore renders the wake horizontally asymmetric. Interestingly, depending on the geometric and initial conditions, the wake may be either fixed on one of two mirrored deflected horizontal locations of the Ahmed body base (see Fig. 1.7b). Thus, given the sign of the base pressure gradient characterizing these two asymmetric wake states, we can distinguish between P (positive) or N (negative) asymmetric states. That said, a further increase of the Reynolds number above a critical value defined by the interval $415 \leq Re \leq 435$ (according to previous experiments and numerical simulations) leads to a periodic vortex shedding regime, that preserves the global wake asymmetric structure defined in the previous regime. Thus, in view of such results, the wakes behind three-dimensional blunt-based bodies, either axisymmetric or square-back models, seem to share a common scenario of bifurcations and laminar regimes (Brackston, 2017).

For turbulent flow regimes, the symmetry of the problem is restored on average, and the previously mentioned asymmetric states are not fixed anymore. Thus, the wake begins to switch randomly between the two mirrored deflected states, which are explored with the same probability, similarly to the azimuthal wake reorientations described for axisymmetric bodies. The coexistence of both asymmetric states is commonly called *bistability* and it was firstly found by Herry et al. (2011) for a three-dimensional double backward facing step geometry. In addition, Grandemange et al. (2013a,b) characterized the bistability in the wake behind the square-back Ahmed body, identifying the ground clearance and the cross-sectional body aspect ratio as key parameters for the presence of such random long-time dynamics. In particular, they found that the direction of such bistable switching may be varied from an horizontal plane to a vertical plane for cross-section height-to-width aspect ratios larger than one, as it is sketched in Fig. 1.7(b). Additionally, the yaw angle is also shown to play a relevant role, since it modifies the probability equilibrium between horizontal asymmetric states, fixing a preferred state for values as low as 0.5°. It should be noted that, from a mathematical point of view, this bistability results from an imperfect supercritical pitchfork bifurcation that can be modeled by means of a Langevin equation, as described by Cadot et al. (2015) and Rigas et al. (2015).

In addition to the aforementioned bistability, the turbulent wake behind the Ahmed body features a complex short-time dynamics which is mainly characterized by three distinguished mechanisms, namely: a coherent vortex shedding with a dominant frequency of $St \sim 0.2$ (Grandemange et al., 2013b; Barros et al., 2016a), together with a low frequency pulsation of the recirculation bubble (at $St \sim 0.07$ according to Khalighi et al. (2001); Volpe et al. (2015)), and a high frequency shear layer instability mechanism (Duell and George, 1999; Barros, 2015), whereby short-scale vortical structures roll up at the mixing layers. Figure 1.7(c) shows some of these features at the turbulent wake, i.e. an asymmetric pressure distribution for one of the two mirrored deflected state (left) and vortical structures detaching from the corresponding deflected near wake (right).

Interestingly, the existence of the aforementioned asymmetric states leads to base pressure gradients that induce lift or side force (depending on the plane where the asymmetry is set, what relies on the body base aspect ratio and the experimental conditions). Such induced lateral forces are associated to larger values of the drag coefficient, as demonstrated by Grandemange (2013). Besides, the impact of vortex shedding on the drag coefficient is significantly lower than in the case of two-dimensional bluff bodies. However, the contribution of both features to drag still remains unclear.

1.3 Flow control strategies

A wide variety of strategies has been proposed in the literature to control flow instabilities and to improve the aerodynamic properties of bluff bodies. Different classifications of such strategies can be made for a systematic analysis. For instance, a first distinction may be done in terms of the energy requirements, depending whether they need external energy to operate or not, i.e. *active* or *passive* control techniques respectively. Besides, the actuation may be guided by some type of input information from the flow, being it the case of *closed-loop* or *feedback* approach; or conversely, does not require any kind of input, as in a *open-loop* approach. Several examples of different control devices proposed in the literature are shown in Fig. 1.8. Also, note that in the work included in the present dissertation, no closed-loop strategies were used, and therefore, in the remaining of this Chapter, only closed-loop strategies will be described.

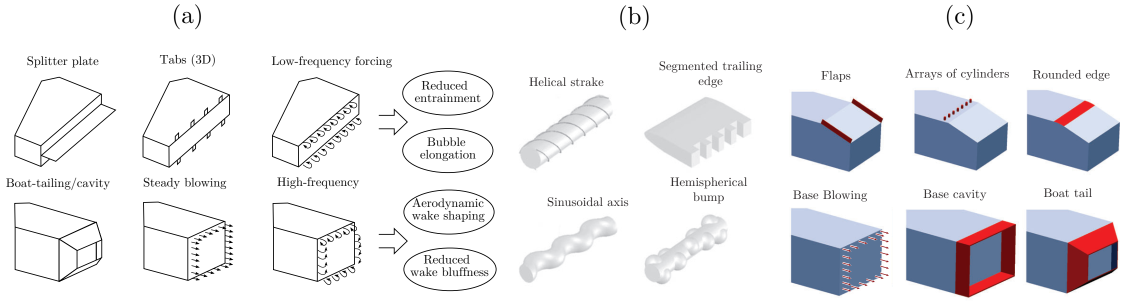

Figure 1.8: Different strategies for bluff bodies wake control and drag reduction. (a) Overview of representative drag reduction devices for blunt-based bodies wakes, adapted from Barros et al. (2016b). (b) Three-dimensional forcing of two-dimensional bluff bodies for aerodynamic purposes (Choi et al., 2008). (c) Rear control strategies applied for slanted and square-back three-dimensional blunt geometries (Choi et al., 2014).

Due to the important role of the near wake region to the drag coefficient, whose contribution is estimated to be approximately a 25% (see Fig. 1.1b), many traditional strategies focus on the base pressure recovery, as those proposed by Gerrard (1966) and Roshko (1993). In particular, such flow control strategies act mainly reducing the wake entrainment and modifying the flow separation, what translates into the elongation of the recirculation bubble or a reduction of the corresponding bluffness. Examples of such methods are summarized in Fig. 1.8(a), and include: splitter plates, tabs, steady or periodic blowing, and boat-tailing or rear cavities. More precisely, the splitter plate may be used in two-dimensional or long aspect ratio bodies to prevent the interaction between free shear layers, what induces a downstream displacement of the vortex formation and a delay on the closure of the recirculation region. As a consequence, the base pressure increases dramatically and the drag coefficient is significantly reduced (Roshko, 1955). Similarly, Choi et al. (2008) presented a review about the effect of three-dimensional perturbations on the wake behind two-dimensional bluff bodies, including the analysis of helical strakes, bumps and irregular rear edges. In summary, a similar control mechanism is found whereby the three-dimensionality acts breaking the coherence at the near wake, what increases the recirculation bubble length and recovers the base pressure, while attenuating the strength of vortex shedding (see Figs. 1.8a,b). In the context of active control strategies, Pastoor et al. (2008) and Krajnović and Fernandes (2011) employed low frequency forcing in the wake of a two-dimensional D-shaped body, to act on the vortex shedding by delaying the shear layer interaction, what efficiently reduced the vortices magnitude and consequently the fluctuating drag coefficient.

Regarding simplified models of heavy vehicles, a wide number of control strategies have been analyzed in Choi et al. (2014), and some of them are presented in Fig. 1.8(c), for slanted (top) and square-back (bottom) Ahmed bodies. For the slanted model, the control strategies are mostly focused on avoiding the flow separation or reattaching the flow upwards from the body base (Fourrié et al., 2011; Beaudoin and Aider, 2008; Pujals et al., 2010). On the other hand, the control strategies applied to the square-back Ahmed body concern similar techniques as those previously described for blunt-based two-dimensional bodies, as splitter plates (Gilliéron and Kourta, 2010; Khalighi et al., 2001; Duell and George, 1999), periodic forcing (Barros et al., 2016a,b), jets (Brackston et al., 2016; Li et al., 2017; Evstafyeva et al., 2017) or rear cavities and flaps (Grandemange et al., 2015; Lucas et al., 2017; Bonnavion and Cadot, 2018), whose effect will be analyzed in depth below.

In the case of axisymmetric bodies, the physical mechanisms that allow to reduce the drag are also related to the increase of the recirculating region length or the reduction of their bluffness. In particular, most of the studies are focused on the control of the unsteady global dynamics (Mair, 1965; Viswanath, 1996; Sevilla and Martínez-Bazán, 2004; Bohórquez et al., 2011; Jiménez-González et al., 2013, 2014). In the context of turbulent regimes, ventilated cavities have shown to recover the base pressure by reducing the wake asymmetry (García de la Cruz et al., 2017). Regarding open-loop strategies, low frequency forcing seems to be more efficient in terms of base pressure increase than high frequency ZNMF (zero-net-mass-flow) jets (Morrison and Qubain, 2009), although the use of pulsed jets at high frequency provides also with important aerodynamic improvements as shown by Oxlade et al. (2015).

Apart from the aforementioned classical techniques, control approaches based on adjoint sensitivity techniques have become widely used in the flow control community during the recent years. In particular, such approaches rely on the global nature of flow instabilities, whereby a small, localized perturbation on the flow may significantly alter the whole wake dynamics. As shown in the seminal work of Strykowski and Sreenivasan (1990), the unsteady global mode at the wake behind a circular cylinder can be experimentally attenuated by placing a small control cylinder at certain regions of high sensitivity in the near wake. A similar study was experimentally undertaken by Parezanović and Cadot (2012) at the turbulent wake behind a D-shaped cylinder, showing that the vortex shedding frequency and the base pressure can be significantly altered when the perturbation is placed in the vicinity of the shear layers. Another experimental sensitivity analysis has been recently performed within the context of vortex-induced vibrations by Jiménez-González and Huera-Huarte (2017), at the wake behind a flexibly-mounted circular cylinder, demonstrating that the placement of small cylinders at similar sensitive regions of the near wake may lead to important attenuation of the vibrations amplitude. Such experimental background is supported by several theoretical works based on adjoint sensitivity approaches, which have helped identifying the structural sensitivity of global modes both in laminar (Marquet et al., 2008) and turbulent wakes behind cylinders (Meliga et al., 2012). Similarly, Meliga et al. (2014) computed the sensitivity of drag and lift forces to localized perturbations for the flow around a square cylinder under steady, unsteady and turbulent

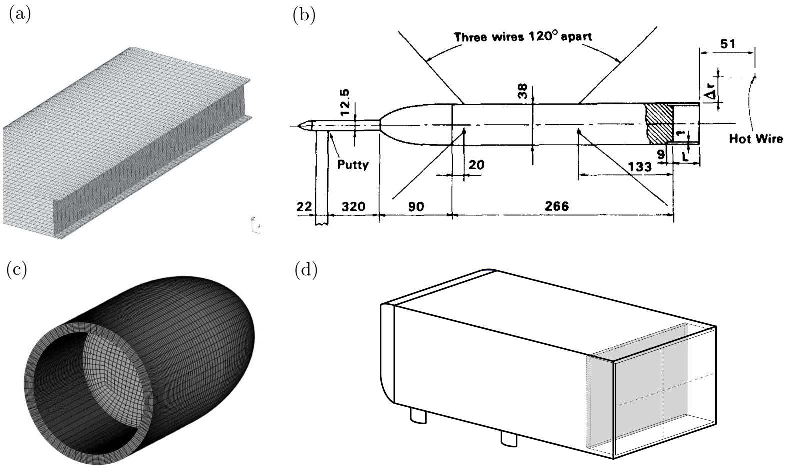

Figure 1.9: Use of base cavities as control devices for different bluff bodies. (a) Two-dimensional D-shaped body (Martín-Alcántara et al., 2014). (b, c) Axisymmetric bodies of different length-to-diameter aspect ratio (Morel, 1979; Sanmiguel-Rojas et al., 2011). (d) Square-back Ahmed body (Evrard et al., 2016).

conditions, showing that a important decrease or increase of both drag and lift coefficients may be obtained depending on the region where the control cylinder is placed. Interestingly, these sensitivity distributions of aerodynamic forces could be used to guide shape modifications of bodies or control devices, through optimization process, to improve the aerodynamic performance, as shown by Othmer (2014) for real vehicles.

After such review, two particular control strategies will be analyzed in depth, on account of their relevance in practical applications and their efficiency to control the wake and reduce the drag. In particular, base cavities will be first presented as efficient passive devices, whereas the steady blowing will be subsequently studied as a more complex active method.

1.3.1 Base cavities

Among all the previously presented control strategies, the use of base cavities or boat-tailing have been shown to be very efficient in terms of drag reduction regardless of the bluff body geometry concerned (see Fig. 1.9). For instance, Nash et al. (1963) reported a base pressure recovery of nearly a 50% in the wake of a two-dimensional body when a extended cavity was placed at the trailing edge. Part of this drag improvement comes from the attenuation of the vortex shedding process (Kruiswyk and Dutton, 1990; Cai and Chng, 2009; Martín-Alcántara et al., 2014). Furthermore, Molezzi and Dutton (1995) experimentally investigated the interaction between the instantaneous separated flow and the cavity plates, finding that the drag reduction is linked to an increase of the vortex shedding frequency.

The effect of a rear cavity implemented on axisymmetric bodies was investigated initially by Morel (1979) and Viswanath (1996), who reported smaller base drag reduction than those obtained for two-dimensional bodies. In particular, the modification of the periodic vortex shedding does not seem to influence the drag coefficient significantly. More precisely, as shown by Sanmiguel-Rojas et al. (2011) for laminar regimes, the cavity attenuates the unsteady nature of the flow, and modifies the mean near flow, inducing a downstream displacement of the separated vortical structures (associated to low pressure values). Such modifications translate into base pressure recovery and consequently, to the drag coefficient improvement.

In the case of square-back Ahmed models, Evrard et al. (2016) found that a deep base cavity was able to provide a 9% drag reduction and to cancel the bistable dynamics and the wake asymmetry induced by the deflected RSB modes. However, it is not clear how much drag reduction can be attributed to the increased distance between the body base and the low pressure recirculating cores at the wake or to the flow symmetrization through the mitigation of the RSB states and their associated induced drag. Similar results were found for industrial-scale models (Bonnavion, 2018; Grandemange et al., 2015) or real vehicles (Irving Brown et al., 2010). Similarly, boat-tailing has been also found to be an efficient method, even improving the results of base cavities under certain conditions, due to the important reductions of the wake size (Han et al., 1992; Khalighi et al., 2012; Choi et al., 2014). In any case, the performance of rear cavities in terms of drag reduction is strongly related to their depth, in such a way that a deeper cavity provides with larger drag reductions. However, from the practical point of view, this fact may be problematic when they are implemented in real vehicles as add-on devices, since there are usually severe restrictions for the size of additional systems and their design, thus limiting the potential drag reduction provided by deep cavities.

1.3.2 Steady base blowing

Within the framework of active control strategies, rear blowing is one of the most simple and studied approaches in the literature (see Fig. 1.10), due to its efficiency to reduce the drag and to attenuate the vortex shedding. The works of Wood (1964) and Bearman (1967) represents classical studies, where a steady base blowing of velocity U_b is applied at the base of blunt-based profiles. In particular, Bearman (1967) showed that a perimetric air blowing is able to delay the interaction between separated shear layers, leading to the increase of the vortex formation length in a similar manner to a passive splitter plate. Also, he obtained a base pressure recovery of nearly 30% when the blowing was applied at the top and bottom trailing edges, while removing the regular vortex street from the wake, as displayed in Fig. 1.10(a). Similar results were obtained by Wood (1964) by steadily blowing at the center of the base, as depicted in Fig. 1.10(b). More recently, Sevilla and Martínez-Bazán (2004) used a base blowing or *base bleed* to control the turbulent wake behind an axisymmetric body (Fig. 1.10c), showing that, for a sufficiently high base-to-

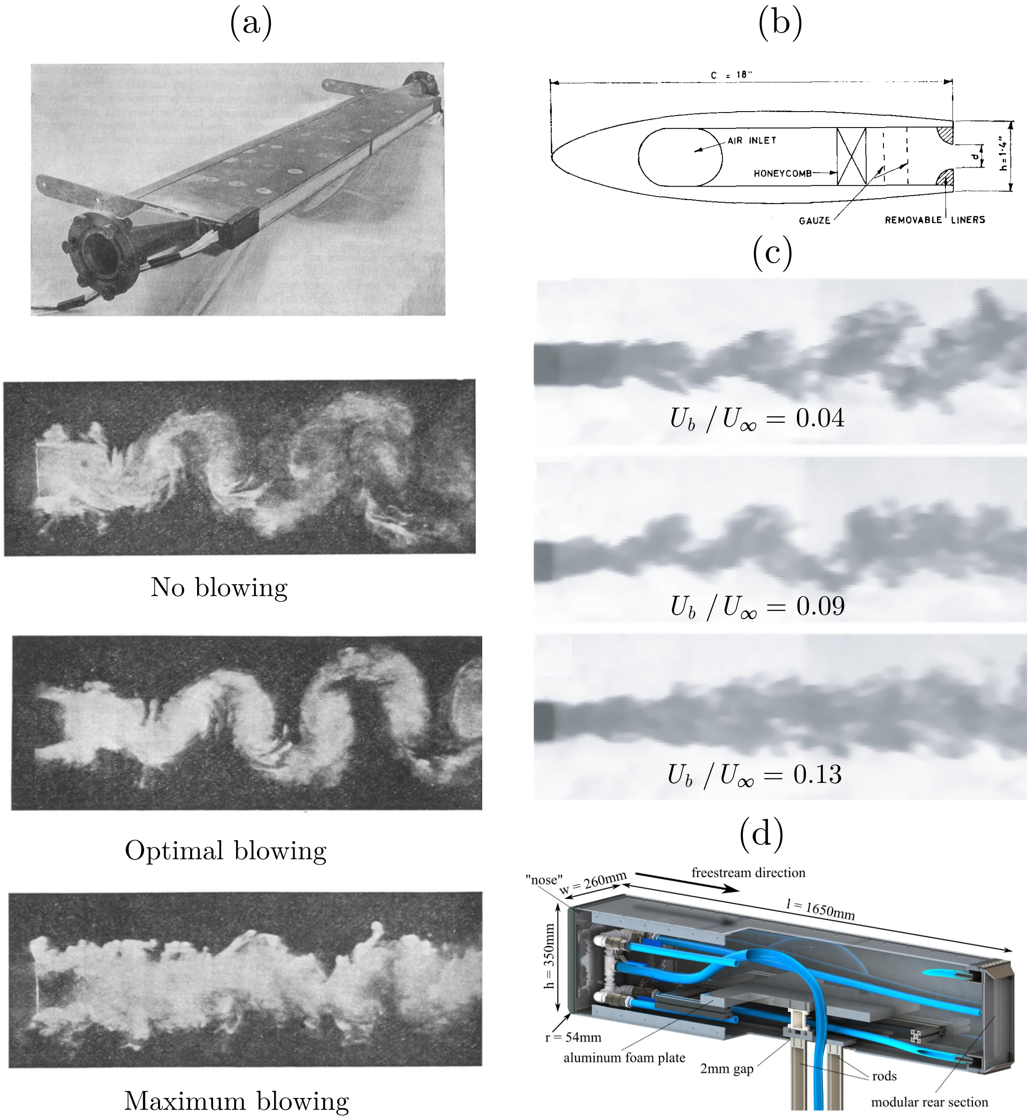

Figure 1.10: Steady base blowing. (a) Experimental model and wakes corresponding to different blowing amplitudes, adapted from Bearman (1967). (b) Sketch of base bleed device for a two-dimensional airfoil from Wood (1964). (c) Wake topology for several base-to-free-stream velocity ratios in the wake of an axisymmetric body (Sevilla and Martínez-Bazán, 2004). (d) Combination of perimetric steady jets and boat-tailing cavity for a rectangular three-dimensional body (Schmidt et al., 2015).

free-stream velocity ratio, U_b/U_∞, the large scale coherent vortex street is inhibited and the mean wake flow becomes axisymmetric on average.

Steady perimetric blowing has been also applied on square-back blunt-based bodies (see e.g. Howell et al., 2003; Rouméas et al., 2009; Wassen et al., 2010; Littlewood and Passmore, 2012), obtaining important drag reductions, whose values depend highly on the spatial configuration of the actuation and the blowing orientation. Thus, when the air injection is efficiently introduced in the separated region, a larger base pressure recovery can be achieved. However, the effect of steady blowing on the RSB modes has not been yet investigated, in spite of its relevance for practical applications. Besides, steady blowing can be also efficiently combined with other passive devices to improve the total aerodynamic performance. In this regard, Woszidlo et al. (2014) and Schmidt et al. (2015) used steady jets in combination with a boat-tailed base cavity (see Fig. 1.10d), achieving a drag reduction of nearly 30% (without accounting blowing power needs). Similarly, Khalighi et al. (2012); Abramson et al. (2011) and Barros et al. (2016b) explored also the efficiency of directing the flow towards the center of the wake, by means of devices that fostered the Coanda effect, finding important base pressure recoveries.

Consequently, the use of steady blowing arises as a powerful solution to improve the aerodynamic features of bluff bodies, although its efficiency should be further investigated under more realistic conditions, including cross-wind or transient flow, as a previous step to any application in industrial vehicles.

1.4 Outline of the dissertation

The present dissertation is organized in two different parts. On the one hand, Part I is focused on the design of improved base cavities in terms of drag reduction for two-dimensional bodies. In this regard, Chapter 2 consists of a numerical study, devoted to obtain an optimized shape for a base cavity placed at the rear part of a D-shaped two-dimensional body, whose aim is to minimize the drag coefficient and wake fluctuations at transitional regimes. To obtain such shape, two-dimensional adjoint sensitivity and shape optimization techniques are applied to design an improved version of a classical straight cavity. A comparative study between the optimized cavity and the straight one is subsequently performed by means of three-dimensional, turbulent simulations. Next, Chapter 3 will be devoted to evaluate the performance of the optimized cavity as control device, under transient conditions, and comparing it with the use of a straight cavity. In particular, experiments and numerical simulations are carried out for different impulsive accelerations of the body, implementing both rear devices.

On the other hand, Part II focuses on the experimental analysis of wakes behind simplified models of road heavy vehicles and their control. First, Chapter 4 studies the performance of the previous optimized, curved cavity implemented on the square-back

Ahmed body, in comparison to the straight cavity, under different yaw angles, to analyze the effect of cross-wind. The geometry of the curved cavity is based on a three-dimensional adaptation of the optimized profile obtained in Chapter 2 by means of adjoint sensitivity and shape optimization approaches. Additionally, Part II includes two other chapters dedicated to the wake control through rear steady blowing. Thus, Chapter 5 studies the effect of a steady, perimetric blowing on the static RSB and periodic vortex-shedding modes at the wake behind the square-back Ahmed body, for several blowing configurations and ratios. Following the same approach, Chapter 6 analyzes the influence of the blowing density on the wake properties. To that aim, three different gases (i.e. air, helium and carbon dioxide) have been used as blowing fluids, to comparatively evaluate the effect of the blowing density on the wake topology and force coefficients. Finally, in Chapter 7 the main conclusions of the previous chapters are drawn, together with some ideas on future perspectives.

Part I

Drag reduction devices in two-dimensional bodies

CHAPTER
TWO

Optimized rear cavities for slender blunt-based bodies

Abstract

In this Chapter, we have investigated the use of the adjoint sensitivity formulation to design efficient passive control strategies aiming at reducing the drag coefficient of a slender blunt-based body with a straight rear cavity. In particular, two control techniques consisting in wake modifications generated by placing small control cylinders in the near wake and by geometry variations of the cavity respectively, have been evaluated numerically. Thus, we have computed the turbulent flow sensitivity of the drag coefficient to localized forcing for a two-dimensional body with a straight cavity at $Re = 2000$, showing that the highest values of sensitivity are obtained near the cavity edges. The effect of placing a pair of control cylinders around the most sensitive locations has been studied, obtaining a largest drag reduction of only 0.6%. Alternatively, a most efficient control strategy based on shape optimization has been thoroughly investigated. The drag shape sensitivity on the body surface (Othmer, 2014), computed using the former linear adjoint formulation, has been used in combination with a free-form deformation algorithm (Han et al., 2011), to guide the local structure deformations of the cavity, providing progressive drag reductions until the optimal, curved, shape is achieved. To deeply analyze the physical mechanisms behind the drag reduction provided by the optimal cavity, we have also performed more realistic three-dimensional numerical simulations using an IDDES model at two different Reynolds number, $Re = 2000$ and 20000. The results corroborate the sensitivity analysis, obtaining a total drag reduction of 25.6% at $Re = 2000$, and 43.9% at $Re = 20000$, with respect to the original body without cavity. These reductions are mainly achieved by the inwards deflection of the flow upon detachment and a flow deceleration at the trailing edge due to an adverse pressure gradient introduced by the curved shape of the optimal cavity walls. Both combined effects reduce the size of the recirculation bubble formed behind the body, increasing the base pressure, and consequently, decreasing the drag. Furthermore, the addition of the optimized base cavity reduces the amplitude of the velocity fluctuations behind the body and stabilizes the wake, which becomes less chaotic and more two-dimensional.

This Chapter is comprised, in part, in the paper: "Drag reduction of slender blunt-

based bodies using optimized rear cavities", by Lorite-Díez, M., Jiménez-González, J. I., Gutiérrez-Montes, C. & Martínez-Bazán, C., published in the Journal of Fluids and Structures (Lorite-Díez et al., 2017).

2.1 Introduction

The flow around heavy vehicles, such as trucks or buses, is highly three-dimensional, chaotic and turbulent. This flow is mainly characterized by a massive flow separation, which induces the development of a wake behind the body and the periodic shedding of vortices, resulting into the appearance of major fluctuating aerodynamic forces in the structure. These forces have a great impact on the vehicle stability and, more importantly, on the fuel consumption, the latter being governed by the drag force. In this regard, it is estimated that 20% of the whole energy in a heavy vehicle is devoted to overcome the aerodynamic losses (Choi et al., 2014). Thus, these kinds of flows have been extensively studied in the last decades (Ahmed et al., 1984; Han et al., 1996; Pastoor et al., 2008) with the aim at better understanding the present features and the governing physical mechanisms as well as to develop new, more efficient flow control methods or to improve the existing ones in terms of drag reduction and flow induced loads.

Many of the aforementioned investigations considered simplified vehicle models (see e.g. Ahmed et al., 1984; Pastoor et al., 2008), which accurately reproduce the flow conditions around real heavy vehicles. As result, a large amount of approaches and devices have been proposed, which can be grouped into active and passive flow control techniques, the latter being easier to implement. In general, these strategies aim at modifying the near wake, and can be implemented either by means of open (Parkin et al., 2014) or closed (Henning et al., 2007; Pastoor et al., 2008) flow control loops. For instance, regarding active flow control systems, sophisticated and complex devices have been studied, some of them being based on the use of actuators (Beaudoin et al., 2006), suction/blowing strategies (Sevilla and Martínez-Bazán, 2004; Sanmiguel-Rojas et al., 2009; Bohórquez et al., 2011; Pasquetti and Peres, 2015), or spinning motions (Jiménez-González et al., 2013, 2014). Their implementation in real problems usually requires an important power input, what limits somehow its applicability and efficiency and renders passive control systems more attractive because of their simplicity. Among other passive strategies, it is worth mentioning the works from Mair (1965) who studied the effect of including plates on the base of the body, Park et al. (2006) who introduced trailing edge modifications in the form of small tabs, those from Sanmiguel-Rojas et al. (2011); Cai and Chng (2009) and Kruiswyk and Dutton (1990) on the use of open base cavities or similarly Han et al. (1992); Mair (1978); Choi et al. (2014), on boat-tailed after-bodies. Besides, Martín-Alcántara et al. (2014) proposed a multi-cavity device that produces a maximum drag reduction of 25% at $Re = 20000$, obtaining additionally a less chaotic wake topology. Notwithstanding the aforementioned positive features, the performance of any type of rear cavity as a control mechanism is related to their depth, obtaining larger drag reductions as the cavity deepens (Sanmiguel-Rojas et al., 2011). In that sense, functionality requirements and practical geometrical limitations in vehicles usually restrict the depth, subsequently hindering its capability as control mechanism. Consequently, in order to overcome such limitations, it seems interesting to investigate any potential performance improvement of the addition of a base cavity with a fixed depth, for instance, by means of shape modification.

Most of the above investigations base the design of control strategies on the general knowledge of the physical mechanisms governing the flow around bluff bodies. Alternatively, the use of sensitivity analysis applied to flow control may help to precisely identify the regions which contribute the most to wake instability (Marquet et al., 2008; Meliga et al., 2012) or drag and lift generation (Meliga et al., 2014). This identification allows a more specific design and an optimal placement of control elements aiming at suppressing instabilities or reducing the drag, without having to carry out parametric studies or testing different locations empirically. In fact, these sensitivity analyses have been already satisfactorily proven, obtaining accurate predictions when compared with results from experimental work or numerical simulations (see e.g. Meliga et al., 2012; Parezanović and Cadot, 2012). Regarding aerodynamic forces, Meliga et al. (2014) have recently derived a linearized adjoint formulation to analyze the sensitivity of drag to local force perturbations on the flow around a square cylinder, for laminar and turbulent regimes. By simply introducing small control cylinders in those flow regions featuring the highest sensitivity, reductions up to 20% in the main drag were obtained. Consequently, this adjoint approach stands out as a powerful tool to maximize the drag reduction and to design optimized control devices. In that sense, adjoint-based optimization has long been recognized to be efficient for studies with large numbers of design variables, especially in the aerospace sector (Jameson, 1988; Burgreen and Baysal, 1996). In fact, Othmer (2014) has recently considered the use of adjoint shape optimization techniques applied to car aerodynamics, focusing on the reduction of drag force and using the open source computational fluid dynamics (CFD) toolbox OpenFOAM®. Interestingly, the combined use of sensitivity analysis and body topological modifications provides with efficient solutions for control devices or reduction of the aerodynamic forces acting on the body, which are achieved by means of iterative processes that characterize the sequential interactions between flow and structure. Since, in most applications, the geometry modifications are constrained by functionality and other requirements, it might be interesting to consider, as a solution for flow control and forces reduction, the implementation of control devices whose design stems from adjoint-based sensitivity and optimization analysis, what would ensure a high performance.

Following this idea, the present Chapter explores the use of adjoint formulation to assess the sensitivity of drag to flow and structure topological modifications, in the wake behind a blunt-based body with a base cavity, which is a widespread configuration in real wakes control applications (see e.g. Choi et al., 2014), in an attempt to evaluate the potential for improvement on the efficiency of rear cavities of fixed depth as passive control strategy. Thus, the study aims at achieving additional drag reduction on the wake behind a two-dimensional bluff body of semi-ellipsoidal nose and straight rear cavity, by analyzing the effect of small control cylinders in the wake (Meliga et al., 2014) and optimal geometry modifications of the cavity structure (Othmer, 2008). The predictions of drag reduction obtained by means of the adjoint formulation analysis and topological modifications, will be compared with results from numerical simulations of the flow around the obtained different geometries, which will help appraising the suitability of the sensitivity analysis for wake control and aerodynamics enhancement. Thus, the problem formulation and numerical techniques employed are first described in Sect. 2.2. Section 2.3 is devoted to results, showing first those from the sensitivity analysis of drag to local force perturbations in the wake (Sect. 2.3.1), followed by the evaluation of the inclusion of control cylinders in the regions of highest sensitivity by means of numerical simulations. Next, in Sect. 2.3.2, we present results from the shape optimization of the straight rear cavity, based on the projection of drag sensitivity maps into the body surface. Then, three-dimensional numerical simulations are performed to show the impact of the latter structure modifications on the turbulent flow, whose results are presented in Sects. 2.3.3-2.3.4, where the main flow features are discussed for two different Reynolds numbers, $Re = 2000$ and $Re = 20000$. Finally, the main conclusions are drawn in Sect. 2.4.

2.2 Problem description and numerical aspects

2.2.1 Flow configuration and governing equations

The three-dimensional turbulent flow of an incompressible free-stream of velocity U_∞, density ρ and viscosity μ around a two-dimensional bluff body of semi-ellipsoidal nose is considered herein. Figure 2.1 shows the scheme of the problem and computational domain, Ω, which aims to replicate the flow in a rectangular cross-section wind tunnel. The former domain is similar to those used in previous studies (Krajnović and Davidson, 2003; Pastoor et al., 2008; Guilmineau et al., 2011; Martín-Alcántara et al., 2014), and thus, appropriate for the present Chapter. The body of height H, length $L = 3.83H$ and spanwise width $W = 7.64H$, is embedded by the lateral walls and placed at the half-height of the computational domain. The body presents a streamlined front to avoid flow separation and is characterized by an ellipsoidal nose of major-to-minor-axes aspect ratio equal to 2. The front of the body is located $7.85H$ downstream from the inlet, whereas the domain outlet is placed at a distance of $21H$ downstream from the body base. The dimensions of the wind-tunnel considered as the computational domain are respectively $L_{wt} = 32.68H$, $H_{wt} = 21H$ and $W_{wt} = 7.64H$, with a geometric blockage of the model inside the numerical domain of approximately 5%. The body also implements a straight base cavity of depth $0.3H$ and wall thickness $0.05H$, similar to that proposed by Martín-Alcántara et al. (2014) and Evrard et al. (2016).

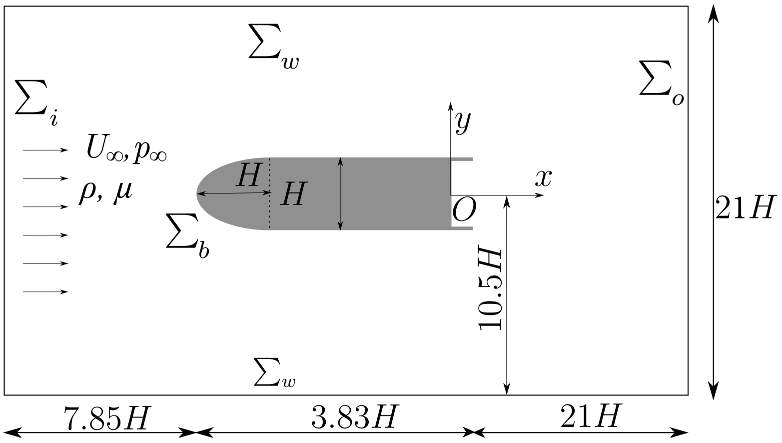

Figure 2.1: Scheme of the flow configuration and computational domain with the two-dimensional, semi-ellipsoidal body.

Under the above conditions, the characteristic length, velocity, time and pressure scales are respectively H, U_∞, H/U_∞ and ρU_∞^2. In the following, all variables will be made dimensionless using these scales, for example, pressure coefficient will be $c_p = (p_i - p_\infty)/(0.5\rho U_\infty^2)$, where p_i is the local static pressure and p_∞ the reference one. Consequently, the Reynolds number is defined as $Re = \rho U_\infty H/\mu$, however, the dimensionless frequency will be $St = \varpi h/U_\infty$, where ϖ is a frequency and h, not necessarily equal to H, the distance between the upper and lower edges of the cavity walls. The flow is governed by the incompressible Navier-Stokes equations,

$$\nabla \cdot \mathbf{u} = 0, \tag{2.1}$$

$$\frac{\partial \mathbf{u}}{\partial t} + \mathbf{u} \cdot \nabla \mathbf{u} + \nabla p - \frac{1}{Re}\nabla^2 \mathbf{u} = 0. \tag{2.2}$$

Besides, appropriate boundary conditions have been used, namely, a uniform fluid stream of velocity $(U_\infty, 0, 0)$, with a turbulent intensity of 1% and a characteristic turbulent length scale of $0.1H$ has been imposed at the inlet, Σ_i, whereas an outflow boundary condition has been applied at the outlet, Σ_o. Furthermore, a no-slip condition has been set at the remaining wall boundaries, i.e. at the body, Σ_b, the top, bottom and side boundaries, Σ_w.

As it has been previously outlined, the present Chapter can be divided into two different parts. A drag sensitivity study is first conducted, in which both the inclusion of control cylinders (Meliga et al., 2014) and the optimal shape geometrical modification (Othmer, 2008) of a base cavity device are subsequently analyzed in Sects. 2.2.2-2.2.3. For the sake of numerical feasibility, the flow is assumed to be two-dimensional in this part of the

Chapter. Secondly, in Sect. 2.2.4, the suitability in more realistic flows of this previously optimized shape is next evaluated, performing three-dimensional numerical simulations, which allow a complete characterization of the main wake features and drag reduction. For such studies, different numerical techniques and models have been used, which are next described.

2.2.2 Drag sensitivity to localized forcing

With the aim at improving the performance of rear cavities as drag reduction devices, we perform a sensitivity analysis of the drag coefficient to modifications of the flow around the body under investigation (Fig. 2.1), induced by a localized control force, **f**, which can be used to model the reacting forces generated by a small control cylinder placed near the body base, or any geometrical modification introduced on the body wall. For this purpose, we adopt the simplified adjoint-based steady analysis developed by Meliga et al. (2014), for unsteady flows, which is capable of retrieving the main information at the most sensitive regions around the body and the drag reduction values at the leading order. This simplified approach allows the determination of a steady sensitivity for unsteady flows, by only considering mean flow variables and the drag as a steady function of such mean variables. Thus, for any given unsteady physical variable, time-dependant variables are denoted by lower case letters a and time-averaged values by upper case letters $A = \overline{a}$. Hence, the mean drag coefficient, C_x, can be expressed as

$$C_x = \frac{2F_x}{\rho U_\infty^2 HW} = C_{xp} + C_{xv}, \tag{2.3}$$

where F_x is the time-averaged mean value of the axial component of the force acting on the body, C_{xp} and C_{xv} are the time-averaged pressure and viscous drag respectively. In a first order approximation, the mean drag variation δC_x induced by an infinitesimal control force $\delta\mathbf{F}$ is estimated by means of

$$\delta C_x = (\nabla_f C_x \mid \delta\mathbf{F}), \tag{2.4}$$

where $\nabla_f C_x$ is the mean drag sensitivity function, $\delta\mathbf{F}$ accounts for the mean component of the control force, and $(\ \mid\ )$ denotes the L_2 inner product in the space domain, Ω,

$$(\mathbf{u}_1 \mid \mathbf{u}_2) = \int_\Omega \mathbf{u}_1 \cdot \mathbf{u}_2 \; dxdy. \tag{2.5}$$

This simplified approach excludes the effects of the fluctuating component $\delta\mathbf{F}'$, and the mean flow correction through the coupling with fluctuating motion and the generation of Reynolds stresses (Maurel et al., 1995). However, Meliga et al. (2014) showed that the most sensitive regions are satisfactorily characterized, since control acts fundamentally via the mean component of the forcing in the flow around a bluff body, even for turbulent

$Mesh$	Number of cells (n)	C_x	$\xi_{C_x}(\%)$	St_{C_x}	$\xi_{St_{C_x}}(\%)$
# 1	$\sim 0.6 \times 10^5$	0.737	1.55	0.439	1.86
# 2	$\sim 1.0 \times 10^5$	0.750	0.23	0.434	0.46
# 3	$\sim 1.4 \times 10^5$	0.750	0.23	0.433	0.23
# 4	$\sim 1.8 \times 10^5$	0.751	-	0.432	-

Table 2.1: Grid sensitivity analysis for the two-dimensional simulations around a bluff body at $Re =$ 2000. Comparison among the values of the mean drag coefficient C_x and vortex shedding Strouhal number, St_{C_x}, obtained from the temporal evolution of c_x, using four different grids. The relative error, ξ, is calculated with respect to mesh #4, which features the largest number of cells, n.

regimes. Therefore, we adopt such strategy for our calculations, in order to identify potential improvements on the performance of the body base cavity, since it represents a good compromise between accurate predictions and limited computational cost.

The mean drag sensitivity $\nabla_f C_x$ is thus obtained by solving a Lagrangian formalism (see Meliga et al., 2014, for details), which considers the drag as the cost function to be minimized, subject to the control variable $\mathbf{F}$, i.e. the forcing, and satisfying the steady governing equations stemming by linearly disturbing the mean basic flow $(\mathbf{U}, P)$, whose time-averaged mean variations are accounted by $(\delta\mathbf{U}, \delta P)$. This linear *direct* system reads,

$$\nabla \cdot \delta\mathbf{U} = 0, \quad \nabla\delta\mathbf{U} \cdot \mathbf{U} + \nabla\mathbf{U} \cdot \delta\mathbf{U} + \nabla\delta P - \frac{1}{Re}\nabla^2\delta\mathbf{U} = \delta\mathbf{F} \quad \text{in } \Omega, \tag{2.6}$$

$$\delta\mathbf{U} = 0 \quad \text{in } \Sigma_b. \tag{2.7}$$

where all infinitesimal terms, $\delta\mathbf{U}$ and δP, are approximations to the mean flow disturbance components.

The sensitivity $\nabla_f C_x$ is then obtained by using a variational technique aiming at computing Lagrange multipliers, $\mathbf{U}^\dagger$ and $P^\dagger$, which hold, in principle, no physical meaning, and are chosen in such a way that variations of the Lagrangian functional with respect to the direct system variables, $(\mathbf{U}, P)$, vanishes. Thus, it can be demonstrated that

$$\nabla_f C_x = \mathbf{U}^\dagger, \tag{2.8}$$

where $\mathbf{U}^\dagger$ is, along with $P^\dagger$, the solution of the linear *adjoint* system,

$$\nabla \cdot \mathbf{U}^\dagger = 0, \quad -\nabla\mathbf{U}^\dagger \cdot \mathbf{U} + (\nabla\mathbf{U})^T \cdot \mathbf{U}^\dagger - \nabla P^\dagger - \frac{1}{Re}\nabla^2\mathbf{U}^\dagger = 0 \quad \text{in } \Omega, \tag{2.9}$$

$$\mathbf{U}^\dagger = 2\mathbf{e}_x \quad \text{on } \Sigma_b, \tag{2.10}$$

and will be, in the following, referred to as adjoint velocity and pressure respectively, due to the similarities between both direct and adjoint systems.

The solution of the adjoint system (Eqs. 2.9-2.10), requires the previous knowledge of the time-averaged mean flow variables, $(\mathbf{U}, P)$, i.e. the basic flow, which can be obtained from numerical simulations. In that sense, we have initially performed a numerical study of the turbulent flow around the body described in Sect. 2.2.1, as a first step to assess the drag sensitivity of the basic flow. We have limited our study to a low value of Reynolds number, i.e. $Re = 2000$, in order to minimize the deviation of the simplified Eq. (2.4) from the total drag variation that would be obtained if the feeding of force fluctuations through the Reynolds stresses were considered. To this end, incompressible turbulent unsteady two-dimensional simulations have been performed using OpenFOAM open source finite-volume toolbox, by implementing a RANS (Reynolds Averaged Navier-Stokes equations) $k - \omega$ model to obtain the basic flow. We have used second order upwind and Green-Gauss linear centered discretization schemes for the spatial terms, a Crank-Nicholson scheme for the time integration, while the pressure-velocity coupling has been treated through the Pressure-Implicit Split-Operator (PISO) algorithm (Issa, 1986), ensuring that the Courant-Friedrichs-Lewy (CFL) number was always below 0.5. The unsteady RANS equations have been solved within the domain depicted in Fig. 2.1, using appropriate boundary conditions, as described in Sect. 2.2.1. In addition, a grid sensitivity study has been carried out for four different meshes, focusing on the time-averaged drag coefficient, C_x, and the corresponding Strouhal number of the periodic structures shed behind the body (see Table 2.1). As an outcome, a mesh consisting of 1.8×10^5 cells, i.e. mesh #4, has been selected to perform the simulations, which features a maximum y^+ value of one. Once the simulations have been conducted, we compute the time-averaged mean magnitudes of velocity and pressure, $\mathbf{U}$ and P. For that purpose, 80 shedding cycles have been averaged once the vortex-shedding regime was established.

After the computation of the direct mean flow variables, we solve the linear adjoint system (Eqs. 2.9-2.10) using the computational domain and mesh described above, implementing an incompressible steady RANS adjoint linear solver in OpenFOAM (Nilsson et al., 2014), which employs second order spatial discretization schemes and a SIMPLE algorithm for the pressure-velocity coupling, and makes use of the frozen turbulence assumption. The latter means that the adjoint system takes the value of the primal (direct) turbulence viscosity, which is a source of inaccuracies in the turbulent regions (Othmer, 2008), although in the present case is acceptable since we are dealing with low Reynolds meshes ($y^+ \simeq 1$). The use of this solver has been limited to solve Eqs. (2.9)-(2.10) to obtain the adjoint variables, without performing any shape modification by neglecting the source porosity term (Nilsson et al., 2014). Thus, as boundary conditions, we set nil adjoint velocity at the inlet Σ_i, no slip conditions at the outer domain Σ_w, and a stress-free condition at the outlet Σ_o. Validation of the adjoint solver is provided by comparing the results of sensitivity and drag variation, induced by a small control cylinder, for the flow around a square cylinder (see Fig. 2.2), with those obtained by Meliga et al. (2014), as it will be presented in Sect. 2.3.1. In that sense, once the linearized adjoint problem is solved and the values of $\mathbf{U}^\dagger$ and $P^\dagger$ are known, the sensitivity of the mean drag to localized forcing is retrieved by means of $\mathbf{U}^\dagger$, what allows a precise prediction of regions in which forcing or shape modification could have a larger impact on the mean drag. Finally, the mean drag variation can be easily obtained using Eq. (2.4), provided that $\delta\mathbf{F}$ is known (for instance, by modeling the reacting force exerted by a control cylinder).

2.2.3 Body shape optimization procedure

As mentioned earlier, the drag sensitivity distribution provides with a clear indication of what type of flow modifications, induced by any local forcing, have a largest effect on the aerodynamic forces. Following that idea, body shape modifications based on the drag sensitivity distribution offer an interesting solution to improve the cavity performance as control strategy, when the depth is restricted, and without having to add external devices, e.g. cylinders. To perform such task, we use the topological optimization algorithm, which governs the body shape deformation based on the aerodynamic shape sensitivities of the drag force, that are used as an input to guide the geometrical modifications of the body base. Following Othmer (2014), the drag shape sensitivity on the body surface can be computed as

$$\frac{\partial c_x}{\partial \beta} = -\partial_n \mathbf{u}^\dagger \partial_n \mathbf{u}, \tag{2.11}$$

where β denotes the normal displacement of the surface node, ∂_n stands for the normal derivative, and $\mathbf{u}^\dagger$ and $\mathbf{u}$ represent respectively the instantaneous adjoint and direct velocities. The shape sensitivity identifies the regions where normal surface displacements result into decreasing (resp. increasing) drag coefficient, when modifications occur in the same (resp. opposite) direction of shape sensitivity map. Thus, the body shape optimizations can be done by coupling the previously described adjoint solver with a standard deformation tool, by mapping the shape sensitivity for each surface node into the morphing control points of the deformation algorithm. The implementation of this coupling process has been done with the optimization toolbox implemented in ANSYS Fluent (www.ansys.com), which allows free-form deformation of control points in a very controlled way. This free-form morphing tool is based on Bernstein polynomials, defined relative to a set of control points, for which the deformation occurs by moving some of them by following the gradient of sensitivity in accordance with the steepest descent method (Han et al., 2011).

The procedure employed in the present study consists in running the adjoint solver described earlier, using as input the primal flow variables calculated from the RANS numerical simulations, i.e. $\mathbf{u}$, p, k and ω; to obtain $\mathbf{u}^\dagger$ and $p^\dagger$. These adjoint variables are read by the optimization tool to implement a drag shape sensitivity analysis (Eq. 2.11)

$Mesh$	Number of cells (n)	C_x	$\xi_{C_x}(\%)$	St_{C_x}	$\xi_{St_{C_x}}(\%)$
# 1	$\sim 0.5 \times 10^5$	0.796	1.49	0.429	5.97
# 2	$\sim 1.0 \times 10^6$	0.819	1.41	0.444	2.92
# 3	$\sim 2.5 \times 10^6$	0.818	1.33	0.449	1.82
# 4	$\sim 4.0 \times 10^6$	0.808	-	0.457	-

Table 2.2: Grid sensitivity analysis for the three-dimensional simulations around a bluff body at $Re = 2000$. Comparison among the values of the mean drag coefficient C_x and vortex shedding Strouhal number, St_{C_x}, obtained using four different grids. The relative error, ξ, is calculated with respect to mesh #4, which features the largest number of cells, n.

and to perform shape modifications through the definition of control points boxes. Since we are interested in the optimal cavity geometrical modification to reduce the drag, the control box is defined around the cavity (see Fig. 2.5a). This control grid is made up of $n_x \times n_y$ points, where $n_x = 100$ and $n_y = 80$ are respectively the number of control points in the x and y directions. In particular, our study aims at carrying out subsequent iterations leading to slight cavity shape modifications, by means of progressive control mesh morphing, whose maximum displacement for each iteration is limited to the size of characteristic control mesh cell. Thus, after several steps, a final shape is obtained, for which further changes do not achieve any relevant additional drag reduction. At this point, the outcome could be considered an optimum. In that sense, as it will be detailed in Sect. 2.3.2, the analysis will be done through successive *one-shot* optimizations (Othmer, 2014), which consists in obtaining converged solutions of time-dependent direct flow quantities, and in computing for a selected instant, adjoint variables and shape sensitivity, whereupon the corresponding shape modification is performed. Next, another RANS numerical simulation around the modified body is performed, to verify the drag reduction after solution convergence and to obtain again the direct flow variables, from which a new iteration starts. Further details on this iterative, optimizing process will be given in Sect. 2.3.2, where final and intermediate forms, and changes experienced by drag coefficient in successive iterations are presented.

2.2.4 Three-dimensional simulations details

To conclude the optimization process of the body base cavity, the shape obtained from the drag sensitivity analysis is assessed and compared with the original body through three-dimensional turbulent unsteady simulations. The whole computational domain is thus accounted, being the simulations conducted in OpenFOAM. Thus, the two-dimensional results are verified and the main features characterizing the new flow are presented and discussed. These simulations have been performed for the originally considered $Re = 2000$ and also extended to $Re = 20000$. To this aim, the IDDES (Improved Delayed

Detached Simulations) turbulence model has been used. This numerical approach is a hybrid RANS-LES (Large Eddy Simulation) model (Fröhlich and von Terzi, 2008), suitable for the simulation of massively separated flows (Shur et al., 2008). In this regard, a RANS simulation is conducted in the attached wall boundary layer, whereas the LES model is activated within the flow core, in the separated flow regions, which results in an intricate but powerful approach for the study of these kinds of flows. Thus, the IDDES model allows to resolve accurately the large scales in the wake region through the LES model, while the RANS model, specifically the Spalart-Allmaras model, is used in the near wall region, with the consequent computational cost saving. Furthermore, regarding the near wall treatment, a Van Driest's law, (van Driest, 1956) has been used. The main advantage of such unified law of the wall is that the first grid point close to the wall can be placed into the buffer or viscous region, $y^+ < 30$, without the loss of accuracy associated with logarithmic approaches. Besides, a second order Gauss Linear central differentiation scheme (Lax and Wendroff, 1960) has been used for the spatial terms, while a second order implicit Euler method backward scheme is employed for the temporal terms (Geurts, 2004). The PIMPLE algorithm (a combination of the PISO and SIMPLE algorithms) has been selected for the pressure-velocity coupling, allowing the use of relatively large time-steps. In addition, a maximum CFL number lower than 1 has been considered to set the time step, which results in a dimensionless time step $\triangle t = 0.008$. Moreover, in all cases, the analysis of frequencies and global time-averaged variables have been done considering at least 700 characteristic periods, i.e. $t \simeq 1600$, once the flow conditions become statistically converged, with no differences reported when using longer averaging periods. Moreover, as it was done for the two-dimensional study, a grid convergence study has been also performed (see Table 2.2). Differences below 1.5% in the value of C_x are observed in all cases, whereas in the case of the characteristic Strouhal number, these are lower than 2% for the two finer grids. Consequently, mesh #3, consisting of 2.5×10^6 cells, has been considered for the three-dimensional computations, due to its best accuracy-to-computational cost ratio. Finally, it must be said that the latter grid presents a $\max(y^+)$ of order unity.

2.3 Results and discussion

We present now results obtained from the different studies described in Sect. 2.2. We will start with the computation of drag sensitivity, and subsequent wake control using two types of local forcing, i.e. small control cylinder, as done in Meliga et al. (2014), and smooth cavity structure deformation, performed using the aforementioned topological optimization algorithm; for the flow around the two-dimensional body at $Re = 2000$. Next, in order to validate the performance of our methodology, and to quantify the drag reduction achieved in a more realistic regime when optimized rear cavities are used, we

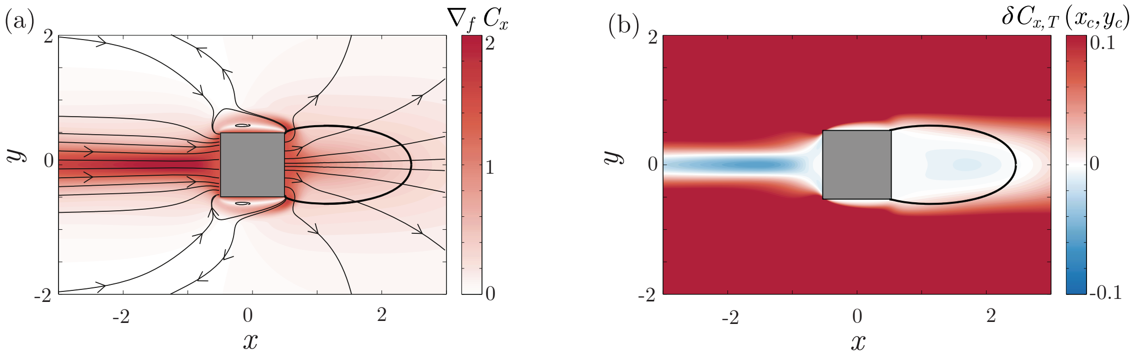

Figure 2.2: (a) Spatial distribution of the mean drag coefficient sensitivity for a square cylinder at $Re = 100$ (contours of the sensitivity magnitude and streamlines of the adjoint velocity). (b) Total drag variation of the two cylinder system, formed by the square cylinder and a control cylinder of diameter $\Theta = 0.1$. Thick solid lines represent the separatrix of the recirculation region.

will analyze the topology and dynamics of the flow around the three-dimensional body for $Re = 2000$ and $Re = 20000$, obtained from numerical simulations implementing a hybrid IDDES turbulence model.

2.3.1 Mean drag sensitivity to localized forcing

As discussed in Sect. 2.2.2, we adopt the simplified steady sensitivity approach for unsteady flows developed by Meliga et al. (2014), focusing on the time-averaged mean drag sensitivity, which is obtained using Eq. (2.8), after solving the adjoint linear system (Eqs. 2.9-2.10) with the help of the corresponding linear adjoint solver. In particular, we applied the method to the unsteady flow at $Re = 2000$, using values of time-averaged mean velocity and pressure, $\mathbf{U}$ and P, previously obtained from unsteady RANS simulations. Before investigating the present flow configuration, shown in Fig. 2.1, we computed the drag sensitivity for the flow around a square cylinder of side H at $Re = 100$, with the aim at comparing results with those included in Meliga et al. (2014) and consequently, validate our numerical procedure. In that sense, Fig. 2.2(a) depicts the mean drag sensitivity distribution, being its magnitude defined by color levels while streamlines indicate the orientation of the sensitivity gradient, indicating that, to decrease the drag, the control force must be oriented in the opposite direction of streamlines arrows. Although the shear layer regions and the recirculation bubble (enclosed by the thick solid line) feature important sensitivity, higher magnitudes are achieved in the front part due the body's bluff form, suggesting that any forcing, either through shape modification or control cylinder placement, should be applied upstream from the body to render the flow more *streamlined*. In that regard, Fig. 2.2(b) shows the total mean drag variation as a function of the position of a small control cylinder of diameter $\Theta = 0.1$. To obtain such map, the reacting force of the small cylinder, whose location is defined by (x_c, y_c), is modeled using the following equation (Meliga et al., 2014),

$$\delta \mathbf{F}(x,y) = -\frac{1}{2}\Theta C_{x_\Theta}(Re_\Theta)\boldsymbol{\varsigma}(x_c,y_c)\delta(x-x_c,y-y_c), \tag{2.12}$$

being $C_{d_\Theta} = 0.8558 + 10.05 Re_\Theta^{-0.7084}$ the drag coefficient of the control cylinder, $Re_\Theta = \Theta\|\mathbf{U}\|(x_c,y_c)Re$ the local Reynolds number based on Θ (denoting $\|\cdot\|$ the inner product norm), and $\boldsymbol{\varsigma}(x_c,y_c) = \|\mathbf{U}\|\mathbf{U}$. Thus, the total drag variation $\delta C_{x,T}$ of the combined system of square and control cylinders, whose map is depicted in Fig. 2.2(b), is obtained by means of Eqs. (2.4) and (2.12) as,

$$\delta C_{x,T}(x_c,y_c) = (\mathbf{U}^\dagger|\delta \mathbf{F}_x) = -\frac{1}{2}\Theta C_{x_\Theta}(\mathbf{U}^\dagger(x_c,y_c) - 2\mathbf{e}_x)\cdot\varsigma(x_c,y_c), \tag{2.13}$$

from which it can be inferred that drag reduction is most efficient in the region located along the symmetry axis, upstream from the body, as foreseen in the previous sensitivity distribution analysis. More interestingly, the drag reduction map depicted in Fig. 2.2(b) is qualitative and quantitatively identical to that computed by Meliga et al. (2014) (see Fig. 12 therein), therefore validating our methodology and numerical schemes. Hence, in the following we will apply such analysis to the flow configuration sketched in Fig. 2.1.

Figure 2.3 shows the mean drag sensitivity for the slender bluff body with rear cavity at $Re = 2000$, along with the total drag variation induced by a control cylinder of diameter $\Theta = 0.016$, computed using Eq. (2.12). The cylinder size has been selected by considering that the maximum local Reynolds number based on its diameter is approximately 40, hence below the critical one giving rise to vortex shedding in the flow. As expected, the more streamlined shape of the bluff body of ellipsoidal nose, provides with lower values of sensitivity magnitude than those featured by the square cylinder case. Interestingly, highest magnitudes are reached at the rear edges of the cavity, although the shear layer and recirculation regions also show intermediate values of sensitivity. These results suggest that the forcing should be applied close to the cavity edges or inside the recirculation bubble in order to achieve largest drag reduction, what is confirmed by the total drag variation map depicted in Fig. 2.3(b). The reduction associated to the placement of a control cylinder in the near wake may be related to a larger base pressure coefficient and a weaker backflow, while a cylinder placed close to the cavity edge should affect the shear layer detachment. Thus, since we are interested in improving the performance of cavities as control devices, we explore the latter scenario in order to quantify potential drag reduction and to evaluate flow modifications leading to such outcome, when control cylinders are placed close to the rear edge, in the most sensitive areas identified in Fig. 2.3(a).

As suggested by the sensitivity distribution in Fig. 2.3(a), in order to achieve largest drag reductions, we placed two small cylinders of diameter $\Theta = 0.016$ at two symmetric positions close to the cavity edge, within the areas of high sensitivity and in locations where the cylinder reacting force opposes the gradient streamlines plotted therein, i.e. $(x_c, y_c) = (0.368, \pm 0.428)$. Interestingly, Parezanović and Cadot (2012) identified a similar location,

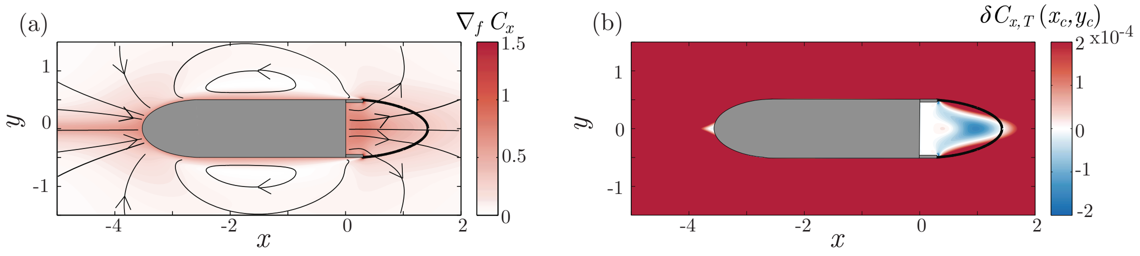

Figure 2.3: (a) Spatial distribution of the mean drag coefficient sensitivity for the bluff body under investigation at $Re = 2000$ (contours of the sensitivity magnitude and streamlines of the adjoint velocity). (b) Total drag variation of the system formed by the bluff body and a control cylinder of diameter $\Theta = 0.016$. Thick solid lines represent the separatrix of the recirculation region.

as a transition region between *inner shear* and *mid-shear* zones, where the introduction of a localized forcing, by means of a single control cylinder, gives rise to important base pressure increase and overall drag reduction, regardless of cylinder size. Consequently, similar effects are expected for the present symmetric configuration of the improved cavity. Thus, in a preliminary step, we first analyze qualitative and quantitative changes in wake dynamics and drag reduction, using unsteady RANS turbulent simulations results at $Re = 2000$. In that line, Table 2.3 lists the values of different global variables of the time-averaged flow for the natural wake and that controlled by placing two small cylinders near the cavity edge. First, it is shown that the minimum base static pressure level, i.e. $\min(C_p)$, increases when the symmetric pair of cylinders are introduced in the flow (controlled wake). This lower overall level is accompanied by an increase in the length of the recirculating region behind the body, L_r, from which it can be inferred that the axial velocity gradient is reduced, and consequently the backflow decreases as well, as the values of $\min(U_x)$ show. Besides, the increase in the base pressure is directly related to a smaller mean drag, which in our case decreases from 0.752 to 0.747, representing a 0.6% drop approximately. The magnitude of such small drag decrease is similar to that predicted using the Eq. (2.12) (see Fig. 2.3b), for which the reduction achieved using a set of control cylinders, placed in the selected location $(x_c, y_c) = (0.368, \pm 0.428)$, amounts to 0.4% approximately. Although slightly different, these results prove that the simple model employed by Meliga et al. (2014) can be used as a quick and first approximation, to estimate drag variation without incurring into large errors.

Besides, regarding the wake instability, since a strong backflow is known to promote local absolute instability (Monkewitz, 1988), what is connected to global instability in wakes (Pier, 2008), the latter flow modifications should translate not only into a drag reduction, but also into a weakening of fluctuation amplitude in the temporal evolution of the drag, c_x, if this amplitude is viewed, in a rough approximation, as a quantitative estimator of the wake global unstable dynamics. At this point, it should be noted that at $Re = 2000$ the dynamics is far from the threshold of unsteadiness in terms of Re,

Case	$\min(C_p)$	L_r	$\min(U_x)$	L_f	C_x
Uncontrolled	-0.372	1.53	-0.150	2.78	0.752
Controlled	-0.370	1.55	-0.148	2.82	0.747

Table 2.3: Comparison between the global time-averaged magnitudes: minimum pressure coefficient, $\min(C_p)$, recirculation length, L_r, minimum recirculation velocity $\min(U_x)$, vortex formation length L_f, and drag C_x, obtained from simulations of the two time-averaged flows under investigation, i.e. natural flow around the bluff body and controlled flow placing small cylinders close to the cavity edge.

and consequently is highly non-linear, so that it cannot be accurately interpreted only in terms of global linear modes. However, weaker fluctuations of c_x would clearly suggest that the wake global dynamics is becoming less unstable, and the oscillator behavior of the flow is being attenuated when the cylinders are used. To check this hypothesis, we include in Fig. 2.4(a) temporal signals of c_x for the two wakes compared, i.e. natural and controlled flow, along with the corresponding Power Spectral Density distribution, PSD(St), of drag fluctuations, $C'_x = c_x - C_x$ in Fig. 2.4(b). First, the aforementioned mean drag reduction induced by cylinders is clearly observed in Fig. 2.4(a), which is accompanied by an additional reduction in the magnitude of drag oscillations, C'_x, what denotes a weakening of the flow unsteadiness and the intensity of shedding vortices (not shown here for the sake of conciseness). Consequently, the identification of sensitive areas also provides with valuable information on the wake control possibilities in terms of global mode dynamics. In fact, in order to quantify such weakening of drag oscillations, we compute the squared amplitude of fluctuations, $|A|^2_{C'_x}$, through integration of the main peak in the PSD(St), around the fundamental shedding frequency St_{C_x} (Fig. 2.4b), as

$$|A|^2_{C'_x} = \int_{St_{C_x}-\Delta St_d}^{St_{C_x}+\Delta St_u} \mathrm{PSD}(St)\, dSt, \tag{2.14}$$

where ΔSt_d and ΔSt_u stand for the interval around St_{C_x} for which the energy drops to 2% the peak value. Such calculation allows us to estimate the reduction of oscillations amplitude in a value of 47% for the case at hand. Furthermore, the attenuation of the flow unsteadiness, i.e. the unstable global dynamics, is also associated with a slight increase of St_{C_x}, which grows in that case from 0.432 to 0.434, according to Fig. 2.4(b).

In general, these effects induced by the control cylinders can be interpreted in terms of the mechanisms described by Parezanović and Cadot (2012), and proposed by Gerrard (1966), whereby the placement of the cylinder in the inner shear tends to thin and reattach the primary shear layer of the blunt body. Consequently, the entrainment of the detached shear layer is reduced in the recirculation region and, as a result, the length of the formation region of the vortex street, enclosed by the eddies roll-up, increases (see values of L_f in Table 2.3). The enlargement of the formation length leads to a subsequent base pressure increase (i.e. drag reduction) and weaker pressure and velocity gradients, resulting into

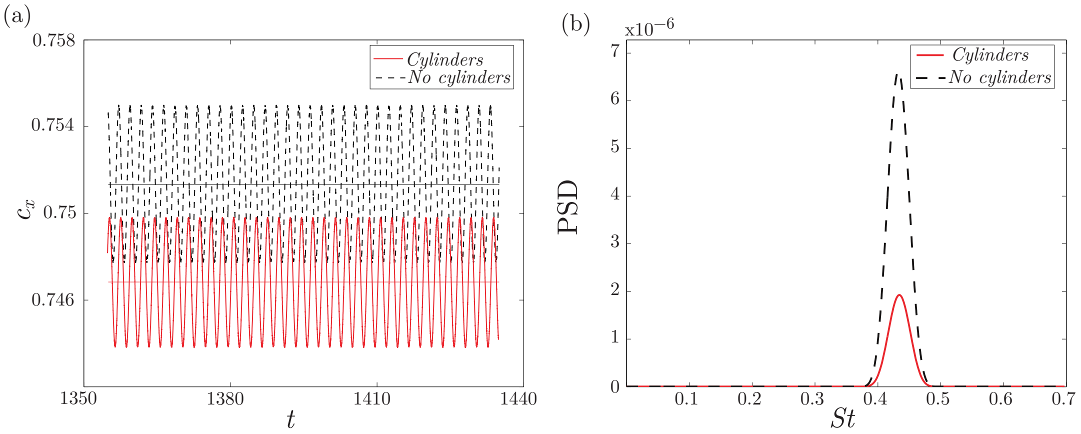

Figure 2.4: (a) Time-evolution of the drag coefficient, c_x, and the mean constant values, C_x, obtained from simulations of the two flows under investigation: natural flow around the bluff body (black dashed line) and controlled flow using small cylinders placed close to the cavity edge (red solid line); and (b) corresponding Power Spectral Density, PSD(St) (arbitrary units), of the drag coefficient fluctuations, $C_x' = c_x - C_x$, for the two aforementioned cases.

a lower radial shear and reverse flow. Moreover, sensitivity analysis by Parezanović and Cadot (2012) and Meliga et al. (2012) also showed that the inner shear region features a positive sensitivity to shedding frequency, so that the placement of a control cylinder within this area leads to a slight increase of the characteristic shedding frequency, St_{C_x}. The presence of control cylinders close to the cavity edges entails positive flow modifications in terms of drag and wake control. However, the drag reduction achieved is barely noticeable, what precluded us from further exploring this way as a strategy to improve rear cavities performance. Hence, we investigate next the effect on the forces and wake variables of cavity topological modifications, based on the sensitivity distributions computed in Sect. 2.3.1. Moreover, from a practical view, this different strategy would not imply the implementation of an additional set-up for the cylinder, what could be also considered an advantage. Nevertheless, its feasibility has to be yet investigated.

2.3.2 Drag variation by means of geometry optimization

As mentioned in Sect. 2.1, the performance of rear cavities as wake and drag control devices is highly dependent on their depth, which in most applications is limited by geometrical and functional requirements. Thus, we now investigate the suitability of cavity shape modifications as a solution to extend the potential for drag reduction when the cavity depth is fixed. After satisfactorily evaluating the viability of sensitivity analysis to predict mean drag and wake oscillations reduction when external control cylinders are implemented, we further explore the applicability of the adjoint-based approach described in Sect. 2.2.3 to the cavity topological optimization, where a drag reduction larger than that obtained with control cylinders is expected. To do so, we employ the optimization toolbox of ANSYS

Fluent, which allows a free-form deformation of control box points. In that sense, since we are only interested in the optimal design of the cavity walls, we limit the structural optimization to the control area depicted in Fig. 2.5(a), which comprises $n_x = 100 \times n_y = 80$ control points, whose movement is determined by the steepest descent criterion.

Besides, the optimal shape calculation is accomplished by means of iterative computations of primal and adjoint flow variables, as mentioned in Sect. 2.2.3. As highlighted by Othmer (2014), accurate computation of adjoint to time-dependent primal variables is not feasible in complex problems due to the large storage requirements for the backward integration, so that only two approaches are usually employed, namely, the computation of sensitivity based on time-averaged primal variables and the implementation of one-shot optimizations for a frozen single instant, for which both primal and adjoint variables are obtained. As shown by Meliga et al. (2014), instantaneous sensitivity may provide with larger values than time-averaged flows (see Figs. 4 and 6 therein), especially when the vortex is being shed from the body edge. Consequently, in order to speed up the shape modification process, we choose to perform one-shot instantaneous optimizations for instants of alternate highest sensitivity near the cavity for each wall, identifying vortex shedding events in each side. Fig. 2.5(b) illustrates the optimization process in terms of normalized drag, c_x/C_{x0}, where C_{x0} is the mean drag coefficient of the body with a straight cavity. For each iteration, defined by a prescribed shape, we first compute a converged time-dependent regime of the primal flow, by means of RANS numerical simulations. Once the flow regime is established, the values of $\mathbf{u}$, p, k and ω for the selected instant of largest sensitivity are plugged into the adjoint RANS solver in order to calculate the adjoint variables, $\mathbf{u}^\dagger$ and $p^\dagger$, assuming the frozen turbulence simplification. Afterwards, the variables are used by the optimization toolbox to compute shape sensitivity (Eq. 2.11) and perform the shape modification, following the steepest descent method. Once the new shape is obtained, the process is repeated, alternating the side of the cavity for which the highest sensitivity is reached, until an approximately constant value of mean drag is obtained and no further optimization is possible.

Using the latter strategy, a converged shape is obtained after approximately 40 iterations, as shown in Fig. 2.5(b) for the case of $Re = 2000$, for which a mean drag reduction of approximately 23% is achieved, being considerably larger than that obtained earlier through the control cylinders. Since the optimization is accomplished using instantaneous sensitivity maps featuring the largest magnitude, the process is guided locally in each iteration, and the shape modifications are mostly concentrated around the cavity edges. However, the successive iterations allow an overall and quick optimization of the shape that can be considered as a global optimum, as explained below. As example, we show in Fig. 2.6 the spatial distributions of the largest instantaneous drag sensitivity to forcing (top half in each panel), i.e. adjoint velocity magnitude, and the corresponding primal axial velocity (bottom half), along with the streamlines of the underlying adjoint and pri-

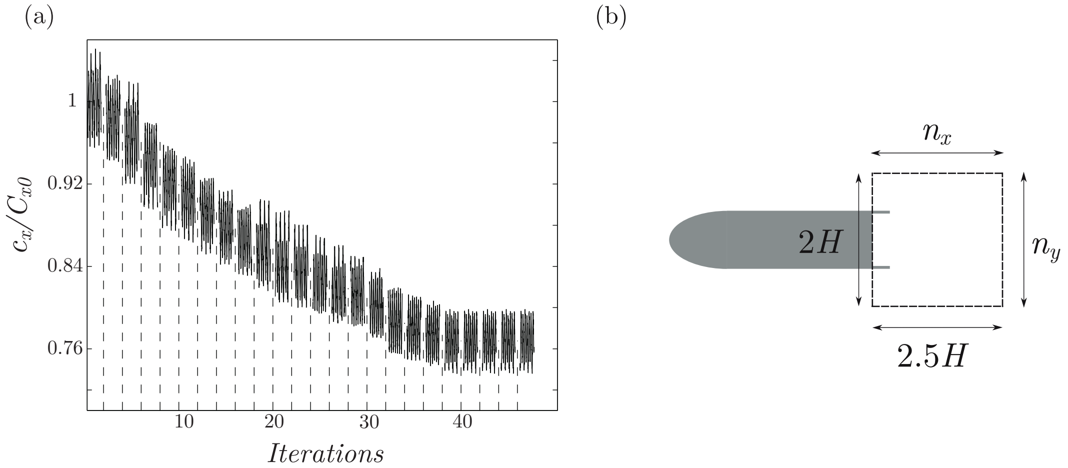

Figure 2.5: Shape optimization of the rear cavity at $Re = 2000$: (a) control volume for free-form morphing, being $n_x = 100$ and $n_y = 80$ the number of control points in each direction; and (b) progressive reduction of the normalized drag c_x/C_{x0} upon successive one-shot optimizations.

mal velocity vectors; for four different solutions of the shape optimization process. First, Fig. 2.6(a) shows the drag sensitivity for the initial shape, whose magnitude is larger than that characterizing the time-averaged drag sensitivity in Fig. 2.3(a), being the locus of highest magnitude concentrated around the rear edge. When the shape sensitivity is obtained (Eq. 2.11) the larger values on the rear edge will give rise to bigger control points shift in the surrounding area, configuring a new shape subject to a lower drag and featuring a weaker drag sensitivity, since the potential for drag reduction has now also decreased. This can be observed in Fig. 2.6(b) for the intermediate shape §1, corresponding to the outcome of the fifteenth iteration in Fig. 2.5(b), computing the sensitivity again after obtaining a converged solution of the RANS primal numerical simulations around the body. As expected, the sensitivity magnitude is clearly lower than that for the initial case (Fig. 2.6a), and now its maximum is slightly displaced towards the lee side of the edge. In general, a lower drag sensitivity and, consequently, its corresponding weaker shape sensitivity, will induce a smoother displacement of control points per iteration. In fact, Fig. 2.6(c) depicts the intermediate shape §2, obtained after twenty-five iterations, that features a pronounced curvature towards the inner side of the base cavity, which again provides with lower magnitude of drag sensitivity to forcing. This hollow cavity entails a local recirculation of the flow, as the distribution of primal velocity shows, that leads to a closer attachment of the boundary layer along the cavity wall and an increase in the curvature of the streamlines. Consequently, the flow leaves the cavity edge with a higher momentum toward the axis in the y coordinate. This configuration, defined by the formation of the vortex ring upstream from the edge, is further promoted during the last stages of the optimization process, as Fig. 2.6(d) shows. The final shape, reached after 40 iterations, can be considered an optimum, since new iterations do not improve the mean

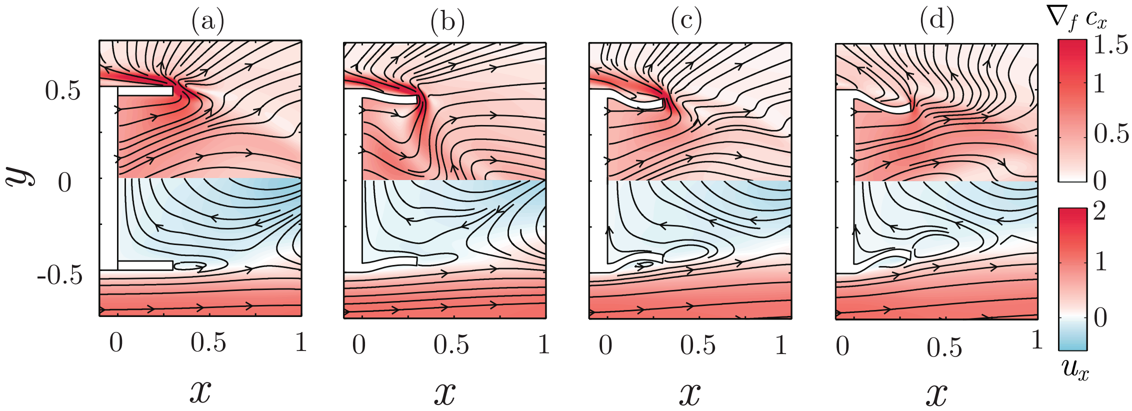

Figure 2.6: Contours of instantaneous drag sensitivity to a localized forcing (top) and primal axial velocity (bottom); along with the corresponding streamlines of the underlying adjoint and primal velocity vectors; for four different steps of the cavity shape optimization process at $Re = 2000$: (a) original shape; (b) intermediate shape §1 (15th iteration in Fig. 2.5b); (c) intermediate shape §2 (25th iteration in Fig. 2.5b); and (d) optimal shape.

drag value (see Fig. 2.5b). In spite of the residual sensitivity existing around the rear edge, any deformation stemming from the current shape sensitivity study implies not only shape modification of the upper wall but also of the lower one in the same sense, which hinders the hypothetical reduction that could be achieved for not having a nil drag sensitivity in Fig. 2.6(d). This subtlety can be observed in the supplementary movie, where slight oscillations of both walls are observed after the transient period of the optimization process.

Moreover, the influence of selecting a random instant to perform successive optimizations by using the adjoint solver, has been also tested to discard any local influence on the final solution. The consequence is a slower process, that requires a larger number of iterations, until the final shape is converged. Thus, the final optimized geometry can be considered as an overall solution for the optimization process, whose effect on the wake has to be yet deeply investigated. In principle, the mentioned effect of the vortex ring formed upstream of the rear edge may be similar to that created by the extension plates configuration tested by Khalighi et al. (2001), whereby flow reattachment before massive separation leads to a narrower recirculation bubble and an increase of the base pressure, which account for the drag reduction. However, this hypothesis will be further investigated in Sects. 2.3.3-2.3.4 performing three-dimensional numerical simulations in more realistic regimes. In that sense, in order to evaluate the performance of the optimized cavity shape at higher Reynolds numbers, we decided to carry out numerical simulations instead of repeating the computational costly optimization procedure, which might be now prone to difficulties and inaccuracies due to the simplifications employed (e.g. frozen turbulence assumption and linearization of adjoint equations). Therefore, to fully understand the

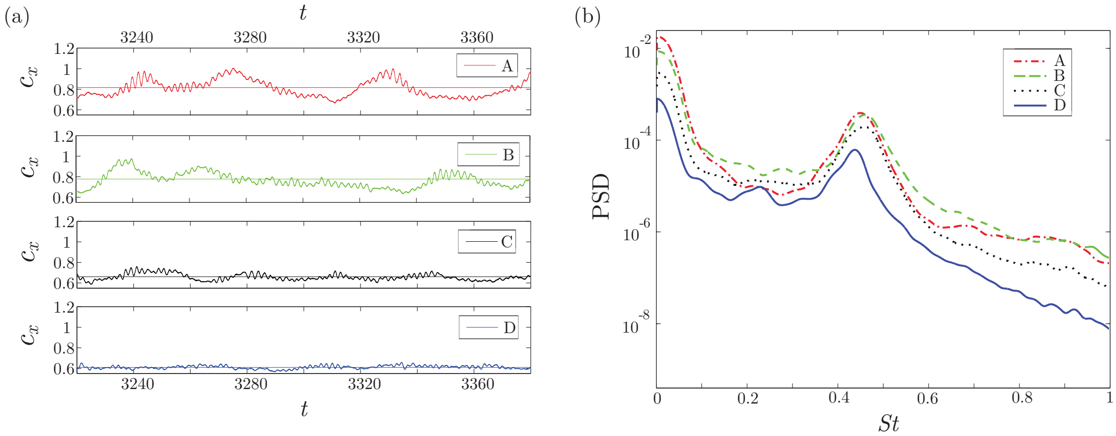

Figure 2.7: (a) Time-evolution of the drag coefficient, c_x, along with their mean value C_x (solid lines), at $Re = 2000$ for four different body geometries: blunt base (model A), straight cavity (model B), intermediate cavity (model C) and optimal cavity (model D). (b) Power spectral density, PSD, in arbitrary units (a.u), of the drag coefficient fluctuations, $C'_x = c_x - C_x$, corresponding to body shapes analyzed in (a). In Fig. 2.7(b), $St = \varpi h/U_\infty$ has been obtained with the distance between the trailing edges of each body, h.

flow modifications induced by the optimal shape and how they affect the wake instability and the drag, we compare in the next Section the flow characteristic of the original wake with those obtained for the optimized cavity (Fig. 2.6d), and the intermediate shape §1 (Fig. 2.6b), which does not present a recirculating flow on the curved wall, for two different Reynolds numbers, i.e. $Re = 2000$ and $Re = 20000$.

2.3.3 Three-dimensional simulations at Re = 2000

In order to corroborate the results previously obtained throughout the optimization process, in the present Section the flow characteristics induced by the different configurations are assessed and compared with those obtained with the original body (the body without a base cavity). Thus, four different symmetrical configurations are considered herein, specifically, the body without cavity (model A), the body with a straight cavity (model B), the body with an intermediate cavity which does not present the detachment of the boundary layer at the outer side of the cavity plates at $Re = 2000$ (model C, intermediate shape §1 in Sect. 2.3.2), and the final geometry obtained from the shape optimization study (model D), in Sect. 2.3.2. The drag coefficient c_x and the characteristic Strouhal numbers, St_{C_x}, as well as the main flow dynamics features, are next presented and described to better understand the effect of adding a cavity of a given shape at the base of the body. To do this, more realistic, accurate three-dimensional unsteady turbulent numerical simulations have been conducted for at $Re = 2000$ as described in Sect. 2.2.4.

The study is first focused on the flow dynamics at $Re = 2000$, which has been originally considered in the optimization study. Thus, Fig. 2.7(a) shows the temporal evolution of

Geometry	C_x	St_v	R(%)
A	0.819	0.224	–
B	0.778	0.230	5.0
C	0.662	0.227	19.2
D	0.609	0.220	25.6

Table 2.4: Drag coefficient, vortex shedding Strouhal number and drag reduction obtained from three-dimensional, turbulent simulations at $Re = 2000$, for the four geometries described in the present Chapter.

the drag coefficient, c_x, for each model at $Re = 2000$. In addition, a thick horizontal line is included representing the mean drag coefficient value, C_x, for which a total number of 1600 dimensionless time steps has been considered. It can be observed how the mean drag value decreases monotonically from model A to D, specifically, from $C_x \approx 0.819$, for the original body without cavity (model A), to $C_x \approx 0.609$, for the optimized geometry (model D), as predicted by the optimization study. In addition, the c_x presents relatively high frequency variations of small amplitude, characteristic of the massive vortex shedding process which takes place at the rear part of the body, and low frequency fluctuations around its mean value, characteristic of the three-dimensional, unstable nature of the flow. Note that the amplitude of the low frequency fluctuations is reduced with the inclusion of the different shape cavities, for which again a monotonic amplitude reduction is observed, i.e. presenting model D the minimum amplitude value. This result indicates that the shape optimization study not only provides with a decrease in the mean drag coefficient, C_x, but also induces a stabilizing effect of the body wake, as shown in Fig. 2.7(b).

Table 2.4 shows the results of the mean drag, C_x, and vortex shedding characteristic Strouhal number, St_v, computed now from the time evolution of axial velocity obtained at a control point, located downstream of the body, in the vicinity of the upper edge of the cavity, specifically at $(x, y, z) = (0.92, 0.5, 0)$. In the computation of the Strouhal number, $St_v = \varpi_v h/U_\infty$, the characteristic height of each cavity geometry has been considered, i.e. the distance between the trailing edges, being $h = 1$ for models A and B, $h = 0.928$ for C and $h = 0.853$ for D. As previously commented, a monotonic mean drag relative reduction, $R(\%) = 100 \times [C_x(\mathrm{A}) - C_x(\mathrm{B, C, D})]/C_x(\mathrm{A})$, is obtained for each geometry, with a total relative reduction of 25.6% achieved with model D (the optimized body) in this case. This result constitutes a significant drag variation, considering the low mean drag value of the original streamlined body, $C_x(\mathrm{A}) = 0.819$, and the relatively low Reynolds number, $Re = 2000$, in which the viscous part of the drag coefficient is still important, as reported by Sanmiguel-Rojas et al. (2011). Furthermore, it is worth mentioning that there is a remarkable agreement between the results obtained from the two-dimensional and the three-dimensional analyses.

To better illustrate the effect of including different shape cavities on the flow char-

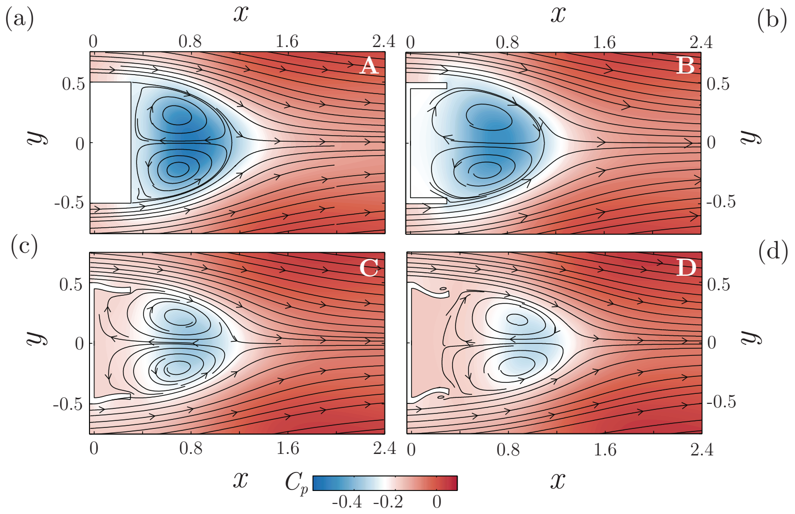

Figure 2.8: Time-averaged flow field at $z = 0$ and $Re = 2000$: contours of pressure and streamlines of the near wake for the different cavity geometries.

acteristic frequencies, Fig. 2.7(b) shows the Power Spectral Density, PSD, corresponding to the drag coefficient fluctuations, $C'_x = c_x - C_x$, for the four models. As it has been previously mentioned, two different peaks can be clearly observed. On the one hand, a high frequency peak can be appreciated at $St_{C_x} \simeq 0.45$, which is equal to twice the characteristic vortex shedding frequency obtained from the time evolution of axial velocity on each side of the cavity, $St_{C_x} \simeq 2St_v$, shown in Table 2.4, since c_x includes the effects of the vortex shedding from the upper and lower sides of the body. On the other hand, a low frequency, more energetic peak is also present, which is characteristic of the three-dimensional, unstable nature of the flow behind the body. In all cases, the inclusion of the subsequent cavities reduces the amplitude of both peaks, being such reduction about 60% when comparing models A and D for the higher St. Therefore, the body with the optimized shape cavity will exhibit a less energetic vortex shedding at the base, as well as a more regularized and less chaotic wake near the body base. In addition, it can also be seen that the peaks become narrower with the inclusion of the different cavities, which indicates the regularization of the flow, as wider peaks are related to three-dimensional disturbances of turbulent wakes, such as vortex dislocations or oblique vortex shedding (Williamson, 1996; Prasad and Williamson, 1997; Parezanović and Cadot, 2012). This amplitude reduction is a consequence of the lower pressure and velocity fluctuations generated in the neighborhood of the body base when a cavity is incorporated, which also provides a less chaotic and narrower wake as it will be shown later. Furthermore, with regard to the vortex shedding at $St_{C_x} \approx 0.45$, characteristic of the massive separation, though St_{C_x} hardly varies with the shape of the cavity added, the same trend is observed for both Re investigated, i.e. it slightly increases from model A to B, whereas decreases monotonically from B to C and subsequently to D. The differences observed in St_{C_x} for

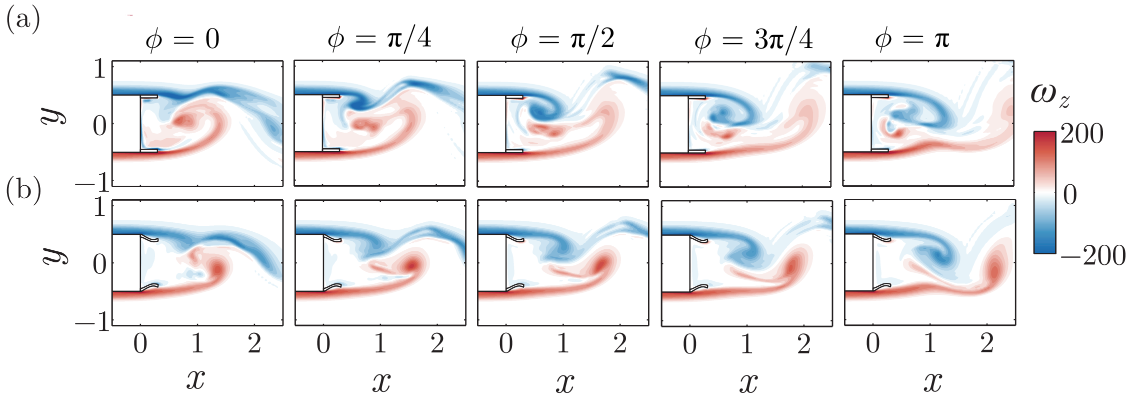

Figure 2.9: Time sequence of half of a shedding cycle, at $Re = 2000$ and $z = 0$, for: (a) a body with a straight cavity and (b) a body with the optimized cavity.

the different models are the consequence of two main factors: the modification of the local shear layer at the separation point and the variation of the distance between the upper and lower shear layers. In particular, an increase of the boundary layer thickness reduces the vortex shedding frequency (Gerrard, 1966; Parezanović and Cadot, 2012) while a decrease of the distance between shear layers increases the characteristic frequency, as reported by Molezzi and Dutton (1995). This latter effect could be caused by the stronger interaction between the upper and the lower vortices shed from the body as the distance between both edges decreases. The interaction between both vortices increases the vortex circulation and, consequently, the induced velocities, which make the vortices separate more rapidly. However, it should be noted that, although the vortex emission frequency maybe larger as the distance between the upper and lower shear layer decreases, the resulting Strouhal number can be lower since it has been defined as $St_{C_x} = \varpi_{C_x} h/U_\infty$, and h decreases from model B to D.

To provide with further understanding of the effect of adding the different cavities on the rear part of the body, the mean flow of the near wake is considered next. Thus, Fig. 2.8 displays the mean near wake flow streamlines together with the corresponding static pressure coefficient contours, C_p, within a vertical plane located at half of the domain, i.e. $z = 0$. Apparently, the drag coefficient reduction produced by the shape optimization is motivated by an important decrease of the pressure contribution to the aerodynamic forces. Specifically, note that the base pressure increases significantly with the inclusion of the different cavities. It can be observed how the addition of a straight base cavity (Fig. 2.8b), not only increases the minimum value of C_p, but also enlarges the dead region nearby the base of the body, displacing downstream the cores of the recirculating flow and thus lengthening it; a phenomenon typically associated to the above-mentioned base pressure increase (Martín-Alcántara et al., 2014). In the case of model C (Fig. 2.8c), with an improved but not optimized cavity, the new cavity walls deflect towards the wake

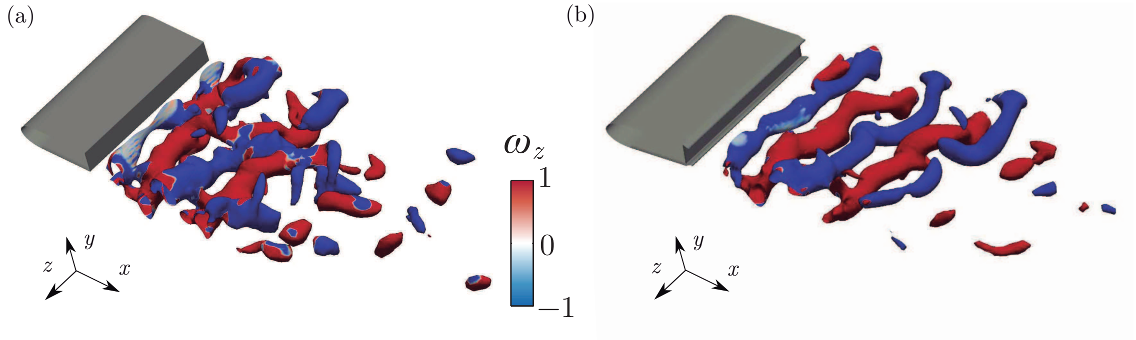

Figure 2.10: Contours of static pressure in the wake ($p = -0.36$), colored by spanwise vorticity: (a) original body without cavity (model A) , and (b) body with the optimized cavity (model D).

axis and adopt a shape that reduces the mean shear near the body edge (Molezzi and Dutton, 1995). Such modification in the geometry of the cavity induces a longitudinal adverse pressure gradient which decelerates the flow, and deflects it inwards, generating a recirculating region thinner than in the cases of the body without a cavity and that with a straight cavity. This effect is similar to that produced by the boat-tail device, which basically modifies the rear part of the body making it more streamlined (Choi et al., 2014). Note that, although the recirculation length hardly varies from model B (with a straight cavity) to model C (with an improved non-optimized cavity), there is a consequent shear reduction and an increase of the minimum pressure. Furthermore, in addition to increasing the minimum value of the pressure behind the body, the new cavity displaces the recirculating bubble away from the body, increasing the base pressure and consequently reducing the drag. In the case of model D, i.e. a body with the optimized cavity, the adverse pressure gradient contributes to recover the pressure nearby the body base, making the flow detach at the outer sides of the cavity walls (see Fig. 2.8d). Since the adverse pressure gradient is greater in the case of model D compared to that of model C, the base pressure increase is larger and, thus, the drag coefficient decreases substantially. The corresponding separated flow over the cavity wall does not contribute significantly to increase C_x, but may act a a natural blowing, displacing the low pressure region downstream from the body with the consequent increase in C_p.

A close inspection of the temporal evolution of the wake structure also reveals the effects of implementing the different types of cavities. In fact, Fig. 2.9 shows five time sequences of the near field spanwise vorticity contours, for half a vortex shedding period, i.e. $t = t_0$ to $t = t_0 + 1/2\, St_v^{-1}$, obtained for models B and D (the bodies with a straight and an optimized cavity, respectively). It is well known that the natural wake that forms behind these kinds of models presents the classical von Kárman vortex street, with an alternating vortex shedding at a characteristic frequency, already identified. It can be observed that, unlike what happens with the optimized cavity, in the case of the straight cavity, the flow remains attached to the body upon reaching the trailing edge. In addition,

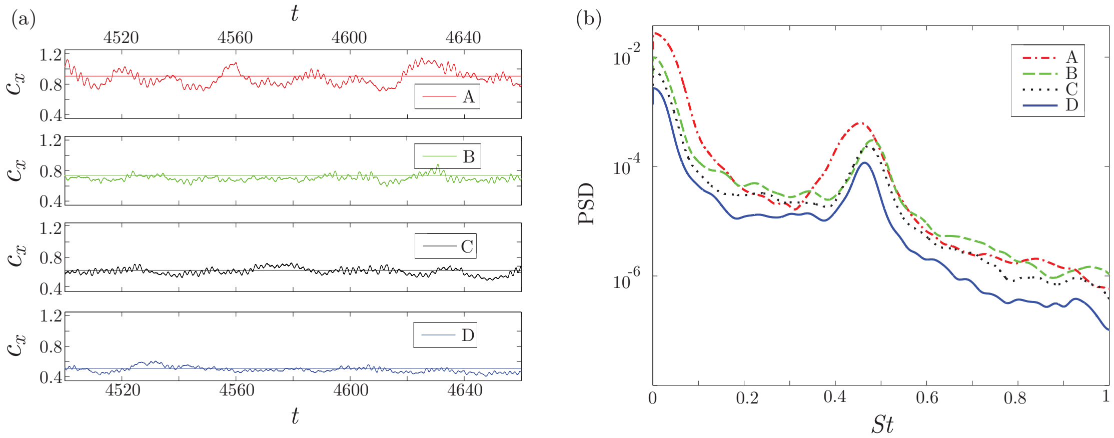

Figure 2.11: (a) Time-evolution of the drag coefficient, c_x, along with their mean value c_x (solid lines), at $Re = 20000$ for the four body geometries described in this Chapter: blunt base (model A), straight cavity (model B), intermediate cavity (model C) and optimal cavity (model D). (b) Power spectral density, PSD, in arbitrary units (a.u) of the drag coefficient fluctuations, $C_x' = c_x - C_x$, corresponding to the different body shapes. $St = \varpi h/U_\infty$ has been obtained with the distance between the trailing edges of each body, h.

the flow is nearly parallel to the straight walls in the first case whereas it deflects inwards in the second one. As a consequence, the strength of the vortices shed is significantly lower in the case of the optimized cavity (model D), which results in an increase of the static pressure, as shown in Fig. 2.8. In this figure, both sequences begin with the formation of a clockwise vortex at the upper plate and the shedding of a counterclockwise vortex at the lower side, which travels downstream, at time $t = t_0$ (ϕ =0). In the case of a body a straight cavity (model B), the vortex grows and partly penetrates into the cavity, times $t = t_0 + 1/8\, St_v^{-1}$ to $t = t_0 + 3/8\, St_v^{-1}$ ($\phi = \pi/4$, $\pi/2$ and $3\pi/4$) presenting the largest levels of vorticity, i.e. the lowest values of pressure, during these stages. Finally, at time $t = t_0 + 1/2\, St_v^{-1}$ ($\phi = \pi$), a counterclockwise vortex starts to form at the trailing edge of the lower plate which grows and eventually displaces the upper vortex downstream. However, in the case of the body with the optimized cavity (model D) the shear layer thickness near the body edge increases, with respect to that of the body with a straight cavity, due to the adverse pressure gradient induced by the curved wall, and the vortex formation process takes place downstream from the body. This, together with the induced inwards velocity component, reduce the spanwise vorticity. Furthermore, note that during the entire shedding cycle, a significantly large *dead* region exists at the rear part of the body, which is the mechanism mainly contributing to the C_x reduction (Viswanath, 1996). The flow dynamics is very similar to that of model B, although in this case there is no spatial coexistence of the two counter-rotating vortices, since they are not confined by the cavity.

Finally, to provide with further evidences of the stabilizing effect of the optimized

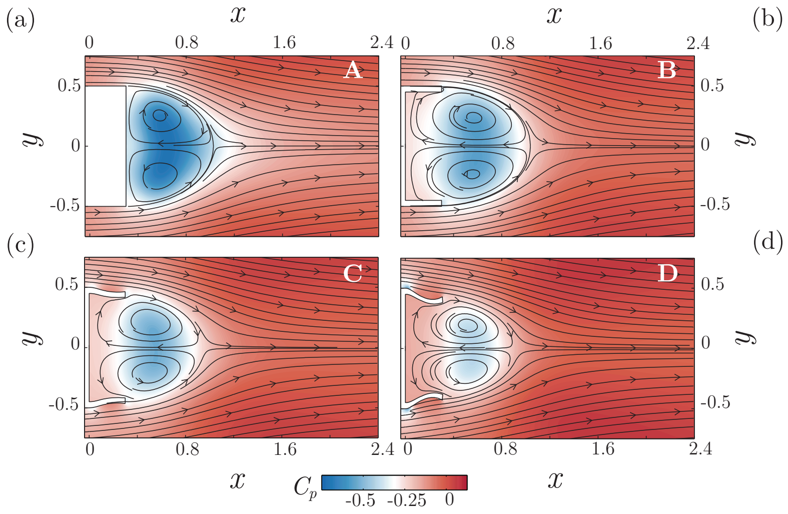

Figure 2.12: Time-averaged flow field at $z = 0$ and $Re = 20000$: contours of pressure and streamlines of the near wake for the different cavity geometries.

cavity, the wake flow three-dimensional structures are shown in Fig. 2.10, which displays static pressure isosurfaces (Park et al., 2006), for $p = -0.36$, colored by the spanwise vorticity, both for the original body (model A), in Fig. 2.10(a), and the one with the optimized cavity (model D), Fig. 2.10(b). Note that the wake is more chaotic and three-dimensional in the case of model A, resulting in the low frequency energetic peak shown in Fig. 2.7(b). Furthermore, smaller and more spatially regularized spanwise structures can also be observed when the optimized cavity is added, inferring the formation of a more slender wake, as it has been previously commented. In this case, the flow becomes more two-dimensional, being the coherent structures shown in Fig. 2.10(b) almost aligned with the trailing edge, reducing the amplitude of the low frequency fluctuations, as shown in Fig. 2.7.

2.3.4 Three-dimensional simulations at Re = 20000

The present analysis has been extended to a more realistic, turbulent flow, in order to evaluate the validity and robustness of the optimization study, when different flow conditions are considered. Thus, the same four models described in Sect. 2.3.3 have been also studied herein at $Re = 20000$. Thus, Fig. 2.11(a) shows the temporal evolution of the drag coefficient, c_x, for each model at $Re = 20000$. It can be inferred from the figure a monotonic reduction of the mean drag, C_x, as well as a decrease of the amplitude of both, the low and the high frequency fluctuations (see Fig. 2.11b), as happens at $Re = 2000$. Note that, the mean drag obtained at this Reynolds number for the body without a cavity, $C_x = 0.907$, is larger than that obtained at $Re = 2000$, $C_x = 0.819$, (Prasad and Williamson, 1997; Sohankar, 2006; Park et al., 2006). In addition, the viscous contribution to the total drag decreases from 16% at $Re = 2000$ to 8% at $Re = 20000$, thus being the pressure forces responsible for the main contribution to the C_x. As a consequence, the potential drag reduction that can be achieved using the optimized shape cavity increases with the Reynolds number (Sanmiguel-Rojas et al., 2011). Indeed, the mean drag value obtained when the optimized cavity is added at the body base decreases from $C_x = 0.609$ at $Re = 2000$ to $C_x = 0.509$ at $Re = 20000$. The aforementioned results are presented in Table 2.5, which reports a total drag reduction of 43.9% for model D, a value significantly larger than that obtained with a straight cavity, $R(\%) = 20.3\%$, or with similar devices, such as a multi-cavity (Martín-Alcántara et al., 2014). Although the values of St_v, also included in Table 2.5, remain almost constant, they follow the same trend observed at $Re = 2000$, i.e. St_v slightly increases from model A to model B, and monotonically decreases from models B to D.

Geometry	C_x	St_v	R(%)
A	0.907	0.227	–
B	0.723	0.241	20.3
C	0.630	0.236	30.5
D	0.509	0.232	43.9

Table 2.5: Drag coefficient, vortex shedding Strouhal number and drag reduction obtained from three-dimensional, turbulent simulations at $Re = 20000$, for the four geometries described in the present Chapter.

An analysis of the mean flow reveals the effect of the inclusion of the different shape cavities on the rear part of the body. Thus, Fig. 2.12 shows the mean flow streamlines together with the corresponding static pressure coefficient contours, C_p, downstream from the body within the $z = 0$ plane. The flow features are similar to those shown in Fig. 2.8 at $Re = 2000$, although in this case of larger Re, the boundary layer nearby the trailing edge is thinner and the shear stresses are greater than in the case of $Re = 2000$, inducing lower values of the base pressure and a shorter recirculation length for model A as shown in Fig. 2.12(a). This results are consistent with the increase of the drag coefficient in the case of the body without a cavity reported in Tables 2.4-2.5. The inclusion of a straight cavity (model B), Fig. 2.12(b), displaces the recirculation flow downstream from the base of the body, increasing the base pressure and, consequently, reducing the drag coefficient. Furthermore, as happens at $Re = 2000$, the pressure coefficient at the base increases monotonically with models C and D due to the combined effect of the inwards flow deflection and the adverse pressure gradient generated on the outer cavity walls, which makes the flow slow down, increasing the boundary layer and, consequently decreasing shear stresses. However, unlike what happens at $Re = 2000$, the flow does not separate over the concave cavity walls of model D since at $Re = 20000$ the momentum of the flow is sufficiently high to avoid flow separation in the region where the adverse pressure

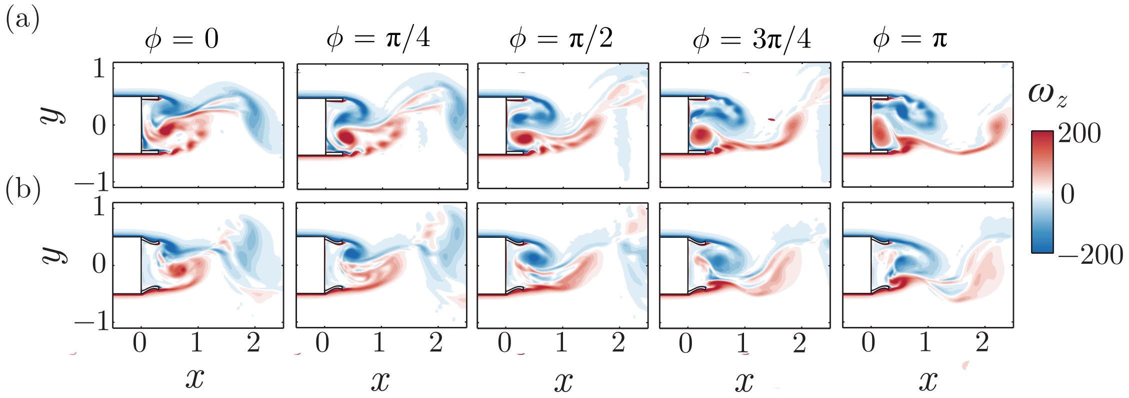

Figure 2.13: Time sequence of half of a shedding cycle, at $Re = 20000$ and $z = 0$, for: (a) a body with a straight cavity and (b) a body with the optimized cavity.

gradient is established. Thus, the flow is no longer ejected downstream from the body and recirculates closer to the base, forming a bubble narrower and shorter than that formed at lower Reynolds numbers because the traverse velocities of the flow at the trailing edge are greater and the growth of the vortices shed is now limited by the cavity. Consequently, in this particular case, the optimized cavity behaved as a tilted rear edge, but with the additional effect of including a cavity.

Figure 2.13 shows five time sequences of the spanwise vorticity contours at the central vertical plane, again for half the corresponding vortex shedding period (from $t = t_0$ to $t = t_0 + 1/2\, St_v^{-1}$), for the body with a straight cavity (model B) and that with the optimized one (model D). The sequence displays the vortex formation, growth and shedding from the upper wall in both cases. It can be observed in Fig. 2.13(a) that the high level of turbulence in the boundary layer produces the vortex fragmentation in the case of the straight cavity (Molezzi and Dutton, 1995; Prasad and Williamson, 1997). Furthermore, in this case the forming vortex penetrates inside the cavity entirely almost from the initial stages and grows, while it remains confined within the cavity plates, until a counter-rotating vortex starts to form at the lower wall. Notice that, the upper, forming vortex tears a piece of a vortex previously shed from the lower wall and pushes it inside the cavity. Although not shown in Fig. 2.13, the same sequence takes place when a vortex begins to form at the lower edge, tearing a portion of the vortex shed from the upper wall. This fact, explains that the mean flow does not exhibit a clear and significant *dead flow* region at the base cavity (see Fig. 2.12b). However, in the case of model D, the upper and lower vortices interact but do not penetrate inside the cavity, displacing the lowest pressure region downstream from the body base. Finally, the stabilization and regularization effect of the optimized cavity can be also inferred from the vortex fragmentation suppression, which indicates that both the level of turbulence and the oscillations amplitude are significantly reduced in this case.

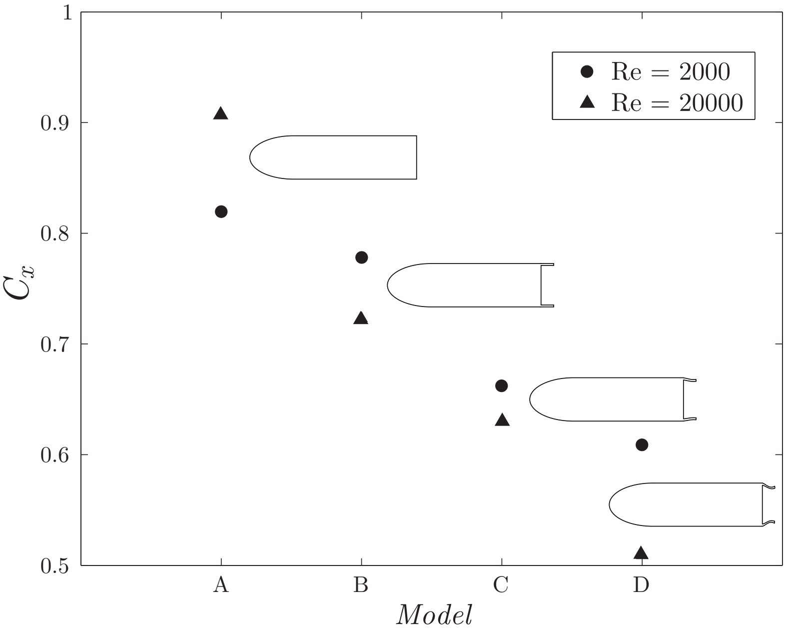

Figure 2.14: Time-averaged drag coefficient obtained for the four different body geometries described in this Chapter at $Re = 2000$ (●) and $Re = 20000$ (▲) respectively.

To summarize, Fig. 2.14 shows the mean drag values, C_x, obtained at $Re = 2000$ and $Re = 20000$ with the four models considered here. It is evident the drag reduction achieved when the geometry of the cavity is conveniently designed applying the shape optimization procedure described in Sect. 2.3.2, which not only reduces the C_x at the Re of study, but which turns out to be also very effective under different flow conditions. Therefore, this mathematically supported technique improves significantly the devices proposed, based on the flow dynamics knowledge and experience, and constitutes a powerful, useful tool to be applied in this field.

2.4 Conclusions

The present Chapter evaluates the efficiency of different mechanisms proposed to reduce the drag coefficient of two-dimensional bluff bodies with rear cavities, whose performance as control device is known to be limited by its depth, using the adjoint-based sensitivity formulation. Considering the flow and the drag sensitivity to a localized forcing, two passive control techniques, consisting in wake modifications by means of the placement of small control cylinders in the near wake and structure topological modifications, have been evaluated to achieve additional drag reduction with rear cavities. Therefore, sensitivity computations have been carried out following the simplified adjoint-based linear steady analysis developed by Meliga et al. (2014) for unsteady flows, for which the drag sensitivity to localized forcing, $\nabla_f C_x$, corresponds to the mean linear adjoint velocity $\mathbf{U}^\dagger$.

This approach has been proven to properly retrieve the main features regarding the most sensitive regions around the bluff body and the drag reduction values. Section 2.3.1 includes the validation analysis in the case of a square cylinder, and drag sensitivity maps for the bluff body with a straight cavity at $Re = 2000$. Fig. 2.3 depicted that the mean drag sensitivity is highest at the rear edges of the straight cavity, where control cylinders should be placed in order to achieve largest drag reduction. A first order prediction of such mean drag decrease is given by Eq. (2.12) (Fig. 2.3b), which provides with a largest reduction of 0.4%, when cylinders are placed in an optimal location $(x_c, y_c) = (0.368, \pm 0.428)$. A deeper analysis on the effect of such configuration on drag and wake properties is performed by means of unsteady RANS simulations. The results show that control cylinders placed in zones of highest sensitivity lead to drag reduction and wake stabilization, by altering the shedding process, as detailed in Parezanović and Cadot (2012). The flow reattaches around each cylinder, reducing the entrainment into the recirculation region, whose length increases, and subsequently the base pressure also increases, what accounts for the drag reduction. Besides, the axial velocity gradient is weakened and the backflow is also hindered, giving rise to an overall wake stabilization observed through reduction of drag fluctuations, C_x', amplitude of approximately 47% (Fig. 2.4). However, the mean drag reduction is very small, i.e. 0.6%, suggesting that a more efficient control alternative must be sought.

A second control strategy based on cavity shape modifications has been analyzed at $Re = 2000$, as a way to overcome the limitations in the drag reduction imposed by fixed cavity depths. After obtaining the drag sensitivity to flow modifications in Sect. 2.3.1, the drag shape sensitivity on the body surface was computed using Eq. (2.11). This variable has been used to guide local structure deformations within a defined control box, obtaining progressive drag reductions by means of an iterative one-shot optimization process, that combines the use of the former adjoint-based sensitivity solver and a free-form deformation CFD toolbox. An instantaneous approach has been employed, whereby we have selected instants of alternate highest sensitivity near the cavity, i.e. vortex shedding events in each cavity side. It has been demonstrated that this strategy helps to design cavity geometries that reduces the drag coefficient of the body, reaching an optimal shape after a few iterations, for which an asymptotic drag reduction of approximately 23% is obtained, as Fig. 2.5 shows. At this point, new local modifications do not improve the mean drag since the sensitivity is barely residual (Fig. 2.6). The optimized shape consists of a curved wall, that promotes local recirculation and an inwards deflection of the flow before massive separation, what leads to a narrower recirculation bubble and an increase of the base pressure.

To deeply explore the physical mechanisms behind the optimized shape that fosters the observed drag reduction, we have performed unsteady three-dimensional IDDES numerical simulations at two different Reynolds numbers, $Re = 2000$ and 20000 respectively. The numerical computations corroborate the results obtained by the drag sensitivity analysis, showing that the drag is monotonically reduced as the cavity walls are conveniently curved. At $Re = 2000$, the optimized shape cavity provides a 25.6% drag reduction, relative to that of the original body, i.e. without cavity, Fig. 2.7(a) and Table 2.4. This reduction is achieved by the combination of an induced inwards flow deflection, which replicates a slanted rear surface, together with the base cavity effect, and a flow deceleration caused by the generation of an adverse pressure gradient near the trailing edge of the body. The curved cavity displaces the recirculation bubble downstream of the body, increasing the mean base pressure coefficient C_p (Fig. 2.8), similar to what happens when base bleed is used as control mechanism (Sanmiguel-Rojas et al., 2009). Furthermore, the addition of an optimized cavity significantly reduces the energy of the flow and the strength of the vortical structures of wake in the near field (Figs. 2.7b, 2.9). Consequently, the flow is also regularized and a narrower, more slender and less chaotic wake forms (Figs. 2.9, 2.10). Although the optimal shape has been obtained for $Re = 2000$, it is also very efficient at $Re = 20000$, demonstrating that the procedure is robust. In fact, the drag reduction achieved at $Re = 20000$ is even larger than that obtained at $Re = 2000$, due to the higher adverse pressure gradient before separation and the decrease of the viscous contribution to the drag coefficient. Altogether, adding an optimized cavity provided a total mean drag reduction of 43.9% (Table 2.5), and reduced the amplitude of the velocity fluctuations generated behind the body (see Figs. 2.11(b), 2.13). Consequently, it has been corroborated that the use of adjoint methods, linked to shape optimization, are efficient tools for the control of flow around bluff bodies, improving the aerodynamic performance of drag reduction devices.

CHAPTER

THREE

Effects of rear cavities on the wake behind an accelerating D-shaped bluff body

Abstract

The present Chapter is devoted to study experimental and numerically the transient development of the wake induced by a constant acceleration of a D-shaped bluff body, starting from rest and reaching a permanent regime of Reynolds number $Re = 2000$, under different values of acceleration and implementing three distinct rear geometrical configurations. Thus, alongside the classical blunt base, two control passive devices, namely a straight cavity and an optimized, curved cavity, recently designed using adjoint optimization techniques, have been also used to asses their performance in transient flow conditions. Particle Image Velocimetry (PIV) measurements were performed in a towing tank to characterize the near wake development in the early transient stages. It has been observed that the flow first develops symmetric shear layers with primary eddies attracted towards the base of the body due to the flow suction generated by the accelerated motion. Eventually, the interaction between the upper and lower shear layers provokes the destabilization of the flow and the symmetry breaking of the wake, finally given rise to an alternate transitional vortex shedding regime. The transition between these phases is sped-up when the optimized cavity is used, reaching earlier the permanent flow conditions. In particular, the use of the optimized geometry has been shown to limit the growth of the primary eddies, decreasing both the recirculation and vortex formation length and providing with a more regularized, more organized vortex shedding. In addition, numerical simulations (DNS) have been performed to evaluate the distribution of forces induced by the addition of rear cavities. In general, the aforementioned smoother and faster transition related to the use of optimized cavity, translates into a lower averaged value of the drag coefficient, together with less energetic force fluctuations, regardless of the acceleration value.

This Chapter is comprised, in part, in the paper: "Effects of rear cavities on the wake behind an accelerating D-shaped bluff body", by Lorite-Díez, M., Jiménez-González, J. I., Gutiérrez-Montes, C. & Martínez-Bazán, C., published in Physics of Fluids (Lorite-Díez et al., 2018).

3.1 Introduction

The flow around bluff bodies constitutes a relevant problem in aerodynamics, due to its importance in many industrial applications, such as transport industry. In particular, wakes behind trucks or heavy vehicles are characterized by a massive detachment of flow behind them, which generates large values of the drag and oscillating forces on the body (Choi et al., 2014). These aerodynamic forces have a significant impact on the fuel consumption, and therefore, on the emission of greenhouse effect gases. In that regard, Bradley (2000) estimated that at least 20% of trailer's fuel consumption (driving at 105 km/h), is related to aerodynamic loses, i.e. drag. More precisely, an approximate 25% of such drag resistance corresponds to the rear part of these types of vehicles (Wood, 2006). Consequently, a large effort has been devoted during the past years to develop flow control and drag reduction strategies, acting on the rear part of bluff bodies, mostly using different simplified models, which retain the main wake features of heavy vehicles (Ahmed et al., 1984; Han et al., 1996; Pastoor et al., 2008; Grandemange et al., 2015; Bonnavion et al., 2017). Regardless of the nature of the control, these strategies usually act modifying the near wake or the boundary layer detachment, using among others: blowing (Bohórquez et al., 2011), rear cavities (Sanmiguel-Rojas et al., 2011; Evrard et al., 2016) or flaps (Brackston et al., 2016). The design of most of such techniques is based on the profound knowledge of the flow features, although the recent application of sensitivity maps (Meliga et al., 2014, 2016), in combination with optimization algorithms (Othmer, 2014), may provide with more efficient control devices. Using these approaches, Lorite-Díez et al. (2017) have proposed an improved curved, optimized rear cavity, implemented in a D-shaped body, similar to that in Pastoor et al. (2008), which is capable of providing with a total drag reduction greater than 25% with respect to the body without cavity.

Traditionally, these studies on drag reduction and wake control are focused on permanent flow regimes, leaving aside the analysis of the performance of such strategies under transient conditions, which are very common in aerodynamics applications, such as vehicles accelerating or overtaking manoeuvres (Liu et al., 2017).

Therefore, it seems natural to extend the aforementioned studies on flow control to more complex, transient flow phenomena. In that sense, several previous works have characterized the flow regimes and force distributions emerging from impulsive dynamics of simplified bluff bodies. For instance, Odar and Hamilton (1964) proposed an analytical equation to model the force on an accelerating sphere, and subsequently validated it through towing tank tests, accounting for the velocity and the acceleration of the sphere as well as time history terms. Later on, Roos and Willmarth (1971) evaluated experimentally the recirculation bubble behind a sphere and a disk, along with the transient forces and moments acting on them, varying the acceleration for Reynolds numbers in the range $5 \leq Re \leq 1 \times 10^5$. These investigations were subsequently extended to cylinders and prims by several authors, both numerical and experimentally (see e.g. Bouard and Coutanceau, 1980; Sarpkaya and Kline, 1982; Chang and Chern, 1991; Finaish, 1991; Chu and Liao, 1992). More recently, Tonui and Sumner (2011) experimentally investigated the effect of prismatic geometries on the near wake topology, using a towing tank and particle image velocimetry (PIV) measurements, focusing on the recirculation length and strength of the vortices shed. In addition, the works by Fernando and Rival (2016) and Fernando et al. (2017), have assessed the separation mechanism, forces and vortex evolution in the wake of accelerating spheres and plates, using a similar experimental set-up. In general, during the body's accelerating period, the drag force is mainly governed by the added mass term. Next, there is a transient period toward the permanent vortex shedding regime, where large amplitude drag variations occur stemming from the evolution of the near wake, which finally lead to the typical alternate shedding at a characteristic natural frequency.

These aforementioned force distributions are strongly linked to near wake transient initial development. Furthermore, it has been also proven that such stages and flow features, are highly dependent on the geometry of the bluff body (Tonui and Sumner, 2011). Consequently, if the performance of any passive control device is to be evaluated in transient flows, a profound characterization of flow dynamics is needed. Within this frame, we study three different rear geometries (i.e. blunt base, straight cavity and curved, optimized cavity) implemented in a D-shaped body, which is accelerated from rest, to evaluate their efficiency in terms of drag reduction and wake oscillations in transient conditions. Following the aforementioned premises, we perform herein experimental and numerical analyses of the transient dynamics, to study flow detachment, vortex formation and shedding, and time evolution of forces; for four different acceleration values and a Reynolds number of $Re = 2000$. These results complement those by Lorite-Díez et al. (2017) in permanent flow regime, with the aim at looking for the most efficient overall control alternative.

Thus, the experimental set-up and numerical techniques employed are first described in Sect. 3.2. Section 3.3 is devoted to the experimental results, obtained in a towing tank, that have allowed the characterization of the early stages of wake development. Next, Sect. 3.4 presents a comparison of the experimental measurements with the results obtained from direct numerical simulations, to subsequently perform a numerical study on the forces distributions and drag reduction. Finally, the main conclusions are drawn in Sect. 3.5.

3.2 Experimental and numerical aspects

3.2.1 Problem description

We study the three-dimensional flow around a D-shaped body of semi-ellipsoidal nose, as in Lorite-Díez et al. (2017) (see Fig. 3.1a), of an incompressible fluid of density ρ

and viscosity μ. The body of height $H = 4$ cm, length $L = 3.83H$ and spanwise width $W = 7.64H$, implements three different rear geometries: a blunt base without cavity (Ref), a straight cavity (Str) and a curved, optimized cavity (Opt) (see Fig. 3.1c). The cavities feature a depth of $0.3H$ and a wall thickness of $0.05H$, while the distance between outer edges for the curved cavity is $h = 0.853H$. The origin of the coordinate system, (x, y, z), is placed at the base of the cavity, and at half of the spanwise and transversal lengths. Note that in the case of the body without cavity, the body base is at $x = 0.3H$. The body is impulsively started from rest, at a constant acceleration, a, reaching a final permanent regime with a constant velocity, $u_{\max} = 5$ cm/s (see inset in Fig. 3.1a). The aforementioned overall dimensions ensure a quasi two-dimensional flow, being the side edge effects negligible in the near wake and force distributions, except for a very small lateral spanwise region. Under the previous conditions, the characteristic scales for length, velocity, acceleration, pressure, and time, are respectively: H, $u_{\max}$, $u_{\max}^2/H$, $\rho u_{\max}^2$ and $H/u_{\max}$. In all, four different dimensionless accelerations, $a^* = aH/u_{max}^2$, have been considered for the analysis, namely $a^* = 0.08,\ 0.2, 0.5$ and 1. Besides, a non-dimensional displacement parameter is defined to quantify the downstream physical distance traveled by the body, Δx, as $s^* = \Delta x/H$. Finally, the permanent regime is characterized by the Reynolds number, $Re = \rho u_{\max} H/\mu = 2000$. The experimental facility used, as well as the numerical model implemented, are next described.

3.2.2 Experimental set-up

The experiments were carried out in a towing tank of 2 m × 0.6 m × 0.6 m, which allows optical access from all sides. The body is towed and controlled through an Adjustable Frequency Drive (AFD), iG5A series, connected to an AC motor that provides a stable linear displacement for velocities up to 0.66 m/s. AFD allows to precisely control the velocity and acceleration, with sensitivities of 70 $\mu m/s$ and $80 \mu m/s^2$ respectively.

The body, manufactured using a three-dimensional, selective laser sintering (SLS) printer, was vertically immersed in the water tank as shown in Fig. 3.1(b), and aligned with respect to the towing direction by means of a 3-Axis stage with micrometric adjustment. In addition, a thin plate, placed at the free surface, was used to remove any perturbation introduced by the free surface waves produced during the experimental measurements. The separation between the body and bottom of the tank was less than H/2 in order to avoid edge effects.

Wake measurements were carried out using time resolved, planar particle image velocimetry (PIV). To that aim, a 5 W, Diode-Pumped Solid State (DPSS) green laser was used to create a sheet, which was positioned horizontally normal to z-axis of the body and centered with respect to y-axis. The flow was seeded with 10 μm, neutrally-buoyant hollow glass spheres and a CCD-sensor, High-Speed Camera, towed alongside the body, was used to record images at a rate of 125 fps, with a resolution of 1024 × 512 pixels. This

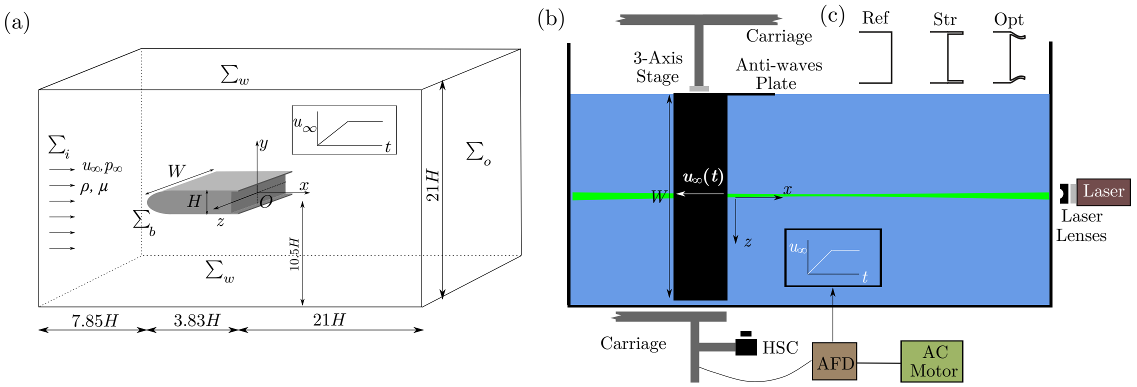

Figure 3.1: (a) Problem configuration and numerical domain, (b) experimental set-up and (c) rear geometries investigated. Insets in (a) and (b) show the time varying inlet velocity $u_\infty(t)$.

set-up provided with an approximate Field of View (FoV) of $4H \times 2H$ behind the body at midspan of water depth, which allowed to properly capture the recirculation region and vortex shedding. The exposure was accordingly adjusted to obtain static particles between consecutive snapshots.

Series of around 2000 pair of images were processed in each experimental case, using the Matlab®toolbox PIVlab (Thielicke and Stamhuis, 2014), applying a pre-processing of images with interrogation windows size of 16 × 16 pixels with 50% overlapping area, what results into a vector field of 124 × 62 and a spatial resolution of $0.03H$. The associated uncertainty was estimated to be ±5%.

3.2.3 Numerical details

Additionally, direct numerical simulations (DNS) were performed to complement and extend the experimental measurements, for the same flow conditions. To that end, the incompressible Navier-Stokes equations were solved numerically using the finite volume toolbox OpenFoam®, within a prismatic domain (see Fig. 3.1a), extending in the axial x-coordinate $21H$ downstream of the body rear edges, $7.85H$ upstream of the body nose, and spanning $21H$ in the transversal y-coordinate, and $7.64H$ in the spanwise z-coordinate. Appropriate boundary conditions were imposed, namely no-slip condition at the body wall, Σ_b, slip conditions at the domain sides, Σ_w, and an outflow condition for the outer boundary, Σ_o. At the inlet, we imposed a prescribed time varying velocity field normal to the boundary Σ_i, i.e. $(u_x, u_y, u_z) = (u_\infty^*, 0, 0)$, where the dimensionless input velocity, $u_\infty^*(t^*)$, follows,

$$u_\infty^*(t^*) = \begin{cases} a^* t^* & t^* \leq 1/a^*, \\ \\ 1 & t^* > 1/a^*. \end{cases} \tag{3.1}$$

The equations were discretized using Gauss linear second-order schemes for the spatial terms of the Navier-Stokes equations, a Crank-Nicholson scheme for the temporal integration, whereas the pressure-velocity coupling was solved by means of a Pressure-Implicit Split-Operator (PISO) algorithm (Issa, 1986). A grid sensitivity study was conducted as in Lorite-Díez et al. (2017) to guarantee that the results did not depend on the mesh used. As an outcome, a mesh of nearly 3×10^6 cells was selected, which concentrates nodes close to the body wall and cavity edges, where larger physical gradients are present. Finally, the Courant-Friedichs-Lewy (CFL) number was limited to a maximum value of 0.5, to guarantee computational stability. On the other hand, in the remaining, non-dimensional variables will be used, with the asterisk dropped to simplify the notation, unless otherwise stated.

3.3 Experimental results: early stages wake characterization

This Section presents experimental results which describe the main flow characteristics, for the three rear geometries under study, and the different selected accelerations. Thus, we first describe the wake development obtained experimentally, to subsequently characterize the recirculation region and vortex downstream evolution.

3.3.1 Experimental flow description

As mentioned in Sect. 3.2, wake measurements were performed using PIV technique, which provided with a detailed description of the wake regimes and vortex development for the three base geometries under study, allowing to identify the main differences exhibited in terms of transient flow events. To that end, we will describe the main flow features using time sequences of the spanwise vorticity, ω_z, where

$$\omega_z = \frac{\partial u_y}{\partial x} - \frac{\partial u_x}{\partial y}, \tag{3.2}$$

to analyse the role of different geometries and acceleration values.

Figure 3.2 shows the initial stages of the flow for the optimized cavity (Opt) and an intermediate value of acceleration, $a = 0.5$. In addition to provide the dimensionless time, t, we have included the value of the distance traveled by the body, s, given by,

$$s(t) = \begin{cases} at^2/2 & t \leq 1/a, \\ \\ t - 1/2a & t > 1/a. \end{cases} \tag{3.3}$$

The body starts from rest at $t = 0$, within a quiescent flow (Fig. 3.2a), and during and shortly after the impulsive motion (notice that at $t = 2$ the body's motion reaches the

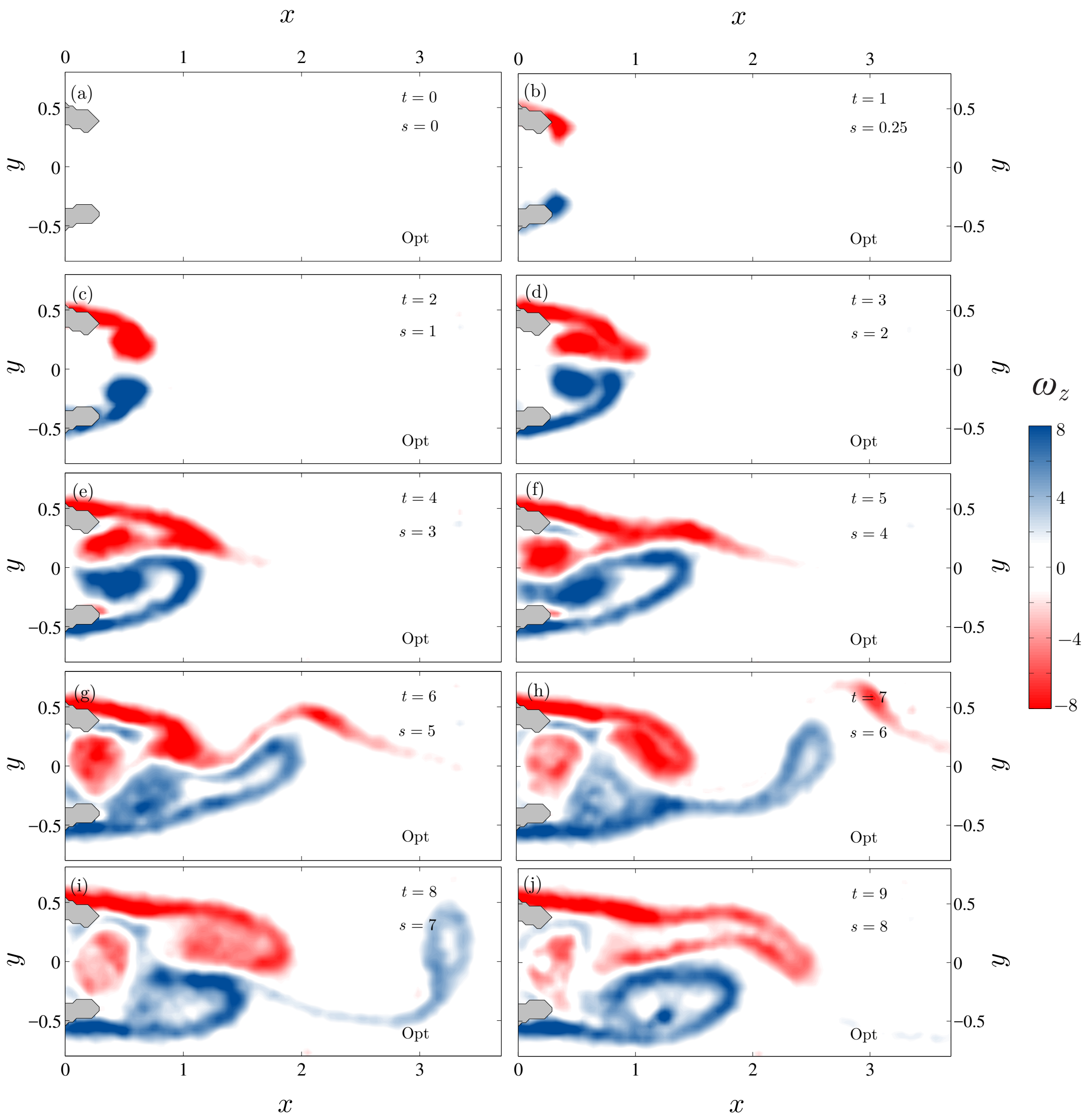

Figure 3.2: Time sequence of spanwise vorticity ω_z of the near wake, obtained by PIV measurements, for the optimized cavity at $Re = 2000$ and $a = 0.5$. Contours of vorticity range $\omega_z \in [-8, 8]$. Here the negative vorticity contours are in red and the positive ones in blue.

permanent velocity regime), the flow separates at the rear cavity edges, and the shear layer rolls up forming two symmetric counter-rotating eddies, which grow with time (Figs. 3.2b,c). As it will be shown later in Sect. 3.4, the inertial motion generates a low pressure region near the base of the body that, together with the strong circulation of eddies, drives them towards the cavity, while preserving a quasi symmetric wake configuration (Fig. 3.2d). These primary vortices grow inside the cavity (Fig. 3.2e), whose size precludes them from further growing, producing the vortex detachment (Figs. 3.2f,g). In particular, Fig. 3.2(g) shows that, for the case at hand, the primary eddy with negative,

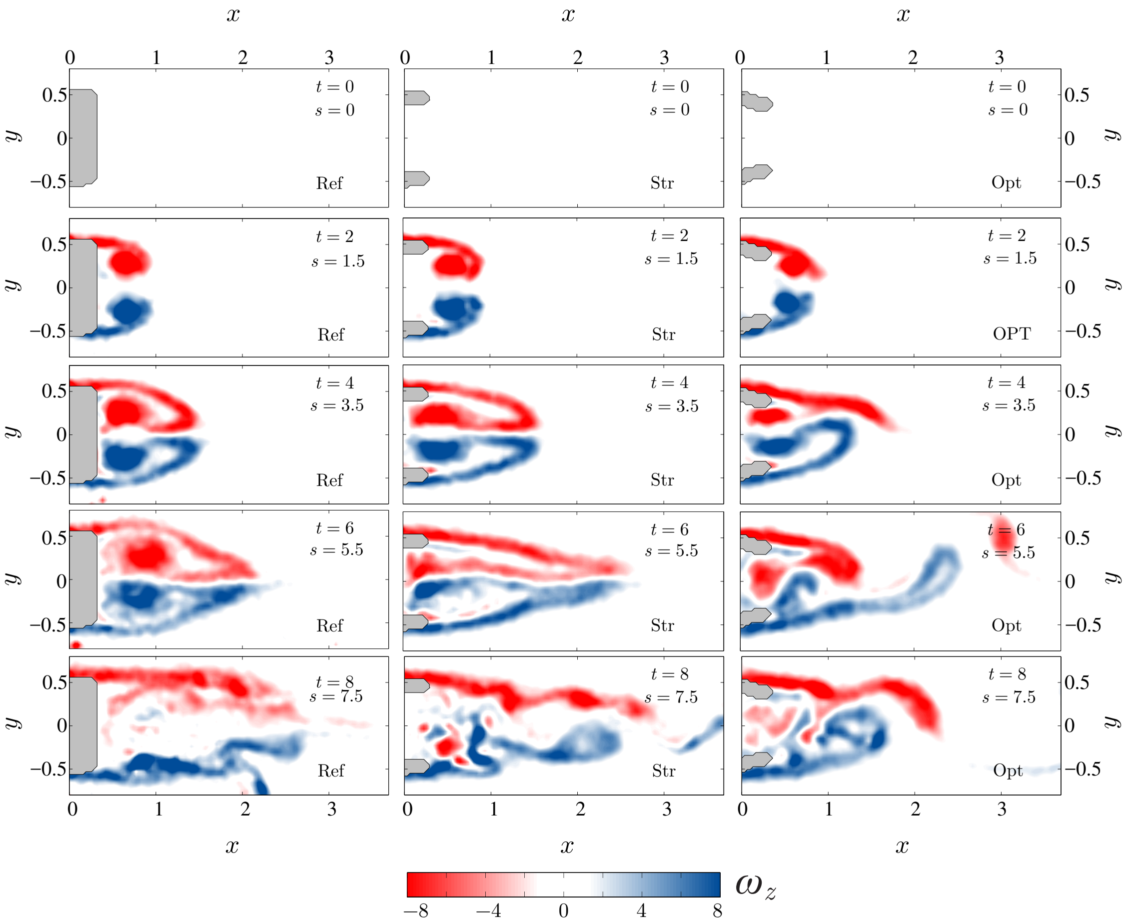

Figure 3.3: Time sequence of spanwise vorticity ω_z of the near wake, obtained by PIV measurements, for the blunt-based body (left column), a body with a straight cavity (central column) and a body with a optimized cavity (right column) at $Re = 2000$ and $a = 1$. Contours of vorticity range $\omega_z \in [-8, 8]$.

clockwise vorticity remains inside the cavity, while the positive, counterclockwise one is ejected. Simultaneously, due to the unstable nature of the flow at $Re = 2000$, the symmetry is broken and the interaction between upper and lower shear layers triggers a vortex shedding process (Figs. 3.2g-j), which eventually will lead to the characteristic alternate vortex shedding in permanent regime (note that for $t = 7$, a negative small vortex is being already convected downstream, while a positive one starts to detach). At the same time, the former primary eddy, which was trapped inside the cavity, progressively dissipates giving rise to an irrotational region inside the cavity, as Fig. 3.2(j) suggests. For the sake of a clearer interpretation of the results, three different phases can be defined during the transient process, namely, *phase A* or initial symmetric wake development (Figs. 3.2a-d); *phase B* characterized by the vortices interaction and symmetry breaking without shedding (Figs. 3.2e,f); and *phase C* in which the shedding process begins (Figs. 3.2g-j).

The described dynamics is highly related to the distribution of forces acting on the body, as it will be shown later in the discussion of the numerical results (see Sect. 3.4). Therefore, a noticeable modification of the drag value might be obtained if important flow topology changes are introduced during the early transient stages, for instance, by means of controlling on the vortex formation distance or limiting the size of eddies.

In this regard, to evaluate the effect of geometry, Fig. 3.3 shows the near wake evolution, characterized through vorticity contours, for the three rear configurations considered herein, namely, the blunt-based body, and the bodies implementing straight and optimized cavities, respectively, for the largest value of acceleration $a = 1$. At initial stages ($t < 4$), a symmetric wake development takes place for all geometries, although the shear layer and vortex topologies are different. In the case of the blunt-based body (left column, Fig. 3.3), primary eddies are located very close to the base, whereas for the bodies with cavities, the formation takes place outside the cavity (see middle and right columns). Besides, while the straight cavity leads to shear layers which are initially aligned with the cavity blades, in the case of the optimized cavity, the curved geometry induces an inward transversal flow, which makes the shear layers fold towards the axis, decreasing the distance between the cores of both vortices. At $t = 4$, the primary vortices move towards the body base in the case without a cavity and get inside the cavity in the bodies with a straight and a curved cavities. However, whereas for the two first configurations (blunt base and straight cavity) the wake remains symmetric, i.e. phase A has not been yet completed, the wake behind the optimized cavity body is already asymmetric, indicating that phase B has already started. Physically, the wake behind the blunt-based body is aligned with the streamwise direction, but the absence of any transversal barrier does not limit the growth of the eddies, curving the shear layers in the vicinity of the rear edges, while preserving its symmetry (see $t = 6$, phase A). Conversely, for the bodies with cavities the growth of eddies is transversally restricted by the cavity, which accelerates the asymmetry of the wake and elongates the primary vortices. The latter is concomitant with the formation of auto-induced shear layers of opposite signs in the vicinity of the flow detachment (as it can be seen for the straight cavity at $t = 6$). In the particular case of the optimized cavity, the closer and more intricate interaction between vortices, together with the larger space restriction, triggers earlier the shear layer oscillations and symmetry breaking, characterizing the transition to phase B (at $t = 4$), and the subsequent non-regular vortex shedding inception defining phase C (for $t \geq 6$). Similarly, for the straight cavity, the phase B does not take place until $t = 6$ and vortex shedding is first discernible for $t = 8$, whereas the phase B, symmetry breaking scenario appears for $t \geq 8$ for the blunt-based body. Interestingly, at the last stages of the described early transients, a nearly irrotational region forms at the body base (especially noticeable for the blunt base case) which stems from the flow deceleration that occurs after the steady motion of the body is set ($t > 1$). This deceleration translates into a local pressure increase that promotes the downstream convection of eddies, which coexist with the dissipation of vortices trapped inside this region. This phenomenon gives

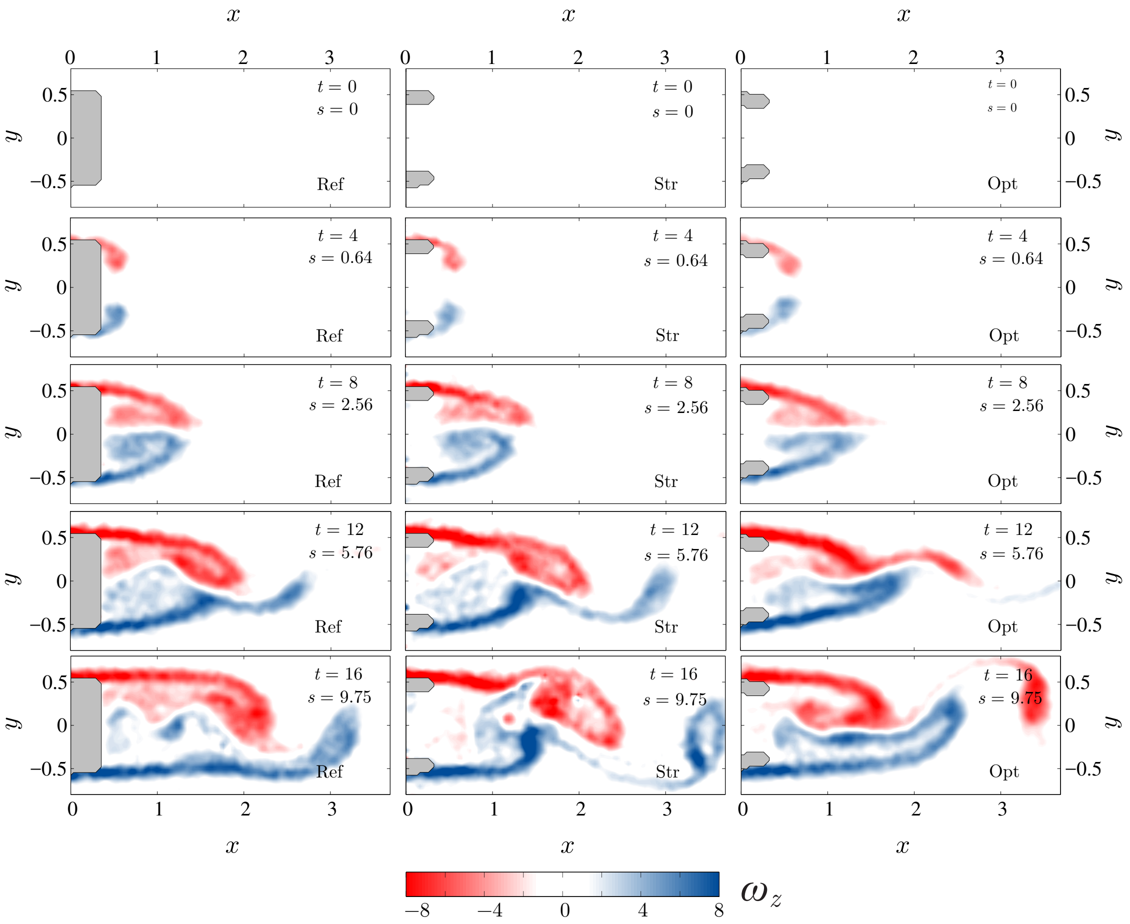

Figure 3.4: Time sequence of spanwise vorticity ω_z of the near wake, obtained by PIV measurements, for the blunt-based body (left column), a body with a straight cavity (central column) and a body with an optimized cavity (right column) at $Re = 2000$ and $a = 0.08$. Contours of vorticity range $\omega_z \in [-8, 8]$.

rise to an unsteady flow regime characterized by the alternate, non-regularized shedding of vorticity, which is accompanied by the lengthening of the near wake and recirculation bubble (as it will be shown below), and that eventually will conclude with the characteristic regular permanent flow regime at a constant Re. Finally, notice that this process is weaker for the optimized geometry, as Fig. 3.3 shows, which clearly provokes a faster transition towards the mentioned non-regular shedding. Consequently, different behaviors of drag time sequences are expected for these three geometries.

Similar flow features can be observed for lower values of acceleration, a. In that sense, Fig. 3.4 depicts time sequence of vorticity contours for the three geometries at $a = 0.08$. Unlike the previous case of $a = 1$, for which the body's accelerating time scale is much shorter than the corresponding flow impulsive response time, the lower value of a induces weaker vortical structures, while the transitions between different phases take longer times (note that, for the case at hand, the steady body's motion is reached at $t = 12.5$). The

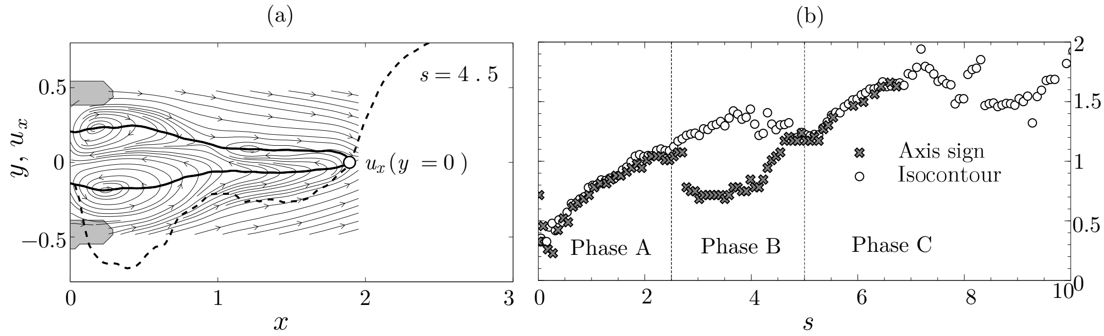

Figure 3.5: (a) Methods to quantify the recirculation length, l_r: "*axis sign*" - streamwise velocity distribution at the axis $y = 0$, $u_x(x, 0, 0)$ (dashed line); "*isocontour*" - furthest downstream axial location of isocontour of nil streamwise velocity, $u_x = 0$ (white circle on solid isocontour superimposed on the streamlines) for the straight cavity and $a = 0.5$. (b) Evolution of l_r with the physical traveled distance, s, for the optimized cavity and $a = 1$, using the two identification methods for l_r. Transient phases thresholds have been included for the sake of discussion.

occurrence of slower, less intense processes, involves the balance between phases duration for the different geometries. For instance, phase A remains present for $t \leq 8$, while for $t \geq 12$ phase C has already begun for all bodies. In this case, the primary vortices are smaller and less intense than those forming for $a = 1$, and do not completely penetrate inside the cavity, being easily convected downstream as the flow evolves. Therefore, low accelerations with this particular flow dynamics are expected to have a smaller effect on the drag coefficient.

3.3.2 Temporal variation of recirculation region

To better identify the differences between flow dynamics concerning the three geometries under study and the role of the acceleration, we next present quantitative results of major variables characterizing the near wake, namely, the recirculation bubble length and the vortex core postion i.e. temporal axial location and transversal distance. The analysis of such variables will shed some light on the performance and potential drag reduction, which will be later addressed.

We first discuss the influence of geometry and acceleration on the recirculation length, l_r, for which two different criteria have been employed (see Fig. 3.5a). The first method, denoted as "*axis sign*", determines l_r as the distance where the streamwise velocity at the axis $y = 0$, $u_x(x, 0, 0)$, changes from negative to positive (see dashed line in Fig. 3.5a). The second one, identified as "*isocontour*", corresponds to the furthest downstream axial location of the isocontour of zero streamwise velocity, $u_x = 0$ (see white circle on isocontour in Fig. 3.5a). Notice that this point does not necessarily have to be located on the axis. Figure 3.5(b) shows the evolution of l_r as a function of the physical traveled distance, s, for the body with the optimized cavity and $a = 1$, computed by means of the two aforementioned methods. Such evolution of l_r is intrinsically associated to the wake development. In the early transient, which is characterized by the symmetric wake evolution phase A, trends are nearly identical for the two methods, and l_r presents a monotonic increase, which extends further than the accelerating time in this case (notice that, for this case, the accelerated body motion stops at $t = 1$ or, similarly, $s = 1/2\,at^2 = 0.5$). This behavior represents the longer impulsive flow response to the short accelerating motion of the body. At $s \simeq 2.5$, there is a sudden change in l_r defined by the axis sign method, related to the beginning of phase B, where the wake symmetry is broken, as corroborated by the vorticity contours in Fig. 3.3. In particular, once the symmetry is broken, the recirculation bubble borders are shifted transversally, away from the axis. Consequently, its furthest downstream location does not coincide with that generated by the intersection of such region with the x-axis, and the two methods described to determine l_r differ, allowing the identification of the phase B threshold. The transition between phases has been highlighted in Fig. 3.5(b) using dashed lines. After the symmetry breaking and the subsequent recirculation bubble tilting, the interaction between shear layers provokes the detachment of the first vortex downstream, thus giving rise to an effective shortening of the instantaneous recirculation region, i.e. l_r decreases, which marks the beginning of phase C. At this new stage, oscillations of l_r begin as a consequence of the transient shedding, accompanied by an overall growth of the recirculation region, which stems from the aforementioned primary eddies dissipation close to the base, and the associated pressure increase. From this point on, the recirculation region continues evolving, characterized by the growth of an irrotational region near the body base and the alternate shedding of vortices, eventually reaching the l_r permanent value (approximately 1.2 according to Lorite-Díez et al., 2017).

The influence of the geometry and the acceleration value, a, on the recirculation length, l_r, determined by the isocontour criterion, is summarized in Fig. 3.6 at the very early transient stages. As it has been previously mentioned, for low acceleration values, i.e. $a = 0.08$ (see Fig. 3.6a), the transient evolution is slower and the range of s plotted corresponds to phase A and phase B, where there are no major differences between the three geometries, although the body without cavity presents a slightly larger instantaneous l_r. In fact, according to Fig. 3.4, symmetry breaking has already occurred around $t \simeq 12$, i.e. $s \simeq 5.76$, for all cases. At larger acceleration rates, $a = 1$ (Fig. 3.6b), the role of the optimized cavity becomes more evident. Thus, the inwards velocity component induced by the curved blades, promotes an earlier transition from symmetric to asymmetric wake (phase B), and the subsequent vortex shedding (phase C). However, the evolutions of l_r are similar for the blunt-based body and the body with a straight cavity. The effect of the acceleration value, a, is further investigated for the optimized cavity and the blunt base in Figs. 3.6(c,d). In both cases, the evolution of l_r almost coincides during phase A. However, as expected, the threshold of symmetry breaking occurs sooner at larger values

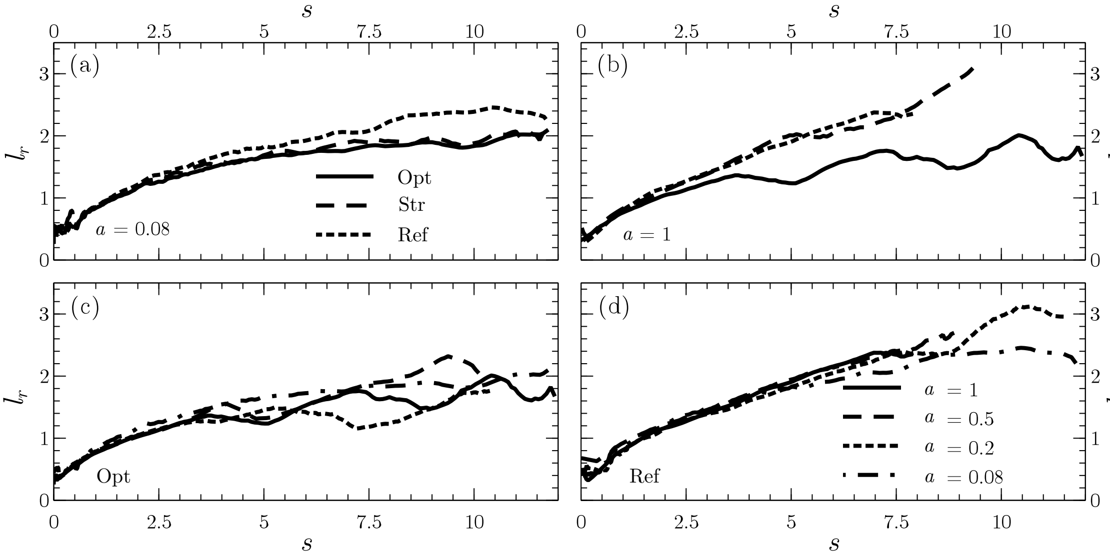

Figure 3.6: Evolution of the recirculation length l_r versus physical traveled distance s for different geometries (top row) at (a) $a = 0.08$ and (b) $a = 1$; and different acceleration values (bottom row) for (c) the optimized cavity and (d) the body without cavity. Here l_r has been computed using the described isocontour method.

of a, as the earlier local drop of l_r indicates. This effect is more acute for the optimized cavity, as the comparison between Figs. 3.6(c,d) suggests.

3.3.3 Vortex dynamics

We next discuss the evolution with the traveled physical distance, s, of the primary eddies and vortices shed as the transient process evolves. To analyze the primary eddies displacement, we will compute the maximum and minimum values of spanwise vorticity, $\max(\omega_z)$ and $\min(\omega_z)$, in the near wake. The latter variables will define the axial location of eddies' cores of positive and negative vorticity, as $x_{e,+} = x(\omega_z = \max(\omega_z))$ and $x_{e,-} = x(\omega_z = \min(\omega_z))$ respectively, as well as the corresponding transversal spacing, $d_e = |y(\omega_z = \max(\omega_z)) - y(\omega_z = \min(\omega_z))|$. A graphical representation of such variables is included in Fig. 3.7(a), where points of maximum and minimum vorticity ω_z have been depicted. As it can be observed, these points detect the cores of eddies in the recirculation bubble for the early stages, and their tracking may allow us to identify the incipient transition to an asymmetric wake (phase B). Once the eddies are mitigated, this measurement will be no longer meaningful. In addition, in order to track the shed vortices during the whole time history, two new variables will be computed, namely, the axial position of the shed vortices, x_v, and their transversal distance with respect to the $x-$axis, y_v. To that aim, we use the method proposed by Pawlak et al. (2007), which is based on integral functions proportional to flux of momentum, transversal velocity changes or mass variations, throughout a defined planar region. Thus, several criteria were presented by Pawlak et al.

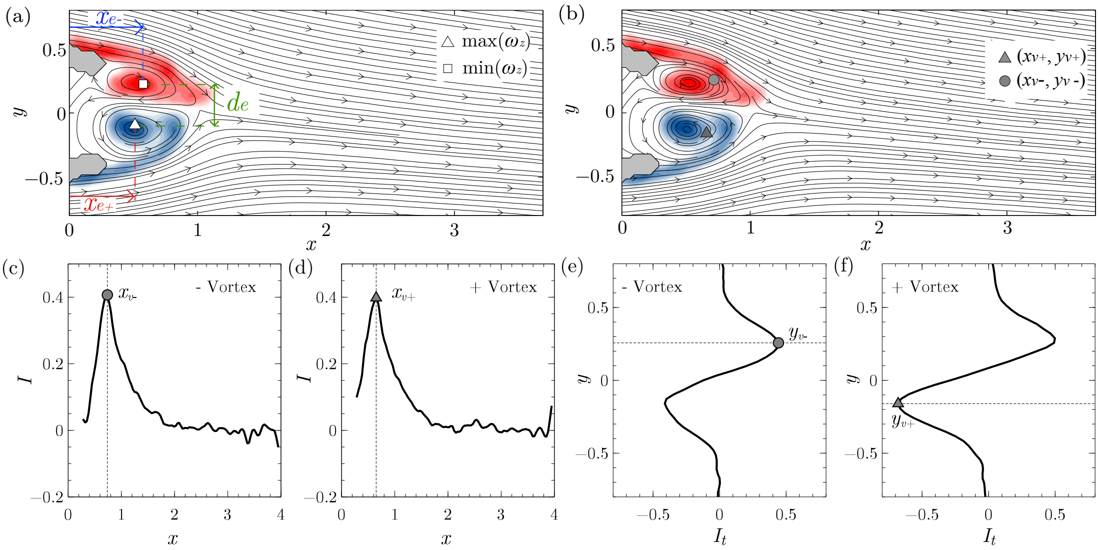

Figure 3.7: Identification of primary eddies cores and shed vortices front for the optimized cavity and $a = 0.5$, when $s = 2$: (a) axial location, $x_{e,+}$ and $x_{e,-}$, and transversal distance, d_e, obtained using the spanwise vorticity criterion; and (b) location of shed vortices, (x_{v+}, y_{v+}) and (x_{v-}, y_{v-}), obtained by means of integral magnitudes defined in Eqs. (3.4) and (3.5). (c-f) Computation of integral magnitudes and identification of maxima and minima (dashed lines) to provide with values of x_v and y_v in (b). Contours of vorticity range $\omega_z \in [-8, 8]$.

(2007) to identify the axial and transversal location of a leading vortex in a starting jet. In particular, to determine x_v, we will choose the maximum of:

$$I(x,t) = \int_{y_{\min}}^{y_{\max}} u_x^2(x,y,t)dy, \tag{3.4}$$

where the integration limits lye between $y_{\min} = 0$ and $y_{\max} = 1$, for the negative vorticity region (denoted as "- *Vortex*") and $y_{\min} = -1$ and $y_{\max} = 0$, for the positive vorticity region (denoted as "+ *Vortex*"). Once the axial locations for both positive and negative vortices are computed, i.e. x_{v+} and x_{v-}, the transversal location, y_v, is computed according to,

$$I_t(y,t) = \int_{x_v}^{x_v+L_i} u_y dx, \tag{3.5}$$

where $L_i = 0.4$ is the axial range of integration employed in the present Chapter. These integral variables are computed for $a = 0.5$ and the optimized cavity for $t = 3$ (or $s = 2$), and presented in Figs. 3.7(c-f). The results corroborate the robustness of the integral quantities, since they provide with maximum to identify x_v and y_v, as the dashed thin lines in Figs. 3.7(c-f) show. Note that, we have denoted the position of the primary eddies obtained from the maximum and minimum values of spanwise vorticity as $x_{e,+}$ and $x_{e,-}$ respectively. However, (x_{v+}, y_{v+}) and (x_{v-}, y_{v-}) have been used to denote the vortex position given by the integral methods presented in Eqs.(3.4-3.5).

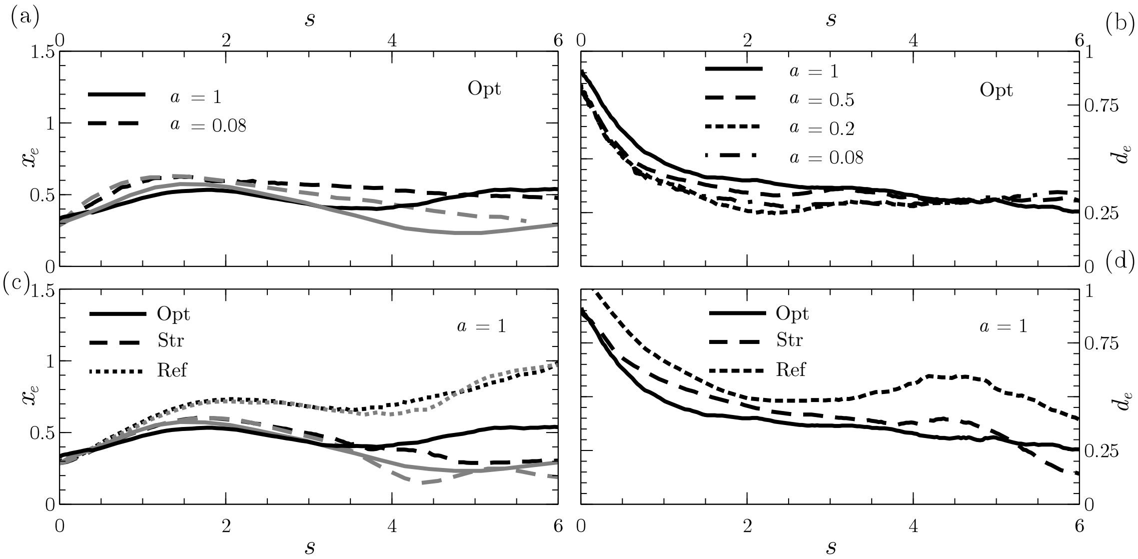

Figure 3.8: Evolution of primary eddies with the physical traveled distance s: axial location x_e (a,c) and transversal distance between cores d_e (b,d), for the optimized cavity at $a = 0.08$ and 1 (top row); and for the three geometries under study at $a = 1$ (bottom row). Grey lines in (a,c) represent negative vorticity eddies, $x_{e,-}$, whereas black lines stand for positive ones, $x_{e,+}$.

The values of axial locations x_e and x_v will initially match until the primary eddies move towards the base, whereas the recirculation region continues developing evolving downstream of the body. At this point, the integral criteria will better track the leading vortex front.

Figure 3.8 depicts evolution of axial location of positive and negative vorticity primary eddies, $x_{e,+}$ and $x_{e,-}$, and vertical distance between them, d_e, versus s. More precisely, Fig. 3.8(a) shows the axial location of the upper and lower eddies emitted from the optimized cavity for the maximum and the minimum acceleration values, $a = 0.08$ and 1 respectively, whereas Fig. 3.8(b) depicts the corresponding transversal distance d_e for all accelerations. Thus, for small s ($s \approx 2.5$ for $a = 0.08$ and $s \approx 3.5$ for $a = 1$) the flow symmetry becomes evident, as inferred by the nearly identical evolutions of x_e corresponding to the upper and the lower vortices. In the same line, after this early period, curves start to diverge, indicating the beginning of the asymmetric phase. Moreover, the circulation of the vortices emitted increases with a, what makes them roll up faster and move towards the cavity more rapidly for $a = 1$ than for $a = 0.08$, as shown in Figs. 3.3, 3.4. Besides, d_e decreases quickly with s in both cases, caused by the geometrical configuration of the optimized cavity which induces an inwards transversal component in the flow. Moreover, a quasi asymptotic value of d_e is reached, which is related to the size of the cavity hollow. In fact, this value is attained for shorter traveled distance at low values of a. Notice that for $a = 1$, d_e is no longer meaningful for $s \simeq 6$ since an unsteady flow has already started and primary eddies do not coexist anymore inside the cavity. Figures 3.8(c-d) show a comparison of the previous variables form the three geometries used and $a = 1$. First, the evolutions of x_e obtained with the bodies with the straight and the optimized cavities are very similar since the cavity induces a reverse flow that makes the eddies penetrate inside it. Conversely, in the case of the blunt-based body, eddies are allowed to grow and extend without transversal limitation, what precludes them from further approaching the base, and facilitates their downstream convection. This distinct behavior will translate into qualitatively different forces distribution, as it will be later discussed in Sect. 3.4. Besides, the use of cavities makes the symmetry-breaking occur earlier than in the case of bodies without cavities, where the trends of positive and negative vorticity eddies nearly overlap for the whole range of s plotted, what is in line with the observations displayed in Fig. 3.3. Moreover, the difference between the axial positions of the vortices is greater for the optimized cavity than for the straight one, indicating a larger asymmetry of the flow. Finally, the evolutions of transversal distance d_e displayed in Fig. 3.8(d) show a initial decrease with s for the three geometries. However, the value of d_e undergoes a subsequent, slight growth in the wake behind the blunt base body because, in this case, the vortices can grow without any constraint. In addition, the role of the optimized cavity seems to be associated to a regularization and more intricate interaction of eddies, as inferred from the smother trend and lower values of d_e.

Now, we focus on the evolution of front vortices with s, obtained by the integral methods described by Eq. (3.4), for different geometries and acceleration values. In particular, in Fig. 3.9(a), we show the evolution of $x_{v,-}(s)$ for the optimized cavity and $a = 0.08$ and 1, whereas the comparison of $x_{v,-}(s)$ for different geometries at $a = 1$ is included in Fig. 3.9(b). Values of $x_{v,+}(s)$ are not shown for the sake of clarity, since they feature trends that are similar to those of $x_{v,-}(s)$. The first curves of each plot represent the incipient formation of the recirculation region, which is characterized by a slight growth of x_v, followed by the detachment and convection of the first vortex at the end of each trend, associated to the sudden decrease in x_v. This gap is related to the identification of a new vortex with a stronger circulation that starts to form close to the base, and end up being shed again, with the consequent increase of x_v and later sharp fall off. These discrete patterns characterize the vortex shedding process in the transient flow. The latter transient character becomes evident by the fact that both, the shedding frequency and the minimum value of x_v in each event, evolve towards the characteristic asymptotic values of the permanent regime. Regarding the role of the acceleration (see Fig. 3.9a), it seems clear that a larger value of a, leads to a shortening in vortex formation and occurrence of alternate shedding (or phase C). After the first shedding event, similar behaviors of x_v, in terms of frequencies, are observed for different values of a, as the transient flow approaches the permanent regime. On the other hand, with regard to the geometry (Fig. 3.9b), it becomes apparent that the optimized cavity promotes an earlier beginning of vortex shedding than in other cases, along with a more regularized pattern of x_v. These features may

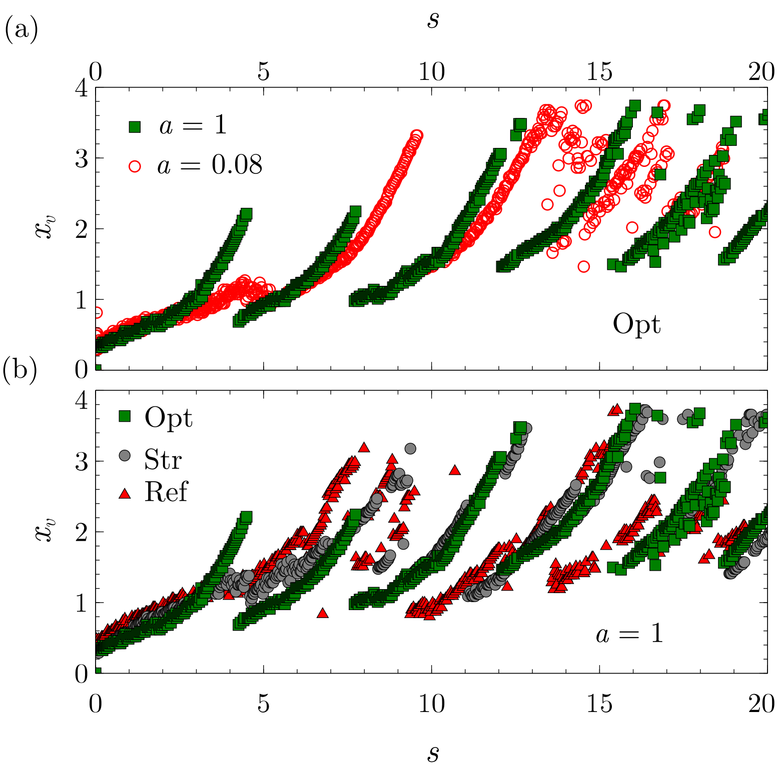

Figure 3.9: Evolution of the axial location of negative front vortices, $x_{v,-}$, with the physical traveled distance, s: (a) dependence of x_v on the acceleration value a for the optimized cavity; and (b) dependence of x_v on the geometry for $a = 1$.

entail a beneficial impact on the forces distribution and the body stability, which will be next discussed.

3.4 Numerical results: analysis on hydrodynamic forces

The previous experimental work was devoted to the characterization of the early transient stages, evaluating the influence of both, the geometry and acceleration values on the near wake development and topology. In view of the major modifications encountered for the main wake parameters, especially when the optimized cavity is implemented, i.e. earlier promotion of transient shedding, shortening of the recirculation and vortex formation lengths, as well as the distance between primary eddies, among others; it is relevant to evaluate the impact of such curved, optimized geometry on the forces acting on the body. Hence, to extend the previous results beyond the early transient stages, here we make use of numerical simulations, which provide with exhaustive information on the flow dynamics for larger times, until the permanent shedding regime is set. Therefore, we will first validate the numerical procedure by means of comparisons with experimental results, to subsequently analyze the time evolution of forces, with particular emphasis on the potential drag reduction and weakening of oscillations amplitude that the optimized cavity may provide with.

3.4.1 Validation of numerical model

We now validate the numerical procedures by comparing the experiments and numerical results in terms of major variables, characterizing the near wake topology and vortex dynamics. Two parameters have been assessed, namely, the vortex strength, by means of the circulation, Γ, and the near wake extension characterized using the recirculation length, l_r. While both the numerical and experimental evolutions of the recirculation length have been calculated using the aforementioned method isocontour (see Sect. 3.3.2), the circulation of the eddies in the early stages has been computed as

$$\Gamma = \iint_A \omega_z(x,y)dydx \simeq \left[\Sigma_i \Sigma_j \omega_{z,ij} \Delta x \Delta y\right]_A , \tag{3.6}$$

defining A as the region comprising the eddy being tracked, where the spanwise vorticity distribution $\omega_z(x,y)$ is integrated. The analysis of vortex circulation in the first impulsive flow stages, namely phase A and phase B, will allow the characterization of the shear layer roll-up and the vortex formation, which govern the flow evolution in the transient. In that sense, Fig. 3.10(a) depicts the numerical and experimental evolutions of the vortex circulation, Γ, with the physical travelled distance, s, for the straight cavity and $a = 0.5$. As it can be observed, until $s \simeq 6$ (which corresponds to $t = 7$) both trends nearly overlap, what indicates the capability of numerical simulations to accurately reproduce the evolution of eddies during the wake impulsive dynamics. In particular, as it was commented before, when the body starts to move, an incipient eddy forms due to the roll-up of the shear layer. The vortex extends spatially, increasing its circulation monotonically as vorticity is fed from the shear layer. Eventually, a maximum is reached before the vortex detaches and is expelled from the shear layer, from which we stop the computation of circulation as the vortex is convected downstream. Furthermore, a slight variation in the value of Γ between trends is observed at the very end of the analyzed process, which corresponds to the beginning of the characteristic alternate shedding process of phase C in the experimental results. This difference may stem from the fact that the experimental flow is subjected to small mechanical perturbations (e.g. towing system vibrations, subtle misalignments, initial movement of seeding particles) which provokes an earlier transition to unsteadiness through their convective amplification downstream from the base. However, the good agreement between the experiments and the numerics is corroborated by the evaluation of snapshots of spanwise vorticity ω_z (see Figs. 3.10c-f), for selected instants marked in Figs. 3.10(a,b), in which quite similar topologies can be observed. In particular, flows are nearly identical for early stages, until $s \simeq 5$, although the experimental wake shows already a slight asymmetry, as it can be observed in Fig. 3.10(e).

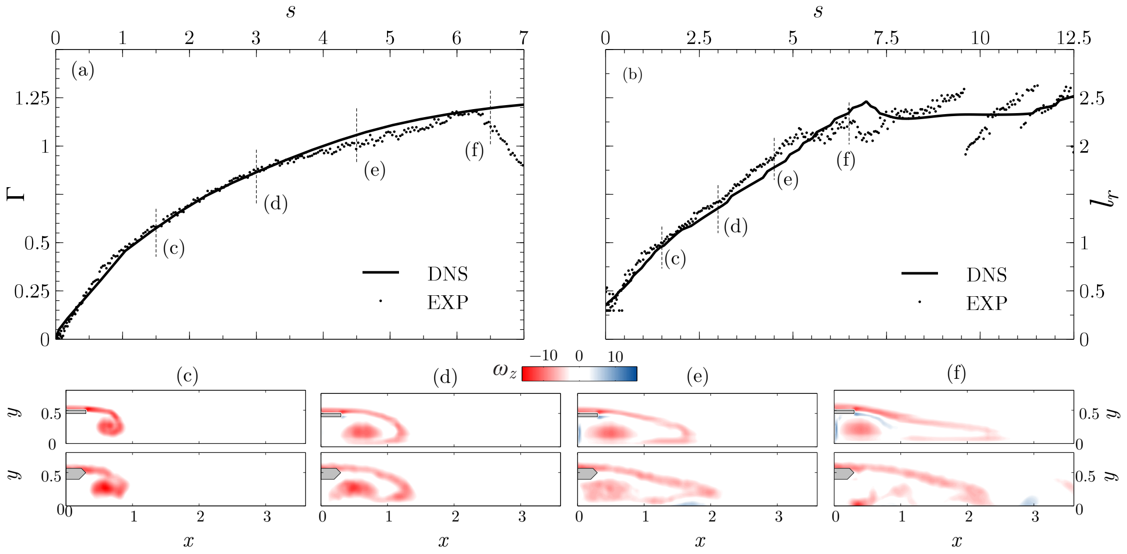

Figure 3.10: Comparison between numerical and experimental results for Str geometry at $a = 0.5$: (a) vortex circulation and (b) recirculation length. Snapshots of spanwise vorticity, ω_z, (c-f) for selected distances identified in (a,b) obtained experimentally (upper row) and numerically (lower row). Contours of vorticity range $\omega_z \in [-16, 16]$.

The discrepancies previously commented, become more evident in Fig. 3.10(f), at $s = 6.5$ where, the noisier experimental flow exhibits a vortex already shed, which is not yet observable in the numerical results. However, the qualitative features of the near wake are still quite similar.

The latter phenomenon is also observed when the evolutions of the recirculation lengths, $l_r(s)$, are compared, as in Fig. 3.10(b). This measurement gives a hint on the near wake extension. Again, the agreement between numerical and experimental trends is fairly good for $s \leq 7$, from which the experiments show an oscillating behavior, as already mentioned above. Conversely, the numerical flow presents a more stable behavior, until $s \simeq 12$. It is worth highlighting that, despite of the different initial conditions associated to the background disturbances which provides with noisier measurements from experiments, both results show similar values and evolutions with s. In view of these results, the validity of numerical simulations can be considered satisfactory, and consequently we next proceed to extend the analysis towards later stages of the transient to asses the possible benefits of the use of the optimized cavity in terms of drag coefficient and body dynamics stability.

3.4.2 Forces evolution

We first analyze the transient evolution of the drag coefficient, $c_x = f_x/(0.5\rho u_\infty^2 WH)$, where f_x is the calculated force on the $x-$axis, for the optimized cavity and $a = 0.5$, which is plotted in Fig. 3.11. This figure also includes selected snapshots with contours

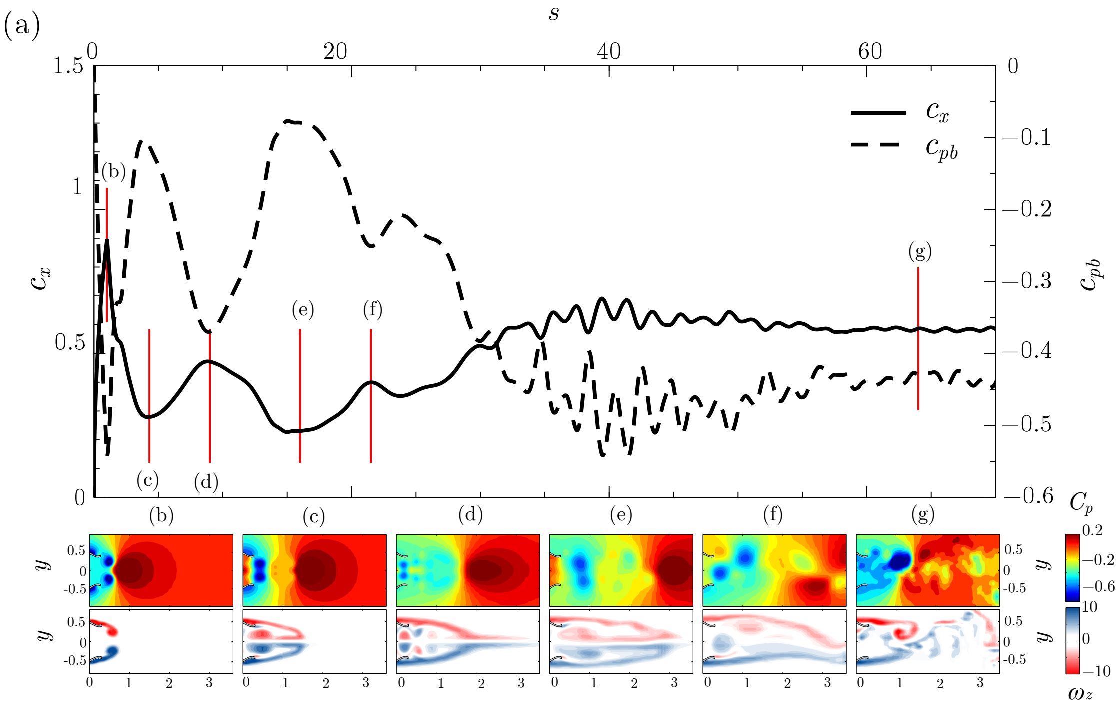

Figure 3.11: (a) Drag and base pressure coefficient evolutions with physical traveled distance, $c_x(s)$ (solid line) and $c_{p_b}(s)$ (dashed line), for the optimized cavity and $a = 0.5$. (b-g) Snapshots with contours of pressure coefficient (top row) and spanwise vorticity (bottom row) corresponding to selected values of s identified in (a). Note that $c_{p_b}(s)$ is obtained by averaging pressure values taken at 100 points belonging to a staggered grid placed at the base region $(x, y, z) = (0, \pm 0.5, \pm 2)$.

of spanwise vorticity, ω_z, and pressure coefficient, $c_p = (p_i - p_\infty)/(0.5\rho u_\infty^2)$, where p_i is the local static pressure and p_∞ the reference one. Additionally, Fig. 3.11(a) displays the evolution of the base pressure coefficient, c_{p_b}, which has been computed by averaging the local pressure values p_i obtained for 100 points belonging to a staggered grid placed at the body base $(x, y, z) = (0, \pm 0.5, \pm 2)$. The comparison of c_x and c_{p_b} will enlighten the discussion on the strong link between the near wake dynamics, previously described, and force coefficients. Thus, the evolution of the drag coefficient presents an initial peak at very early times, which corresponds to an added-mass effect stemming from the fluid acceleration caused by the body impulsive motion. Once the steady body velocity is reached at $s = 0.5$, a sudden decrease is observed for c_x, related to the flow suction and deceleration at the base, creating a stagnation region of high pressure (see snapshots in Fig. 3.11c). Simultaneously, the two primary eddies grow and approach the cavity. Next, for the acceleration at hand, the primary eddy detaches from the shear layer and gets inside the cavity, inducing a decrease of the base pressure (see c_p distribution and snapshots of Fig. 3.11d) and a subsequent increase in c_x. This event gives rise to a second local maximum in the drag at $s \approx 10$. This primary eddy interacts with the following one generated by the roll up of the shear layer, being engulfed and ejected from the cavity (panels *d* and *e*), which increases the base pressure and decreases the drag, as shown at $s \approx 16$ in Fig. 3.11(a) and Fig. 3.11(e). Finally, the eddy is tore apart, getting closer to the cavity, what decreases the base pressure and leads to the local maximum at $s \approx 21$ in the evolution of c_x. Thus, this new maximum corresponds to the shedding of a vortex that separates from the shear layer, which has been identified previously as the beginning of phase C (see snapshots in Figs. 3.11e,f). A similar dynamics and forces distributions have been reported by Fernando and Rival (2016), in the case of elliptical and rectangular accelerating plates of different aspect ratios. Afterwards, a more chaotic, oscillating behavior is observed from $s \geq 30$ to $s \leq 50$, in which c_x increases. The initial steep growth is correlated with a shortening of the vortices formation length with time, together with the vortex shedding (note that the recirculation region in panel *e* is larger than that in panel *g*). In this interval of time, vortex shedding goes through a transient period, modulating the amplitude of the c_x and c_{pb} oscillations, until it reaches a periodic permanent behavior at $s > 50$, characterized by the natural oscillations frequency and time-averaged value of drag, i.e. $St_v = \varpi_v h/u_\infty = 0.22$ and $c_x \simeq 0.61$. The aforementioned drag evolution strongly correlates with the c_{pb} evolution displayed in Fig. 3.11(a), showing a nearly opposite correspondence. Therefore, it seems evident that, for the value of Re at hand, the main contribution to drag reduction is the form drag, guided by the pressure field around the body.

The effect of geometry and acceleration value is analyzed in Fig. 3.12, where distributions of drag coefficient for the three bodies under study, are included, for $a = 0.08$ (Fig. 3.12a) and $a = 1$ (Fig. 3.12b). At first sight, it becomes evident that the added-mass peak for low values of a is smaller, as a consequence of the lower inertial effect. In all cases, c_x rapidly decreases after the accelerated motion stops, as previously commented. However, note that, such decrease is steeper for the bodies with cavities, that undergo a monotonic increase of c_x after a while. In that sense, two different behaviors have been identified concerning this drag valley prior to the monotonic increase, which are strongly linked to the effect of acceleration and geometry. Thus, for low acceleration values, i.e. $a = 0.08$, this transition occurs smoothly, whereas for large acceleration values, i.e. $a = 0.5$ and 1, local maxima are identified (see Figs. 3.11-3.12b), which, as commented earlier, emerge from the effect of primary eddies and shed vortices in the drag coefficient. Actually, the lack of such secondary peaks for the low accelerated motion is due to the fact that, in this case, the vortex circulation is not sufficiently large to make them go towards the cavity and they are convected downstream by the mean flow (see values of ω_z for comparison in Figs. 3.3 and 3.4). Conversely, the body without cavity shows a nearly constant value of minimum drag for a longer period, which is related to a longer residence time of the primary eddies close to the base. The latter turns into a later transition to the alternate oscillating shedding period, where the drag attains significantly large oscillating

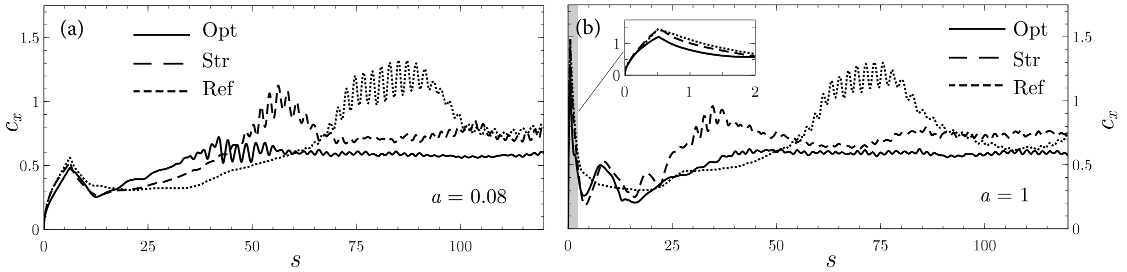

Figure 3.12: Comparison of drag coefficient evolutions with physical traveled distance, $c_x(s)$, for the optimized cavity (solid line), straight cavity (dashed line) and blunt-based body (dotted line), for (a) $a = 0.08$ and (b) $a = 1$.

values, as it can be seen for $s > 60$ in Figs. 3.12(a,b). Moreover, the beginning of this oscillating behavior for the drag takes place earlier for the bodies with a cavity. However, both the oscillations amplitude and the maximum value of c_x reached are smaller for the body with the optimized cavity than for the other two geometries, thus providing with a relevant potential drag reduction at the late stages of the transient ($s > 40$ for $a = 0.08$ and $s > 25$ for $a = 1$). This effect becomes more evident for larger values of a, where the transition to the permanent, asymptotic regime occurs much faster and even without any oscillations in the case of the body with the optimized cavity.

In order to quantify the benefits of the optimized cavity provided by the more rapid transition toward the permanent regime in the wake, characterized additionally by a weaker oscillating behavior, we will next calculate the time to reach the permanent state, as well as the averaged and integrated values of the drag coefficient over the total transient period. The latter values will be computed considering the transient spatial horizon or traveled distance until the flow reaches the permanent regime, s_p, for every geometry at each acceleration value. Furthermore, the integrated value of the drag coefficient is related to the energy needed to overcome the drag. The value s_p will be defined as the traveled distance fulfilling the following two conditions: first, the averaged drag value within a window of extension $\Delta s = 10$, must reach the permanent averaged drag value, with a difference of ±5%; and second, the drag coefficient standard deviation must be below 1% of the permanent value of c_x. Now, the accumulated total transient drag or dimensionless consumed energy to overcome the drag, E_{c_x}, is defined as,

$$E_{c_x} = \int_0^{s_p} c_x(s)ds. \tag{3.7}$$

Table 3.1 lists the values of the physical traveled distance needed to reach the permanent regime, s_p, together with the corresponding consumed energy and averaged drag, E_{c_x} and C_x, for the three geometries and accelerations $a = 0.08$ and $a = 1$. The reduction of drag coefficient within the transient, with respect to the body without cavity is also included, $R(\%) = (C_x^i - C_x^{\mathrm{Ref}})/C_x^{\mathrm{Ref}}$. In order to evaluate the real energy expense during

	Geometry	s_p	C_x	E_{c_x}	$R(\%)$
$a = 0.08$	Ref	230	0.731	168.9	-
	Str	107	0.612	65.4	61.3
	Opt	65	0.450	29.3	82.6
$a = 1$	Ref	210	0.740	155.4	-
	Str	80	0.642	51.4	66.9
	Opt	50	0.448	22.4	85.5

Table 3.1: Transient regime drag reduction: physical traveled distance needed to reach the permanent regime, s_p, averaged drag coefficient, C_x, accumulated drag coefficient, E_{c_x}, and drag reduction relative to the body without cavity, $R(\%) = (C_x^i - C_x^{\mathrm{Ref}})/C_x^{\mathrm{Ref}}$. Time-averaged values of drag coefficients computed by Lorite-Díez et al. (2017) in the permanent regime are respectively: $C_x^{\mathrm{Ref}} = 0.819$, $C_x^{\mathrm{Str}} = 0.778$ and $C_x^{\mathrm{Opt}} = 0.609$.

transient period and its reduction, we choose as integration limit for each geometry their own value of s_p.

Moreover, the values of s_p corroborate the faster transition to permanent regime induced by the use of the optimized cavity. Besides, the values of averaged drag and consumed energy clearly show the significant improvement provided by the optimized cavity, compared to both the blunt-based body and the one with the straight cavity. Quantitatively, the optimized geometry leads to a transient drag reduction $R(\%)$ of nearly 82.6% for $a = 0.08$ and 85.5% for $a = 1$ when compared to the blunt base, which correspond to respective reductions of 55.2% and 56.4% with respect to the straight cavity, thus extending to impulsively motions the better performance of the optimized geometry previously reported for permanent regimes (Lorite-Díez et al., 2017). Such reduction, translates into a significantly lower energy needed, E_{c_x}, and consequently an expected smaller transient aerodynamic load. In view of such results, this configuration can be potentially considered as an efficient passive device to reduce the effect of aerodynamics forces on the body, as well as to improve the body motion stability. The results reported in this Chapter are expected to apply for more realistic flow conditions, as already corroborated by Lorite-Díez et al. (2017), who observed that, in the permanent regime, the drag reduction obtained when an optimized cavity is implemented at the base of the body increases with the Reynolds number.

3.5 Conclusions

We have presented experimental and numerical studies on the flow induced by an impulsive motion of a simplified bluff body from rest, under different values of acceleration and three distinct rear geometrical configurations, inspired on wake passive control devices. The main goal of the present study is to assess the performance of such topologies in transient flow conditions, which are very common in real transport applications and usually not evaluated in classical studies on wake control. Thus, in view of the complexity that wakes behind three-dimensional bluff bodies imply, and to better identify the physical mechanisms governing the dynamics and instability of such flows, we have analyzed the impulsive motion of a D-shaped body implementing a blunt base, a straight cavity and a curved cavity, for four different values of dimensionless acceleration, i.e. $a = 0.08,\ 0.2,\ 0.5$ and 1, starting from rest and reaching a permanent regime of $Re = 2000$. Special focus has been paid on the latter geometry, which constitutes a new control wake device design, whose shape is obtained through adjoint-based optimization algorithms, thus providing with a large reduction of the drag coefficient and a more regularized and less chaotic wake in permanent flow regimes (Lorite-Díez et al., 2017). Therefore, the impact on the near wake evolution and forces distributions has been considered, which is strongly linked to body's motion stability and more importantly, their aerodynamic loads.

First, an experimental characterization of the near wake development has been performed in a towing tank, using PIV measurements. Contours of spanwise vorticity have been analyzed to identify the different phases characterizing the transient flow evolution and variations of wake features during such flow development. A first stage, denoted as phase A, is observed during the early period, in which symmetric shear layers roll up into two primary eddies, configuring a symmetric wake. As a consequence of the flow suction caused by the impulsive motion at the base, primary eddies are attracted towards the rear part of the body, while they continue growing, as observed in Figs. 3.2, 3.4. This initial phase is characterized by the monotonous growth of the recirculation length, l_r, and the eddies circulation Γ (see Figs. 3.5, 3.10, respectively). Eventually, the interaction between shear layer provokes the destabilization of the flow and the wake symmetry is broken, what represents the beginning of a new period, denoted phase B. The identification of such transition is related to a local decrease of the recirculation length value l_r, along with a deviation on the evolution of the axial location of primary eddies, x_e (Fig. 3.8). After a short interval, the flow instability settles down and an alternate transitional shedding of front vortices begins, giving rise to the so-called phase C, that features large variations on the recirculation length value. The alternate shedding is further investigated by means of the tracking of axial position of front vortices, x_v, which is identified employing integral methods, as defined in Eqs. (3.4)-(3.5) (Pawlak et al., 2007). Such process has been noted to be a developing stage in which both the formation length and the vortex detachment location evolve with time (see Fig. 3.9), at the end of which the permanent flow regime is expected to be retrieved, as it has been later shown by means of numerical simulations. Furthermore, different transient behaviors have been observed in terms of acceleration values and geometry. More precisely, larger values of a have been proven to foster the earlier transition between described phases. This effect becomes more evident when the axial location of front vortices, x_v, is evaluated (see Fig. 3.9). Additionally, a higher acceleration is related to a stronger suction of primary eddies, which move closer to the base (Fig. 3.8a), presenting larger values of vorticity which allow them to reside longer periods by the base (Figs. 3.3, 3.4). With regard to the role of geometry, the use of cavities has been shown to limit the growth of the primary eddies, due to the influence of the hollow size, which contributes to a speeding-up of the transitions between phases. As far as the new optimized, curved cavity is concerned, it has been shown to have a significant impact on the near wake features when compared to the remaining geometries. In summary, the optimized configuration leads to a shortening of both the recirculation length and the formation length, while producing a shorter transition between phases (see e.g. Figs. 3.3, 3.6), along with a more regularized, less chaotic alternate shedding, as the neat trends in the distributions of x_v displays (Fig. 3.9b).

Next, in order to explore the beneficial effects of the optimized cavity in terms of drag and force fluctuations reduction, we have performed direct numerical simulations, that have allowed to extend the previous results to longer temporal horizons. Thus, a validation analysis has been first conducted to ensure the accuracy and appropriateness of the numerical results. To that aim, selected flow variables, such as eddies circulation and recirculation length, along with snapshots of spanwise vorticity (Fig. 3.10), have been compared. A remarkable agreement between experiments and simulations has been found for the early stages, where values and trends match, whereas slight differences have been detected only for longer times (note that an earlier triggering of alternate shedding in the experiments takes place as a consequence of the larger level of background noise, e.g. mechanical vibrations).

A subsequent analysis of drag coefficient has allowed to relate near wake dynamics and forces values (Fig. 3.11), corroborating the previous hypothesis on the potential positive effect of the use of optimized cavity. The latter becomes clear when the drag c_x is compared for the three geometries at hand (Fig. 3.12). In general, the aforementioned smoother and faster transition gives rise to a general smaller averaged value of drag together with less energetic instantaneous fluctuations of c_x, regardless the acceleration value. Finally, a quantification of such potential drag reduction and shortening of the transient regime has been computed, as shown in Table 3.1. In particular, the limit of the developing wake has been characterized by means of the variable, s_p, which represents the traveled distance until the flow reaches the permanent regime.

Thus, the value of s_p corresponding the optimized cavity is, for the case at hand, one fourth of that from the body without cavity, and always considerably lower than that associated to the classical straight cavity. Furthermore, in all cases, an important drag reduction in terms of averaged values, c_x, or consumed energy, E_{c_x}, has been obtained for the optimized cavity, which attains almost a 55% reduction for both acceleration values evaluated, when compared to the straight cavity (and nearly 85% regarding the blunt-based body).

In summary, the optimized cavity configuration has demonstrated to be an appealing and efficient passive device which shows a great potential to reduce both the drag coefficient averaged value and instantaneous drag oscillations for impulsively flow regimes. The features may help improving the body motion stability, and could be used in practical transport applications. These observations extend the corresponding beneficial effect already reported for permanent regimes (Lorite-Díez et al., 2017), and highlight the relevance of the use of optimization algorithms applied to flow control.

Part II

Drag reduction strategies in three-dimensional blunt models of road vehicles

CHAPTER
FOUR

Effect of the rear cavities shape: behaviour at different yaw angles

Abstract

The use of rear cavities at the base of a square-back Ahmed body has been experimentally evaluated as a passive control device in wind tunnel tests at $Re = 1 \times 10^5$ under different incident wind conditions, by means of pressure, force and velocity measurements. The optimization of the shape of such passive devices is based on the adaptation of a two-dimensional profile obtained using adjoint sensitivity and shape optimization techniques. A comparative study has been performed considering the reference square-back body (without any passive control device), a body implementing a straight cavity and body with a curved cavity. In general, the optimized, curved, cavity has been shown to be more efficient than the classical straight cavity in terms of wake control and drag reduction, and especially under cross-wind conditions, where the performance of a straight cavity is considerably hindered. In particular, when the free-stream is aligned with the body, the curved cavity provides a stronger attenuation of the periodic vortex shedding and the bistable dynamics of the wake (characteristic of the wake behind a square-back Ahmed body) than the straight one. Besides, the reduced size of the near wake induced by such device, which is limited by the span between the rear edges of the curved cavity, modifies the structure of the recirculating region and reduces the intensity of the vorticity and backflow, leading to an important base pressure recovery. The latter translates into relative reductions of the mean drag and base drag coefficients of 9.1% and 58.1% with respect to the reference case (i.e. 2.6% and 44.8%, with respect to the straight cavity). Such results are considerably improved under cross-wind conditions, since, although the force and the base drag coefficients increase with the yaw angle for all configurations, the corresponding variations are smaller for the model with the optimized cavity. Then, the relative reduction of the mean drag coefficient with respect to the reference body, at a yaw angle of 10Âº, becomes 9.6%, what represents an extra 8.4% with respect to the drag improvement achieved with the straight device. Furthermore, flow visualizations show that the wake is deflected as the incident flow is increasingly yawed, leading to the formation of a single leeward vortex core that approaches progressively the body, decreasing the base pressure. However, this phenomenon is weakened when a curved cavity is implemented,

attenuating the low pressure values induced at the body base.

This Chapter is comprised, in part, in the paper: "Effect of the shape of rear cavities on the drag reduction of a three-dimensional blunt body at different yaw angles", by Lorite-Díez, M., Jiménez-González, J. I., Pastur, L., Cadot, O. & Martínez-Bazán, C., submitted to the Journal of Wind Engineering and Industrial Aerodynamics (Lorite-Díez et al., 2019a)

4.1 Introduction

Road transportation represents approximately a 70% of the global transport industry (see e.g. Acker, 2018), and its energy consumption and environmental impact have become major social concerns in the last decades. An important part of the associated energy expenses are due to aerodynamic loads. In that regard, Choi et al. (2014) state that at least a 21% of trailer's fuel total consumption (driving at 105 km/h), is related to aerodynamic drag, which increases quadratically with the relative vehicle velocity. Consequently, road transportation constitutes a major source of emissions of greenhouse effect gases, such as CO_2, due to the large fuel consumption needed, in part, to overcome aerodynamics loads. The latter justifies the intense research work devoted to develop strategies of flow control and drag reduction in heavy vehicles, aiming at reducing the environmental impact (see e.g. Hucho and Sovran, 1993; Choi et al., 2014, and references therein).

The bluff geometry of heavy ground vehicles, especially conceived to maximize the transportation capacity and simplify the loading process in docks, entails the massive separation of the flow at back end, thus leading to the generation of a turbulent wake, which is responsible for the modest vehicle aerodynamic performance. In particular, it is estimated, that approximately the 25% of the aerodynamic drag resistance is connected to the rear end of these types of vehicles (Wood and Bauer, 2003). Consequently, most of the flow control strategies developed over the past years, have been mainly designed to act on the flow separation at the rear edge of the vehicle and the near-wake region. Besides, the complexity of the flow around heavy vehicles has led to the establishment of simplified vehicle models, which retain most of the features of the wake of heavy vehicles. Classical examples of three-dimensional bluff models with rounded fore-body are the one proposed by Ahmed et al. (1984), which is characterized by a slanted rear surface, and the corresponding square-back version used by Han et al. (1996). Interestingly, such square-back bodies are known to exhibit an unsteady vortex shedding from the shear layers, together with a bistable random dynamics characterized by the intermittent switching between two horizontally deflected mirror positions (Grandemange et al., 2013a,b), whose origin stems from the destabilization of steady Reflectional Symmetry Breaking, RSB, modes (Grandemange et al., 2012a) at the laminar flow. These two wake RSB states produce lateral loads on the body, with sudden reversals of the force and an increase of the drag. Therefore, an efficient flow control should also satisfactorily attenuate such random bistable dynamics.

Among the different rear flow control strategies that have been proposed in the literature, rear cavities or flaps (see e.g. Sanmiguel-Rojas et al., 2011; Martín-Alcántara et al., 2014; Evrard et al., 2016; Brackston et al., 2016) stand out as efficient passive devices in terms of wake pressure recovery, drag reduction and attenuation of vortex shedding. In particular, their efficiency depends highly on the cavity or flap depth, what may represent a limitation in practical applications where size restrictions exist for add-on devices (as occurs with European legislation for heavy transport weight and dimensions). Thus, shape optimization techniques based on adjoint sensitivity analyses (Meliga et al., 2014; Othmer, 2014) constitute relevant design tools to improve the performance of such passive devices given a fixed length. Such approach has been recently employed by Lorite-Díez et al. (2017), where a curved rear cavity is designed, for a two-dimensional D-shaped body (similar to that used in Pastoor et al., 2008), after shape optimization of a straight cavity with a depth of $0.3h$, being h the body's height. Such curved cavity was shown to reduce the drag coefficient by a 30% with respect to the straight cavity configuration under permanent turbulent flow regimes, i.e. Reynolds number of 20000. Similar results were later obtained for transient flow conditions, by analyzing experimentally the starting wake created by a body that accelerates from rest (Lorite-Díez et al., 2018). However, the performance of such curved cavity still needs to be investigated on a square-back Ahmed-like model under more realistic turbulent conditions.

On the other hand, the presence of side wind can significantly alter the flow detachment and the near wake properties, thus leading to the increase of side and drag forces, and vehicle's instability (Hucho and Sovran, 1993). On average, road vehicles operate most of the time at wind conditions which are not aligned with the road; and therefore it is usual to evaluate forces and flow features of simplified heavy vehicle models over wide ranges of the yaw angle, β, which accounts for the misalignment of the model with respect to the incident free-stream. In particular, typical studies of cross-wind are focused on the range defined by $\beta = \pm 10^\circ$, which are representative limits of yaw angle for typical driving conditions (Gardell, 1980; Hucho and Sovran, 1993), and are in line with the new requirements for vehicles testing in the European Union. Variations of force coefficients within such region are characterized by important monotonic growths with the yaw angle, as shown by Bello-Millán et al. (2016) for a 25° slanted Ahmed body in the range of $\beta \leq 60^\circ$. In addition to the increase of the frontal apparent area as the value of β grows, the growth in drag coefficient is also associated to the development of streamwise vortices along the vehicle's length (Rao et al., 2018), leading to lower values of pressure in the near wake region (McArthur et al., 2018). Therefore, a complete analysis of the performance of passive control devices requires the evaluation of flow features and force coefficients for different values of the yaw angle (as e.g. in Grandemange et al., 2015; Hassaan et al.,

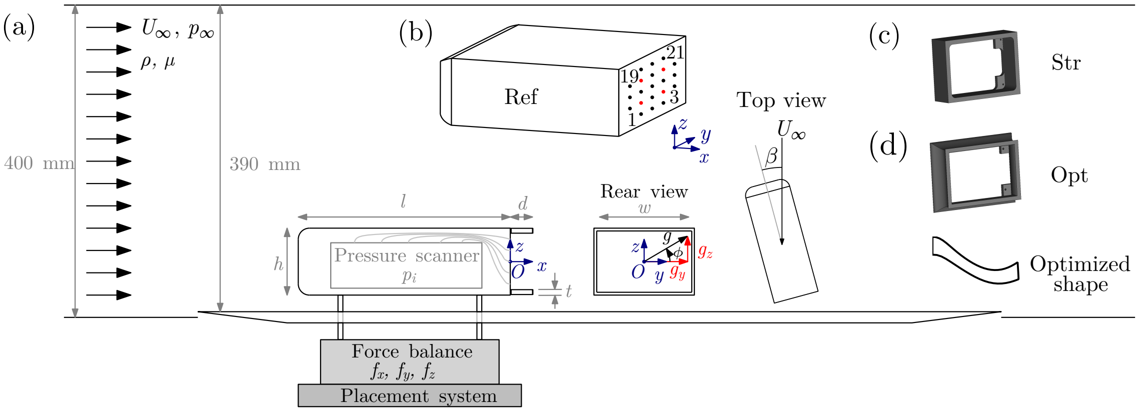

Figure 4.1: (a) Sketch of the experimental set-up, along with rear and top views of the model. (b) Pressure taps distribution at the base of reference (Ref) configuration. (c,d) Rear passive devices, including the (c) straight cavity and the (d) optimized curved cavity with its corresponding profile shape.

2018).

That said, the present Chapter investigates experimentally the turbulent wake behind a square-back Ahmed-like body implementing straight and curved rear cavities as flow control and drag reduction devices, at different yaw angles. Such analysis will allow to evaluate comparatively the performance of a curved cavity, whose profile has been obtained by shape optimization in Lorite-Díez et al. (2017), and therefore, the suitability of simplified two-dimensional adjoint optimization approaches to design efficient flow control strategies devices in more realistic flow conditions. Thus, the Chapter is organized as follows: the problem definition and experimental details are introduced in Sect. 4.2. Next, Sect. 4.3 is devoted to analyze the results, comparing force, pressure and velocity measurements obtained with the different configurations. In particular, we first describe in Sect. 4.3.1 the main flow features, while the effect of cross-wind conditions and the yaw angle is presented in Sect. 4.3.2. Finally, the main conclusions are drawn in Sect. 4.4.

4.2 Problem description and experimental details

4.2.1 Experimental set-up

We investigate experimentally the turbulent flow around a square-back Ahmed-like body of length $l = 291$ mm, width $w = 97.25$ mm and height $h = 72$ mm. The model is placed inside an Eiffel-type wind tunnel of 390 mm × 390 mm test section (see Fig. 4.1a), using a rotatory placement system which allows to modify the yaw angle β of the body (see top view at Fig. 4.1a) with an accuracy of 0.01°. Four holding cylinders of 7.5 mm diameter ($0.104h$) are used to support the model with a ground clearance of $c/h = 0.278$.

Two different passive control devices, namely straight and curved cavities of depth $d/h = 0.3$ and thickness $t/h = 0.05$ (Figs. 4.1c,d), are implemented at the rear of the reference model to evaluate their effect on the turbulent wake behind the body. In particular, the curved cavity represents a three-dimensional adaptation of the rear device obtained by means of adjoint sensitivity and shape optimization approaches by Lorite-Díez et al. (2017). A detail of the profile of the curved cavity is displayed in Fig. 4.1(d). The performance of both optimized cavity (Opt model) and straight cavity (Str model), as drag reduction and wake control devices, will be analyzed by adding them to the reference square-back model (Ref model) of original length $l/h \simeq 4$, thus leading to a extended length of $l+d \simeq 4.3$. Notice that such set-up is thought to mimic geometrical conditions in real heavy vehicles applications, where add-on devices are appended to the basic geometry of trucks.

The wind tunnel was set to produce a uniform free-stream velocity of $U_\infty = 20$ m/s, with a turbulent intensity below 0.5% and a velocity homogeneity over the test section better than 0.3% (further details as the incoming velocity profile shape can be found in Grandemange et al., 2013b). The Reynolds number based on the height of the model h is $Re = \rho U_\infty h/\mu \simeq 10^5$, where ρ and μ are respectively the density and viscosity of air. Besides, the effect of cross-wind is investigated by varying the yaw angle β, i.e. the incoming flow angle (see Fig. 4.1a), within the range of $0 \leq \beta \leq 10°$, with increments of $\Delta\beta = 1°$.

The origin of the Cartesian coordinates system (x, y, z) is located at the center of the body base, with x being the direction aligned with the longitudinal body axis, z the vertical direction, and y the side direction that forms a direct trihedral. The velocity vector can be then decomposed into these directions, being their components $\mathbf{u} = (u_x, u_y, u_z)$.

4.2.2 Pressure, force and velocity measurements

Pressure measurements were performed at the base of the reference geometry by means of 21 pressure taps distributed along a structured, equispaced grid with $\Delta y = 19$ mm and $\Delta z = 13$ mm, as displayed in Fig. 4.1(b). Pressure values, p_i $(i = 1, 2, \ldots, 21)$, were acquired with a Scanivalve ZOC22B/32 5″ H_2O pressure scanner and a gle/SmartZOC-100 acquisition and control unit (accuracy of 3.75 Pa), using a sampling frequency of 50 Hz per channel, during 250 s for typical experiments. Such conditions have been proven to be good enough to resolve the main wake properties and the bistable dynamics. Moreover, the static pressure value, p_∞, was measured far upstream from the model at the inlet of the test section. The pressure taps were connected through vinyl tubing to the pressure scanner, which was placed inside the model to limit the tubing length and its associated filtering effect. Base pressure measurements will be expressed in terms of the dimensionless pressure coefficient as

$$c_{p,i}(y, z, t) = \frac{p_i(y, z, t) - p_\infty}{\rho U_\infty^2/2}. \tag{4.1}$$

The uncertainty of the pressure coefficient is approximately ±0.002. These measurements will be used to evaluate instantaneously the base drag coefficient (Roshko, 1993), given by

$$c_B = -\frac{1}{n}\Sigma_{i=1}^{n} c_{p,i}(y_i, z_i, t), \tag{4.2}$$

where $n = 21$ is the total number of base pressure taps. Besides, the wake asymmetry can be quantified by means of horizontal and vertical pressure gradients, i.e. g_y and g_z respectively, calculated using values of the four pressure taps highlighted in red in Fig. 4.1(b), namely taps $i = 5, 7, 15, 17$; as done in (Grandemange et al., 2013a; Lorite-Díez et al., 2019c). Such pressure gradients are computed as

$$g_y = \frac{\partial c_p}{\partial y} \simeq \frac{h}{2}\left[\frac{c_p(y_{17}, z_{17}, t) - c_p(y_{15}, z_{15}, t)}{y_{17} - y_{15}} + \frac{c_p(y_7, z_7, t) - c_p(y_5, z_5, t)}{y_7 - y_5}\right], \tag{4.3}$$

$$g_z = \frac{\partial c_p}{\partial z} \simeq \frac{h}{2}\left[\frac{c_p(y_{15}, z_{15}, t) - c_p(y_5, z_5, t)}{z_{15} - z_5} + \frac{c_p(y_{17}, z_{17}, t) - c_p(y_7, z_7, t)}{z_{17} - z_7}\right]. \tag{4.4}$$

Note that the statistical evaluation of the value of g_y will allow to characterize the occurrence of the two asymmetric RSB modes identified by Grandemange et al. (2013b). Therefore, a positive RSB state (P state) will be present at the wake when $g_y > 0$, while the negative RSB state (N state) will exist for $g_y < 0$. Also, as depicted at the rear view in Fig. 4.1(a), both horizontal and vertical pressure gradients are components of an asymmetry gradient vector (Bonnavion and Cadot, 2018) whose modulus, g, and phase, φ, are respectively computed as $g = \sqrt{g_y^2 + g_z^2}$ and $\varphi = \arctan(g_z/g_y)$. Therefore, the value of g can be used to quantify the strength of the global asymmetry of the wake.

Besides, the aerodynamic forces were also obtained for all geometries and body orientations with of a multi-axial load cell (model AMTI-MC3A-100lb) which was connected to the model through the four cylindrical supports, allowing to measure the instantaneous forces along the coordinate axes, i.e. the drag force f_x, the side force f_y and the lift force f_z. Such force signals were recorded during 30 s at a sampling rate of 1 kHz. The measurements uncertainty was estimated (using specifications of crosstalk, non-linearity and hysteresis) to be below 0.002 N for the x and y directions and below 0.006 N for the z direction. Moreover, since the load cell and the model were jointly installed on top of the placement system (Fig. 4.1), they rotate together as the turntable moves to set the yaw angle β of interest. Therefore, forces on x and y axes are combined to obtain the drag force in the wind direction, f_d, as depicted in Fig. 4.1 (top view):

$$f_d = f_x \cdot \cos\beta + f_y \cdot \sin\beta. \tag{4.5}$$

The non-dimensional force coefficients were defined as

$$c_i = \frac{f_i}{\rho U_\infty^2 hw/2}, \tag{4.6}$$

where the base area hw was used as reference, with an accuracy of ± 0.001 for c_x, c_y or c_d, and ± 0.003 for c_z.

Additionally, near wake spatial characterization was obtained by means of Particle Image Velocimetry (PIV) measurements, at two different planes located at $z = 0$ and $0.35h$, to obtain the velocity fields $\mathbf{u_{xy}} = (u_x, u_y, 0)$, in order to observe the main features of the recirculating region and the flow massive separation close to the upper edges, respectively. The PIV system used a dual pulse laser (Nd:YAG, 2 x 135mJ, 4ns) synchronized with a FlowSense EO, 4 Mpx, CCD camera. The laser sheet was pulsed with time delays of 50μs, and the set-up acquired 500 pairs of images at 10 Hz, ensuring a good resolution in terms of the number of images to properly obtain the velocity averaged fields. Besides, to ensure the repeatability and improve results, three different PIV tests were run for each experiment. The interrogation window was set to 16×16 pixels with an overlap of 50%, resulting into a spatial grid of 222×295 points, whose resolution is approximately 1% of body's height.

To complement the PIV velocity measurements, acquisitions of local of streamwise velocity, $u_x(t)$, were performed with a hot wire probe (wire of 5μm diameter and 1.25 mm length) placed at the location $P_{\mathrm{hwa}}(x, y, z) = (2.5h, 0, 0.35h)$, aiming at characterizing, with good temporal resolution, the wake fluctuations associated to the vortex shedding process. Such tests were performed with a sampling frequency of 1 kHz during 120 s. To identify the dominant angular frequencies at the wake, ϖ, power spectral density distributions (PSD) were used, with a sliding averaging window of 2 s. Values of frequencies can be expressed in non-dimensional form, as Strouhal numbers

$$St = \frac{\varpi h}{2\pi U_\infty}. \tag{4.7}$$

Finally, note that, as indicated above, conditional statistic will be performed to identified the RSB positive (P) and negative (N) states at the wake, by evaluating the value of the horizontal pressure gradient, g_y. Thus, since pressure and PIV measurements were simultaneously recorded, an appropriate conditional averaging on the velocity fields can be performed to capture the wake topology corresponding to P and N states. In the following, the results will be expressed in dimensionless variables, using h, U_∞, $0.5\rho U_\infty^2$ and h/U_∞ as characteristic length, velocity, pressure, and time scales respectively. Besides, the time-averaged of any instantaneous variable $a(x, y, z, t)$, will be denoted as $A = \overline{a}$, whereas its corresponding standard deviation, employed to evaluate the amplitude of the fluctuations, will be expressed as $A' = \sqrt{\overline{(a - A)^2}}$. Also, we will denote by a superscript P or N the conditional averaging of any variables related to deflected P or N states.

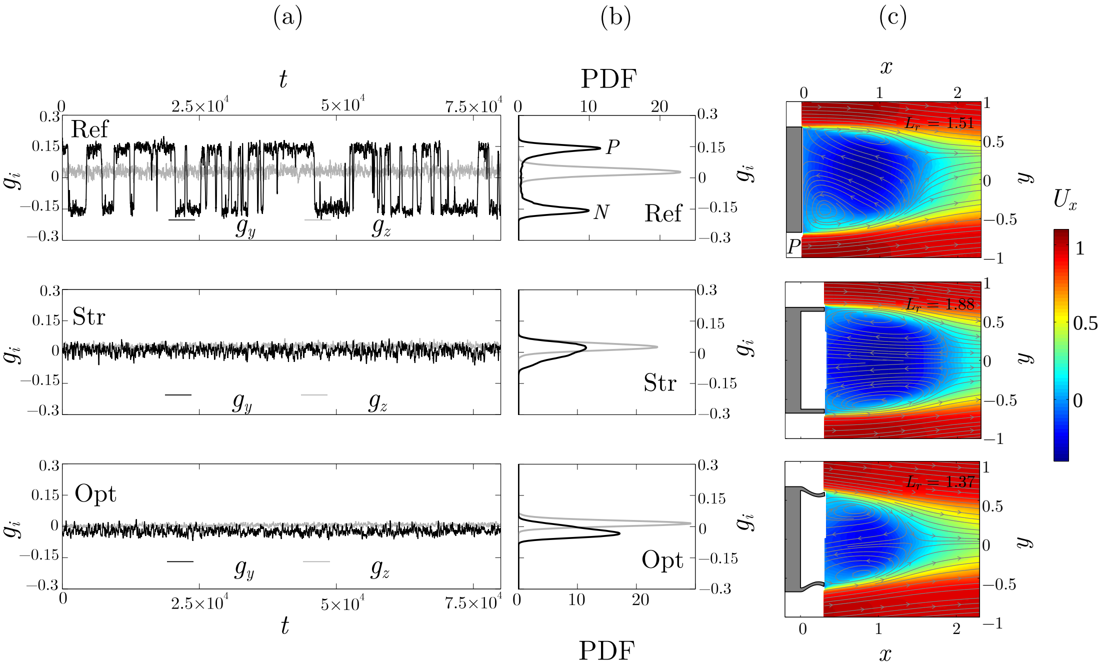

Figure 4.2: (a) Time evolution of horizontal, g_y, and vertical, g_z, base pressure gradients for all configurations (reference case, Ref, straight cavity, Str, and optimized cavity, Opt) and (b) corresponding Probability Density Functions (PDF). (c) Contours of averaged streamwise velocity, U_x, and flow streamlines at the horizontal plane $z = 0$. Note that for the reference case (Ref) only the conditionally-averaged P state is shown.

4.3 Results

We next describe the main results obtained from the force, pressure and velocity measurements for the three configurations, i.e. the reference square-back model, and the models with straight and curved rear cavities respectively. First, the main flow features will be analyzed for aligned flow conditions ($\beta = 0°$) in Sect. 4.3.1, while the effect of cross-wind on the main flow variables are subsequently described in Sect. 4.3.2.

4.3.1 Flow features for $\beta = 0°$

The wake behind the reference square-back model (Ref case) sustains a long-time bistable dynamics, characterized by the intermittent switching between two horizontally deflected wake RSB states (Grandemange et al., 2013b). Such bistable behavior in the $y-$axis is clearly identified by a random switching of the horizontal pressure gradient, g_y, in Fig. 4.2(a). The corresponding probability density function (PDF) in Fig. 4.2(b) shows that the wake exhibits, with the same probability, two mirrored states, denoted P and N, characterized respectively by conditionally-averaged values $G_y^{P,\mathrm{Ref}} = 0.137$ and $G_y^{N,\mathrm{Ref}} = -0.137$. The near wake topology corresponding the asymmetric P state is depicted in

Fig 4.2(c), through contours of conditional averaged streamwise velocity U_x and flow streamlines at the plane $z = 0$. As observed, the recirculation bubble displays two asymmetric cores, which deflect the backflow towards the $y > 0$ region, leading to a positive value of g_y at the base (note that the N state simply displays a mirrored symmetry with respect to the plane $y = 0$). On the other hand, the vertical pressure gradient, g_z, displays a nearly constant positive value, with mean $G_z^{\mathrm{Ref}} = 0.031$, which stems from a slight wake asymmetry on the vertical $y = 0$ plane (not shown here), due to the ground presence effect. The total wake asymmetry can be then quantified by means of the modulus $g = \sqrt{g_y^2 + g_z^2}$, which for the reference case yields a mean value of $G^{\mathrm{Ref}} = 0.142$. Moreover, the recirculation length, L_r, is computed as the furthest downstream location where $U_x \leq 0$, providing a value of $L_r^{\mathrm{Ref}} = 1.51$.

As it was reported by Evrard et al. (2016), the addition of a straight cavity of depth $d \gtrsim 0.25$, leads to the attenuation of the bistable dynamics and the symmetrization of the wake. Such outcome is clearly observed in Fig. 4.2(a), where now the horizontal pressure gradient remains constant and close to zero, with $G_y^{\mathrm{Str}} = 0.033$, and is characterized by a single peak in the corresponding PDF (Fig. 4.2b). Consequently, the magnitude of total pressure gradient, $G^{\mathrm{Str}} = 0.046$, is considerably smaller than that reported for the reference case, despite the fact that the vertical pressure gradient, $G_z^{\mathrm{Str}} = 0.026$, is barely affected. As expected, the near wake displays a nearly symmetric wake topology in Fig. 4.2(c). Interestingly, it is shown that the recirculation bubble becomes longer after the implementation of the straight cavity, leading to a mean value of $L_r^{\mathrm{Str}} = 1.88$. Such enlargement might be caused by the horizontal asymmetry suppression and the consequent vortex interaction inside the base cavity, in agreement with the observations made by Lucas et al. (2017) through numerical simulations for $\mathrm{Re} = 4 \times 10^5$.

When the optimized curved cavity is used instead, an efficient attenuation of the bistable dynamics in the y-axis is also obtained, according to Fig. 4.2(a), whose mean value is $G_y^{\mathrm{Opt}} = -0.022$. As a result, the amplitudes of the fluctuations of g_y and g_z are smaller in this case than in the straight cavity and the reference cases. Moreover, a wake symmetrization is also observed at the vertical plane, since the mean value of pressure gradient $G_z^{\mathrm{Opt}} = 0.017 < G_z^{\mathrm{Str}}$, what leads to a weaker magnitude of the total pressure gradient, $G^{\mathrm{Opt}} = 0.035$. Regarding the near wake topology, the symmetric recirculation region becomes considerably smaller and thinner in comparison with the other geometries (see Fig. 4.2c), with the recirculation length decreasing up to a value of $L_r^{\mathrm{Opt}} = 1.37$. Besides, a closer look to the flow streamlines anticipates the existence of a stagnated flow region near the body base, while the contours of streamwise velocity, U_x, display a lower magnitude of backflow at the axis for the optimized cavity, which, altogether, contribute to increase the base pressure.

For the sake of comparison among the geometries under study, the mean values of the aforementioned main global flow variables, such as pressure gradients and recirculation

Configuration	G_y	G_z	G	L_r	C_B	C_x
Ref	0.137 (P)	0.031	0.142	1.510	0.179	0.329
Str	0.033	0.026	0.046	1.880	0.136	0.307
Opt	-0.022	0.017	0.025	1.370	0.075	0.299

Table 4.1: Mean values of main global flow characteristics for the reference model (Ref), model with straight cavity (Str) and optimized cavity (Opt): horizontal, vertical and total pressure gradients, G_y, G_z and G; recirculating bubble length, L_r, mean base drag coefficient, C_B, and mean drag coefficient, C_x.Note that the horizontal pressure gradient for the reference case corresponds to the conditional averaged value for the P state, G_y^P.

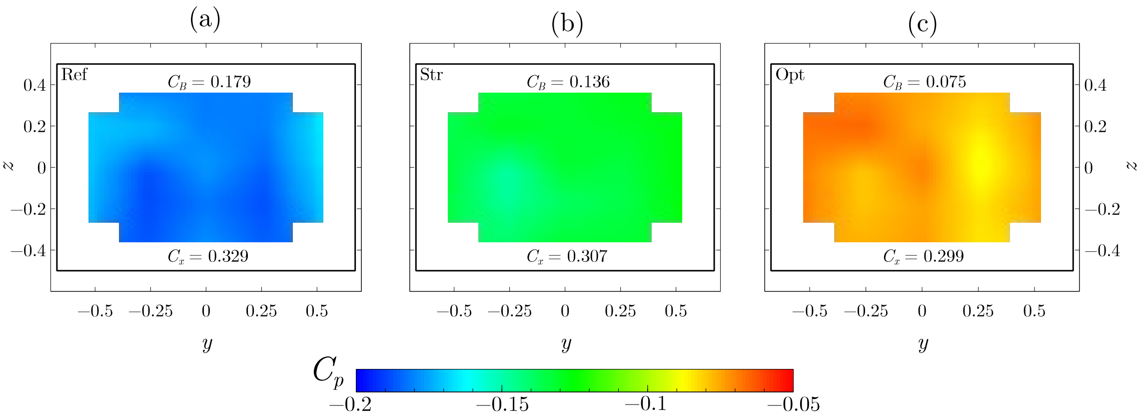

Figure 4.3: Mean base pressure distribution, $C_p(y, z)$, and values of men base drag, C_B, and drag coefficients, C_x, for the three configurations under study: (a) reference case, (b) model with straight cavity and (c) model with optimized cavity. Background black lines represent base perimeter.

length, are listed in Table 4.1. Notice that the implementation of the curved cavity provides a reduction of 82.4% in the magnitude of the total pressure gradient, G, with respect to the reference square-back model, what represents an additional reduction of 15.4% when compared to the straight cavity. Therefore, it constitutes a more efficient device in terms of wake symmetrization. Table 4.1 also lists values of mean base drag coefficient, C_B, and the mean drag coefficient, C_x, and their respective relative variations, which will be subsequently discussed.

Let us now describe Fig. 4.3, which depicts contours of the time-averaged pressure, $C_p(y, z)$, measured at the base of the square-back model ($x = 0$), for the reference case (Fig. 4.3a), the model with a straight cavity (Fig. 4.3b), and the model with the optimized cavity (Fig. 4.3c). In particular, the reference wake displays a nearly symmetric averaged pressure distribution in Fig. 4.3(a) (on account of the contributions of both equally probable P and N asymmetric states), characterized by low values of C_p. Thus, the base drag coefficient stemming from the spatial averaging of such pressure distribution is $C_B^{\mathrm{Ref}} = 0.179$. Moreover, as detailed earlier, force measurements were also performed to obtain the mean drag coefficient, obtaining a value of $C_x = 0.329$ for the reference square-back model. Thus, the base drag coefficient represents 54.4% of the mean drag coefficient C_x, which is a similar to the contribution of the form drag for the Ahmed body reported by Ahmed et al. (1984) and Evrard et al. (2016).

The addition of a rear straight cavity, and the consequent attenuation of the bistable dynamics, translates into a spatially uniform base pressure distribution (Fig. 4.3b) that yields a lower base drag coefficient of $C_B^{\mathrm{Str}} = 0.136$, representing a 24.0% decrease with respect to the value C_B^{Ref}, as listed in Table 4.1. As highlighted by Lucas et al. (2017), such pressure recovery at the base is linked to a downstream shift of the two cores of recirculation identified in Fig. 4.2(c), when the cavity is installed. In terms of forces, it translates into a 6.7% decrease of the mean drag coefficient value, $C_x^{\mathrm{Str}} = 0.307$, with regard to the reference case. Note that such relative reduction is slightly lower than that reported at $Re = 4 \times 10^5$ for similar cavity depths in Evrard et al. (2016) and Lucas et al. (2017), where the models with and without cavity had the same length. Thus, the differences may partially stem from a slight increase of the friction drag on account of the longer body geometry at the present study, since the cavity here is designed as an extension of the reference model (as occurs in practical applications of heavy vehicles).

The use of the optimized curved cavity gives rise to improved base drag and drag coefficients values with respect to the straight cavity. In particular, as displayed in Fig. 4.3(c), the base pressure increases considerably, leading to a base drag coefficient of $C_B^{\mathrm{Opt}} = 0.075$, which is nearly half of that obtained with the straight cavity. The associated drag coefficient yields $C_x^{\mathrm{Opt}} = 0.299$, which is a 9.1% lower than C_x^{Ref}. Therefore, the optimized curved cavity constitutes an improved control device with respect to a classical straight cavity, not only in terms of wake asymmetry, but also regarding the drag coefficient. However, it should be noted that the large increase of C_B produced by the optimized device when compared to the straight cavity, does not fully translate into a massive drag coefficient reduction, what may be an indication of the existence of additional friction drag and form drag sources that contribute to hinder the improvement of the total drag coefficient, C_x. In particular, it is known that for three-dimensional blunt-based bodies, not only the base pressure distribution is an important factor on the form drag coefficient, but also the emission of vortical structures stemming from the rear massive separation may be a major source of unsteady aerodynamic loads. In this regard, boat-tailed rear ends are able to dramatically increase base pressure, although such slanted configurations may induce an adverse pressure gradient that can lead to flow separation upstream from the body trailing edge or the appearance of strong streamwise vortices produced by pressure differences between the base sides, as shown in Wong and Mair (1983). Such longitudinal vortices, which are also known as $C - pillar$ vortices in the literature (see e.g. Krajnović and Davidson, 2005; Beaudoin and Aider, 2008; Grandemange et al., 2015), may hinder the decrease of the drag coefficient.

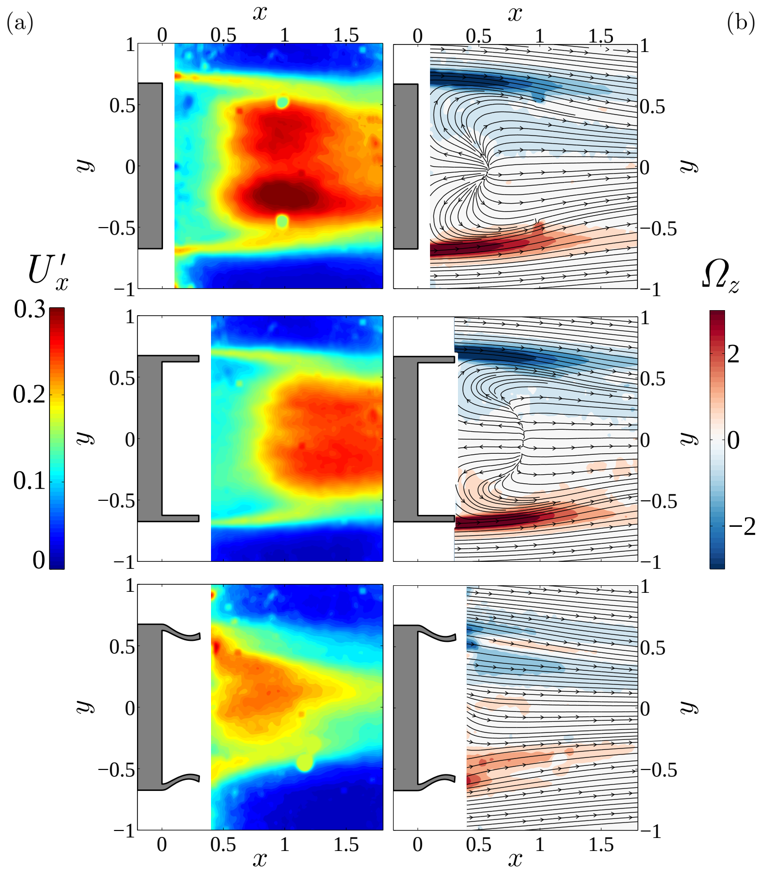

Figure 4.4: Near wake topology at $z = 0.35$ for the three configurations under study: Contours of (a) averaged streamwise velocity fluctuations, U'_x, and (b) averaged spanwise vorticity, Ω_z, along with corresponding flow streamlines.

Following the previous concern, we will next analyze the flow separation at the rear edge and its effect on the model's aerodynamics properties. In that sense, PIV measurements were also performed for an horizontal plane located at $z = 0.35$, which lies close to the upper edge of the curved cavity, for the three configuration under study. Fig. 4.4(a) depicts the corresponding contours of averaged streamwise velocity fluctuations, U'_x, whereas contours of averaged z-vorticity, Ω_z, and flow streamlines are presented in Fig. 4.4(b). First, the wakes behind the reference square-back model and the model with the straight cavity present important similarities and some differences. Without a cavity, it can be observed a source point at $(x, y) = (0.52, 0)$ from which the flow is ejected radially from the recirculating region and bends downstream as it approaches the body base. On the other hand, for the model with a straight cavity, the flow is ejected from the recirculating bubble through a curve line and starts to bend downstream in a region closer to the body edges than in the body without a cavity, being the back flow more uniform. This results indicates that the low pressure region is located around $y = \pm 0.5$, being the pressure in the central part of the body base higher than in the model without a cavity.

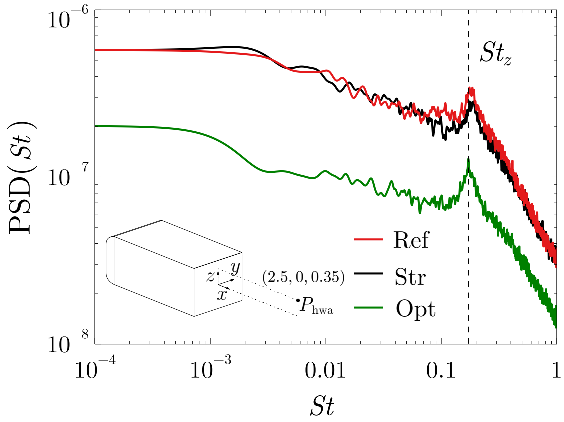

Figure 4.5: Power spectral density (PSD) of the streamwise velocity fluctuations, u'_x, measured at the location $P_{\text{hwa}}(x, y, z) = (2.5, 0, 0.35)$ (see inset), for the three configurations under study.

The beginning of the large velocity fluctuations coincides with the location of the source point in the reference model and with the location of the source line in the model with the straight cavity. Moreover, the shear layers are clearly identified in both cases as regions of high vorticity and moderate fluctuations at $y \simeq \pm 0.7$, with the same inclination and extension. Besides, Fig. 4.4(a) shows that, for the reference wake, two strong fluctuating cores exist at $(x, y) \simeq (1, \pm 0.2)$, while there is a single uniform fluctuating zone of weaker magnitude at $x \gtrsim 1$ for the straight cavity case. The differences in the morphology of the high velocity fluctuations region rely on the fact that the straight cavity attenuates the bistable dynamics which is responsible for the random switching between the deflected RSB states (P and N in Fig. 4.2a), that leads to the formation of such loci of long-time fluctuations. For the optimized cavity, there is a single fluctuating region of weak amplitude, whose reduced transversal extension suggests a more streamlined wake behind the body than for the other two cases.

A detailed inspection of flow streamlines in Fig. 4.4(b) reveals that the PIV plane at $z = 0.35$ cuts the recirculation bubble behind the square-back model and the model with the straight cavity, since there is backflow close to the rear edge. As mentioned above, such recirculation zone extends further downstream when the straight cavity is installed, as expected from the fact that $L_r^{\text{Ref}} < L_r^{\text{Str}}$. Conversely, no backflow is observed behind the optimized cavity at $z = 0.35$, which is an evidence of the formation of a smaller and thinner recirculation bubble, whose transversal extension is limited by the rear cavity edges. Additionally, the wake behind such cavity displays zones of counter-rotating vorticity along both lateral shear layers. For instance, at $y > 0$, the averaged clockwise (negative) vorticity region is split in two parts by a counter-clockwise (positive) vorticity strip. Such topology is believed to be caused by the formation of $C - pillar$ vortices on the curved cavity corners, what would partially hinder the large potential for drag reduction that the base pressure recovery reported in Fig. 4.3(c) should provide.

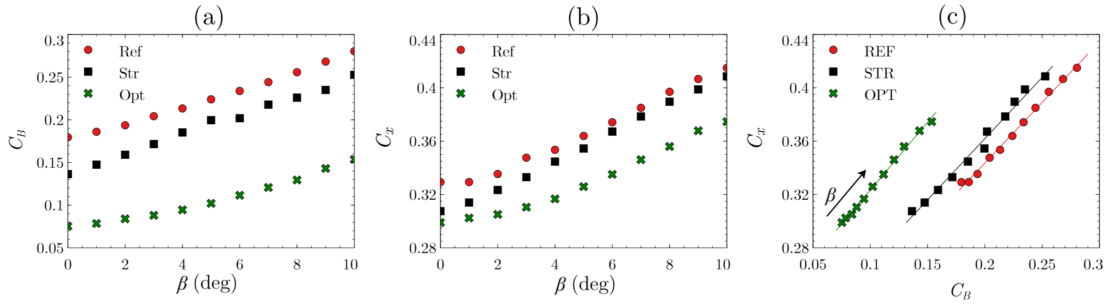

Figure 4.6: Mean base pressure and force coefficients under cross-wind conditions for the three configurations under study. (a) Evolution of the mean base drag coefficient, C_B, with β. (b) Evolution of the body-axis mean drag coefficient, C_x, with β. (c) The body-axis mean drag coefficient, C_x, against the mean base drag coefficient, C_B, for increasing values of the yaw angle, β. The arrow in (c) indicates the increasing values of β, while solid lines represent linear fits of the experimental data.

Finally, the overall fluctuating dynamics at the wake and the periodic vortex shedding mode are next analyzed for the three configurations with help of Fig. 4.5, which depicts the PSD of the streamwise velocity fluctuations, $u'_x = u_x - U_x$, measured using a hot-wire anemometry (HWA) probe placed at $P_{\mathrm{hwa}}(x, y, z) = (2.5, 0, 0.35)$ (see black point in inset of Fig. 4.5). As observed, the spectrum of the reference wake is characterized by a dominant frequency, $St_z = 0.175$, which corresponds to the global vertical shedding mode emanating from the interaction between the upper and lower shear layers. Such value is in good agreement with those reported by Grandemange et al. (2013b) and Lorite-Díez et al. (2019c), and remains barely unaltered when the rear cavities are installed. In general, the addition of a straight cavity induces only a slight weakening of velocity fluctuations amplitude near the resonant frequency, indicating a less energetic shedding process. However, when optimized cavity is incorporated, an overall attenuation of the velocity fluctuations is achieved. The general reduction of wake oscillations and the limited extension of the near wake render the optimized curved cavity an efficient control device under conditions of flow aligned with the body. Nevertheless, as it will be subsequently shown, such advantages become more evident under cross-wind conditions.

4.3.2 Flow features under cross-wind conditions ($\beta > 0$)

As it was discussed in Sect. 4.1, real vehicles are usually subject to cross-wind conditions that lead to resultant incident fluid streams which are not aligned with the body. The wind incident angle, or yaw angle β (see Fig. 4.1), rarely exceeds the effective value of 10° on the average (Hucho and Sovran, 1993), which is the limit selected for the present study. That said, we will first analyze the effect of yaw angle on the mean base pressure and force coefficients. Thus, Fig. 4.6(a) shows the evolution of the mean base drag coefficient as β increases for the three different models considered in the present Chapter. As observed, for the three cases, C_B increases quadratically with β although the relative increase of C_B

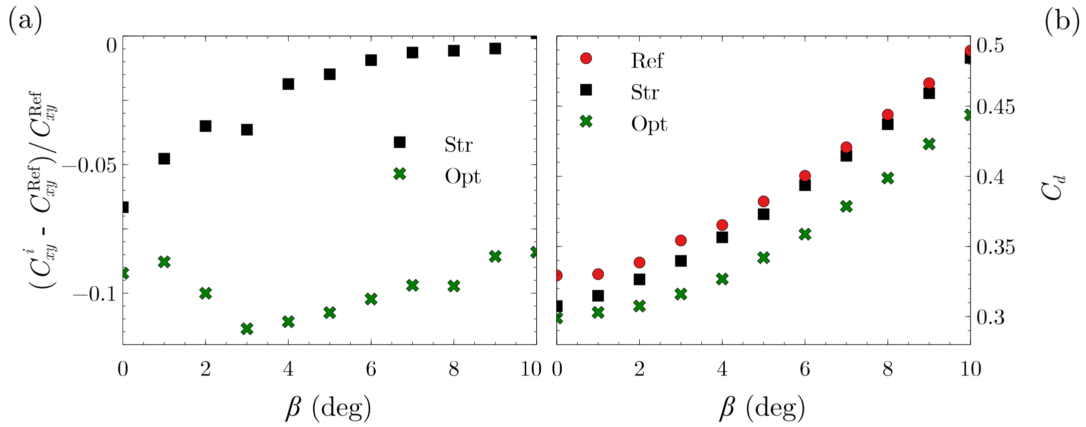

Figure 4.7: (a) Relative variation of the horizontal force coefficient, C_{xy}, with respect to the reference case, $(C_{xy}^{i} - C_{xy}^{\mathrm{Ref}})/C_{xy}^{\mathrm{Ref}}$, as a function of the yaw angle, β. (b) Drag coefficient in the wind direction, C_d, as a function of the yaw angle, β.

is more prominent for the reference case (model without a cavity) and for the model with a straight cavity. Similarly, Fig. 4.6(b) displays that the drag coefficient in the body-axis frame of reference, C_x (note that the body and load cell turn jointly in the set-up), also increases with β. The figure shows that, with respect to C_x, the improved behavior of the straight cavity becomes negligible for $\beta \geq 6°$, however the performance of the optimized cavity gets even better as β increases. Finally, Fig. 4.6(c) depicts the force coefficient, C_x, against the mean base drag coefficient, C_B, for increasing values of the yaw angle β and the three geometries considered. As expected, both C_x and C_B are linearly correlated and increase with the yaw angle regardless of the model configuration. Interestingly, the reference and the straight cavity cases show nearly parallel trends, however the efficiency of the straight cavity decreases as β increases, leading to smaller C_B reductions with respect to the reference case at larger values of β (i.e. $(C_B^{\mathrm{Str}} - C_B^{\mathrm{Ref}})/C_B^{\mathrm{Ref}}|_{\beta=0°} = -24.0\%$ versus $(C_B^{\mathrm{Str}} - C_B^{\mathrm{Ref}})/C_B^{\mathrm{Ref}}|_{\beta=10°} = -9.6\%$).

On the other hand, the optimized cavity case exhibits lower values of both coefficients for the whole range of yaw angle investigated. More precisely, C_x and C_B display smaller variations, and are therefore more robust to cross-wind conditions than the other two configurations, and especially with respect to the straight cavity. For example, note that for $\beta = 10°$ the drag coefficient values for the three configurations are $C_x^{\mathrm{Ref}} = 0.415$, $C_x^{\mathrm{Str}} = 0.409$ and $C_x^{\mathrm{Opt}} = 0.374$, what represent relative reductions with respect to the reference case of $(C_x^{\mathrm{Str}} - C_x^{\mathrm{Ref}})/C_x^{\mathrm{Ref}}|_{\beta=10°} = -1.4\%$ and $(C_x^{\mathrm{Opt}} - C_x^{\mathrm{Ref}})/C_x^{\mathrm{Ref}}|_{\beta=10°} = -9.6\%$ for the straight and optimized cavities respectively. Thus, it is clear that the optimized cavity represents an efficient drag reduction strategy under cross-wind conditions, while the straight cavity reduces dramatically its performance as β increases.

In the same line, the side force coefficient in the body-axis frame of reference, C_y, also increases more significantly for the straight device with β, although it is not shown for the sake of conciseness. Instead, the combined effect of the yaw angle for the different configurations is obtained by computing the total horizontal force coefficient, $C_{xy} = \sqrt{C_x^2 + C_y^2}$ (i.e. the magnitude of the horizontal force acting on the body, equal to the composition between the local axes for drag and side forces), which also increases quadratically with β but with a different growth magnitude for the tested configurations. In that sense, Fig. 4.7(a) depicts the relative variation of the combined coefficient C_{xy} with respect to the reference case, i.e. $\Delta C_{xy} = (C_{xy}^i - C_{xy}^{\mathrm{Ref}})/C_{xy}^{\mathrm{Ref}}$, for both the straight and optimized cavities. In particular, the straight device shows a decrease of the variation when the yaw is increased, that becomes nearly negligible for $\beta > 6°$. However, the use of the optimized device (with the same total length as the straight cavity configuration) displays reductions in C_{xy} of at least 8% over the whole range of β, indicating a lower total aerodynamic resistance to different flow conditions, what is important in terms of driving stability and fuel consumption.

Such advantage is also clearly evidenced if the drag coefficient in the wind direction, C_d (see Eq. 4.5), is considered instead, as Fig. 4.7(b) shows. As observed, C_d grows quadratically with β for all cases, being it related to a corresponding quadratic increase in C_B shown in Fig. 4.6(a). However, the straight device displays a steeper growth, in such a way that for $\beta \gtrsim 6°$ the values of the drag coefficient nearly collapse with those of the reference model, being the relative reduction of drag coefficient approximately 1% at $\beta = 10°$. Conversely, the optimized cavity provides drag reductions similar to 10% for the whole range of yaw angle investigated. Hassaan et al. (2018) reported, for a similar square-back model, that under cross-wind conditions, elongated vortices emanating from the leading edges and the rear bottom of the base interact with the original streamwise $C-pillar$ vortices, to create a near-wake toroidal vortical structure, which was associated to a low pressure region bounded by the recirculation bubble. However, in the presence of boat-tails, such structure was weakened, and a similar effect is expected in the case of the optimized cavity presented here. Therefore, the near wake will be next analyzed using PIV measurements in order to shed light on the mechanisms behind such differences on force and pressure coefficients.

The near-wake for selected yaw angles is displayed in Fig. 4.8, through time-averaged contours of spanwise vorticity, Ω_z, along with corresponding flow streamlines for the three configurations. The wake behind the reference square-back body at $\beta = 0°$ shows a nearly symmetric recirculating bubble (due to the contribution of both asymmetric P and N states) with two counter-rotating eddies, which are associated to moderate values of vorticity (barely discernible because of the considerably higher value of Ω_z at the shear layers) and regions of minimum pressure within the vortex cores. As observed for $\beta = 5°$ and 10°, the body misalignment induces the deflection of the recirculation bubble towards the leeward side, which displays a single core of recirculation arising by the strengthening of the original clockwise (negative) vorticity core. The vortex core is progressively displaced

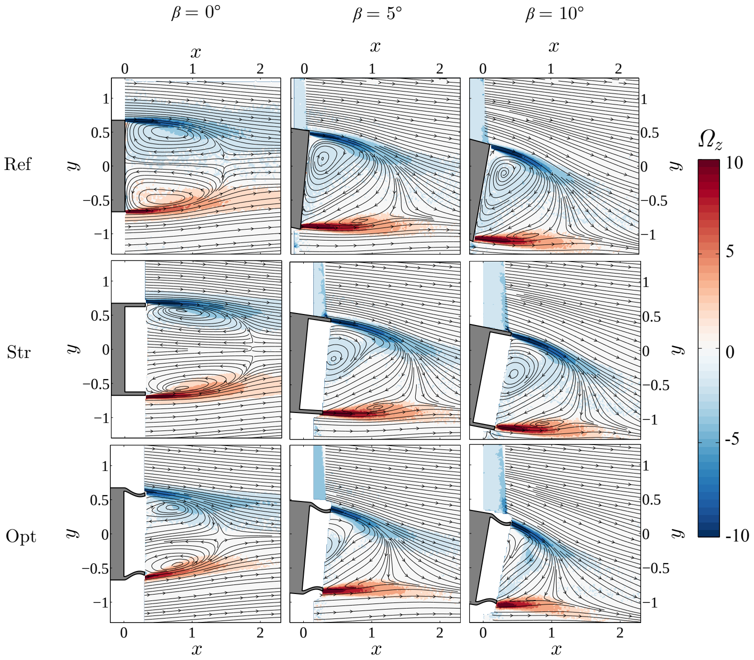

Figure 4.8: Contours of time-averaged spanwise vorticity, Ω_z, and corresponding flow streamlines for selected yaw angles, $\beta = 0°, 5°$ and $10°$, for the three configuration under study.

toward the base as β grows, a phenomenon typically associated to the above-mentioned base pressure decrease. As far as the model with straight cavity is concerned, a similar modification process of the recirculation bubble is observed as β grows. The initial symmetric elliptical recirculating region, gives rise to a single deflected clockwise vortex core under cross-wind conditions, that features a smaller size and is located further downstream than in the reference wake, thus leading to higher base pressure. Finally, the near-wake behind the model with optimized cavity displays the smallest size. In spite of the higher curvature of flow streamlines, which may induce larger base suction according to Roshko (1993), the extension of deflected clockwise vortex core developed under increasing yawed incident flow is very limited by the span between the rear edges of the cavity. Thus, although such vortex may enter the cavity, its contribution as source of low pressure is considerably attenuated, as seen in Fig. 4.6(a).

In general, starting from nearly symmetric shapes at $\beta = 0°$, the recirculating bubbles are shown to deflect in the direction of the cross-wind for $\beta \neq 0$, and become progressively shorter as β grows. Such trends are clearly observed in Fig. 4.9, where the time-averaged recirculation region length, L_r, is represented as a function of β. As observed, the value of L_r decreases monotonously with the yaw angle for the three configurations, being always $L_r^{\mathrm{Str}} > L_r^{\mathrm{Ref}} > L_r^{\mathrm{Opt}}$, regardless of the yaw angle. Interestingly, the shortening of the recirculation bubble follows a nearly linear trend for the straight cavity case, with important differences between values at $\beta = 0°$ and $10°$, indicating a large impact of the flow misalignment on the near wake. For the optimized device, the relative decrease of L_r is similar, but quadratic, thus featuring a softer adaptation under cross-wind conditions at low β. Moreover, as observed in Fig. 4.8, the recirculating bubble is less deflected by the increasing yaw angles while its corresponding width remains limited by the cavity edges, and therefore, the impact on the base pressure decrease is less acute.

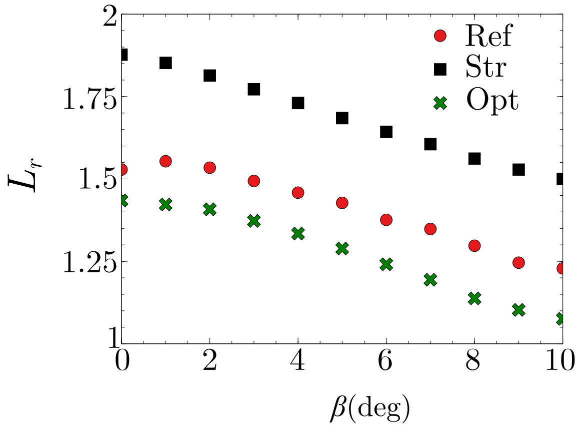

Figure 4.9: Recirculation length, L_r, as a function of the yaw angle β, for the three configurations under study.

4.4 Conclusions

The performance of a rear curved cavity as a passive control device at the base of a square-back Ahmed body, has been experimentally evaluated at $Re = 1 \times 10^5$, and under cross-wind conditions, by means of pressure, force and velocity measurements. The design of such device constitutes a three-dimensional adaptation of the shape obtained by Lorite-Díez et al. (2017) by means of adjoint sensitivity and shape optimization techniques, for two-dimensional wakes. A comparative study based on the evaluation of force and pressure coefficients and near wake topology, has been performed considering the reference square-back body (without any passive control device), and bodies implementing the curved cavity and a straight cavity of same depth and thickness ($d/h = 0.3$ and $t/h = 0.05$ respectively, with h being the model's height). Both passive devices have been implemented as add-on parts, thus increasing the reference model's length, as would occur in practical heavy vehicles applications where devices are appended to the base.

In general, the optimized device has been shown to be more efficient than the classical straight cavity in terms of wake control and drag reduction, and especially under cross-wind conditions, where the performance of a straight cavity is considerably hindered. In particular, for a incident free-stream aligned with the body, both devices have been shown to efficiently attenuate the bistable dynamics in the horizontal axis, characterized by the switching between the two mirror asymmetric P (positive) and N (negative) modes, although the curved cavity improves the total wake asymmetry. The reduced size of the near wake induced by such device, which is limited by the span between the rear edges of the cavity, modifies the structure of the recirculating region, reducing the intensity of the vorticity and therefore the pressure gradients. Additionally, such limited size of the recirculating region together with a weaker backflow, produces an important base pressure recovery, which translates into relative reductions of drag coefficient and base drag coefficients of $(C_x^{\mathrm{Opt}} - C_x^{\mathrm{Ref}})/C_x^{\mathrm{Ref}}|_{\beta=0^\circ} = -9.1\%$ and $(C_B^{\mathrm{Opt}} - C_B^{\mathrm{Ref}})/C_B^{\mathrm{Ref}}|_{\beta=0^\circ} = -58.1\%$ with respect to the reference case. Regarding the periodic vortex shedding mode, the amplitude of fluctuations are more efficiently attenuated by the optimized cavity, due to a reduced transversal extension of the wake, and a more regular shedding process as in the two-dimensional wake analyzed by Lorite-Díez et al. (2017).

The effect of cross-wind has been also evaluated by modifying the yaw angle. Interestingly, in spite of the common trends for the three configurations, characterized by quadratic increases of the force coefficients (and base drag coefficient) with the yaw angle, the corresponding variations are smaller for the model with the optimized cavity, which appears as a more robust device under cross-wind. In particular, the relative reduction of drag coefficient (in the wind direction) provided by the straight cavity with respect to the reference square-back model falls up to a value of $(C_x^{\mathrm{Str}} - C_x^{\mathrm{Ref}})/C_x^{\mathrm{Ref}}|_{\beta=10^\circ} = -1.4\%$ at $\beta = 10^\circ$, whereas the optimized device provides $(C_x^{\mathrm{Opt}} - C_x^{\mathrm{Ref}})/C_x^{\mathrm{Ref}} = -9.6\%$ within the whole range of yaw angle investigated. Such dramatic decrease on the performance of the straight cavity stems partially from the considerable shortening of the recirculation region as the wake is deflected when the incident flow is yawed. Additionally, the leeward clockwise vortex core formed at the corresponding near wake is wider than that observed for the optimized cavity, whose size is limited by the span of the rear edges, and consequently, its contribution as source of low pressure is also reduced.

All in all, the suitability of simplified two-dimensional adjoint optimization approaches to design efficient flow control strategies has been satisfactorily proven for a three-dimensional turbulent wake implementing a rear curved cavity. Nonetheless, the use of such device should be further tested at industrial scale to confirm the reported trends and results prior to application in real vehicles.

CHAPTER

FIVE

Sensitivity of three-dimensional wake modes to perimetric base blowing

Abstract

Wake modes of a rectangular base body near a wall are investigated at a Reynolds number Re $= 10^5$. The targeted modes are the static symmetry breaking mode and 2 antisymmetric periodic modes. The static mode orientation is aligned with the horizontal major y-axis of the base and randomly switches between a positive P and a negative N state leading to long-time bistable dynamics of the turbulent wake. The periodic modes have Strouhal numbers based on the minor length of the base $St_y = 0.121$ for oscillations aligned with the major y-axis direction and $St_z = 0.175$ for those aligned with the minor z-axis. The modifications of these modes are studied when continuous blowing is applied at different locations through 4 slits along the base edges (denoted L, R, T, B) in either 4 single asymmetric configurations or 2 double symmetric configurations (denoted LR and TB). Two regimes are clearly identifiable for all configurations. The *mass regime* is poorly sensitive to blowing momentum and location. It is characterized by the growth of the recirculating bubble as the global injected mass flow rate is increased. It is associated with a base drag reduction and interpreted as resulting from the equilibrium between mass fluxes feeding and emptying the recirculating region as introduced by Gerrard (1966) for two-dimensional bodies. A simple budget model is shown to be in agreements with entrainment velocities measured for isolated turbulent mixing layers. The strength of the static mode is reduced with a maximum of 20% when the bubble length reaches its maximum value. There is no change in the periodic mode frequencies in the mass regime. The *momentum regime* is characterized by the deflating of the recirculating bubble associated with base drag increase. It is interpreted by an activation of the shears by the momentum injection increasing the entrainment velocity thus emptying the recirculating bubble. In this regime the static mode orientation is imposed by the blowing symmetry. L and R configuration are respectively selecting a P and N state in the horizontal direction while the T and B configuration are forcing the N and P state in the vertical direction. Bistable dynamics persist for the symmetric LR and TB configurations. It is found that the wake frequencies are slightly modified, and that the periodic modes shape basically follow the main changes of the static mode orientation. The transition between the two regimes is shown to be

governed by both the global injected mass flow rate and the localisation of injection.

This Chapter is comprised, in part, in the paper: "Sensitivity of 3D wake modes to local base blowing", by Lorite-Díez, M., Jiménez-González, J. I., Pastur, L., Martínez-Bazán, & C.Cadot, O., submitted to the Journal of Fluid Mechanics (Lorite-Díez et al., 2019c)

5.1 Introduction

The seminal work of Wood (1964) considers a blunt trailing edge airfoil with base height h implemented with a central bleed slit of width d. Wood (1964) shows that the base drag decreases almost independently to the blowing jet momentum, determined by the mean jet velocity U_b (also related to the slit's width d) when the mass bleed coefficient $C_q = dU_b/hU_\infty$ is increased from zero. However, the maximum drag reduction depends on the blowing jet momentum, which is reached for a coefficient of mass that is larger as the jet velocity is small. Increasing further the mass coefficient leads to an asymptotic regime of base drag increase with a constant slope. Below the optimal value for base drag reduction, the vortex formation length measured as the distance from the base to the point of maximum velocity fluctuations in the wake moves downstream. This correlation is clarified by Bearman (1967) showing the unique affine relationship of base drag with the inverse of the formation length. Formation lengths varying from $0.3h$ to $1.1h$ were obtained with different wake controls applied to a D-shaped cylinder involving base blowing/suction or splitter plates. Both works report a variation of the Strouhal number of the periodic mode with mass bleed that first augments by 20% and then decreases with a similar magnitude before the disappearance of a definite wake frequency.

To the authors knowledge, there is no equivalent incompressible experimental investigations of mass injection for three-dimensional bodies in the literature. Actually most of the research has focused on compressible flows with transonic and supersonic regimes of axisymmetric bodies (Tanner, 1975; Viswanath, 1996). The incompressible wake dynamics of three-dimensional bluff bodies involve few dominant modes. The static mode shape of the rectangular (Grandemange et al., 2012a) or circular (Rigas et al., 2014) base has a permanent asymmetry or deflection in a lateral direction defined by an azimuthal phase. The mode is reminiscent of the first steady symmetry breaking at low Reynolds number (Fabre et al., 2008; Grandemange et al., 2012a). In the turbulent regime, the static mode undergoes long-time stochastic dynamics that restore statistically the experimental symmetry. The typical time scale is about 100 to 1000 orders of magnitude larger than the convective time scale thus justifying the name of static mode. For circular base, Rigas et al. (2015) showed that the azimuthal phase of the static mode follows a diffusive dynamics. For the rectangular base studied by Grandemange et al. (2013a,b) with different aspect ratio, the stochastic phase dynamics is restricted to random switches and drift between two opposite azimuthal phases aligned with the major axis of the base. The case of a reflectionnal symmetry in the major axis direction leads to a bistable dynamics between two equiprobable mirrored states. The antisymmetric oscillating mode is characterized by a single frequency with a Strouhal number of approximately 0.2 for circular base (see Sakamoto and Haniu (1990) for a sphere). In case of elliptical or rectangular bases (Kiya and Abe, 1999), there are two different Strouhal numbers with the higher (resp. smaller) frequency corresponding to lateral antisymmetric oscillations aligned with the minor (resp. major) axis of the base.

Base blowing has been used for bodies with rectangular base essentially to control the free shears for drag reduction (Rouméas et al., 2009; Wassen et al., 2010; Littlewood and Passmore, 2012). For these cases, large momentum equal or larger to that of the incoming flow is injected through perimetric slits located at proximity of separations. Drag reduction is found to be sensitive to the jet orientation, and optimal when jets are orientated inwards the centre of the base. It is related to the change of the free shear layers angle at separation that recalls the beneficial boat tailing effect on drag of square-back bodies (Wong and Mair, 1983). For unclear reasons likely to be produced by the turbulent modelling, both uncontrolled computed flows of Rouméas et al. (2009) and Wassen et al. (2010) do not reproduce the expected horizontal asymmetry due to the static mode (Grandemange et al., 2013b). These have been since retrieved numerically by Pasquetti and Peres (2015); Lucas et al. (2017) and Dalla Longa et al. (2019). Interestingly, Wassen et al. (2010) triggered the static mode for few blowing cases even so respecting the reflectional symmetry. Attempts to control the static mode was recently made using pulsed jet, known to have much more authority on free shears than continuous blowing at lower mass injection rate (Greenblatt and Wygnanski, 2000). Barros et al. (2016b) and Li et al. (2016) showed that pulsed jets on one side of the base actively selects the orientation of the static mode. Li et al. (2016) uses this actuation in a closed loop control and achieved a wake symmetrization with a simple opposition control strategy.

Axisymmetric bodies with homogenous base bleed have been investigated theoretically in Sevilla and Martínez-Bazán (2004) and Bohórquez et al. (2011) through linear stability analysis. They show a stabilization of both the first steady and second periodic instabilities. The stabilization of the second instability is supported by flow visualization of vortex shedding suppression but no experimental evidence of the inhibition of the static mode strength (reminiscent of the first instability) is reported.

The aim of the Chapter is to investigate the effect of base blowing in a three-dimensional wake with a specific focus on the recently identified static mode (Grandemange et al., 2013b) and periodic modes. Fundamental questions such as: does base blowing mitigate the strength of the static mode? for which blowing intensity and location blowing has control authority on the orientation of the static mode? have not been yet addressed. The following experimental study is based on the same geometry as Grandemange et al. (2013b) with additional blowing slits at different locations of the base. The present Chap-

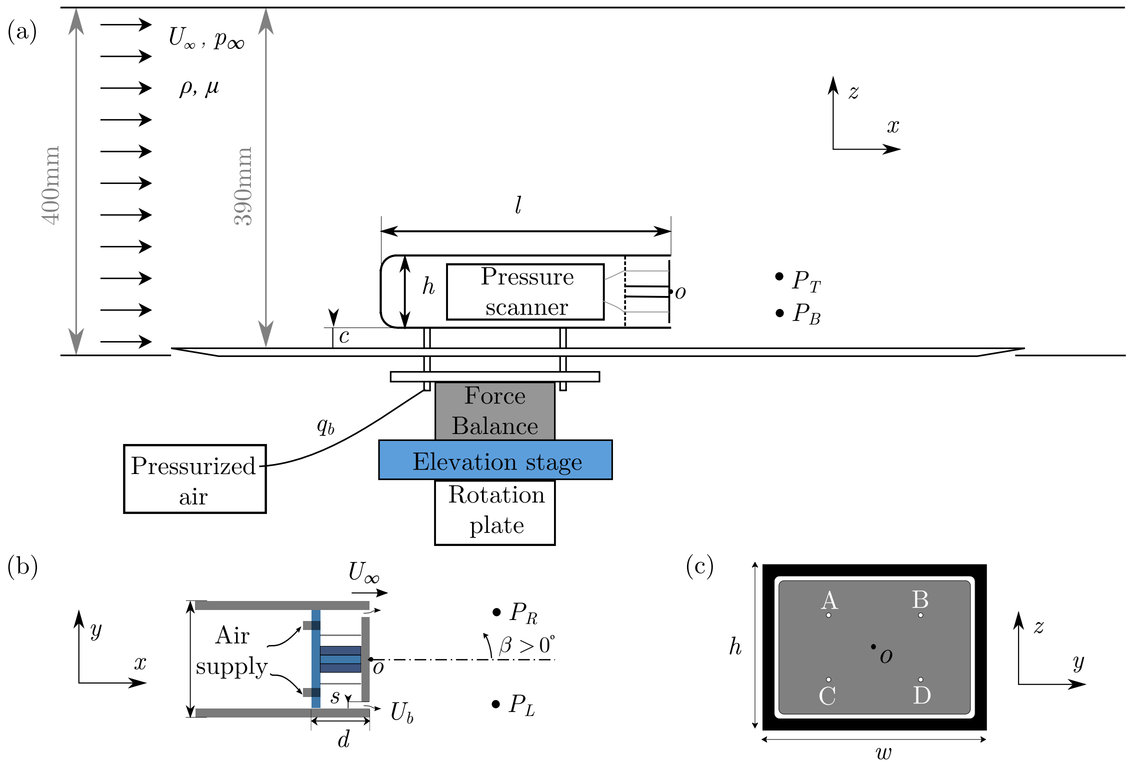

Figure 5.1: (a) Sketch of the experimental set-up. (b) Top view of the body, showing the internal arrangement of the blowing system. (c) Rear view of the bluff body depicting the 4 pressure tap positions (A,B,C,D) and the rectangular slit (white rectangle).

ter is organized as follows. The experimental set-up is described in Sect. 5.2. Results in Sect. 5.3 first present a reminder of the modes identification in Sect. 5.3.1 followed by the effect of base blowing on the base drag in Sect. 5.3.2. The sensitivity analyses of the static and periodic modes are respectively investigated in Sects. 5.3.3, 5.3.4 and 5.3.5. The mean flow modifications are studied for the wake momentum in Sect. 5.3.6 and recirculating length in Sect. 5.3.7. The results lead to 3 discussions in Sect. 5.4, about the modes sensitivity in Sect. 5.4.1, the drag reduction mechanism in Sect. 5.4.2 and the critical blowing to achieve optimal base drag reduction in Sect. 5.4.3. The conclusions in Sect. 5.5 end the Chapter.

5.2 Experimental set-up

5.2.1 Model geometry, blowing device and wind tunnel

A three-dimensional body of length $l = 291$ mm, width $w = 97.25$ mm and height $h = 72$ mm, whose geometry corresponds to the square-back model used by Ahmed et al. (1984), is placed over a ground plate as shown in Fig. 5.1(a). It is held by four cylindrical supports of 7.5 mm diameter (i.e. $0.104h$) leaving a ground clearance of $c/h = 0.278$. The model is

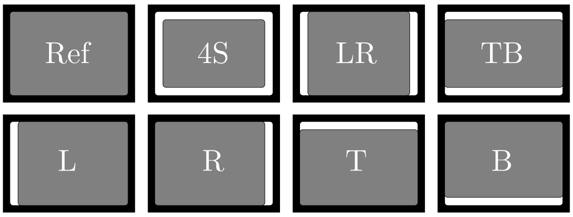

Figure 5.2: Sketch views of the rectangular base showing the reference case and the open slits configurations used for base blowing (see text). The open slits appear white on the rectangular base.

mounted on a turntable to adjust the yaw angle β of the body (rotation with respect to the z-axis) with an accuracy of 0.01°.

The rear of the body is constituted of a frame of depth $d/h = 0.417$ (see Fig. 5.1b) creating an internal cavity partially blocked at the base by a central plate. The plate is smaller than the cavity dimensions to leave a rectangular perimetric slit of width $s/h = 0.028$ as depicted by the white rectangle in Fig. 5.1(c). The cavity is pressurized by injecting air through 4 internal tubes (sketched in Figs. 5.1b,c) with a steady controlled flow rate q_b. The velocity produced at the slit denoted U_b is illustrated in Figs. 5.1(a,b). The blowing system is connected to a 6 bar compressed air-feeding line through a pneumatic tube with an Aalborg digital mass flow meter, an air valve and a pressure regulator, which ensures stability and constancy of the flow rate q_b.

Seven blowing configurations shown in Fig. 5.2 are realized by partially blocking the rectangular slit by leaving open either one side (asymmetric configurations) or both opposite sides (symmetric configurations). These configurations allow to explore the sensitivity to different spatial distribution of blowing. The good symmetry properties of the injection is attested in Fig. 5.3 showing the velocity U_b along the active slits and in the absence of wind. The configurations are shown in Fig. 5.3(a); left (L), right (R), top (T), bottom (B) for asymmetric configurations, and both left and right (LR), both top and bottom (TB). The blowing inhomogeneity along a slit respects satisfactorily the reflectional symmetries of the rectangular base. Consequently, the blowing of the symmetric configurations is symmetric, and each blowing of the 4 asymmetric configurations only breaks the reflectional symmetry of the base as it has been designed for. The symmetric configuration corresponding to the full rectangular slit did not have the expected symmetry and this configuration cannot be used as a spatially controlled disturbance of the wake mode. Nevertheless base drag effect will be shown.

The uniform wind is produced in an Eiffel-type wind tunnel with a 3/4 open jet facility of 390 mm × 400 mm aperture (identical facility of Grandemange et al. (2013b)). The wind speed is fixed at $U_\infty = 20$ m/s with a turbulent intensity below 0.5% and a spatial inhomogeneity smaller than 0.3%. The Reynolds number based on the height h of the body is $Re = U_\infty h/\nu \approx 10^5$, where ν is the kinematic viscosity of air. The mass blowing coefficient is defined as $C_q = q_b/(U_\infty wh)$ and the momentum blowing coefficient as $C_u =$

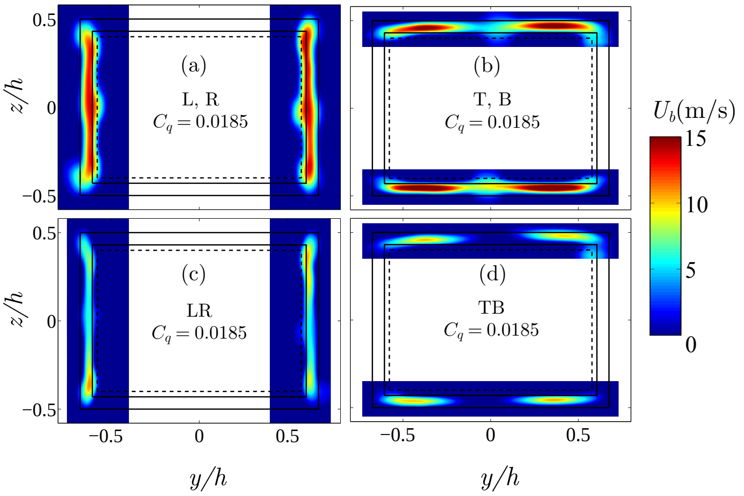

Figure 5.3: Contours of time-averaged blowing velocity obtained by means of hot wire anemometry measurements at $x = 0.1h$ and no wind for the 6 blowing configurations: (a) left (L) or right (R); (b) top (T) or bottom (B); (c) both left and right (LR), (d) both top and bottom (TB). For all configurations, the corresponding blowing coefficient is $C_q = 0.0185$ (taking $U_\infty = 20$ m/s) that is the maximum value for the experiments.

$q_b/(U_\infty S_b)$ where S_b is the total blowing surface composed of the sum of the active slits surfaces. The maximum blowing coefficient investigated in the Chapter is $C_q = 0.0185$ which corresponds to $C_\mu = 1.1$ in the single vertical slit configuration.

The origin of the cartesian coordinate system (x, y, z) is placed at the center of the body base, being x the streamwise direction, z the transverse direction normal to the ground, and y the side direction that forms a direct trihedral. The velocity vector can be therefore decomposed into respective components $\mathbf{u} = (u_x, u_y, u_z)$. The origin of the yaw angle is defined as in Evrard et al. (2016), $\beta = 0$ corresponds to a bistable dynamics with equal probability of both deflected wake states. The difference with the geometrical alignment is 0.22°.

5.2.2 Pressure, velocity and force measurements

Pressure values are measured at four different locations $(y, z) = (\pm 0.3h, \pm 0.2h)$ (indicated as A, B, C and D in Fig. 5.1c). A Scanivalve ZOC22 pressure scanner is placed inside the model, thus reducing the length of vinyl tubes required to connect the 4 pressure taps to the pressure sensor. The local pressures at the base are recorded at a sampling rate of 100 Hz each with an accuracy of ±3.75 Pa and during 250 s for typical experiments. In the following, pressure will be expressed as instantaneous pressure coefficient

$$c_p(y, z, t) = \frac{p(y, z, t) - p_\infty}{\rho U_\infty^2/2}, \tag{5.1}$$

where ρ is the air density, p_∞ is the reference static pressure at the inlet of the test section.

These four measurements are used to assess instantaneously the drag and the wake asymmetry. The drag is evaluated through the base drag or suction coefficient (Apelt and West, 1975; Roshko, 1993) calculated as

$$c_B(t) = -\frac{1}{4}\Sigma_{i=1}^{4} c_p(y_i, z_i, t), \tag{5.2}$$

The precision on mean pressure coefficients, and then mean base drag is estimated to ±0.001. The wake asymmetry, as previously satisfactorily investigated in Grandemange et al. (2013b) and Bonnavion and Cadot (2018), is assessed by means of the non-dimensional base pressure gradient whose horizontal and vertical components, g_y and g_z, are computed as

$$g_y = \frac{\partial c_p}{\partial y} \simeq \frac{h}{2}\left[\frac{c_p(y_B, z_B, t) - c_p(y_A, z_A, t)}{y_B - y_A} + \frac{c_p(y_D, z_D, t) - c_p(y_C, z_C, t)}{y_D - y_C}\right]; \tag{5.3}$$

$$g_z = \frac{\partial c_p}{\partial z} \simeq \frac{h}{2}\left[\frac{c_p(y_A, z_A, t) - c_p(y_C, z_C, t)}{z_A - z_C} + \frac{c_p(y_B, z_B, t) - c_p(y_D, z_D, t)}{z_B - z_D}\right]. \tag{5.4}$$

Polar coordinates are also useful representation of the gradient since the modulus $g = \sqrt{g_y^2 + g_z^2}$ is related to the strength of the wake asymmetry and the phase angle $\varphi = \arccos(g_y/g)$ to its orientation. The mean pressure gradient precision deduced from that of the mean pressure coefficient given above is ±0.003 and ±0.005 for the y and z component respectively.

In order to make accurate and repeatable base pressure measurements, we leave the wind tunnel working and the pressure scanner acquiring during about two hours before investigating one blowing configuration. Experiments are started when no drifts from the sensor signal are observed. We first acquire the non-blowing case, and then, we increase by increments the blowing flow rate until the maximum value $C_q = 0.0185$, recording pressure signals for each selected blowing rate. Once the series are achieved, a non-blowing case is again measured to remove any residual drift effects during the experiment. By subtracting the mean values of blowing and non blowing case, measurements of $\Delta C_B(C_q) = C_B(C_q) - C_B(C_q = 0)$ is obtained varying C_q. The protocol is repeated for all configurations. The measurements of $C_{B0} = C_B(C_q = 0, U_\infty)$ is realized separately where the mean value obtained with no wind is subtracted to the mean value with the wind.

Near wake velocity fields in the two perpendicular planes $y = 0$ and $z = 0$ are investigated to obtain respectively the fields $\mathbf{u_{xz}} = (u_x, 0, u_z)$ and $\mathbf{u_{xy}} = (u_x, u_y, 0)$ by means of Particle Image Velocimetry (PIV) measurements. The PIV system uses a dual pulse laser (Nd:YAG, 2 x 135mJ, 4ns) synchronized with a FlowSense EO, 4 Mpx, CCD camera. For typical measurements 500 pairs of images at 10 Hz are acquired. Velocities are computed from an interrogation window of 16 × 16 pixels with an overlap of 50%, resulting into a spatial resolution of approximately 1% of body's height.

The PIV system is supplemented with a single hot wire probe placed further downstream to provide the frequency of the global periodic wake modes. Four measurement locations are investigated, they are shown in Fig. 5.1 denoted by $P_L(x, y, z) = (2.5h, -0.5h, 0)$, $P_T = (2.5h, 0, 0.3h)$, $P_R = (2.5h, 0.5h, 0)$ and $P_B = (2.5h, 0, -0.3h)$. The wire is orientated in such a way to measure the modulus u_{xz} for the vertical positions at P_T and P_B and the modulus u_{yz} for the lateral positions at P_L and P_R. The hot wire signal is sampled at 1 kHz and dominant frequencies are extracted from averaged power spectral density (PSD). It is computed with pwelch function employing a sliding window of 2 seconds over a signal duration of 120 s, resulting into a frequency resolution of 0.5 Hz.

The aerodynamic force exerted on the body is measured with a multi-axial load cell (model AMTI-MC3A-100lb) connected to the four cylindrical supports (see Fig. 5.1). Time series of drag, side and lift components, i.e. f_x, f_y and f_z respectively, are recorded during 60 s at a sampling rate of 1 kHz. The uncertainty of the measurements is estimated (using specifications of crosstalk, non-linearity and hysteresis) to be 0.002 N for the x and y directions and 0.006 N for the z direction, due to its bigger range.

The drag, side and lift coefficients are defined as

$$c_i = \frac{f_i}{hw\rho U_\infty^2/2}, \tag{5.5}$$

with a corresponding uncertainty of approximately ±0.001 for C_x, C_y and ±0.003 for C_z.

Since we are interested in values without the thrust and slits head loss produced by the blowing itself, we subtract to the mean force $F_i = F_i(C_q, U_\infty)$ obtained for a given blowing and wind speed, the mean force at the same blowing but with no wind $F_i(C_q, U_\infty = 0)$. Thus

$$\tilde{C_i} = \frac{F_i(C_q, U_\infty) - F_i(C_q, U_\infty = 0)}{hw\rho U_\infty^2/2} \tag{5.6}$$

is supposed to be the force coefficient when blowing jet effects are removed. For accurate measurements of $\tilde{C_i}$ we operate as follows. For each C_q and in a single acquisition run, we measure with blowing alone for 15 s (wind tunnel switched off), we then turn on the wind tunnel to capture 30 s of aerodynamic force, and stop the wind tunnel to measure again with blowing alone for another 15 s. Making the average of the two blowing alone stages, and subtracting to the mean force measured during 30 s, we obtain $\tilde{C_i}$. Measurements of C_i with no blowing are realized separately where the mean value obtained with no wind is subtracted to the mean value with the wind.

In the following, the results will be expressed in dimensionless variables using h, U_∞, and h/U_∞ as characteristic length, velocity, and time scales respectively, unless otherwise stated. Notation St, for Strouhal number is used to designate a non-dimensional frequency using h and U_∞ as $St = \varpi h/U_\infty$. Conditional statistics are realized on any measurements presented above to extract the characteristics of the P or N state (Grandemange et al.,

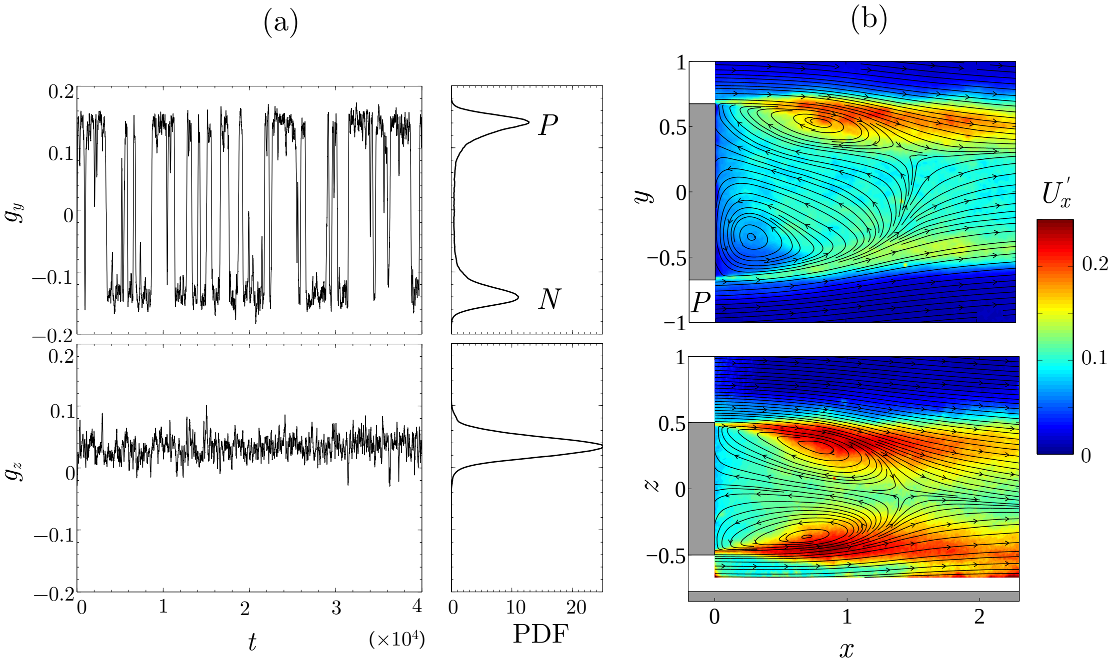

Figure 5.4: Reference case (no slits): (a) time-series of the pressure gradient components $g_y(t)$, $g_z(t)$ and their corresponding probability density functions (PDF). (b) Streamlines of the mean velocity field U^P_{xy} (top), U_{xy} (bottom) superimposed to the fluctuation $U_x^{'P}$ (top), $U_x^{'}$ (bottom).

2013b). They correspond to events such that the horizontal component of the pressure gradient $g_y > 0$ (for P state) or $g_y < 0$ (for N state). For the remainder of the Chapter, we will denote by a superscript ^{P} or ^{N} the conditional averaging of any variables following this rule. Pressure is always simultaneously recorded with the PIV measurements to proceed for conditional averaging on the velocity fields.

5.3 Results

We now present the flow at $Re = 10^5$. The results Section is organized as follows. It starts with a preliminary characterization of the reference case (no slits) and then takes into account the different configurations of open slits without blowing in Sect. 5.3.1. Two regimes of blowing referred to as mass and momentum are evidenced in Sect. 5.3.2 on the basis of base drag measurements. The detailed investigations of the wake is focusing on the static symmetry breaking modes in Sects. 5.3.3-5.3.4 and then on the periodic modes in Sect. 5.3.5. The path of the injected mass is assessed for the two blowing regimes in Sect. 5.3.6 and finally, Sect. 5.3.7 characterizes the correlation of the recirculating length and the base drag.

The following notations are used: time-dependent variables are denoted by lower case letters a, time-averaged values by upper case letters $A = \overline{a}$ and standard deviations by

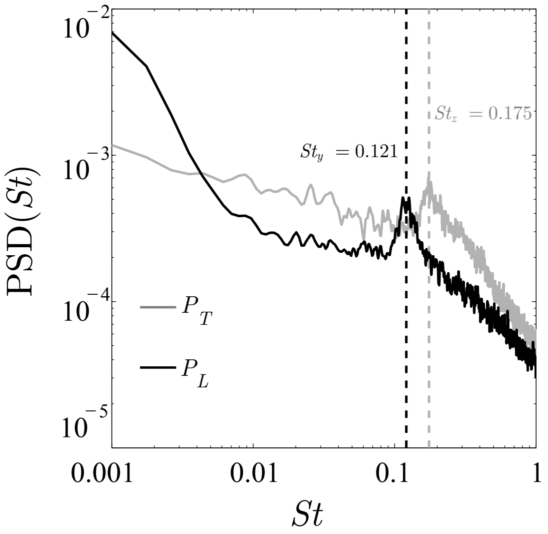

Figure 5.5: Reference case (no slits): power spectral density of the local velocity at P_T and P_L (see Fig. 5.1). The resonant peaks indicate the presence of the periodic asymmetric modes of the wake with a high frequency $St_z = 0.175$ for the vertical mode and a low frequency $St_y = 0.121$ for the horizontal mode (Grandemange et al., 2013b).

$A' = \sqrt{\overline{(a-A)^2}}$. As defined at the end of Sect. 5.2, conditional statistics denoted A^i and A'^i are respectively the average and standard deviation of the $i = P$ or N state. We will use the notation $A_0 = A(C_q = 0)$ for a measurements with no blowing and ΔA for a difference with the no blowing case: $\Delta A = A(C_q) - A_0$.

5.3.1 Flow without blowing

The wake of the body in the absence of slits at the base is referred to as the reference case. It exhibits the well known long-time bistable dynamics due to the y-instability as reported in Grandemange et al. (2013a,b). This behavior is clearly observed by the random switches of the horizontal component of the pressure gradient g_y in Fig. 5.4(a). They occur between two well defined mirrored states denoted P and N in the corresponding probability density function. The time spent in one state can be as large as few orders of magnitudes of the convective time scale. The vertical component of the pressure gradient g_z remains almost insensitive to the switching dynamics in Fig. 5.4(a). Its positive value is introduced by the presence of the body support and the ground. The wake topology corresponding to the P state is obtained in Fig. 5.4(b) and reveals the static mode of the wake as reported in the literature. The N state (not shown here) is a mirror symmetry ($y \to -y$) of the P state.

The two periodic modes of the wake are identified in the PSD shown in Fig. 5.5 of the local velocity measurements in the wake. In accordance to the wake characterization of Grandemange et al. (2013b), we find a low resonant frequency denoted $St_y = 0.121$ (captured by the local velocity at P_L) associated with the global lateral motion and a high

C_x^{Ref}	0.371	C_y^{Ref}	0.002	C_z^{Ref}	-0.055	C_B^{Ref}	0.177
$C_x'^{\mathrm{Ref}}$	0.005	$C_y'^{\mathrm{Ref}}$	0.019	$C_z'^{\mathrm{Ref}}$	0.010	L_r^{Ref}	1.45
G^{Ref}	0.133	G_z^{Ref}	0.037	$G_y^{P,\mathrm{Ref}}$	0.127	$G_y^{N,\mathrm{Ref}}$	-0.126
St_y	0.121	St_z	0.175				

Table 5.1: Reference case (no slits): mean values of force coefficients, base drag, recirculating bubble length, base pressure gradient modulus of the static mode with components for its N and P states, Strouhal numbers of the periodic modes.

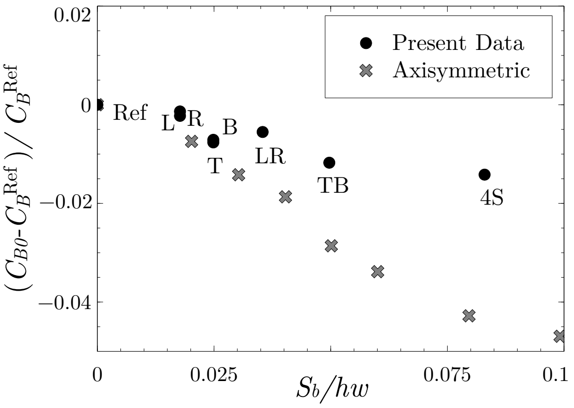

Figure 5.6: Base drag modification for all slit configurations as displayed in Fig. 5.2 without blowing versus slits area. The axisymmetric data are from García de la Cruz et al. (2017).

resonant frequency denoted $St_z = 0.175$ (captured by the local velocity at P_T) associated with the global vertical motion. Table 5.1 summarizes the main global flow characteristics of the reference case such as force coefficients, recirculating bubble length, base drag and mean pressure gradient. Recirculation region extension has been characterized as the maximum x coordinate where $U_x \leq 0$. All these values are in accordance with previous measurements for similar square-back geometries. However strict comparison with other published works is meaningless because none of the geometries are identical with significant variations such as forebody shape, supports design, ground clearance, and body dimensions. We can see in Table 5.1 that the floor and support produce a negative lift coefficient $C_z = -0.055$, the bistable dynamics between the two asymmetric states is responsible for the large fluctuation in the side force coefficient $C_y' = 0.019$ due to the random switches of the y component of pressure gradient between the mean values of both states $G_y^{N,\mathrm{Ref}}$ and $G_y^{P,\mathrm{Ref}}$. The mean pressure gradient modulus $G^{\mathrm{Ref}} = 0.133$ gives the strength of the permanent wake asymmetry.

We denote by C_{B0} the base drag obtained for the open slits configuration as displayed in Fig. 5.2 without blowing ($C_q = 0$). A slight reduction of C_{B0} is obtained from the reference case, as it was also found by Bearman (1967) for a two-dimensional blunt-based body and García de la Cruz et al. (2017) for an axisymmetric blunt body. The relative

Configuration	L	R	T	B	LR	TB	4S
C_{B0}	0.176	0.176	0.175	0.175	0.176	0.175	0.174
G_{y0}^{P}	0.129	0.129	0.127	0.128	0.134	0.133	0.135
G_{z0}^{P}	0.035	0.036	0.047	0.031	0.037	0.038	0.036
G_{y0}^{N}	-0.127	-0.127	-0.125	-0.125	-0.131	-0.130	-0.133
G_{z0}^{N}	0.037	0.038	0.049	0.033	0.039	0.040	0.038
G_0	0.135	0.135	0.136	0.131	0.139	0.138	0.140

Table 5.2: Passive effect values ($C_q = 0$) for all configurations.

change of base drag coefficient $(C_{B0} - C_B^{\mathrm{Ref}})/C_B^{\mathrm{Ref}}$ is shown in Fig. 5.6 against the slits area normalized by the base area, S_b/hw. The decrease obtained by García de la Cruz et al. (2017) with a perimetric slit on a circular base is also reported in the figure. The rectangular perimetric slit (configuration 4S) is shown for comparison with the circular perimetric slit. A much smaller relative base drag decrease is observed with the wake of the rectangular base that is approximately 1.5% compared to the 4% of the circular base. This reduction is interpreted in García de la Cruz et al. (2017) as an effect associated with a decrease of the intensity of the wake asymmetry and likely to be produced by the stabilization of the static mode. In order to check this result in our geometry, Table 5.2 shows base drag and mean pressure gradients for all configurations. In contradiction, it appears that as a general trend in our accuracy, the asymmetry strength given by G_0 is rather increased in comparison to the reference value of 0.133 with open slits. However, according to the precision of ±0.005 for the mean pressure gradient and ±0.001 for the base drag, these weak effects seem unfortunately at the limit of our measurements that may lead to unreliable conclusions. A significant effect is however detectable on the z component of the pressure gradient for B and T configurations pointing out a local pressure increase on the side of the open slit thus enhancing the vertical component in the T configuration and reducing it in the B configuration.

5.3.2 Blowing effect on the base drag

The base drag variation $\Delta C_B = C_B - C_{B0}$ is shown for all configurations as a function of C_q in Fig. 5.7(a) and C_u in Fig. 5.7(b). We recall that the L and R configurations are symmetrically equivalent explaining why the corresponding curves are superimposed.

A same trend is observed for all configurations, characterized by an initial base drag reduction with increasing values of the blowing intensity, followed by a constant slope increase of base drag. This general behavior is similar to that obtained by Wood (1964) for two-dimensional bodies implementing rear blowing. Two blowing regimes have to be distinguished, we will refer to as the mass regime, the small blowing for which the

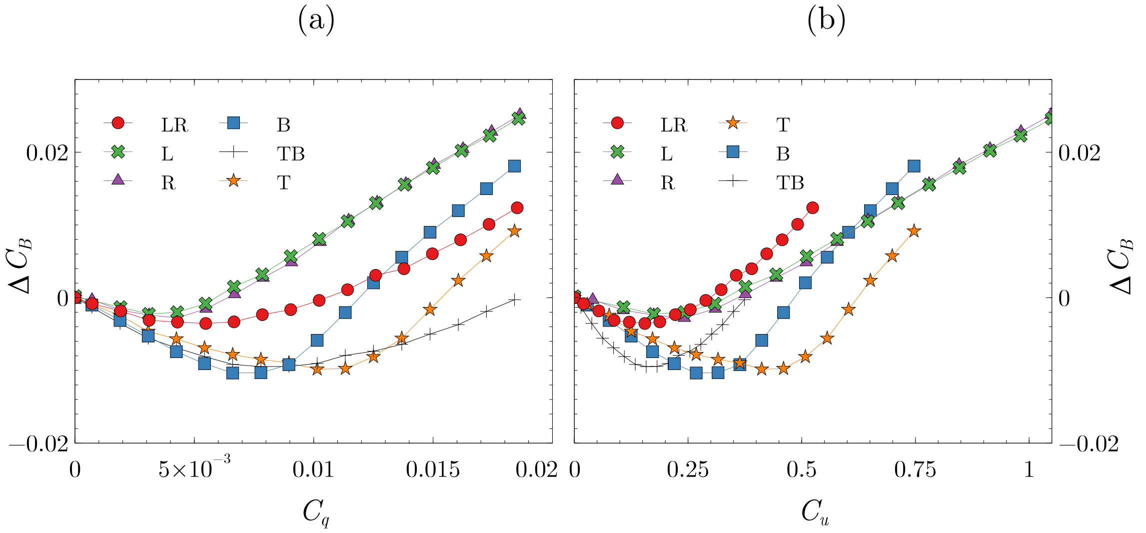

Figure 5.7: Base drag coefficient variation $\Delta C_B = C_B - C_{B0}$ versus the mass blowing coefficient C_q (a) and momentum coefficient C_u (b).

Configuration	L	R	T	B	LR	TB
C_q^{Opt} (10^{-3})	4.3	4.3	10.2	6.6	5.5	7.8
C_u^{Opt}	0.242	0.242	0.412	0.268	0.155	0.158
BDR (%)	1.5	1.6	5.7	6.2	2.1	5.5
$\frac{\partial C_B}{\partial C_q}\|_0$	-0.78	-0.79	-1.07	-1.65	-0.99	-1.51
$\frac{\partial C_B}{\partial C_u}\|_\infty$	0.036	0.036	0.074	0.072	0.049	0.052
b_∞	-0.014	-0.014	-0.046	-0.035	-0.014	-0.020

Table 5.3: Data extracted from Fig. 5.7. Optimal values of base bleed coefficients for maximum base drag reduction BDR (%) $= -\Delta C_B^{\text{min}}/C_{B0}$ for all configurations. Parameters of the linear fit in the mass regime $\Delta C_B = \frac{\partial C_B}{\partial C_q}|_0 C_q$ and in the momentum regime $\Delta C_B = \frac{\partial C_B}{\partial C_u}|_\infty C_u + b_\infty$.

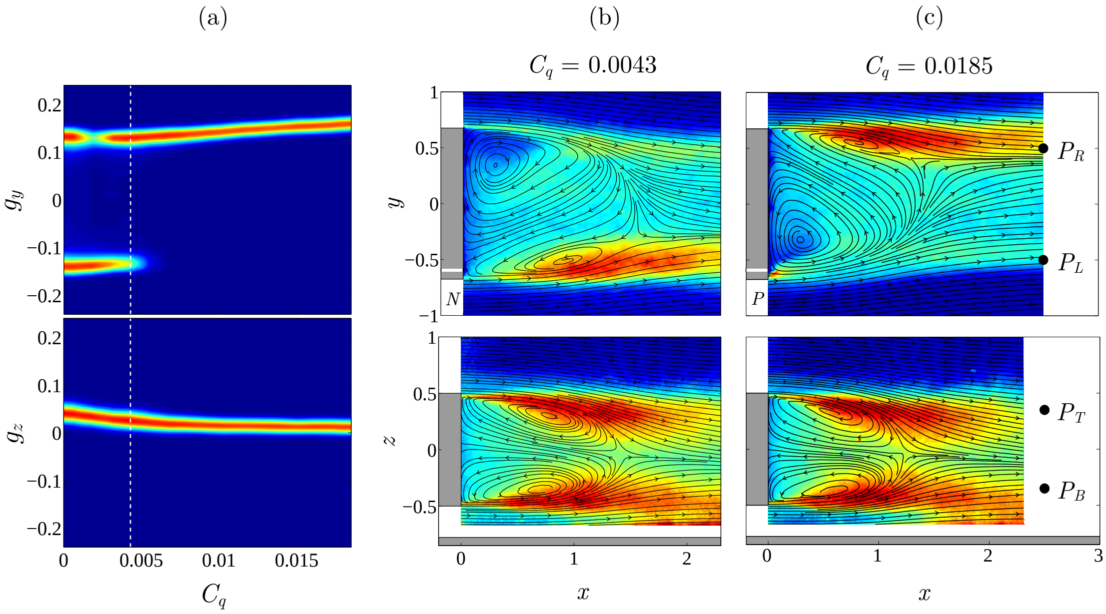

Figure 5.8: Blowing in L configuration. (a) Sensitivity maps of the Cartesian components, g_y and g_z of the base pressure gradient. The white dashed line marks the C_q^{opt} value for which the mean base drag C_B is minimum. (b,c) Contours of the conditional averaged streamwise velocity fluctuations, U_x', superimposed to flow streamlines for (b) $C_q^{\mathrm{opt}} = 0.0043$ and (c) $C_q = 0.0185$. The white band in (b,c) indicates the blowing slit.

base drag is decreased and the momentum regime, the larger blowing for which the base drag is increased. Both regime are fitted with linear regressions whose parameters are given in Table 5.3. The maximum of base drag reduction (approximately from 1% to 7%) and the corresponding optimal blowing coefficients summarized in Table 5.3 show a substantial dependency with the blowing configuration. Maximal reductions involve the top or bottom slits whether the configuration is symmetric or not. The B configuration achieves the best reduction. There is no evidence of simple relation between in either the optimal C_q or C_u with the blowing configurations. This high and non-trivial sensitivity to the blowing location and intensity is investigated in the next parts by studying the wake modes interaction with the blowing.

5.3.3 Static modes manipulation under asymmetric blowing configurations

Both configurations L and R have been identically investigated and the experimental data are, as expected, symmetrically equivalent. For brevity of the Chapter we only present results for one configuration, and the results for other can be deduced by the left to right reflectional symmetry.

The sensitivity map of the Cartesian components of the base pressure gradient for the L

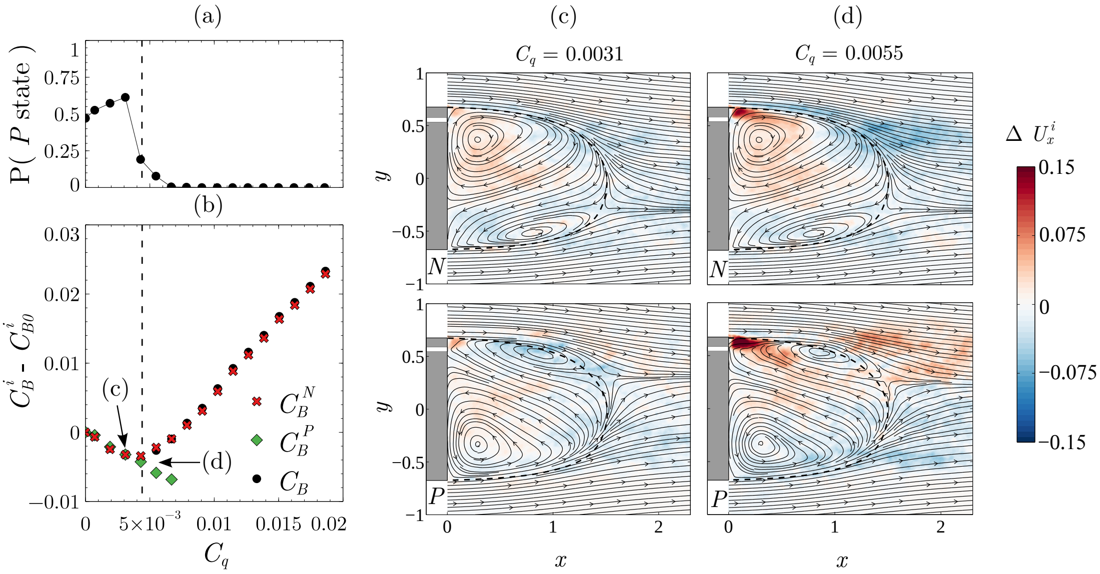

Figure 5.9: Blowing in R configuration: (a) Probability of occurrence of the P state (top) and relative variation of base drag (b) for N and P states versus the blowing coefficient. The dashed line marks the C_q^{opt} value for which C_B is minimum. (c,d) Contours of the mean streamwise velocity difference $\Delta U_x^i = U_x^i - U_{x0}^i$ of states $i = P, N$ superimposed to the mean flow streamlines for $C_q = 0.0031$ (c) and $C_q = 0.0055$ (d). White bands in (c,d) indicate the blowing slits.

configuration is displayed in Fig. 5.8(a). The vertical dashed line locates the optimal value of blowing that separates the mass and momentum regime as defined above. The positive (resp. negative) branch correspond the P state (resp. N state). It can be seen that the change of blowing regime is accompanied with a permanent wake reversal towards the P state (Fig 5.8c) that was predominantly in the N state (Fig. 5.8b) in the mass regime. The momentum regime is then associated with a selected P state in L configuration, where the blowing jet (clearly identified by its large localized fluctuation U_x' in front of the slit) is fixing the steady circular recirculation of the bubble. In the mass regime, $C_q < C_q^{\mathrm{opt}}$, the dynamics is bistable involving both P and N states. From the initial case at $C_q = 0$ where both states are equiprobable, we see a significant change in their probability of presence as blowing is increased, promoting the N state. The preferential state selection in the mass regime is then opposite to that of the momentum regime. It is also worth mentioning that there is almost no trace of the blowing jet for the largest blowing in the mass regime reached when $C_q = C_q^{\mathrm{opt}}$ in Fig. 5.8(b). However a direct effect of the blowing can be identified through the additional linear increase of g_y in Fig. 5.8(a). The blowing is likely to produce a positive pressure gradient proportional to C_q that is not affected by the wake state whether it is P or N.

We now turn to the effect of the L or R blowing during the bistable dynamics. Actually, there should be a distinction whether the wake is in an N or P state. Indeed, the blowing jet is either in a reversed velocity region as depicted in Fig. 5.8(b,top) or in an adverse

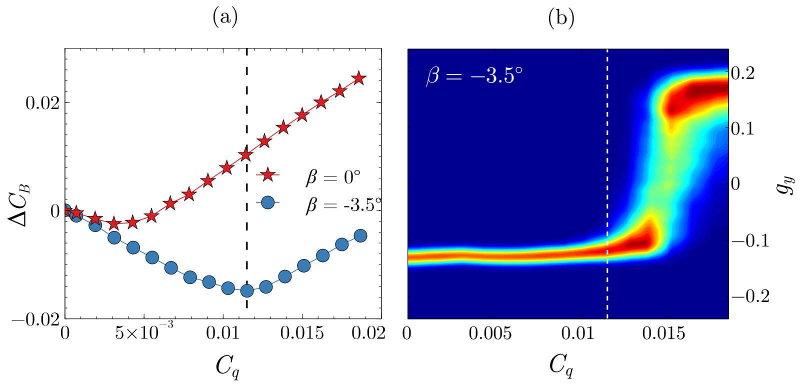

Figure 5.10: Blowing in L configuration with yaw. Relative variation of base drag (a) versus the injection coefficient for the body yawed at $\beta = -3.5°$. The case $\beta = 0°$ is added for comparison. The dashed line marks $C_q^{\text{opt}} = 0.0115$ for which the mean base drag C_B is minimum. Sensitivity map of the horizontal component of the base pressure gradient component.

velocity region as depicted in Fig. 5.8(c,top). Conditional averaging is thus performed next to distinguish the two cases. Figure 5.9 are results obtained with configuration R. As can be seen in Fig. 5.9(a), the mass regime preferentially selects the P state with a probability larger than 0.5 and the momentum regime selects the N state. These are actually the expected results for the R configuration that can be deduced from the mirror symmetry of the above observations concerning the L configuration described in Fig. 5.8. The mean base drag and mean velocity field of each state are respectively shown in Fig. 5.9(b) and Figs. 5.9(c,d). There is no distinctions in the base drag of the two states until the blowing coefficient reaches $C_q = C_q^{\text{opt}}$. Bistable dynamics occur as far as the P state is observable, that extends beyond C_q^{opt} until $C_q = 7.8 \times 10^{-3}$. Around this blowing limit, the velocity fields displayed by the streamlines of the two states in Fig. 5.9(d) are globally mirrored from each other, while the corresponding base drag reduction are significantly different. The P state is likely to be in a mass regime with a base drag reduction that is still increasing linearly with the blowing coefficient while the N state produces a base drag increase characteristic of the momentum regime. We deduce that it is more favourable for base drag reduction to blow in the reversed velocity flow region than in the adverse velocity region. Since the blowing jet is hardly discernible in the mean flows, we superimposed to the streamlines in Fig. 5.9(c,d) the difference of the mean streamwise velocity with that of the flow at $C_q = 0$, say $\Delta U_x^i = U_x^i - U_{x0}^i$ where $i = P$ or N denotes the state. The blowing jet is not discernible in the mass regime in Fig. 5.9(c) for both states at $C_q = 0.0031$, indicating that the injected momentum is efficiently mixed (i.e. dissipated) in the asymmetric recirculating bubble independently to the injection location. On the other hand, the jet is clearly observable in Fig. 5.9(d) at $C_q = 0.0055$. For both states it contributes to increase the momentum, obviously more when located in the reversed flow region in the P state in Fig. 5.9(d, bottom) than in the N state in Fig. 5.9(d, top).

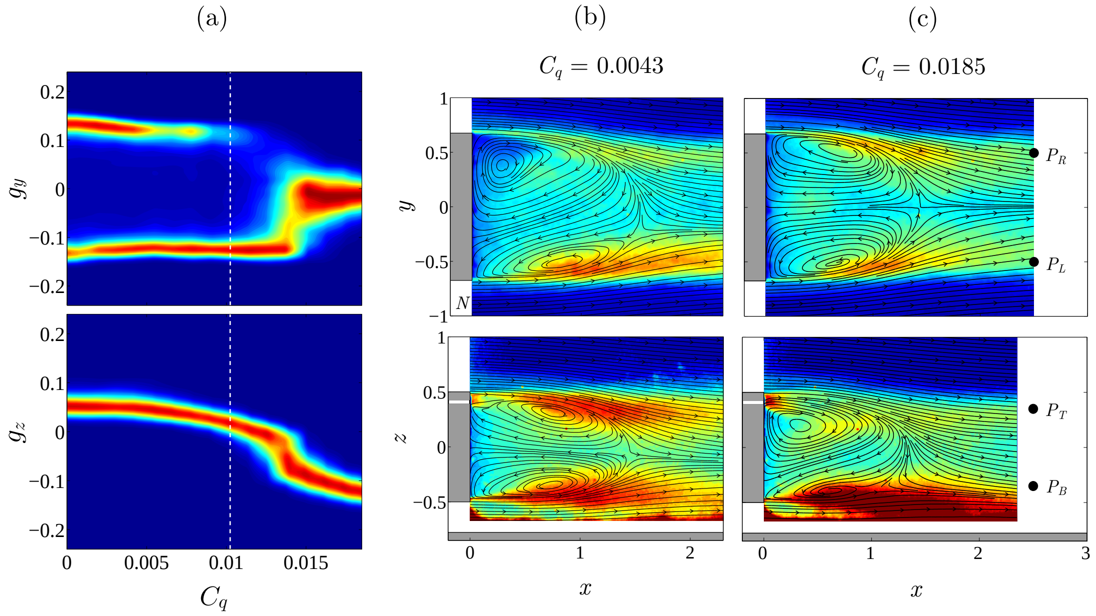

Figure 5.11: Blowing in T configuration. (a) Sensitivity maps of the Cartesian components, g_y and g_z of the base pressure gradient. The white dashed line marks the C_q^{opt} value for which the mean base drag C_B is minimum. (b,c) Contours of the conditional averaged streamwise velocity fluctuations, U'_x, superimposed to flow streamlines for (b) $C_q^{\text{opt}} = 0.0102$ and (c) $C_q = 0.0185$. The white band in (b,c) indicates the blowing slit.

The favourable configuration (injection in the reversed flow region of the bubble) can be forced by applying a yaw angle β to the body. It has been previously shown (Volpe et al., 2015) that a yaw of 1° is sufficient to permanently selects a P (resp. N) state with a positive (resp. negative) yaw without any modification of the base pressure gradient modulus (Bonnavion and Cadot, 2018). Figure 5.10(a) shows the base pressure variation where the body has been yawed to $\beta = -3.5°$ to select an N state. As expected, the mass regime is extended by a blowing in the L configuration compared to the unforced wake ($\beta = 0°$). It reaches a larger limit value $C_q^{\text{opt}} = 0.0115$ and an increased maximum base drag reduction of 7.5%. The sensitivity map of the horizontal component of the pressure gradient shows that in the mass regime, the gradient magnitude of the forced N state remains unchanged until bistable dynamics appear due to compensation effect (Bonnavion and Cadot, 2018) of asymmetries between yaw and local momentum injection.

The L or R blowing configuration studied above breaks the same symmetry as the static modes (i.e. left/right symmetry), leading in the momentum regime to the permanent selection of unique state. The B or T blowing configuration we now investigate breaks the top/bottom symmetry and will show very different interaction with the wake. The sensitivity map of the base pressure gradient in the T configuration is shown in Fig. 5.11(a). A bistable dynamics is observed during the entire mass regime. At the maximum of drag reduction, the wake topology (Fig. 5.11b) remains very similar to that of the reference

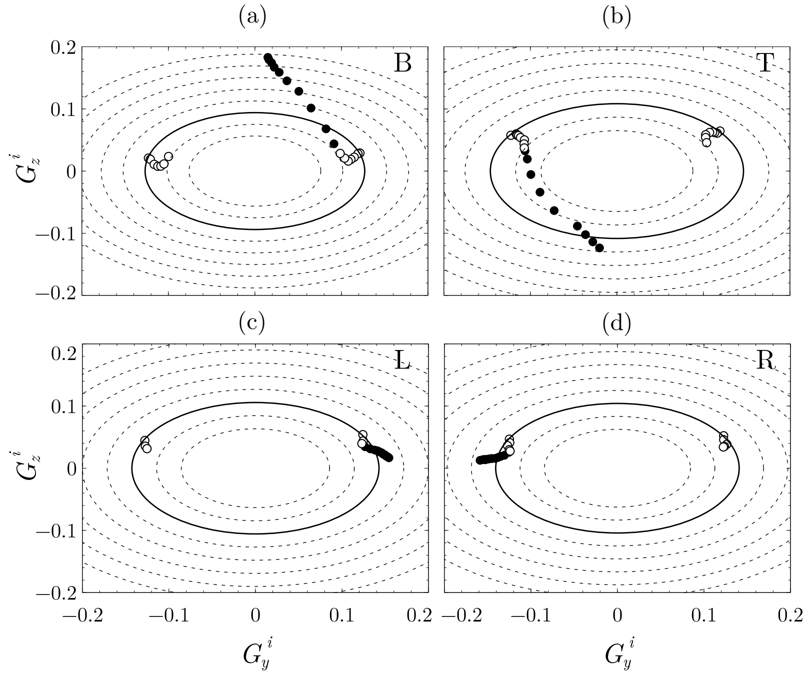

Figure 5.12: Blowing in asymmetric configurations: (a) T, (b) B, (c) L and (d) R. Mean Pressure gradient components of the wake states (G_y^i, G_z^i) with $i = N, P$ in mass regime (empty symbols) and momentum regime (filled symbols). The solid line ellipse is the model of Bonnavion and Cadot (2018) (see text) and dashed ellipses are standing for variations of 20% of the gradient magnitude obtained with no blowing.

flow. The momentum regime is first marked by the disappearance of the N state and then to the suppression of the asymmetry in the y-direction since the horizontal component g_y eventually fluctuates around a unique value equal to zero. This suppression is simultaneously accompanied with an increase of the gradient component g_z in the z-direction. It indicates that the blowing at the upper part of the base has rotated the two states to a single state with a vertical asymmetry leading to a P state in the z direction. This is clearly illustrated by the velocity fields in Fig. 5.11(c) for the largest blowing coefficient. The P state in the z-direction that is forced by blowing in the B configuration actually reproduces the same situation observed in the momentum regime (Fig. 5.8c) with the P state in the y-direction selected by blowing in the L configuration. These two cases are deduced from each other by a simple $\pi/2$ rotation.

The gradual rotation of the base pressure gradient as the blowing is increased is better quantified in Fig. 5.12 that summarizes the base pressure gradient evolution for all asymmetric blowing configurations. Each point of the plot represents the mean gradient of a corresponding wake state either P or N obtained through conditional averaging. By definition, the P branch develops on the right hand side of the plot and the N branch on the left. The continuous ellipse is modelling all the possible pressure gradients of the

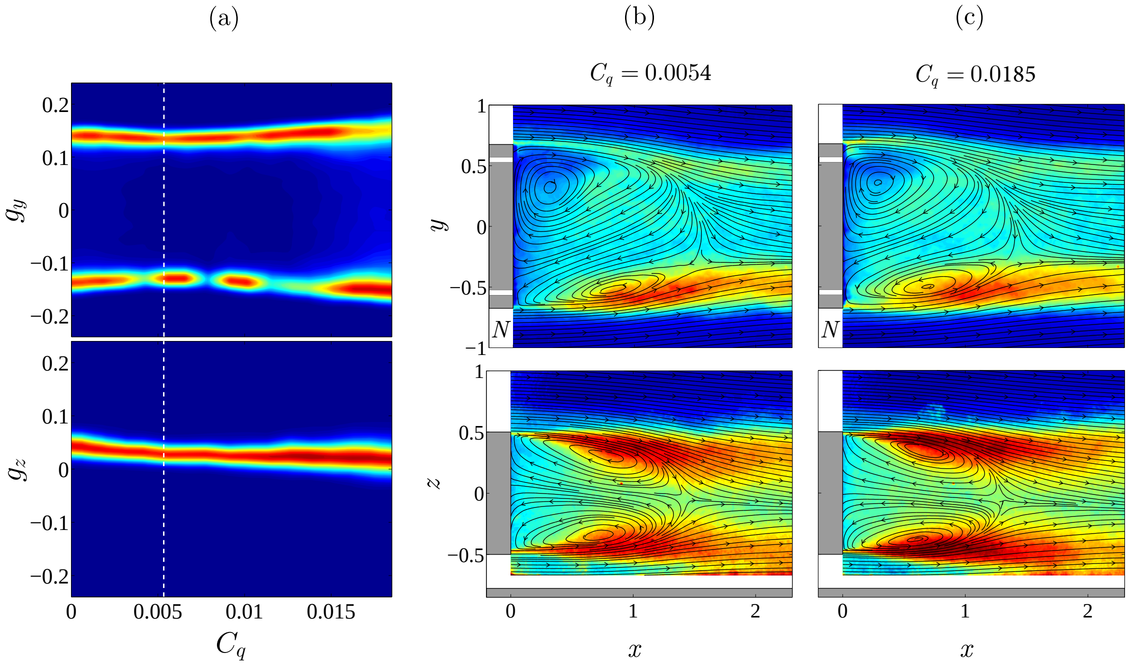

Figure 5.13: Blowing in LR configuration. (a) Sensitivity maps of the Cartesian components, g_y and g_z of the base pressure gradient. The white dashed line marks the C_q^{opt} value for which the mean base drag C_B is minimum. (b,c) Contours of the conditional averaged streamwise velocity fluctuations, U_x', superimposed to flow streamlines for (b) $C_q^{\text{opt}} = 0.0054$ and (c) $C_q = 0.0185$. The white bands in (b,c) indicate the blowing slits.

unstable wake (i.e. dominated by a static mode) that would have been passively selected by steady disturbances of pitch and yaw of the body in absence of blowing (Bonnavion and Cadot, 2018). This view gives useful information about the wake asymmetry strength measured as the modulus of the gradient. Gradient located on the initial ellipse indicate no modification of the asymmetry strength compared to that naturally developed by the body geometry. The mass regime (empty symbols) in the T and B configurations in Fig. 5.12 (a,b) leads to a decrease of 20% of the initial mean gradient modulus. However, the momentum regime (filled symbols) in which the rotation occur shows a significant amplification of the asymmetry likely to be fed by the blowing jet. The same representation of the gradient of the wake states for the L and R blowing configuration (Fig. 5.12 c,d) indicates as well an attenuation of the asymmetry during the mass regime (approximately 10%) and an amplification in the momentum regime. The reduction of the asymmetry is mainly ascribed to a decrease of the horizontal component of the gradient for B or T configurations and of the vertical component for L or R configurations.

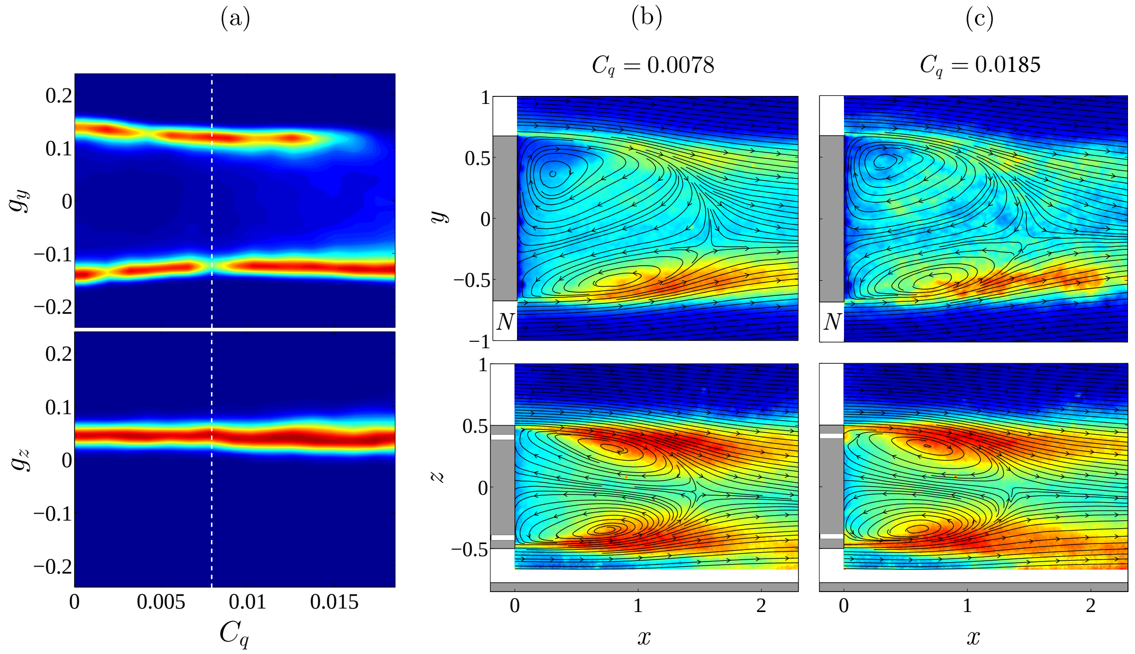

Figure 5.14: Blowing in TB configuration. (a) Sensitivity maps of the Cartesian components, g_y and g_z of the base pressure gradient. The white dashed line marks the C_q^{opt} value for which the mean base drag C_B is minimum. (b,c) Contours of the conditional averaged streamwise velocity fluctuations, U_x', superimposed to flow streamlines for (b) $C_q^{\text{opt}} = 0.0078$ and (c) $C_q = 0.0185$. The white bands in (b,c) indicate the blowing slits.

5.3.4 Symmetric blowing configurations influence on static modes

The two symmetric configurations, either obtained with a simultaneous blowing in the left and right slits (LR) or top and bottom slits (LT) give very similar results. The sensitivity maps of the base pressure gradient, respectively given in Fig. 5.13(a) and Fig. 5.14(a) indicate that bistable dynamics are conserved as expected by the blowing symmetry. The two P and N states remain also very similar whatever the blowing injection is as can be seen in Fig. 5.13(b,c) and Figs. 5.14(b,c). However, the horizontal gradient component g_y reaches a small value for the optimal blowing coefficient in both Figs. 5.13(a), 5.14(a) showing that maximum base drag reduction is associated with a strength reduction of the asymmetry.

Figure 5.15 recaps the base pressure gradient evolution for the two symmetric blowing. We observe an attenuation of the asymmetry strength given by the mean gradient modulus of approximately 10% for the LR configuration mainly caused by a decrease of the vertical component and 20% for the TB configuration due to a decrease of the horizontal component.

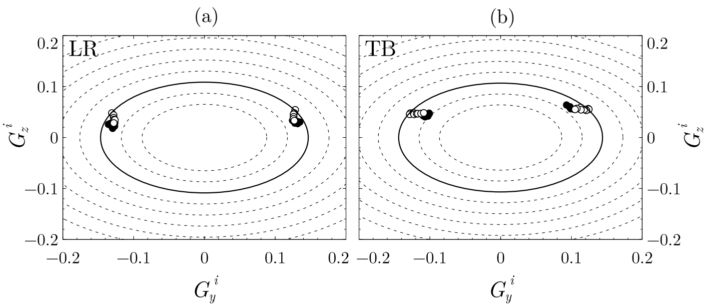

Figure 5.15: Blowing in symmetric configurations: (a) LR and (b) TB. Mean Pressure gradient components of the wake states (G_y^i, G_z^i) with $i = N, P$ in mass regime (empty symbols) and momentum regime (filled symbols). The solid line ellipse is the model of Bonnavion and Cadot (2018) (see text commenting Fig. 5.12) and dashed ellipses are standing for variations of 20% of the gradient magnitude obtained with no blowing.

5.3.5 Periodic modes

The global periodic modes are studied for the L and T blowing configurations only, owing each to 3 local points velocity measurements in the wake. Their locations (see Sect. 5.2.2) are displayed in Fig. 5.16 with a sketch view towards the base, but they are also displayed in the velocity fields in Fig. 5.8 (L blowing configuration) and Fig. 5.11 (T blowing configuration) to specify their relative position in the spatial distribution of the turbulent fluctuations. The power spectral densities are computed at each location varying the blowing coefficient and displayed as a colormap versus the non-dimensional frequency St and C_q in Fig. 5.16(a) for the L configuration and Fig. 5.16(b) for the T configuration.

The two shedding frequencies initially observed at $St_z \approx 0.121$ and $St_y \approx 0.175$ with no blowing are clearly identifiable in Fig. 5.16 when the blowing coefficient is increased. We can see that the only significant frequency modification is observed for the well defined low frequency that increases from 0.121 to about 0.15 with wider energy distribution when blowing in the L configuration in Fig. 5.16(a). Apart from this effect, the major changes lie in the intensity of the resonance peaks that directly reflects the anisotropy of the fluctuations of the static mode together with its interaction with the local blowing presented in Sects. 5.3.3-5.3.4. Changes in intensities coincide with the transition between the mass and momentum regime at the optimal blowing C_q^{opt}. For the L configuration in Fig. 5.16(a), the N state is predominantly present in the mass regime such that the probe P_L is more often in a high level of fluctuation as shown by Fig. 5.8 (b) than P_R. The situation inverts in the momentum regime that permanently selects the P state producing high fluctuation at P_R location and smaller at P_L location. Similarly the intensity variations in the T configuration also reflects the $\pi/2$ rotation of the static mode from horizontal bistability between P and N states producing high fluctuations at P_L to a vertical N state with reduced fluctuations at P_L.

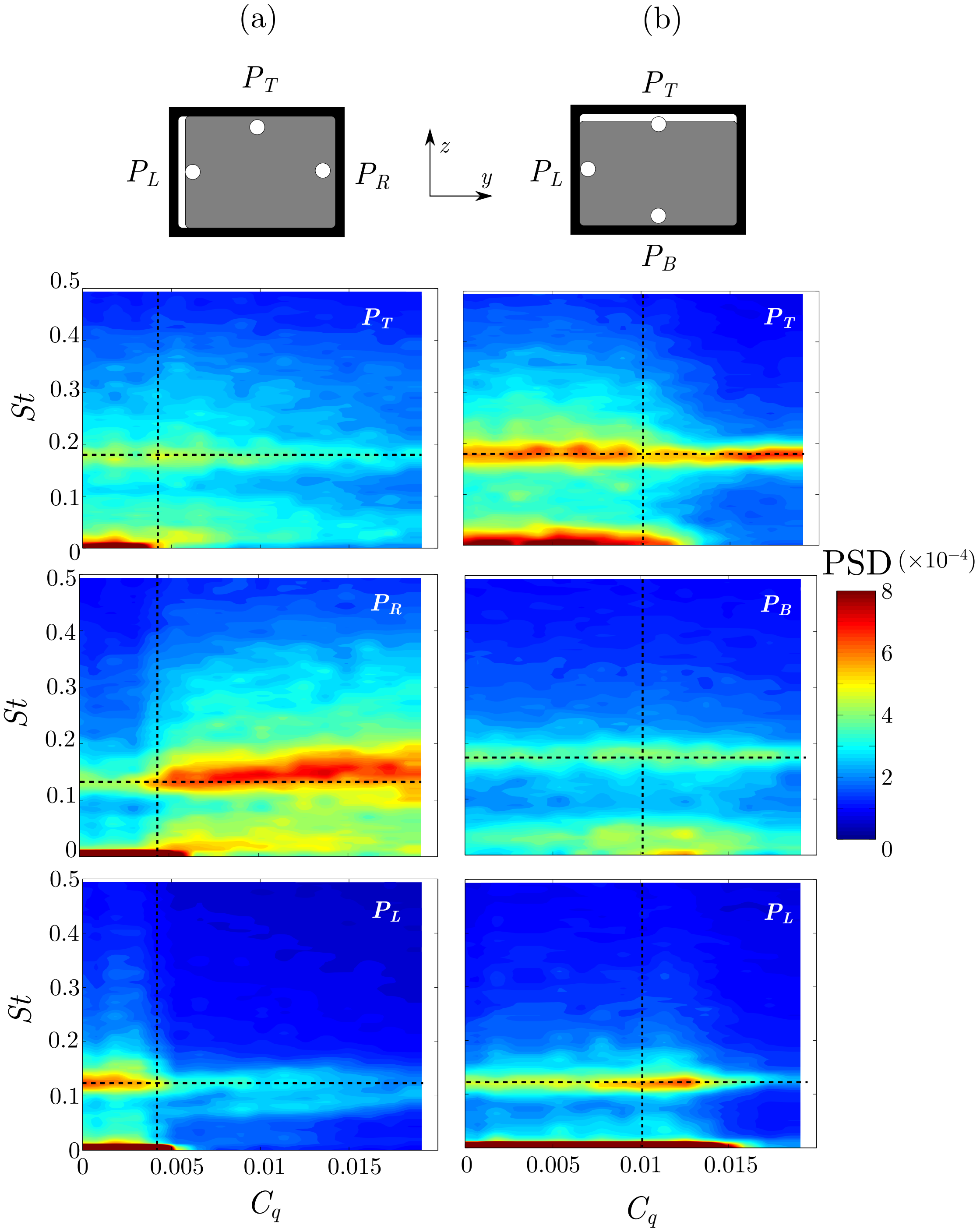

Figure 5.16: Effect of blowing on the wake periodic modes in L (a) and T (b) configurations. Contours of power spectral density (PSD) of local velocity measured at P_L, P_R, P_T and P_B (see §5.2.2) as depicted in the top of the figure and also in Fig. 5.8 and Fig. 5.11. The horizontal dashed lines are the values of the Strouhal numbers, $St_y = 0.121$ and $St_z = 0.175$ of the reference case. The vertical dashed lines mark the C_q^{opt} value for which the mean base drag C_B is minimum.

5.3.6 Leakage of the recirculating region

The experimental implementations do not allow for the tracking of the injected mass but the injected momentum can be assessed by looking at the difference between the mean velocity modulus at a given blowing rate with that of $C_q = 0$, say $\Delta U^i_{xy} = U^i_{xy} - U^i_{xy0}$ in the $z = 0$ plane and $\Delta U_{xz} = U_{xz} - U_{xz0}$ in the $y = 0$ plane where $i = P$ or N denotes the state. Both cases will be referred to as mean momentum modifications. We superimpose to the mean flow streamlines in Fig. 5.17 the mean momentum modification when blowing in the LR configuration. We only display the optimal C_q^{opt} (Fig. 5.17a) and maximum injection $C_q = 0.0185$ (Fig. 5.17b) corresponding to the extreme cases of respectively low and high base drag. The blowing jets are not distinguishable in the mass regime (Fig. 5.17a,top), but a momentum reduction is clearly visible outside the bubble. It is an indication that the bubble is sweating low momentum by leaking the continuous injection mass. The bubble size is slightly increased when compared to the dashed curve representing the separatrix obtained with no injection. For the maximum injection coefficient in Fig. 5.17(b,top), the bubble size is decreased, the momentum is significantly increased at the slits exit inside the bubble. There are also indications of leakage shown by the momentum decrease just outside the bubble at the right hand side injection and momentum increases aft the bubble closure (also observable in the perpendicular plane in Fig. 5.17b,bottom). In both cases, it reveals that momentum from the bubble has mixed with the flow outside the bubble and then been naturally transported downstream: at the right outer edge with high speed flow and in the wake with low speed flow.

The evacuation of the injected mass by the wake is also observable in Fig. 5.18 for TB configuration. The optimal blowing is associated with an overall momentum reduction outside the bubble in Fig. 5.18(a) and the maximum blowing to momentum increase aft the bubble in Fig. 5.18(b,top). The leakage pattern in the momentum regime is dominant in the plane $z = 0$ and very different to the LR configuration observed in Fig. 5.17(b,top). The optimal blowing at $C_q = 0.0078$ also produces a larger bubble size (Fig. 5.18a) and the maximum blowing a smaller bubble size (Fig. 5.18b).

Similar results are obtained for all other configurations, whose main differences lay only in the leakage pattern of the momentum regime. As a conclusion, the path of the injected flow is never detectable in the mean flow displayed with streamlines as ideally sketched in Bearman (1967) in the theoretical case of a steady wake but mixed and then evacuated in the wake through the unsteady dynamics of the shears and bubble closure.

5.3.7 Drag and recirculation length

The base drag coefficient variation versus the drag coefficient variation in Fig. 5.19(a) deviates slightly from the linear law of slope 1. This linear law is expected for a blunt-based geometry when pressure drag is the only source of drag. The slope of 1 is however

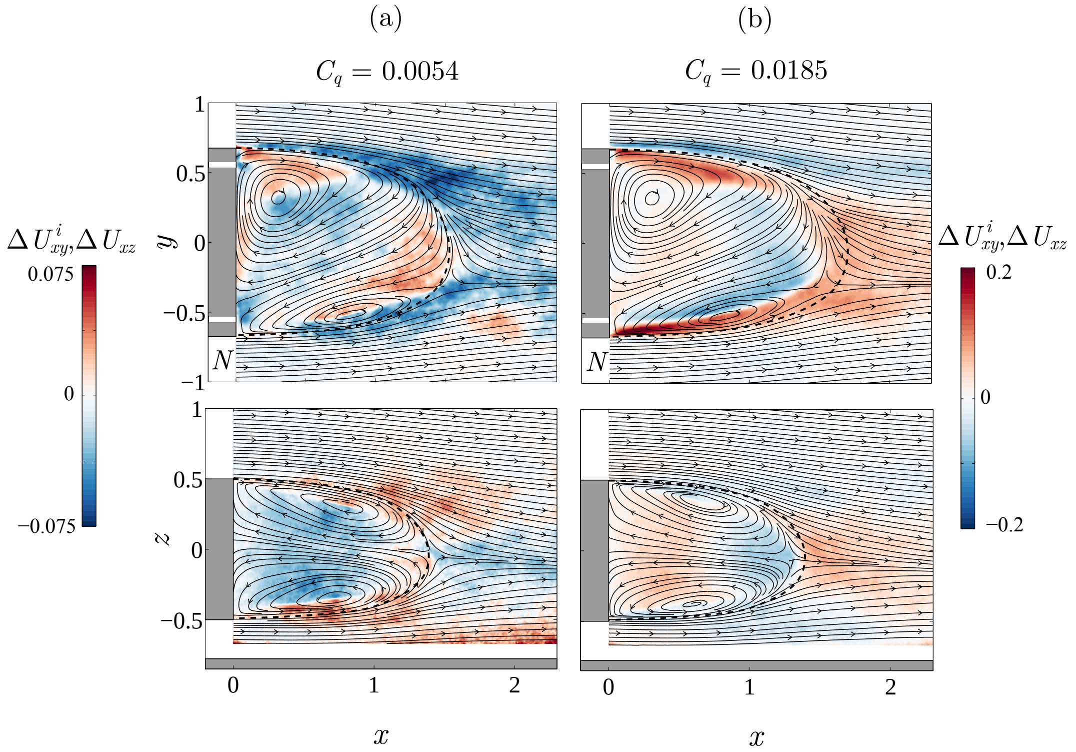

Figure 5.17: Blowing in LR configuration. Mean momentum modification superimposed to the mean streamlines for (a) $C_q = C_q^{\text{opt}}$ and (b) maximum injection $C_q = 0.0185$. (a,top): $\Delta U^i_{xy} = U^i_{xy} - U^i_{xy0}$, (b,bottom): $\Delta U_{xz} = U_{xz} - U_{xz0}$, $i = P$ or N denotes the state. The dashed curve represents the separatrix of the recirculating bubble with no injection.

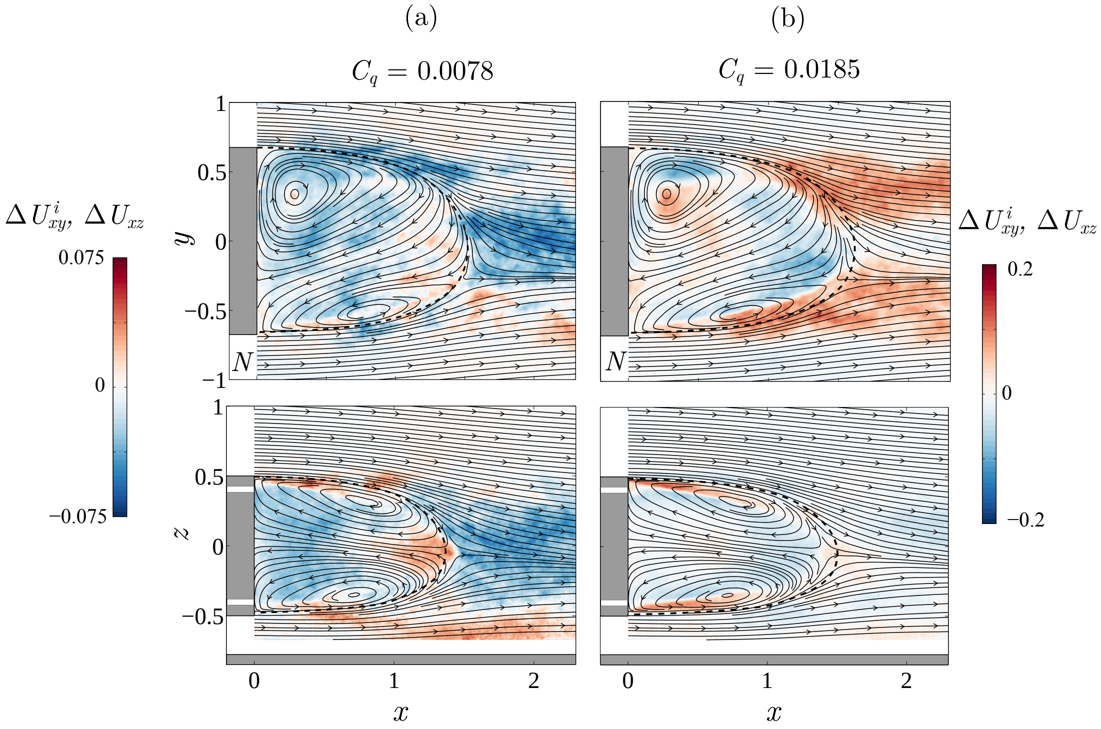

Figure 5.18: Blowing in TB configuration. Mean momentum modification superimposed to the mean streamlines for (a) $C_q = C_q$opt and (b) maximum injection $C_q = 0.0185$. (a,top): $\Delta U^i_{xy} = U^i_{xy} - U^i_{xy0}$, (b,bottom): $\Delta U_{xz} = U_{xz} - U_{xz0}$, $i = P$ or N denotes the state. The dashed curve represents the separatrix of the recirculating bubble with no injection.

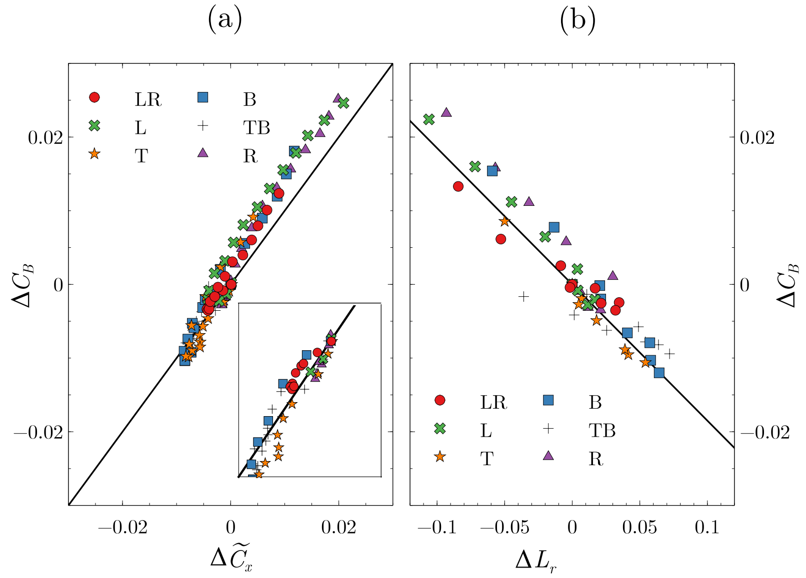

Figure 5.19: Base drag coefficient vs. drag coefficient (a) and recirculating bubble length (b). The subscript 0 denotes values obtain with $C_q = 0$. In (a), continuous line: $\Delta C_B = \Delta\tilde{C}_x$, inlet: close-up view of the plot showing data in mass regime only. In (b), continuous line: $\Delta C_B - = -0.185\Delta L_r$.

satisfactorily achieved for the mass regime which concerns all the data points from zero to the optimal values of lower drag (Fig. 5.19a, inlet). A significant curvature is observed when the blowing is further increased above the optimal values (momentum regime) leading to drag increase. This effect is likely to be due to the non linear interaction of the blowing jet with the flow at the base that cannot be assessed in the simple expression of thrust and slit head loss removals as used in Eq. (5.6). The plot also points out the good accuracy of the base drag estimation using the four pressure taps.

The bubble recirculating length is correlated to the base drag as can be seen in Fig. 5.19(b). The larger the bubble the smaller the base drag and vice-versa. It also indicates that increasing blowing in the mass regime (resp. momentum regime) increases (resp. decreases) the recirculating lenght. This relationship is illustrated by the results shown in both Fig. 5.17 and Fig. 5.18 displaying the shape of the recirculating bubble for lowest (a) and highest (b) base drag of two blowing configurations. The relation between separation length and base drag is a classical result for blunt-based bluff bodies, either two-dimensional (Bearman, 1967), axisymetric (Mariotti et al., 2015) or three-dimensional (Grandemange et al., 2013a). The small variations compared to the no blowing value produce the affine relationship as observed in Fig. 5.19(b):

$$C_B = C_{B0} - 0.185(L_r - L_{r0}) \tag{5.7}$$

5.4 Discussion

5.4.1 Wake modes sensitivity to local blowing

The sensitivity of the static mode to the local base blowing is summarized in Fig. 5.12 for all the asymmetric configurations of blowing and Fig. 5.15 for all the symmetric ones. The static mode strength is weaken by the blowing during the mass regime (empty symbols) with a maximum reduction of 10% to 20% depending on the configuration. Figure 5.20(a,b) shows the correlation of the base drag variation with the base pressure gradient modulus. Whatever the configuration, there is a well defined correlation in the mass regime as shown in Fig. 5.20(a) indicating that base drag reduction is associated with permanent asymmetry reduction. In the momentum regime, the plot in Fig. 5.20(b) is more scattered with different configurations indicating no straightforward relationship between asymmetry and drag.

Static mode orientation, given by the orientation of the base pressure gradient of the state, is found to be sensitive to local blowing. For all asymmetric configurations in the momentum regime, blowing is able to impose the mode orientation as can be seen in Fig. 5.12. While L or R configuration corresponds to state selection, the T and B configurations forces a non trivial rotation of the static mode. Similar static mode rotation was observed by introducing steady disturbances breaking the top/bottom symmetry of the rectangular base either obtained by small obstructions (Barros et al., 2017) or by pitching the body (Bonnavion and Cadot, 2018). The orientation sensitivity of the static mode has a large impact on the aerodynamic force as shown in Fig. 5.20. In Bonnavion and Cadot (2018) the lateral force produced by the P and N state is shown to be $C_i = \pm 0.02$ ($i = y, z$ denotes the direction of the instability). Thus for $C_q = 1.5C_q^{\text{opt}}$ in Fig. 5.20(c), the lateral force is mostly produced by the strength of the re-orientated static mode rather than by the jet itself.

As characterized in Grandemange et al. (2013b), the spatial envelops of the low and high frequency modes are intimately related by the static mode orientation. Since we do not observe any significant changes in the two frequency values independently to the jet intensity and mode orientation in the analysis presented in Fig. 5.16, it is likely that the periodic modes sensitivity is essentially explained by the static mode orientation sensitivity to the blowing.

5.4.2 Base drag reduction model for mass and momentum regimes

Model

We propose a simple mechanism for the base drag variation aiming at understanding the complexity of the Fig. 5.7. The starting point is the well established relationship between the mean bubble recirculation length and base drag for this type of geometry.

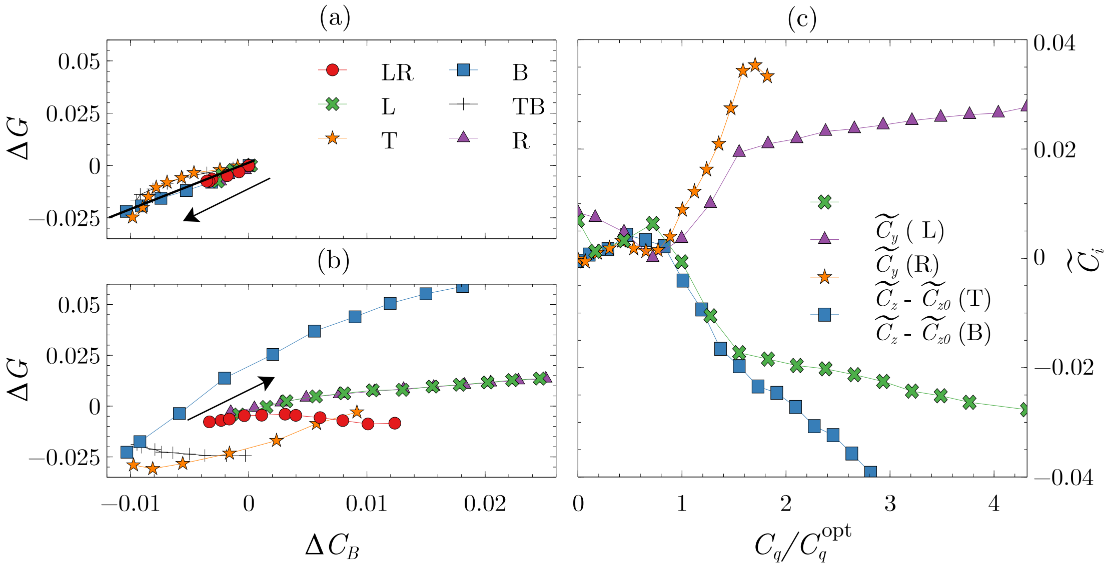

Figure 5.20: Variation of base pressure gradient modulus $\Delta G = G - G_0$ in the mass (a) and momentum (b) regimes vs. base drag variation $\Delta C_B = C_B - C_{B0}$ for all configurations. In (a,b) the arrows indicate the direction of blowing coefficient C_q increase. Lateral force coefficients (c) vs. the reduced blowing coefficient C_q/C_q^{opt} for asymmetric slits configurations.

The correlation is supported by the inviscid cavity models (Wu, 1972) that establish a general behavior of base pressure evolving as power laws ($n > 0$) of the inverse of the cavity length. Physically, the low base pressure is produced by the flow curvature around the cavity. For viscous wake flows at large Reynolds number, this trend still remains with the recirculating bubble playing the role of the cavity (Roshko, 1993). In our case, the variations of the bubble length reported in Fig. 5.19(b) are small compared to the reference value of 1.45 which linearizes the power law to the approximation (Eq. 5.7). In addition, we will denote with an asterisk *, the new dimensional variables employed in this model.

We follow now the mechanism proposed by Gerrard (1966) for the adjustment of the recirculating bubble length behind a bluff body. It results from the equilibrium of mass fluxes filling and emptying the recirculating region. For the natural case, the growth rate of the free shear layers is associated with velocity entrainment along the shear, feeding the shear layer by emptying the recirculating region. This total flux of mass is denoted by b. The key point is that this flux depends on the free shear length, and thus increases as L_r^* increases and decreases as L_r^* decreases. The intense unsteady activity at the bubble closure such as Kelvin-Helmholtz like instabilities produces rolls-up allowing a feedback flux c^* to fill the recirculating region together with a fluid engulfment with flux a^* in the shed vortices. Momentum of flux c^* is strongly reduced by dissipation. Fluxes a^* and b^* are dominated by the inviscid dynamics of the roll-up. The equilibrium of fluxes is $a^* + b^* = c^*$. In our case, the mixing layer should be considered as turbulent, known to have a constant growth rate (Champagne et al., 1976; Pope, 2000), equivalent to a constant entrainment velocity $V_E^* = V_E U_\infty$ along the shears. The flux entrained by the mixing layers delimiting the whole separated region is estimated to $b^* = V_E^* \ell L_r^*$, where ℓ is the peripheral length of the mixing layers (i.e. $\ell = 2(h+w)$ for our geometry). The equilibrium for the natural case gives $a^* + V_E^* \ell L_{r0}^* = c^*$, where L_{r0}^* is the natural bubble length (i.e. without blowing).

The mass regime is characterized by an external mass flux that feeds the recirculating region but whose momentum is dissipated. Compared to the natural scenario described above, we only need to take into account the additional source of mass $q^* = q_b$ to c^*. The new equilibrium leads to $a^* + V_E^* \ell L_r^* = c^* + q_b$. As momentum of flux q_b is dissipated, we should not expect any significant modifications of the flow, and so for fluxes a^* and c^* from the natural case. Hence the mass budget gives:

$$L_r^* = L_{r0}^* + \frac{q_b}{V_E^* \ell}. \tag{5.8}$$

For this mass regime, the recirculation length increases as the injection flux q_b increases with a slope depending on the mean entrainment velocity of the extended shears length. This can be pictured as the inflation by the base blowing of the recirculating bubble, thus increasing mass flux leaking through the shears, until these two fluxes compensate. The leaking is evidenced with the observation of low momentum sweating in the results (Sect. 5.3.6).

On the other hand, the momentum regime is characterized by a deflating of the recirculating bubble with a reduction of the recirculating length as base blowing is increased (see Sect. 5.3.7). On the contrary to the mass regime, the momentum of the blowing flux must strongly modifies the flow by entirely evacuating the mass flux q_b through the shears together with increasing the shears entrainment velocity. This modification would be responsible for emptying the recirculating region: no mass injection in the recirculating region, $q^* = 0$, and an increase of flux b that would re-adjust the bubble length. To retrieve the observed effect, the flux entrained by the shears must be a combination of disturbed and undisturbed free shear layers, $b^* = (\alpha_1 U_\infty + \alpha_2 U_b) d L_r^*$, and that the contributions of a^* and c^* are constant. We obtain from the mass budget $a + (\alpha_1 U_\infty + \alpha_2 U_b) d L_r^* = c^*$ that:

$$L_r^* = \frac{L_{r1}^*}{1 + \frac{\alpha_2}{\alpha_1}\frac{U_b}{U_\infty}} \approx L_{r1}^*(1 - \frac{\alpha_2}{\alpha_1}\frac{U_b}{U_\infty}), \tag{5.9}$$

Non-dimensional expressions for Eqs. (5.8)-(5.9) are:

$$L_r = L_{r0} + \frac{w}{V_E \ell} C_q, \qquad L_r = L_{r1}(1 - \frac{\alpha_2}{\alpha_1} C_u), \tag{5.10}$$

Mass regime

The values of V_E displayed in table 5.4 are computed from Eq. (5.10) using the correlation

(Eq. 5.7) providing $\frac{\partial C_B}{\partial C_q} = -0.185 L_r$ and the measured slope $\frac{\partial C_B}{\partial C_q}|_0$ in Table 5.3:

$$V_E = -0.185 \frac{w}{\frac{\partial C_B}{\partial C_q}|_0 \ell}, \tag{5.11}$$

Classical measurements in mixing layers (Champagne et al., 1976; Dimotakis, 1991; Pope, 2000) report the parameter S, defined as $S = \frac{U_C^*}{U_S^*}\frac{d\delta}{dx^*}$ where U_C^* is the mean shear velocity, U_S^* the velocity jump and $\frac{d\delta}{dx^*}$ the growth rate of the mixing layer. In our case $U_S^* = U_\infty$ for which a simple mass budget gives $V_E^* dx^* = U_C^* d\delta$, thus $S = V_E$. The range of reported value is from $S \approx 0.06$ to $S \approx 0.11$ for undisturbed mixing layers (Dimotakis, 1991). This wide range is related to high sensitivities to the initial condition of the mixing layer at separation. The values we obtained for V_E in Table 5.4 match satisfactorily this range indicating that the budget mass model is plausible to explain the drag reduction in the mass regime. The assumption that injected momentum does not modify the flow dynamics in the mass regime, implies an independence of the bubble growth with the mass injection location. It is actually almost the case for the L, R and LR configuration for which the V_E values are in the range $0.059-0.075$. It is even better shown by the identical slopes in Fig. 5.9(b) whether injection occurs in the adverse flow region (Fig. 5.9d,top) or reversed flow region (Fig. 5.9d,bottom) of the separated bubble. For these 3 configurations, flow characteristics given in table 5.1 are almost identical. This is not the case for the T and B configurations indicating significant changes in the vertical base pressure gradient component. Hence, one can argue than the free shear properties, and then the V_E values can change from one configuration to the other due to an influence of the slit on the initial condition of the free shear layers development.

Momentum regime

The ratio $\frac{\alpha_2}{\alpha_1}$ can also be estimated using again the correlation (Eq. 5.7) in Eq. (5.10) providing

$$C_B - C_{B0} = -0.185(L_{r1} - L_{r0}) + 0.185 L_{r1}\frac{\alpha_2}{\alpha_1} C_u \tag{5.12}$$

and the linear regression obtained in the momentum regime displayed in table 5.3. Values for $\frac{\alpha_2}{\alpha_1}$ are displayed in Table 5.4. The ratio is a measurement of the efficiency of the activated shears by the momentum injection to evacuate mass from the recirculating region. We can see in Table 5.4 a wide variation of the ratio, and the basic expectation of having twice the value of the single slit configurations for the double slits configurations is not all respected.

The smallest value is obtained for the L or R blowing, for which the corresponding forced flow is shown in Fig. 5.8(c). The largest ratio is obtained in either the T or B configurations, for which the forced flow is shown in Fig. 5.11(c). For all of these single slit configurations, the jet is blowing in an adverse flow region of the static mode, at the outer edge of the steady vortex. The main difference between the vertical and horizontal

Configuration	L	R	T	B	LR	TB
V_E	0.075	0.074	0.055	0.036	0.059	0.039
$\frac{\alpha_2}{\alpha_1}$	0.127	0.127	0.235	0.237	0.174	0.180

Table 5.4: Parameters (see text) of the mass budget model for the mass (Eq. 5.8) and momentum (Eq. 5.9) regimes for all blowing configurations.

blowing is that the global rotation of the static mode has inverted the base aspect ratio of the recirculating region. It is likely that the difference in the wake base aspect ratio is the cause for the discrepancies in the shear ratio values $\frac{\alpha_2}{\alpha_1}$.

Intermediate values are found for the symmetric configurations for which bistability persists, and where the static mode still remains orientated in the horizontal direction (Fig. 5.14a). For the case of the TB configuration, the blowing are never located at the outer edge of the steady vortex as for the single T injection (Fig. 5.11c), but in the highly fluctuating shears as shown in Fig. 5.14(c), likely to be much less efficient to evacuate mass from the recirculation region. For the LR configuration (Fig. 5.13c), there is one blowing slit located at the outer edge of the steady vortex as for the single L or R injection (Fig. 5.8c), while the other slit blows in the reversed flow region at the proximity of a highly fluctuating shear. This permanent asymmetry plausibly explains why the value of $\frac{\alpha_2}{\alpha_1}$ for the LR configuration is lower than twice that of the L or R configuration.

5.4.3 Critical blowing of the transition

The transition defined by the minimum base drag value is triggered when the momentum coefficient C_u is large enough to modify the wake properties. In Fig. 5.7(b) the transitions always occur for much smaller C_u for LR and TB configurations than for L, R, T or B configurations. It is then unlikely that the critical blowing could be determined by a critical momentum coefficient C_u. By looking at the transition in mass coefficient in Fig. 5.7(a), the transition value for the TB configuration $C_q^{\text{opt}} = 7.8 \times 10^{-3}$ is comprised within the two transition values $C_q^{\text{opt}} = 10.2 \times 10^{-3}$ of the T configuration and $C_q^{\text{opt}} = 6.6 \times 10^{-3}$ of the B configuration and matches approximately the average value. For LR configuration, the flow is always bistable, which means than during the random switching dynamics between the P and N state, one slit is permanently injecting in the adverse flow region while the other is permanently injecting in the reversed flow region (see Fig. 5.13). For consistency with the T, B and TB configurations discussed above, we would expect that the LR transition value should match the average of the transition values for a single injection in the reversed flow region and a single injection in the adverse flow region. These two transition values are given for the wake either locked in a P state or a N state with a single slit injection. It is exactly the case studied in Fig. 5.9 in the R blowing configuration. The transition for the N state occurs at $C_q^{\text{opt}} = 4.3 \times 10^{-3}$ while for the P state $C_q^{\text{opt}} > 7 \times 10^{-3}$. The transition value $C_q^{\mathrm{opt}} = 5.5 \times 10^{-3}$ of the LR configuration is then also comprised within the two single cases and approximately corresponds to their average. This consistency between the configurations shows that the transition between the mass and the momentum regime is governed by the injected mass flow rate and the location of the injection but not to the local momentum of the blowing jet. It seems contradictory to results of Wood (1964) and may emphasize differences whether the injection is localized in the middle of the base (Wood, 1964) or at the proximity of the shears (the present study).

Finally, to extend the mass regime and then to increase the base drag reduction it is favourable to inject in a reversed flow region of the recirculating bubble (see Figs. 5.9 and 5.10). It is likely that the injected jet momentum dissipation is enhanced in this case.

5.5 Conclusions

There are two very distinctive sensitivities of three-dimensional wake modes to local base blowing whether blowing is in the mass or momentum regime. The mass regime shows almost no dependency on the injection location and is characterized by a reduction of the static mode strength accompanied with the recirculating bubble inflating producing the drag reduction. The regime transitions to the momentum regime for a critical mass flow rate depending on the injection location. The momentum regime is characterized by interaction with the static mode, either selecting a pre-existing state or forcing a rotation of the static mode orientation. The periodic modes shapes are found to simply follow the modification of the static mode orientation. These strong modifications lead to non trivial base drag variation with blowing location and intensity. There is no straightforward correlation with the static mode strength, but globally, the regime is associated with a recirculating bubble deflating associated with drag increase. The experimental results are used to build a mass budget model of the recirculating region taking into account shear modification for the momentum regime. This Chapter offers an experimental data basis with comprehensive interaction of base blowing with the three-dimensional wake and its main modes. It could be used in the future for flow control in the presence of a static wake mode.

CHAPTER
SIX

Effect of the base blowing density

Abstract

Base bleed is an efficient mechanism used to stabilize the wake behind bluff bodies. Thus, in the present Chapter, the effect of injecting a stream of gas through a horizontal slit placed near the bottom trailing edge of an Ahmed-like body has been explored experimentally at $Re = 6.4 \times 10^4$. In particular, two different gases, i.e. air and helium, have been used to vary the density of the bleed fluid with respect to that of the free-stream. This mechanism has been shown to increase the base pressure, decreasing the mean drag coefficient, C_x, with the bleed coefficient, defined as $C_\rho = \sqrt{\frac{\rho_b}{\rho}} \frac{U_b}{U_\infty}$. The study also reveals that injecting a light fluid is more effective than blowing with a fluid of the same density as the free-stream, or even with a heavier fluid. In fact, reductions of the mean base drag coefficient, C_B, which is a measure of the base pressure, and the drag coefficient, C_x, larger than 10% and 4% respectively are achieved when helium is used as bleed fluid while reductions of 6% and 2% respectively are obtained if air is injected. The beneficial effect of base bleed is related to the increase of the length of the recirculating bubble that forms at the base of the body, providing $C_B = C_{B0} - \alpha(L_r - L_{r0})$ where $\alpha = 0.18$, L_r is the length of the recirculating bubble, and $C_{B0} = 0.181$ and $L_{r0} = 1.45$ are the mean base drag coefficient and the recirculating length corresponding to $C_\rho = 0$. Furthermore, when helium is injected the recirculation region is elongated longer than when air is supplied, a result that is associated to the greater reduction in C_B and C_x reported.

This Chapter is comprised, in part, in the paper: "On the role of base blowing density on the drag reduction of three-dimensional blunt bodies", by Lorite-Díez, M., Jiménez-González, J. I., Pastur, L., Cadot, O. & Martínez-Bazán, C., submitted to Physical Review Fluids (Lorite-Díez et al., 2019b)

6.1 Introduction

Improving the aerodynamic performance of road vehicles is paramount in terms of reducing transport industry fuel consumption and the associated green-house gases emissions. In particular, aerodynamic loads are responsible for more than 70% of non-engine-related energy expenses on heavy vehicles (Bonnavion, 2018) and its importance increases with the vehicle velocity. Heavy vehicles bluffness provokes a massive flow separation on their rear end, inducing a low pressure recirculating region, surrounded by convectively unstable free shear layers that produce self-sustained large scale oscillations and conform a wide and unstable turbulent wake. Such wake represent more than 25% of the heavy vehicle total aerodynamic load (Wood and Bauer, 2003). Due to its aforementioned key importance, numerous scientific studies have been developed to understand, describe and characterize the main wake flow features (Ahmed et al., 1984; Krajnović and Davidson, 2003; Choi et al., 2008; Grandemange et al., 2013b). In these studies, several simplified models are analyzed to understand the fundamental phenomena related to aerodynamic drag production and different devices have been designed to reduce it. All devices or techniques proposed to modify the wake that develops behind bluff bodies and, therefore, their associated drag, are based on several physical mechanisms such, the reduction of wake entrainment, the damping of strong force fluctuations induced by the periodic shedding of coherent turbulent structures, the displacement of the low pressure region away from the body base by means of elongating the recirculating bubble or the reduction of wake bluffness by modifying the trailing edge body geometry, among others (see Barros et al. (2016b)).

Amidst the proposed techniques, Wood (1964) and Bearman (1967) showed that the base pressure could be increased injecting an additional air flow rate through the base of bodies with blunt trailing edges, for certain blowing flow rates, thus reducing the aerodynamic drag. They both found a common physical mechanism that could explain the improved aerodynamic performance by increasing the length of the recirculating region formed behind the body. Furthermore, Bearman (1967) found a direct correlation between the base pressure recovery and the increase of the vortex formation length, following the same behavior as that taking place when a splitter plate is added behind the body. In the case of axisymmetric bodies, Sevilla and Martínez-Bazán (2004) and Bohórquez et al. (2011) analyzed the effect of blowing through the whole body base with the aim of inhibiting the near wake fluctuations in laminar regimes. However, few studies have been devoted to explain and analyze the effect of perimetric steady blowing in a fully three-dimensional turbulent wake and the physical mechanisms that will drive the eventual improved aerodynamic performance.

In this regard, Lorite-Díez et al. (2019c) showed that injecting a steady stream of gas through a perimetric slit of an Ahmed-like blunt body was efficient in terms of base pressure recovery and drag reduction. They also showed that, depending on the perimetric blowing configuration, base pressure and wake topology were differently affected. Among the different options, injecting air close to the bottom trailing edge was found to be the most efficient configuration in terms of drag reduction and gas flow rate to inject, quantified by the base bleed parameter $C_q = q_b/(U_\infty A_b)$, where q_b is the flow rate of gas, U_∞ is the free-stream velocity and A_b is the body base area. In the aforementioned work, two different flow regimes were reported depending on blowing flow rate. For values of the base bleed lower than the optimal one, $C_q < C_q^{\mathrm{opt}}$, being C_q^{opt} the blowing rate that produces the largest drag reduction, base pressure increases with C_q, decreasing the drag coefficient and increasing the length of the recirculation region formed behind the body. This regime was denoted the mass regime. However, for $C_q > C_q^{\mathrm{opt}}$, base bleed decreases the base pressure what increases the drag coefficient, denoting this regime the momentum regime.

In some occasions, steady blowing is not the most appropriate mechanism in terms of energetic efficiency compared to other active control techniques. Thus, to employ this type of system in real applications, some alternative solutions have been proposed to obtain the additional air flow rate needed, without any energetic cost, such passive ventilation (Suryanarayana et al., 1993) or employing the combustion gases. Sevilla and Martínez-Bazán (2006) studied the near wake topology changes on the recirculating region induced by injected a stream of gas of density different from that of the ambient through the whole base of an axisymmetric body. They performed a linear stability analysis at laminar regimes, concluding that injecting gas of density lower than the ambient fluid had a stabilizing effect on the body wake although larger bleed coefficients are required to remove the recirculating region than in the case of injecting a gas of the same density. In addition, Sevilla and Martínez-Bazán (2006) also observed that the recirculating velocities inside the recirculating bubble were larger when light fluid was injected what contributed to increase the base pressure and, consequently, decrease the drag coefficient. In the present Chapter, the preliminary results from Sevilla and Martínez-Bazán (2004) are experimentally tested by injecting a flow rate of gas through the bottom slit of an Ahmed-like body, using air and helium as bleed gases to analyze the effect of the gas density on the drag reduction efficiency.

Thus, the Chapter is organized as follows: the experimental set-up and measurement details are described in Sect. 6.2. Next, Sect. 6.3 is devoted to analyse the experimental results, comparing the performance of both blowing gases, focusing on near wake topology (Sect. 6.3.1), pressure and forces distribution on the blunt body (Sect. 6.3.2) and recirculation region main features (Sect. 6.3.2). Finally, the main conclusions are drawn in Sect. 6.4.

6.2 Experimental method

6.2.1 Set-up description

An Ahmed-like body of length $l = 291$ mm, width $w = 97.25$ mm and height $h = 72$ mm, whose geometry corresponds to a square-back version of the model used by Ahmed et al. (1984) was placed on a ground plate inside the test section of a wind tunnel to characterize its turbulent wake (see Fig. 6.1a). The body was held using four cylindrical supports of 7.5 mm diameter, i.e. $0.104h$, connected to electronic rotation and elevation platforms to be able to modify the orientation of the body and the distance to the ground with

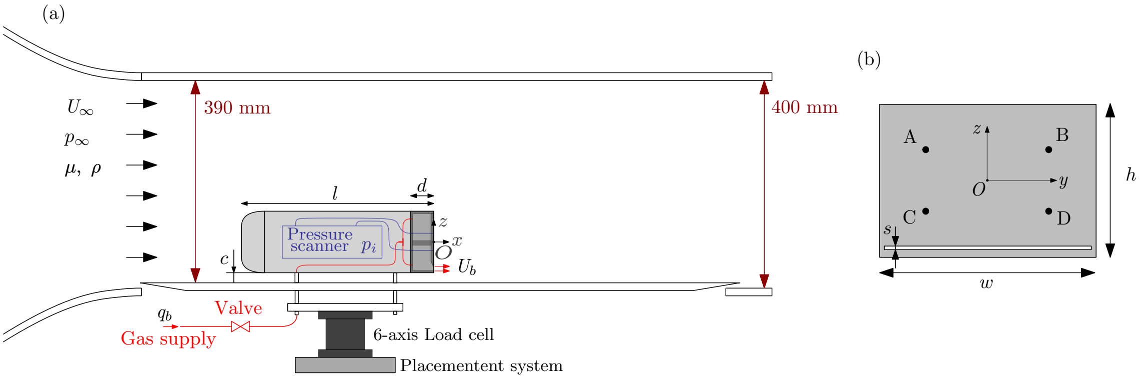

Figure 6.1: (a) Sketch of the experimental set-up, including the wind tunnel and the body geometry. (b) Rear view of the bluff body depicting the pressure tap positions and the slit configuration.

an accuracy of 0.01° and 1μm, respectively. In particular, ground clearance was fixed at $c/h = 0.278$. The blowing device and gas injection system used in Lorite-Díez et al. (2019c) was employed to inject a gas stream through an open slot along the width of the body located at the bottom of the body base (see Fig. 6.1b). An uniform stream of velocity U_∞, density ρ and viscosity μ was provided by an Eiffel-type wind tunnel over a 390 mm × 390 mm test section (see Fig. 6.1a). In the present Chapter, the wind tunnel velocity was fixed at 13.3 m/s, with a turbulent intensity below 0.5% and a velocity homogeneity over the test section better than 0.3% (more details can be found in Grandemange et al. (2013b)). Thus, the Reynolds number based on body height h was $\mathrm{Re} = \rho U_\infty h/\mu \approx 6.4 \times 10^4$. In order to test the effect of the density of the blowing gas on the wake properties, two different gases were used, i.e. air and He, being the air-to-helium density ratio $\rho_{\mathrm{He}}/\rho_{\mathrm{Air}} = 0.14$. Air and He were injected through a narrow horizontal slit located at the bottom of the body base, connecting the gas supply to the body base with a pneumatic tube which included digital mass flow meters adapted for each gas, precision valves and a pressure regulator to ensure a stable, constant flow rate of blowing gas, q_b. In the case of He, 3 bottles of ALPHAGAZ 2 L50, with an He purity greater than 99.99%, were employed during present experiments. In this case, since the density of the bleed fluid may be different from that of the ambient, the bleed coefficient is defined as,

$$C_\rho = \sqrt{\frac{\rho_b}{\rho}}\frac{U_b}{U_\infty}, \tag{6.1}$$

where ρ_b is the injected gas density and U_b the blowing velocity, obtained dividing blowing flow rate, q_b, by the bottom slit area, S_b. C_ρ is a quantification of the momentum injected in the wake by the blowing jet. Given our experimental set-up, the blowing system was able to supply a maximum bleed coefficient of 0.4 for helium and 1.1 for air, indicating that in some cases the velocity of the bleed fluid could be slightly greater than that of the ambient. The origin of the cartesian coordinate system (x, y, z) was placed at the center of the body base, being x the streamwise direction, z the transverse direction normal to the ground, and y the side direction that forms a direct trihedral. The velocity vector can be therefore decomposed into respective components $\mathbf{u} = (u_x, u_y, u_z)$.

6.2.2 Measurements details

Pressure values were measured at four different locations $(y, z) = (\pm 0.3h, \pm 0.2h)$ (indicated as A, B, C and D in Fig. 6.1b). A Scanivalve ZOC22 pressure scanner was placed inside the model, reducing the length of vinyl tubes required to connect the 4 pressure taps to the pressure sensor. The values of the local pressure at the base was recorded at a sampling rate of 100 Hz per channel during 60 s for typical experiments. In the following, pressure measurements will be expressed by the instantaneous, local pressure coefficient

$$c_p(y, z, t) = \frac{p(y, z, t) - p_\infty}{\rho U_\infty^2/2}, \tag{6.2}$$

where p_∞ is the reference static pressure at the inlet of the test section. The uncertainty of pressure coefficient, c_p, was always below ±0.002. These four measurements were used to determine the instantaneously base drag coefficient to evaluate the base pressure recovery (Apelt and West, 1975; Roshko, 1993),

$$c_B(t) = -\frac{1}{4}\Sigma_{i=1}^{4} c_p(y_i, z_i, t). \tag{6.3}$$

Additionally, near wake velocity fields in the two perpendicular planes $y = 0$ and $z = 0$ were experimentally measured using Particle Image Velocimetry (PIV) to obtain $\mathbf{u_{xz}} = (u_x, 0, u_z)$ and $\mathbf{u_{xy}} = (u_x, u_y, 0)$ respectively. The PIV system used a dual pulse laser (Nd:YAG, 2 x 135mJ, 4ns) synchronized with a FlowSense EO, 4 Mpx, CCD camera. For typical measurements, 500 pairs of images taken at 10 Hz were acquired. Velocities were computed from an interrogation window of 16 × 16 pixels with an overlap of 50%, resulting into a spatial resolution of approximately 1% of the body's height.

The aerodynamic force exerted on the body was measured with a multi-axial load cell (model AMTI-MC3A-100lb) connected to the four cylindrical supports (see Fig. 6.1). Time series of the drag, side and lift components, i.e. f_x, f_y and f_z respectively, were recorded during 30s at a sampling rate of 1kHz. The uncertainty of the measurements was estimated (using specifications of crosstalk, non-linearity and hysteresis) to be 0.002 N for the x and y directions and 0.006 N for the z direction, due to its bigger range. The drag, side and lift coefficients were thus defined as

$$c_i(t) = \frac{f_i(t)}{hw\rho U_\infty^2/2}, \tag{6.4}$$

with a corresponding maximum uncertainty of 0.001 for $(c_x,\ c_y)$ and 0.003 for c_z. In Eq. (6.4), the thrust and slit head loss produced by the blowing system, was compensated to account only for the forces that the external flow exerted on the body.

In the following, h, U_∞, $0.5\rho U_\infty^2$ and h/U_∞ will be used as characteristic length, velocity, pressure, and time scales respectively, being all the variables reported herein dimensionless. Also, time-dependent variables will be denoted by lower case characters a, time-averaged values by upper case characters $A = \overline{a}$ and standard deviations by $A' = \sqrt{\overline{(a-A)^2}}$.

6.3 Results

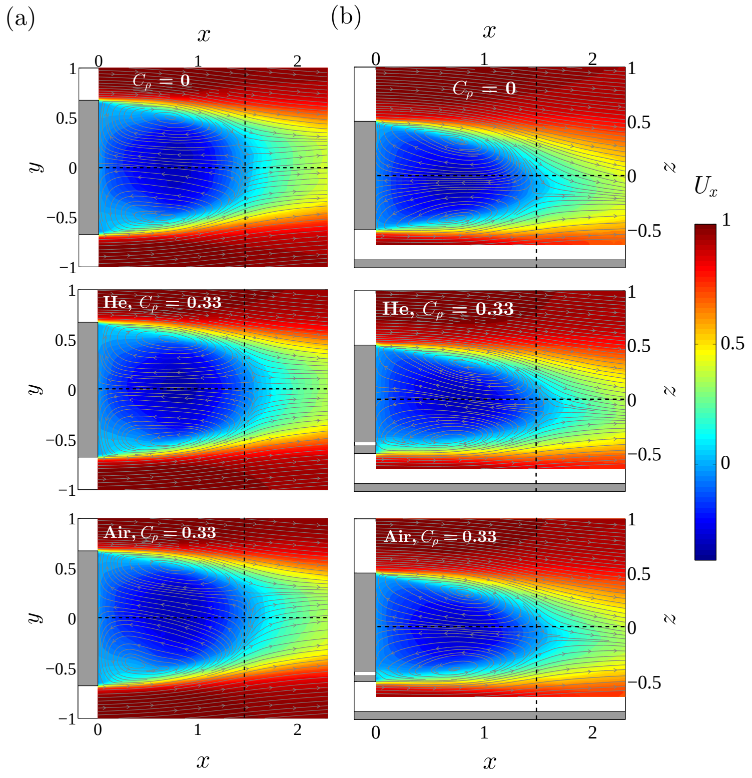

Figure 6.2: Wake topology modifications induced by injecting gas through a slit placed horizontally at the bottom of the body base for both tested gases at the two measured PIV planes. (a) Averaged streamwise velocity, U_x, contours together with averaged flow streamlines at $z = 0$ plane. (b) Averaged streamwise velocity, U_x, contours along with averaged flow streamlines at $y = 0$ plane. Horizontal dashed lines indicate symmetry planes and vertical dashed lines the L_{r0}. White slots in Fig. 6.2(b) indicate the blowing slit in the vertical plane.

6.3.1 Flow topology

We will first describe the wake topology obtained at the planes $y = 0$ and $z = 0$ without base bleed, $C_\rho = 0$, and for $C_\rho = 0.33$, in both cases, injecting air and helium. Figure 6.2 shows the averaged streamwise velocity, U_x, contours, along with the flow streamlines in the $z = 0$ and $y = 0$ planes for $C_\rho = 0$ and for $C_\rho = 0.33$. In the $z = 0$ plane, as displayed in Fig. 6.2(a), the flow field seems to be nearly symmetric, but is characterized a bistable behavior for $C_\rho = 0$ in the horizontal axis, as described by Grandemange et al. (2013b). Such dynamics consists of a random switching of the lowest pressure location between two mirror positions with respect to $y = 0$, which are respectively associated to positive (P state) or negative (N state) values of the horizontal pressure gradients, and stem from the destabilization of static symmetry-breaking modes at laminar regimes (Grandemange et al., 2012a). Although the wake remains symmetric in the $z = 0$ plane when helium is injected with a bleed coefficient of $C_\rho = 0.33$, it becomes slightly asymmetric when air is injected, showing a preferred P state, which indicates that the lowest pressure location stays more often in the $y < 0$ half. Furthermore, in the case without base bleed, the wake exhibits an important recirculation region of length $L_{r0} = 1.45 \pm 0.01$, determined by the maximum streamwise position where $U_x \leq 0$. Similar recirculation lengths were found for the same body at $\mathrm{Re} = 10^5$ by Lorite-Díez et al. (2019c) and for a different aspect ratio, squareback blunt body at $\mathrm{Re} = 3 \times 10^5$ by Barros et al. (2016b). However, it can be noticed in Fig. 6.2(a) that L_r slightly increases when base bleed is applied, providing values of $L_r^{\mathrm{He}} = 1.57$ and $L_r^{\mathrm{Air}} = 1.54$ when helium or air are respectively injected.

Similar behavior is observed in the vertical plane, at $y = 0$, where it can be seen in Fig. 6.2(b) that the recirculating length also increases slightly when base bleed is used. It should be noted that for the three cases, the wake is deflected downwards due to the ground effect (see Fig. 6.2b). This vertical deflection remains when base bleed is applied and barely no changes have been observed for the values of C_ρ shown in Fig. 6.2, indicating that the selected base bleed, $C_\rho = 0.33$, falls within the so-called mass regime (Lorite-Díez et al., 2019c).

Taking into account the near wake flow topology reported above, no significant wake modifications have been found when both, helium and air, are injected. The most relevant characteristic is the increase observed to some extent in the recirculation length when base bleed is applied.

6.3.2 Effect of gas injection density on wake global variables

After having described the near wake structure, we will next analyze the effect of base bleed on some global parameters, paying attention to the influence of gas density by comparing the results obtained using air and helium as blowing gases. Let us begin with the averaged base pressure, characterized by the mean base drag coefficient defined in Eq. (6.3), C_B, and its evolution with the bleed coefficient, C_ρ. Figure 6.3(a) shows that the mean base drag coefficient decreases with C_ρ, indicating that the base pressure increases, until it reaches a minimum value at C_ρ^{opt}, which represents the transition between the mass and the momentum regimes. For $C_\rho > C_\rho^{\mathrm{opt}}$ the mean base drag coefficient starts to increase with C_ρ. Interestingly, the optimal bleed coefficient obtained when helium is injected is slightly lower than that found for air, being $C_\rho^{\mathrm{opt}}|_{\mathrm{He}} = 0.33$ for He and $C_\rho^{\mathrm{opt}}|_{\mathrm{Air}} = 0.36$

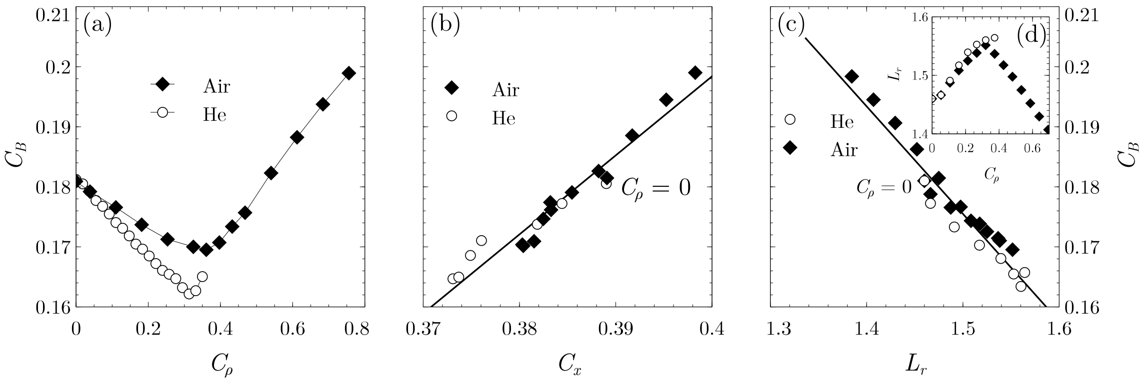

Figure 6.3: (a) Evolution of the mean base drag coefficient, C_B, with the bleed coefficient, C_ρ. (b) Correlation between aerodynamic drag, C_x, and mean base drag, C_B, coefficients. (c) Base drag coefficient, C_B, versus the recirculation region length, L_r. Figure 6.3(d) shows an inset of the evolution of the recirculating length with C_ρ highlighting the non-monotonic behavior observed when air is injected.

for air. Figure. 6.3(a) also shows that injecting a light gas is more efficient than injecting a gas of the same density as the ambient. In fact, it can be noticed that the mean base drag coefficient decreases faster when helium is blown through the bottom slit, achieving a lower minimum mean base drag for the optimal base bleed (note that the maximum mean base drag reduction is 6.3% for air and 10.6% for He).

With respect to the averaged drag coefficient measured with a multi-axial load cell, C_x, it is known that base pressure is strongly correlated to aerodynamic forces in blunt bodies. In particular, for the three-dimensional rectangular blunt-based body at hand, both magnitudes are highly related as reported in Barros et al. (2016a) and Bonnavion and Cadot (2018). Fig. 6.3(b) depicts the evolution of C_B with C_x when air and helium are used as bleed gases, showing a linear dependence in both cases. It can be seen that, injecting a light fluid is more effective in terms of reducing C_x since, as mentioned above, lower values of C_x are also achieved when helium is used instead of air. Thus, C_x decreases with C_ρ when helium is injected, reaching a 4.1% in drag reduction for $C_\rho^{\mathrm{opt}}|_{\mathrm{He}}$.

Finally, we would like to focus on the relation between the mean base drag coefficient, C_B, and the recirculating length, L_r, for the two different gases injected, as displayed in Figs. 6.3(c,d). As already stated by Grandemange et al. (2013a) and Lorite-Díez et al. (2019c), for the present body geometry, an increase in the recirculation region can be associated to a reduction in the mean base drag coefficient. Thus, C_B has been plotted versus L_r in Fig. 6.3(c) when helium and air are injected through the bottom slit. For the tested values of C_ρ, Fig. 6.3(c) shows that a reduction in C_B is associated to an increase of L_r in both cases. In fact, C_B decreases linearly with L_r, independently of the gas density, as $C_B = C_{B0} - \alpha(L_r - L_{r0})$, where $C_{B0} = 0.181$ and $L_{r0} = 1.45$ are the mean base drag coefficient and the recirculating length corresponding to $C_\rho = 0$ respectively and $\alpha = 0.18$. Note that, in the case of air injection, L_r increases and C_B decreases for

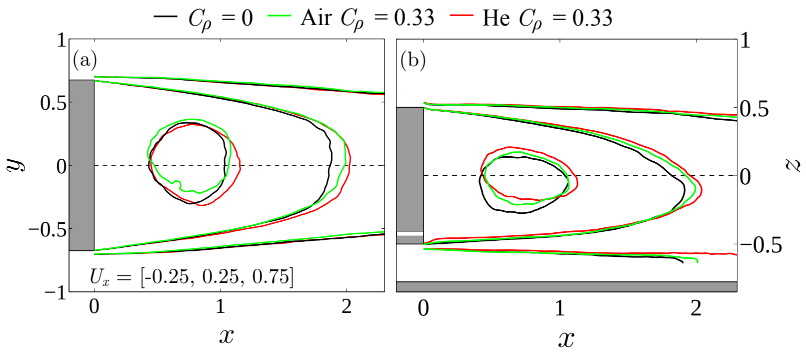

Figure 6.4: Wake topology modifications induced using helium and air as injection gases at $C_\rho = 0.33$. Contours of averaged streamwise velocity for some selected values $U_x = [-0.25, 0.25, 0.75]$ at (a) $z = 0$ and (b) $y = 0$ planes. Dashed line indicate symmetry planes. White slot in Fig. 6.4(b) highlights the blowing slit location.

values of base bleed lower than the optimum one, $C_\rho < C_\rho^{\text{opt}}|_{\text{Air}}$, however L_r decreases for $C_\rho > C_\rho^{\text{opt}}|_{\text{Air}}$ (see Fig. 6.3d), corresponding to the increase of C_B observed in Fig. 6.3(a). Furthermore, when helium is injected the recirculation region is elongated longer than when air is supplied, a result that is associated to the greater reduction in C_B and C_x observed in Figs. 6.3(a,d). Nevertheless, a close analysis of the recirculation region features is provided below to elucidate the beneficial effects in terms of drag reduction of injecting a low density gas.

In order to explain the improved efficiency of adding helium rather than air in terms of base pressure recovery, a detailed analysis of the near wake features has been performed. For example, Fig. 6.4 depicts contours of three streamwise velocities, namely $U_x = [-0.25, 0.25, 0.75]$, for the cases presented in Fig. 6.2. No significant changes are observed in the shear layers that enclose the recirculation bubble, so the observed differences must be related to L_r changes and the different flow dynamics inside the recirculating region. At $z = 0$ plane, the wake characteristics are naturally affected by the presence of static asymmetric modes, however, since the wake is nearly bistable for the studied cases, an almost symmetric wake distribution can be observed (see Fig. 6.4a). Nevertheless, as shown in Figs. 6.3(c, d), bottom base bleed is able to enlarge the recirculation region, an effect corroborated by the more elongated velocity contours obtained when air or helium is injected. In fact, since the density of helium is lower than that of air, the mass and the momentum of the gas injected are also lower, and higher injecting velocities can be achieved before transitioning from the mass to the momentum regime. Thus, for the same bleed coefficient, since the injection velocity is higher when helium is used, the flow rate of gas added to the recirculating bubble is higher, increasing its length and consequently reducing the mean drag coefficient. Figure 6.4(b) shows that, in the vertical $y = 0$ plane, the velocity contours corresponding to the case without base bleed are slightly tilted downwards due to ground effect. However, when bottom base bleed is applied the flow

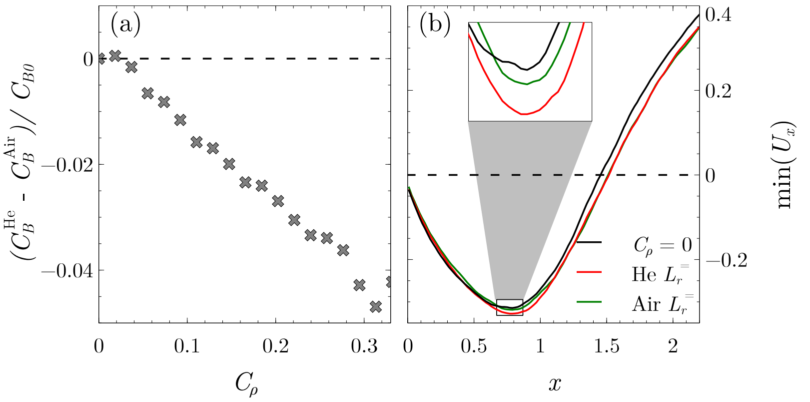

Figure 6.5: (a) Relative difference in the base drag coefficient obtained using helium and air, $(C_B^{\mathrm{He}} - C_B^{\mathrm{Air}})/C_{B0}$, with respect to blowing parameter, C_ρ. (b) Downstream evolution of the maximum averaged recirculating velocity for the case without base bleed (black), a case injecting helium at $C_\rho = 0.17$ (red) and a case injected air at $C_\rho = 0.18$ (green). Here, the lengths of the recirculating regions obtained in the cases injecting air and helium were identical as shown in Fig. 6.5(b). The subscript 0 corresponds to the passive slit configuration, meaning that $C_\rho = 0$ in this case.

becomes more symmetric and, as in the $z = 0$ plane, the contours elongate inferring that the recirculating length increases. Furthermore, Fig. 6.3(c) clearly shows that by adding helium the recirculating region can be lengthened more than injecting air before achieving the minimum value of C_B. Thus, the lowest pressure location inside the recirculating region is also displaced downwards from the body base increasing the base pressure. In fact, Fig. 6.5(a) presents the relative variation of ΔC_B, obtained by subtracting C_B^{Air} to C_B^{He} evolutions from Fig. 6.3(a), showing that the difference between base drag coefficients obtained with helium and air increases with the base bleed.

Sevilla and Martínez-Bazán (2006) indicated that the maximum backflow velocity at the axis of a wake behind a slender body with an axisymmetric blunt trailing edge is increased when a light fluid is injected through the base of the body. Such increase in the recirculating velocity is translated into an increase in pressure near the body base. Having this in mind, Fig. 6.5(b) depicts the averaged streamwise velocity minima distribution over x coordinate for three selected cases: flow without base bleed (black line), base bleed with helium at $C_\rho = 0.17$ (red) and base bleed with air at $C_\rho = 0.18$ (green). The figure shows that the maximum recirculating velocity slightly increases when base bleed is applied, being the increase more prominent when a light fluid (helium) is injected (see the inset in Fig. 6.5b). Thus, it is believed that the overall stabilization of the wake improves when a light fluid is injected due to density effects and, consequently, higher injection velocities can be achieved before transitioning from the mass to the momentum regime. In addition, for the same bleed coefficient, C_ρ, the flow rate of base fluid injected in the recirculating bubble increases as its density decreases, increasing L_r and the magnitude of the recirculating velocities, contributing both effects to the increase the base pressure. To

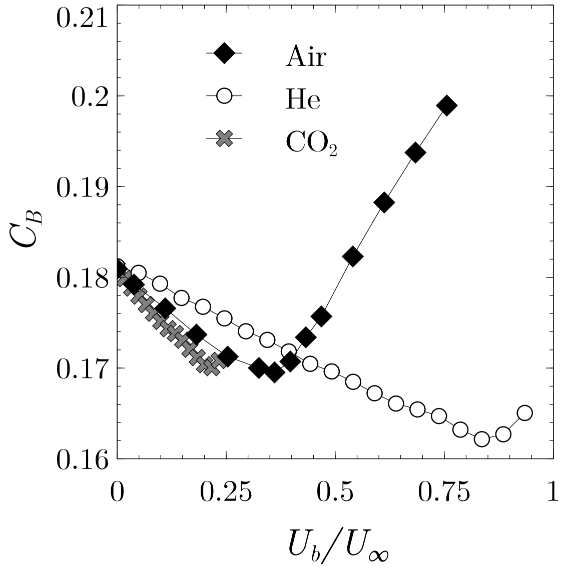

Figure 6.6: Evolution of the mean base drag coefficient, C_B, with the bleed-to-free-stream velocity ratio, U_b/U_∞, using a heavier gas (CO_2) a gas of the same density (air) and a lighter gas (helium).

corroborate this result, additional measurements of C_B where performed using a heavier bleed fluid (CO_2 in this case). It can be noticed in Fig. 6.6 that the minimum value of C_B obtained when CO_2 is injected is slightly larger than that obtained using air. In addition, the velocity ratio at which the transition from the mass to the momentum regimen takes place decreases with the density of the bleed fluid, indicating that the maximum flow rate that can be injecting to obtain beneficial results decreases as the density of the gas increases. Interestingly, for a given value of the bleed-to-free-stream velocity ratio, U_b/U_∞, the mean base drag coefficient decreases as the density of the bleed fluid increases since a larger momentum is injected in the wake of the body.

6.4 Conclusions

The influence of gas injection on the drag reduction of an Ahmed-like blunt body at Re $= 6.4 \times 10^4$ has been analyzed. The gas has been injected through a horizontal slot placed at the bottom of the body base. In particular, two different gases, helium and air, have been used to explore the effect of gas density on the wake structure and the base pressure recovery. The experimental measurements indicate that, when base bleed is applied the base pressure increases and the drag coefficient decreases for values of the bleed coefficient lower than the optimal one, $C_\rho < C_\rho^{\mathrm{opt}}$, corresponding to the known as mass regime. However, for values of the base bleed larger than the optimal one, corresponding to the momentum regime, the base pressure decreases, increasing the drag coefficient. Although this behavior is independent of the gas density, the value of C_ρ^{opt} slightly decreases as density of the bleed fluid decreases, being $C_\rho^{\mathrm{opt}}|_{\mathrm{He}} = 0.33$ for helium and $C_\rho^{\mathrm{opt}}|_{\mathrm{Air}} = 0.36$ for air. Furthermore, the length of the recirculating bubble generated behind the body, L_r, increases with the base bleed, showing the mean base drag coefficient a linear decrease with L_r as $C_B = C_{B0} - \alpha(L_r - L_{r0})$ where $C_{B0} = 0.181$ and $L_{r0} = 1.45$ are the mean base drag coefficient and the recirculating length corresponding to $C_\rho = 0$. Thus, the fact that the recirculating bubble is more elongated when base bleed is applied displaces downstream from the body base the low pressure position, recovering the base pressure. The additional benefits found when a light fluid (helium) is injected are associated to the stabilizing density effects on the wake of the body (Sevilla and Martínez-Bazán, 2006), retarding the value of the velocity ratio U_b/U_∞ at which the transition from the mass to the momentum regime takes place. Thus, a higher flow rate of light fluid can be insufflated inside the recirculating bubble before achieving the corresponding optimal base bleed coefficient, what translates in increasing values of the recirculating length and, consequently, smaller drag coefficients.

This result opens the possibility of using the combustion gases and/or air preheated by the engine as bleed fluids, increasing thus the performance of the vehicle and decreasing gas emissions without including any mechanical or sophisticated active control system.

CHAPTER

SEVEN

Conclusions and future work

7.1 General conclusions

The work presented in this Thesis focuses on the design and analysis of improved control techniques applied to bluff bodies with the aim of reducing the body drag and weakening the wake oscillations. Experimental measurements and numerical simulations have been performed to characterize the main wake flow features and the modifications induced after implementing the control strategies. In particular, base cavities and steady perimetric blowing have been tested for two-dimensional and three-dimensional bluff bodies at high Reynolds numbers. In the following, we summarize the main conclusions and ideas developed and described in Chapters 2-6.

Chapter 2 evaluates the possibility of improving the efficiency of base cavities as drag reducing devices when they are implemented on a two-dimensional bluff body at $Re = 2000$. Given a fixed cavity depth, which is strongly related to its performance, adjoint formulation is used to obtain the drag sensitivity to a localized forcing and, thus, to determine the most receptive positions to actuate. Two types of perturbations have been explored to achieve additional improvement in the aerodynamic performance of the original body, i.e. the introduction of small control cylinders and cavities of optimized geometry.

Sensitivity computations have been carried out following the simplified adjoint-based linear steady analysis developed by Meliga et al. (2014) for unsteady flows. This approach has been proven to properly retrieve the main features related to the most sensitive regions around the bluff body in terms of drag reduction. Chapter 2 shows that the most sensitive region to modify the mean drag is nearby the rear edges of the straight cavity, where localized forcing should be introduced to achieve the largest drag reduction. However, when two control cylinders are placed in symmetric positions of high drag sensitivity, the total drag is barely reduced although important wake stabilization effects, due to modifications on the shedding process, are observed, as detailed in Parezanović and Cadot (2012).

Considering this limited efficiency in terms of drag reduction, a second control strategy, based on cavity shape modification was applied. Thus, after obtaining the drag sensitivity to modifications of the body surface, local deformations were implemented during an iterative process which was guided by unsteady drag sensitivity. After a few iterations, an optimal cavity shape, which provided an asymptotic drag reduction of approximately 23% with respect to that achieved with a straight base cavity, was obtained. The optimized shape consisted of a curved wall, that promotes local recirculation and an inwards deflection of the flow before separating, what leaded to a narrower recirculation bubble and an increase of the base pressure.

To deeply explore the physical mechanisms behind the beneficial effects of the optimized shape which fosters the observed drag reduction, unsteady three-dimensional IDDES numerical simulations at two different Reynolds numbers, i.e. $Re = 2000$ and 20000 respectively were performed. The numerical computations corroborate the results obtained by the drag sensitivity analysis, showing that the drag is monotonically reduced as the cavity walls are conveniently curved. Furthermore, the addition of an optimized cavity significantly reduces the energy of the flow fluctuations and the strength of the vortical structures in the near wake. Consequently, less chaotic and noisy turbulent structures are shed from trailing edges of the body. Furthermore, at $Re = 20000$, the drag reduction achieved is even larger than that obtained at $Re = 2000$, due to the higher adverse pressure gradient before separation and the decrease of the viscous contribution to the drag coefficient, demonstrating that the procedure is robust. Consequently, it has been corroborated that the use of adjoint methods, linked to shape optimization, are efficient tools for improving the existing passive control techniques in terms of drag reduction.

Following the study, in order to extend the range of applicability of the obtained optimized cavity, Chapter 3 is devoted to analyze the flow induced by an impulsive motion of a simplified bluff body from rest, under different values of acceleration and three distinct rear geometrical configurations. The main goal of the study is to assess the performance of the three rear geometries, i.e. a blunt base (Ref), straight (Str) and optimized (Opt) cavities, in transient flow conditions, which are very common in real transport applications and usually not evaluated in classical studies on wake control. Thus, the impulsive motion of the same D-shaped body used in Chapter 2 has been analyzed for four different values of dimensionless acceleration, starting from rest and reaching a permanent regime of $Re = 2000$. First, an experimental characterization of the near wake development has been performed in a towing tank through PIV measurements. Contours of spanwise vorticity have been analyzed to identify the different phases or stages characterizing the transient flow evolution and the variations in the wake features as the the flow evolves. As a result, larger values of the acceleration have been proven to foster the transition between the different phases observed. In fact, higher accelerations are found to generate stronger suction of the primary eddies, which push them closer to the body base and increase their residence time. Regarding the base geometry, the use of cavities has been shown to limit the growth of the primary eddies, due to the influence of the hollow size, which contributes to speed-up the transitions between phases. As far as the optimized, curved cavity is concerned, it has been shown to have a significant impact on the near wake features when compared to the remaining geometries. In summary, the optimized configuration leads to a shortening of both the recirculation length and the formation length, while producing a shorter transition between phases along with a more regularized, less chaotic alternate shedding. Next, we have performed direct numerical simulations, that have allowed to extend the previous results to longer temporal horizons. A subsequent analysis of drag coefficient has allowed to relate near wake dynamics and forces values, corroborating the previous hypothesis on the potential positive effect of the use of optimized cavity. In general, the aforementioned smoother and faster transition gives rise to a general smaller averaged value of drag together with less energetic instantaneous fluctuations of the drag coefficient, C_x, regardless the acceleration value. Finally, a quantification of such potential drag reduction and shortening of the transient regime has been computed by means of the variable, s_p, which represents the traveled distance until the flow reaches the permanent regime. Thus, the value of s_p corresponding the optimized cavity is one fourth of that from the body without cavity, and always considerably lower than that associated to the classical straight cavity. In summary, the optimized cavity configuration has demonstrated to be an appealing and efficient passive device which shows a great potential to reduce both the mean drag coefficient and the instantaneous drag oscillations in impulsively flow regimes.

Continuing with the application of the optimized cavity in more realistic flow conditions, Chapter 4 analyzes its performance as a passive control device at the base of a square-back Ahmed body at $Re = 1 \times 10^5$, under several cross-wind conditions, by means of pressure, force and velocity measurements. So, the optimal shape obtained in Chapter 2 has been adapted to the three-dimensional geometry of an Ahmed body. A comparative study has been performed considering the reference square-back body (without any passive control device), and bodies implementing the curved cavity and a straight cavity of same depth and thickness ($d/h = 0.3$ and $t/h = 0.05$ respectively, with h being the model's height). Both passive devices have been implemented as add-on parts, thus increasing the reference model's length, as would occur in practical heavy vehicles applications where devices are appended to the base. In general, the optimized device has been shown to be more efficient than the classical straight cavity in terms of wake control and drag reduction. In particular, for a free-stream aligned with the body longitudinal axis, both cavity devices have been shown to efficiently attenuate the asymmetry of the static modes in the horizontal direction. Moreover, the reduced bluffness and length of the near wake induced by the optimal cavity, modifies the structure of the recirculating region, increasing the base pressure. The effect of cross-wind has been also evaluated by modifying the yaw angle. Interestingly, the aerodynamic forces evolutions with the yaw angle show a better performance when the optimized cavity is set, resulting into a more robust drag reduction passive device under cross-wind conditions. All in all, the suitability of simplified two-dimensional adjoint optimization approaches to design efficient flow control strategies has been satisfactorily proven for a three-dimensional turbulent wake implementing a rear curved cavity.

Regarding active control techniques, Chapter 5 explores the three-dimensional wake modes sensitivity to different perimetric blowing configurations. The experimental measurements indicate that, when base bleed is applied the base pressure increases and the drag coefficient decreases for values of the bleed coefficient, C_q, lower than the optimal one, $C_q < C_q^{\mathrm{opt}}$, corresponding to the mass regime. However, for values of the base bleed larger than the optimal one, corresponding to the momentum regime, the base pressure decreases, increasing the drag coefficient. In fact, Chapter 5 highlights two very distinctive sensitivities of three-dimensional wake modes to local base blowing whether blowing is in the mass or momentum regime. The mass regime shows almost no dependency on the injection location and is characterized by a reduction of the static mode strength accompanied with the recirculating bubble inflating producing the drag reduction. The regime transitions to the momentum regime for a critical mass flow rate depend on the injection location. The momentum regime is characterized by interaction with the static mode, either selecting a pre-existing state or forcing a rotation of the static mode orientation. The periodic modes shapes are found to simply follow the modification of the static mode orientation. These strong modifications lead to non trivial base drag variation with blowing location and intensity. There is no straightforward correlation with the static mode strength, but globally, the regime is associated with a recirculating bubble deflating associated with drag increase. The experimental results are used to build a mass budget model of the recirculating region taking into account shear modification for the momentum regime.

Finally, the influence of gas injection on the drag reduction of an Ahmed-like blunt body at $\mathrm{Re} = 6.4 \times 10^4$ has been analyzed in Chapter 6. The gas has been injected with a blowing velocity U_b through a horizontal slit placed at the bottom of the body base. In particular, two different gases, helium and air, have been used to explore the effect of gas density on the wake structure and the base pressure recovery, thus a common blowing parameter has to defined, C_ρ. The experimental measurements indicate that mass and momentum regimes exist independently of the gas density. In this regard, the length of the recirculating bubble generated behind the body, L_r, increases with the base bleed during mass regime, showing the mean base drag coefficient a linear decrease with L_r as $C_B = C_{B0} - \alpha(L_r - L_{r0})$ where $C_{B0} = 0.181$ and $L_{r0} = 1.45$ are the mean base drag coefficient and the recirculating length corresponding to $C_\rho = 0$. Thus, the fact that the recirculating bubble is more elongated when base bleed is applied displaces downstream from the body base the low pressure position, recovering the base pressure. The additional benefits found when a light fluid (helium) is injected are associated to the stabilizing density effects on the wake of the body (Sevilla and Martínez-Bazán, 2006), retarding the value of the velocity ratio U_b/U_∞ at which the transition from the mass to the momentum regime takes place. Thus, a higher flow rate of light fluid can be insufflated inside the recirculating bubble before achieving the corresponding optimal base bleed coefficient, what translates in increasing values of the recirculating length and, consequently, smaller drag coefficients.

7.2 Future work

Along this Thesis some issues have been left open, with the aim at tackling them in the future since they are necessary to complete the picture described throughout this dissertation. In this sense, the use of adjoint methods and shape optimization techniques have been proven to be efficient in terms of drag reduction for several flow configurations and conditions. Moreover, the improved shape of the rear cavity has shown an excellent response reducing the wake oscillations, that is, weakening the periodic (in two-dimensional bodies) and static (for square-back Ahmed body) modes on the wake. Therefore, it seems interesting to test also this procedure to design improved cavities for blunt-based axisymmetric bodies, for which straight cavities have been proven to delay the laminar bifurcations and reduce the drag, although the performance is extremely dependent on the cavity depth, which sometimes is limited by design restrictions. Thus, a shape optimization of these type of cavities should provide with further drag reductions, and would probable have a positive impact on the wake laminar transitions.

Following the same reasoning, a fully three-dimensional shape optimization could be tested, given the actual increased capability of computational resources, to design an optimal passive device which could be directly implemented in three-dimensional simplified vehicle models. Similarly, the blowing slits location and orientation could be also obtained by means of adjoint methods and drag sensitivity procedures.

In addition, the promising results obtained for light base bleed could be extended to other active control approaches as high and low frequency forcing. Such studies may help elucidating if the density plays a role on the boundary layer manipulation that the periodic forcing techniques induce. Similarly, the use of different density gas injection in two-dimensional bodies would be useful to unveil if the recirculation region dynamics and the corresponding base pressure distribution, are strongly affected by the recirculating fluid density. Interestingly, such active blowing may be combined with the use of a rear cavities, with the aim at benefiting from the advantages of both strategies. This novel approach might lead to a better design of efficient control methods of wakes behind different types of bluff bodies.

Finally, although the suitability of rear optimized cavities and perimetric blowing (homogeneous and light) have been satisfactorily proven in terms of drag reduction and wake control for simplified blunt-based bodies, they should be tested in real vehicles and under more realistic conditions. Thus, several tasks should be undertaken in the short future, concerning tests in industrial wind-tunnels with real scale models, and the ulterior application to real vehicles, by means of controlled tests in racing circuits and subsequently, in road tests. Such studies would help to properly measure the actual base pressure recovery and the fuel consumption saving.

Bibliography

P. Abramson, B. Vukasinovic, and A. Glezer. Direct measurements of controlled aerodynamic forces on a wire-suspended axisymmetric body. *Experiments in Fluids*, 50(6): 1711–1725, 2011.

A. Acker. Key transport statistics 2018. Technical report, International Transport Forum, 2018.

S. R. Ahmed, G. Ramm, and G. Faltin. Some salient features of the time-averaged ground vehicle wake. Technical Report 840300, SAE Technical Paper, 1984.

C. J. Apelt and G. S. West. The effects of wake splitter plates on bluff body flow in the range 10^4 to 5×10^4. part 2. *Journal of Fluid Mechanics*, 71(01):145–160, 1975.

D. Barros. *Wake and drag manipulation of a bluff body using fluidic forcing.* PhD thesis, École Nationale Supérieure de Mécanique et d 'Aérotechnique, 2015.

D. Barros, J. Borée, B. R. Noack, and A. Spohn. Resonances in the forced turbulent wake past a 3D blunt body. *Physics of Fluids (1994-present)*, 28(6):065104, 2016a.

D. Barros, J. Borée, B. R. Noack, A. Spohn, and T. Ruiz. Bluff body drag manipulation using pulsed jets and coanda effect. *Journal of Fluid Mechanics*, 805:422–459, 2016b.

D. Barros, J. Borée, O. Cadot, A. Spohn, and B. R. Noack. Forcing symmetry exchanges and flow reversals in turbulent wakes. *Journal of Fluid Mechanics*, 829:R1, 2017.

P. W. Bearman. Investigation of the flow behind a two-dimensional model with a blunt trailing edge and fitted with splitter plates. *Journal of Fluid Mechanics*, 21(2):241–255, 1965.

P. W. Bearman. The effect of base bleed on the flow behind a two-dimensional model with a blunt trailing edge. *The Aeronautical Quarterly*, 18(3):207–224, 1967.

J. F. Beaudoin and J. L. Aider. Drag and lift reduction of a 3D bluff body using flaps. *Experiments in Fluids*, 44(4):491, 2008.

J. F. Beaudoin, O. Cadot, J. L. Aider, and J. E. Wesfreid. Drag reduction of a bluff body using adaptive control methods. *Physics of Fluids (1994-present)*, 18(8):085107, 2006.

F. J. Bello-Millán, T. Makela, L. Parras, C. del Pino, and C. Ferrera. Experimental study on Ahmed's body drag coefficient for different yaw angles. *Journal of Wind Engineering and Industrial Aerodynamics*, 157:140–144, 2016.

E. Berger, D. Scholz, and M. Schumm. Coherent vortex structures in thewake of a sphere and a circular disk at rest and under forced vibrations. *Journal of Fluids and Structures*, 4(3):231–257, 1990.

P. Bohórquez, E. Sanmiguel-Rojas, A. Sevilla, J. I. Jiménez-González, and C. Martínez-Bazán. Stability and dynamics of the laminar wake past a slender blunt-based axisymmetric body. *Journal of Fluid Mechanics*, 676:110–144, 2011.

H. Bolnot, P. Y. Passaggia, T. Leweke, and K. Hourigan. Wake transition of a rolling sphere. *Journal of Visualization*, 14(1):1–2, 2011.

G. Bonnavion. *Dynamics of the unstable wake modes in automotive aerodynamics : from simplified models to real vehicles.* PhD thesis, Université Paris-Saclay, October 2018.

G. Bonnavion and O. Cadot. Unstable wake dynamics of rectangular flat-backed bluff bodies with inclination and ground proximity. *Journal of Fluid Mechanics*, 854:196–232, 2018.

G. Bonnavion, O. Cadot, A. Evrard, V. Herbert, S. Parpais, R. Vigneron, and J. Délery. On multistabilities of real car's wake. *Journal of Wind Engineering and Industrial Aerodynamics*, 164:22–33, 2017.

R. Bouard and M. Coutanceau. The early stage of development of the wake behind an impulsively started cylinder for $40 < Re < 10^4$. *Journal of Fluid Mechanics*, 101: 583–607, 1980.

R. D. Brackston. *Feedback control of three-dimensional bluff body wakes for efficient drag reduction.* PhD thesis, Imperial College London, 2017.

R. D. Brackston, J. M. García de la Cruz, Wynn A., G. Rigas, and J. F. Morrison. Stochastic modelling and feedback control of bistability in a turbulent bluff body wake. *Journal of Fluid Mechanics*, 802:726–749, 2016.

R. Bradley. Technology roadmap for the 21st century truck program. Technical report, US Department of Energy, 2000.

G. W. Burgreen and O. Baysal. Three-dimensional aerodynamic shape optimization using discrete sensitivity analysis. *AIAA Journal*, 34(9):1761–1770, 1996.

Y. Bury and T. Jardin. Transitions to chaos in the wake of an axisymmetric bluff body. *Physics Letters A*, 376(45):3219–3222, 2012.

O Cadot. Stochastic fluid structure interaction of three-dimensional plates facing a uniform flow. *Journal of Fluid Mechanics*, 794:R1, 2016.

O. Cadot, A. Evrard, and L. Pastur. Imperfect supercritical bifurcation in a three-dimensional turbulent wake. *Physical Review E*, 91(6):063005, 2015.

J. Cai and T. L. Chng. On vortex shedding from bluff bodies with base cavities. *Physics of Fluids (1994-present)*, 21(3):034109, 2009.

F. H. Champagne, Y. H. Pao, and I. J. Wygnanski. On the two-dimensional mixing region. *Journal of Fluid Mechanics*, 74(02):209–250, 1976.

C. C. Chang and R. L. Chern. A numerical study of flow around an impulsively started circular cylinder by a deterministic vortex method. *Journal of Fluid Mechanics*, 223: 243–263, 1991.

H. Choi, W. P. Jeon, and J. Kim. Control of flow over a bluff body. *Annual Review of Fluid Mechanics*, 40:113–139, 2008.

H. Choi, J. Lee, and H. Park. Aerodynamics of heavy vehicles. *Annual Review of Fluid Mechanics*, 46:441–468, 2014.

M. Chrust, S. Goujon-Durand, and J. E. Wesfreid. Loss of a fixed plane of symmetry in the wake of a sphere. *Journal of Fluids and Structures*, 41:51–56, 2013.

C. C. Chu and Y. Y. Liao. A quantitative study of the flow around an impulsively started circular cylinde. *Experiments in Fluids*, 13:137–146, 1992.

L. Dalla Longa, O. Evstafyeva, and A. S. Morgans. Simulations of the bi-modal wake past three-dimensional blunt bluff bodies. *Journal of Fluid Mechanics*, 866:791–809, 2019.

R. Dekker, J. Bloemhof, and I. Mallidis. Operations research for green logistics: An overview of aspects, issues, contributions and challenges. *European Journal of Operational Research*, 219(3):671–679, 2012.

P. E. Dimotakis. Turbulent free shear layer mixing and combustion. *High Speed Flight Propulsion Systems*, pages 265–340, 1991.

P. G. Drazin and W. H. Reid. *Hydrodynamic stability.* Cambridge University Press, 2004.

E. G Duell and A. R. George. Experimental study of a ground vehicle body unsteady near wake. *SAE Transactions*, pages 1589–1602, 1999.

A. Evrard, O. Cadot, V. Herbert, D. Ricot, R. Vigneron, and J. Délery. Fluid force and symmetry breaking modes of a 3D bluff body with a base cavity. *Journal of Fluids and Structures*, 61:99–114, 2016.

O. Evstafyeva, A. S. Morgans, and L. Dalla Longa. Simulation and feedback control of the ahmed body flow exhibiting symmetry breaking behaviour. *Journal of Fluid Mechanics*, 817, 2017.

D. Fabre, F. Auguste, and J. Magnaudet. Bifurcations and symmetry breaking in the wake of axisymmetric bodies. *Physics of Fluids (1994-present)*, 20(5):051702, 2008.

J. N. Fernando and D. E. Rival. On vortex evolution in the wake of axisymmetric and non-axisymmetric low-aspect-ratio accelerating plates. *Physics of Fluids (1994-present)*, 28:017102, 2016.

J. N. Fernando, M. Marzanek, C. Bond, and D. E. Rival. On the separation mechanics of accelerating spheres. *Physics of Fluids (1994-present)*, 29:037102, 2017.

F. Finaish. On vortex structures and processes over bluff bodies in impulsive flow. *Experiments in Fluids*, 11:262–267, 1991.

G. Fourrié, L. Keirsbulck, L. Labraga, and P. Gilliéron. Bluff-body drag reduction using a deflector. *Experiments in Fluids*, 50(2):385–395, 2011.

J. Fröhlich and D. von Terzi. Hybrid LES/RANS methods for the simulation of turbulent flows. *Progress in Aerospace Sciences*, 44(5):349–377, 2008.

J. M. García de la Cruz, A. R. Oxlade, and J. F. Morrison. Passive control of base pressure on an axisymmetric blunt body using a perimetric slit. *Physical Review Fluids*, 2(4): 043905, 2017.

L. Gardell. Low drag truck cabs. Technical report, Sacania Division. Saab-Scania, 1980.

J. H. Gerrard. The mechanics of the formation region of vortices behind bluff bodies. *Journal of Fluid Mechanics*, 25(2):401–413, 1966.

B. J. Geurts. Elements of direct and large-eddy simulation. *RT Edwards, Inc.*, 2004.

P. Gilliéron and A. Kourta. Aerodynamic drag reduction by vertical splitter plates. *Experiments in Fluids*, 48(1):1–16, 2010.

M. Grandemange. *Analysis and control of three-dimensional turbulent wakes: from axisymmetric bodies to road vehicles*. PhD thesis, Palaiseau, École polytechnique, 2013.

M. Grandemange, O. Cadot, and M. Gohlke. Reflectional symmetry breaking of the separated flow over three-dimensional bluff bodies. *Physical review E*, 86(3):035302, 2012a.

M. Grandemange, M. Gohlke, V. Parezanović, and O. Cadot. On experimental sensitivity analysis of the turbulent wake from an axisymmetric blunt trailing edge. *Physics of Fluids (1994-present)*, 24(3):035106, 2012b.

M. Grandemange, M. Gohlke, and O. Cadot. Bi-stability in the turbulent wake past parallelepiped bodies with various aspect ratios and wall effects. *Physics of Fluids (1994-present)*, 25(9):095103, 2013a.

M. Grandemange, M. Gohlke, and O. Cadot. Turbulent wake past a three-dimensional blunt body. part 1. global modes and bi-stability. *Journal of Fluid Mechanics*, 722: 51–84, 2013b.

M. Grandemange, O. Cadot, A. Courbois, V. Herbert, D. Ricot, T. Ruiz, and R. Vigneron. A study of wake effects on the drag of ahmed's squareback model at the industrial scale. *Journal of Wind Engineering and Industrial Aerodynamics*, 145:282–291, 2015.

D. Greenblatt and I. J. Wygnanski. The control of flow separation by periodic excitation. *Progress in Aerospace Sciences*, 36(7):487–545, 2000.

E. Guilmineau. Computational study of flow around a simplified car body. *Journal of Wind Engineering and Industrial Aerodynamics*, 96(6-7):1207–1217, 2008.

E. Guilmineau, G. B. Deng, and J. Wackers. Numerical simulation with a DES approach for automotive flows. *Journal of Fluids and Structures*, 27(5):807–816, 2011.

T. Han, D.C. Hammond, and C.J. Sagi. Optimization of bluff body for minimum drag in ground proximity. *AIAA Journal*, 30(4):882–889, 1992.

T. Han, V. Sumantran, C. Harris, T. Kuzmanov, M. Huebler, and T. Zak. Flow-field simulations of three simplified vehicle shapes and comparisons with experimental measurements. Technical Report 960678, SAE Technical Paper, 1996.

T. Han, C. Hill, and S. Jindal. Adjoint method for aerodynamic shape improvement in comparison with surface pressure gradient method. Technical Report 2011-01-0151, SAE Technical Paper, 2011.

M. Hassaan, D. Badlani, and M. Nazarinia. On the effect of boat-tails on a simplified heavy vehicle geometry under crosswinds. *Journal of Wind Engineering and Industrial Aerodynamics*, 183:172–186, 2018.

L. Henning, M. Pastoor, R. King, B. R. Noack, and G. Tadmor. Feedback control applied to the bluff body wake. In *Active Flow Control*, pages 369–390. Springer, 2007.

B. B. Herry, L. Keirsbulck, L. Labraga, and J. B. Paquet. Flow bistability downstream of three-dimensional double backward facing steps at zero-degree sideslip. *Journal of Fluids Engineering*, 133(5):054501, 2011.

J. Howell, A. Sheppard, and A. Blakemore. Aerodynamic drag reduction for a simple bluff body using base bleed. *SAE Transactions*, pages 1085–1091, 2003.

W. H. Hucho. Aerodynamics of road vehicles, society of automotive engineers. *SAE International*, 1998.

W. H. Hucho and G. Sovran. Aerodynamics of road vehicles. *Annual Review of Fluid Mechanics*, 25(1):485–537, 1993.

P. Huerre and P. A. Monkewitz. Local and global instabilities in spatially developing flows. *Annual Review of Fluid Mechanics*, 22(1):473–537, 1990.

Y. A. Irving Brown, S. Windsor, and A.P. Gaylard. The effect of base bleed and rear cavities on the drag of an suv. Technical report, SAE Technical Paper, 2010.

R. I. Issa. Solution of the implicitly discretised fluid flow equations by operator-splitting. *Journal of Computational Physics*, 62(1):40–65, 1986.

A. Jameson. Aerodynamic design via control theory. *Journal of Scientific Computing*, 3 (3):233–260, 1988.

J. I. Jiménez-González. *Study of the stability of jets and wakes. Application to the wake past slender bodies with blunt trailing edge.* PhD thesis, Universidad de Jaén, 2013.

J. I. Jiménez-González and F. J. Huera-Huarte. Experimental sensitivity of vortex-induced vibrations to localized wake perturbations. *Journal of Fluids and Structures*, 74:53 – 63, 2017.

J. I. Jiménez-González, E. Sanmiguel-Rojas, A. Sevilla, and C. Martínez-Bazán. Laminar flow past a spinning bullet-shaped body at moderate angular velocities. *Journal of Fluids and Structures*, 43:200–219, 2013.

J. I. Jiménez-González, A. Sevilla, E. Sanmiguel-Rojas, and C. Martínez-Bazán. Global stability analysis of the axisymmetric wake past a spinning bullet-shaped body. *Journal of Fluid Mechanics*, 748:302–327, 2014.

B. Khalighi, S. Zhang, C. Koromilas, S. R. Balkanyi, L. P. Bernal, G. Iaccarino, and P. Moin. Experimental and computational study of unsteady wake flow behind a bluff body with a drag reduction device. Technical report, SAE Technical Paper, 2001.

B. Khalighi, K. H. Chen, and G. Iaccarino. Unsteady aerodynamic flow investigation around a simplified square-back road vehicle with drag reduction devices. *Journal of Fluids Engineering*, 134(6):061101, 2012.

G. Kirchhoff. Zur theorie freier flüssigkeitsstrahlen. *Journal für die reine und angewandte Mathematik*, 70:289–298, 1869.

M. Kiya and Y. Abe. Turbulent elliptic wakes. *Journal of Fluids and Structures*, 13(7-8): 1041–1067, 1999.

S. Krajnović and L. Davidson. Numerical study of the flow around a bus-shaped body. *Journal of Fluids Engineering*, 125(3):500–509, 2003.

S. Krajnović and L. Davidson. Flow around a simplified car, part 1: large eddy simulation. *Journal of Fluids Engineering*, 127(5):907–918, 2005.

S. Krajnović and J. Fernandes. Numerical simulation of the flow around a simplified vehicle model with active flow control. *International Journal of Heat and Fluid Flow*, 32(1):192–200, 2011.

R. W. Kruiswyk and J. C. Dutton. Effects of a base cavity on subsonic near-wake flow. *AIAA Journal*, 28(11):1885–1893, 1990.

P. Lax and B. Wendroff. Systems of conservation laws. *Communications on Pure and Applied Mathematics*, 13(2):217–237, 1960.

R. Li. *Aerodynamic Drag Reduction of a Square-Back Car Model Using Linear Genetic Programming and Physic-Based Control.* PhD thesis, ISAE-ENSMA Ecole Nationale Supérieure de Mécanique et d 'Aérotechique-Poitiers, 2017.

R. Li, D. Barros, J. Borée, O. Cadot, B. R. Noack, and L. Cordier. Feedback control of bimodal wake dynamics. *Experiments in Fluids*, 57(10):158, 2016.

R. Li, B. R. Noack, L. Cordier, J. Borée, and F. Harambat. Drag reduction of a car model by linear genetic programming control. *Experiments in Fluids*, 58(8):103, 2017.

R. P. Littlewood and M. A. Passmore. Aerodynamic drag reduction of a simplified square-back vehicle using steady blowing. *Experiments in Fluids*, 53(2):519–529, 2012.

L Liu, Y. Sun, X. Chi, G. Du, and M. Wang. Transient aerodynamic characteristics of vans overtaking in crosswinds. *Journal of Wind Engineering and Industrial Aerodynamics*, 170:46–55, 2017.

M. Lorite-Díez, J. I. Jiménez-González, C. Gutiérrez-Montes, and C. Martínez-Bazán. Drag reduction of slender blunt-based bodies using optimized rear cavities. *Journal of Fluids and Structures*, 74:158–177, 2017.

M. Lorite-Díez, J. I. Jiménez-González, C. Gutiérrez-Montes, and C. Martínez-Bazán. Effects of rear cavities on the wake behind an accelerating D-shaped bluff body. *Physics of Fluids (1994-present)*, 30(4):044103, 2018.

M. Lorite-Díez, J.I. Jiménez-González, L. Pastur, O. Cadot, and C. Martínez-Bazán. Effect of the shape of rear cavities on the drag reduction of a three-dimensional blunt body at different yaw angles. *Submitted to Journal of Wind Engineering and Industrial Aerodynamics*, 2019a.

M. Lorite-Díez, J.I. Jiménez-González, L. Pastur, O. Cadot, and C. Martínez-Bazán. On the role of base blowing density on the drag reduction of three-dimensional blunt bodies. *Submitted to Physical Review Fluids*, 2019b.

M. Lorite-Díez, J.I. Jiménez-González, L. Pastur, C. Martínez-Bazán, and O. Cadot. Experimental sensitivity analyses of modes to blowing at the base of a 3D bluff body. *Submitted to Journal of Fluid Mechanics*, 2019c.

J.M. Lucas, O. Cadot, V. Herbert, S. Parpais, and J. Délery. A numerical investigation of the asymmetric wake mode of a squareback ahmed body - effect of a base cavity. *Journal of Fluid Mechanics*, 831:675–697, 2017.

W. A. Mair. The effect of a rear-mounted disc on the drag of a blunt-based body of revolution (drag of body of revolution with blunt base substantially reduced by mounting disk behind body with smaller diameter than body). *Aeronautical Quarterly*, 16:350–360, 1965.

W. A. Mair. Drag-reducing techniques for axi-symmetric bluff bodies. In *Aerodynamic drag mechanisms of bluff bodies and road vehicles*, pages 161–187. Springer, 1978.

A. Mariotti, G. Buresti, and M. V. Salvetti. Connection between base drag, separating boundary layer characteristics and wake mean recirculation length of an axisymmetric blunt-based body. *Journal of Fluids and Structures*, 55:191–203, 2015.

O. Marquet, D. Sipp, and L. Jacquin. Sensitivity analysis and passive control of cylinder flow. *Journal of Fluid Mechanics*, 615:221–252, 2008.

A. Martín-Alcántara, E. Sanmiguel-Rojas, C. Gutiérrez-Montes, and C. Martínez-Bazán. Drag reduction induced by the addition of a multi-cavity at the base of a bluff body. *Journal of Fluids and Structures*, 48:347–361, 2014.

A. Maurel, V. Pagneux, and J. E. Wesfreid. Mean-flow correction as non-linear saturation mechanism. *EPL (Europhysics Letters)*, 32(3):217, 1995.

D. McArthur, D. Burton, M. Thompson, and J. Sheridan. An experimental characterisation of the wake of a detailed heavy vehicle in cross-wind. *Journal of Wind Engineering and Industrial Aerodynamics*, 175:364–375, 2018.

P. Meliga, G. Pujals, and E. Serre. Sensitivity of 2-D turbulent flow past a D-shaped cylinder using global stability. *Physics of Fluids (1994-present)*, 24(6):061701, 2012.

P. Meliga, E. Boujo, G. Pujals, and F. Gallaire. Sensitivity of aerodynamic forces in laminar and turbulent flow past a square cylinder. *Physics of Fluids (1994-present)*, 26 (10):104101, 2014.

P. Meliga, O. Cadot, and E. Serre. Experimental and theoretical sensitivity analysis of turbulent flow past a square cylinder. *Flow, Turbulence and Combustion*, 97:987–1015, 2016.

M. Minguez, R. Pasquetti, and E. Serre. High-order large-eddy simulation of flow over the ahmed body car model. *Physics of Fluids (1994-present)*, 20(9):095101, 2008.

M. J. Molezzi and J. C. Dutton. Study of subsonic base cavity flowfield structure using particle image velocimetry. *AIAA Journal*, 33(2):201–209, 1995.

P. A. Monkewitz. A note on vortex shedding from axisymmetric bluff bodies. *Journal of Fluid Mechanics*, 192:561–575, 1988.

T. Morel. Effect of base cavities on the aerodynamic drag of an axisymmetric cylinder. *The Aeronautical Quarterly*, 30(2):400–412, 1979.

J. F. Morrison and A. Qubain. Control of an axisymmetric turbulent wake by a pulsed jet. In *Advances in Turbulence XII*, pages 225–228. Springer, 2009.

I. Nakamura. Steady wake behind a sphere. *The Physics of Fluids*, 19(1):5–8, 1976.

J. F. Nash, V. G. Quincey, and J. Callinan. *Experiments on two-dimensional base flow at subsonic and transonic speeds*, volume 25070. ARC, 1963.

U. Nilsson, D. Lindblad, and O. Petit. Description of adjointShapeOptimizationFoam and how to implement new objective functions. Technical report, Chalmers University of Technology, 2014.

F. Odar and W. Hamilton. Forces on a sphere accelerating in a viscous fluid. *Journal of Fluid Mechanics*, 18:302–314, 1964.

C. Othmer. A continuous adjoint formulation for the computation of topological and surface sensitivities of ducted flows. *International Journal for Numerical Methods in Fluids*, 58(8):861–877, 2008.

C. Othmer. Adjoint methods for car aerodynamics. *Journal of Mathematics in Industry*, 4(1):1–23, 2014.

A. R. Oxlade, J. F. Morrison, A. Qubain, and G. Rigas. High-frequency forcing of a turbulent axisymmetric wake. *Journal of Fluid Mechanics*, 770:305–318, 2015.

A. Palmer. The development of an integrated routing and carbon dioxide emissions model for goods vehicles. *PhD thesis, Cranfield University*, 2007.

V. Parezanović and O. Cadot. Experimental sensitivity analysis of the global properties of a two-dimensional turbulent wake. *Journal of Fluid Mechanics*, 693:115–149, 2012.

H. Park, D. Lee, W. P. Jeon, S. Hahn, J. Kim, J. Kim, J. Choi, and H. Choi. Drag reduction in flow over a two-dimensional bluff body with a blunt trailing edge using a new passive device. *Journal of Fluid Mechanics*, 563:389–414, 2006.

D. J. Parkin, M. C. Thompson, and J. Sheridan. Numerical analysis of bluff body wakes under periodic open-loop control. *Journal of Fluid Mechanics*, 739:94–123, 2014.

R. Pasquetti and N. Peres. A penalty model of synthetic micro-jet actuator with application to the control of wake flows. *Computers & Fluids*, 114:203–217, 2015.

M. Pastoor, L. Henning, B. R. Noack, R. King, and G. Tadmor. Feedback shear layer control for bluff body drag reduction. *Journal of Fluid Mechanics*, 608:161–196, 2008.

G. Pawlak, C. Marugan-Cruz, C. Martínez-Bazán, and P. García-Hrdy. Experimental characterization of starting jet dynamics. *Fluid Dynamics Research*, 39:711 – 730, 2007.

B. Pier. Local and global instabilities in the wake of a sphere. *Journal of Fluid Mechanics*, 603:39–61, 2008.

S.B. Pope. *Turbulent flows.* Cambridge University Press, 2000. ISBN 0521598869.

A. Prasad and C. H. K. Williamson. The instability of the shear layer separating from a bluff body. *Journal of Fluid Mechanics*, 333:375–402, 1997.

M. Provansal, C. Mathis, and L. Boyer. Bénard-von kármán instability: transient and forced regimes. *Journal of Fluid Mechanics*, 182:1–22, 1987.

G. Pujals, S. Depardon, and C. Cossu. Drag reduction of a 3D bluff body using coherent streamwise streaks. *Experiments in Fluids*, 49(5):1085–1094, 2010.

A. Rao, G. Minelli, B. Basara, and S. Krajnović. On the two flow states in the wake of a hatchback ahmed body. *Journal of Wind Engineering and Industrial Aerodynamics*, 173:262–278, 2018.

G. Rigas, A. R. Oxlade, A. S. Morgans, and J. F. Morrison. Low-dimensional dynamics of a turbulent axisymmetric wake. *Journal of Fluid Mechanics*, 755, 2014.

G. Rigas, A. S. Morgans, R. D. Brackston, and J. F. Morrison. Diffusive dynamics and stochastic models of turbulent axisymmetric wakes. *Journal of Fluid Mechanics*, 778, 2015.

G. Rigas, L. Esclapez, and L. Magri. Symmetry breaking in a 3D bluff-body wake. *Center for Turbulence Research. Proceedings of the Summer Program*, 2017.

F. Roos and W. Willmarth. Some experimental results on sphere and disk drag. *Journal of Fluid Mechanics*, 9:285–291, 1971.

A. Roshko. Some measurements of flow in a rectangular cutout. *National Advisory Committe for Aeronautics*, 1955.

A. Roshko. Perspectives on bluff body aerodynamics. *Journal of Wind Engineering and Industrial Aerodynamics*, 49(1-3):79–100, 1993.

G. Rossitto, C. Sicot, V. Ferrand, J. Borée, and F. Harambat. Influence of afterbody rounding on the pressure distribution over a fastback vehicle. *Experiments in Fluids*, 57 (3):1–12, 2016.

M. Rouméas, P. Gilliéron, and A. Kourta. Analysis and control of the near-wake flow over a square-back geometry. *Computers & Fluids*, 38(1):60–70, 2009.

D. Ruelle and F. Takens. On the nature of turbulence. *Les rencontres physiciens-mathématiciens de Strasbourg*, 12:1–44, 1971.

H. Sakamoto and H. Haniu. A study on vortex shedding from spheres in a uniform flow. *Journal of Fluids Engineering*, 112(4):386–392, 1990.

E. Sanmiguel-Rojas, A. Sevilla, C. Martínez-Bazán, and J. M. Chomaz. Global mode analysis of axisymmetric bluff-body wakes: Stabilization by base bleed. *Physics of Fluids (1994-present)*, 21(11):114102, 2009.

E. Sanmiguel-Rojas, J. I. Jiménez-González, P. Bohorquez, G. Pawlak, and C. Martínez-Bazán. Effect of base cavities on the stability of the wake behind slender blunt-based axisymmetric bodies. *Physics of Fluids (1994-present)*, 23(11):114103, 2011.

T. Sarpkaya and H. K. Kline. Impulsively-started flow about four types of bluff body. *ASME Journal of Fluids Engineering*, 104:207–213, 1982.

H. J. Schmidt, R. Woszidlo, C. N. Nayeri, and C. O. Paschereit. Drag reduction on a rectangular bluff body with base flaps and fluidic oscillators. *Experiments in Fluids*, 56 (7):151, 2015.

A. Sevilla and C. Martínez-Bazán. Vortex shedding in high Reynolds number axisymmetric bluff-body wakes: local linear instability and global bleed control. *Physics of Fluids (1994-present)*, 16(9):3460–3469, 2004.

A. Sevilla and C. Martínez-Bazán. A note on the stabilization of bluff-body wakes by low density base bleed. *Physics of Fluids (1994-present)*, 18(9):098102, 2006.

M. L. Shur, P. R. Spalart, M. K. Strelets, and A. K. Travin. A hybrid RANS-LES approach with delayed-DES and wall-modelled LES capabilities. *International Journal of Heat and Fluid Flow*, 29(6):1638–1649, 2008.

A. Sohankar. Flow over a bluff body from moderate to high reynolds numbers using large eddy simulation. *Computers & Fluids*, 35(10):1154–1168, 2006.

G. Sovran. *Aerodynamic drag mechanisms of bluff bodies and road vehicles.* Springer Science & Business Media, 2012.

P. J. Strykowski and K. R. Sreenivasan. On the formation and suppression of vortex shedding at low reynolds numbers. *Journal of Fluid Mechanics*, 218:71–107, 1990.

G. K. Suryanarayana, H. Pauer, and G. E. A. Meier. Bluff-body drag reduction by passive ventilation. *Experiments in Fluids*, 16(2):73–81, 1993.

M. Tanner. Reduction of base drag. *Progress in Aerospace Sciences*, 16(4):369–384, 1975.

A. Thacker, S. Aubrun, A. Leroy, and P. Devinant. Effects of suppressing the 3d separation on the rear slant on the flow structures around an ahmed body. *Journal of Wind Engineering and Industrial Aerodynamics*, 107:237–243, 2012.

W. Thielicke and E. Stamhuis. Pivlab–towards user-friendly, affordable and accurate digital particle image velocimetry in MATLAB. *Journal of Open Research Software*, 2 (1), 2014.

M. C. Thompson, T. Leweke, and M. Provansal. Kinematics and dynamics of sphere wake transition. *Journal of Fluids and Structures*, 15(3-4):575–585, 2001.

A. G. Tomboulides and S. A. Orszag. Numerical investigation of transitional and weak turbulent flow past a sphere. *Journal of Fluid Mechanics*, 416:45–73, 2000.

N. Tonui and D. Sumner. Flow around impulsively started square prisms. *Journal of Fluids and Structures*, 27(1):62–75, 2011.

E. R. van Driest. On turbulent flow near a wall. *Journal of Aeronautical Sciences*, 23(11), 1956.

M. Van Dyke. *An album of fluid motion.* Parabolic Press Stanford, 1982.

R. Verzicco, M. Fatica, G. Iaccarino, P. Moin, and B. Khalighi. Large eddy simulation of a road vehicle with drag-reduction devices. *AIAA journal*, 40(12):2447–2455, 2002.

P. R. Viswanath. Flow management techniques for base and afterbody drag reduction. *Progress in Aerospace Sciences*, 32(2):79–129, 1996.

R. Volpe, P. Devinant, and A. Kourta. Experimental characterization of the unsteady natural wake of the full-scale square back ahmed body: flow bi-stability and spectral analysis. *Experiments in Fluids*, 56(5):99, 2015.

E. Wassen, S. Eichinger, and F. Thiele. Simulation of active drag reduction for a square-back vehicle. In *Active Flow Control II*, pages 241–255. Springer, 2010.

C. H. K. Williamson. Vortex dynamics in the cylinder wake. *Annual Review of Fluid Mechanics*, 28(1):477–539, 1996.

D. T. M. Wong and W. A. Mair. Boat-tailed afterbodies of square section as drag-reduction devices. *Journal of Wind Engineering and Industrial Aerodynamics*, 12(2):229–235, 1983.

C. J. Wood. The effect of base bleed on a periodic wake. *The Aeronautical Journal*, 68 (643):477–482, 1964.

R. M. Wood. A discussion of a heavy truck advanced aerodynamic trailer system. *Proceedings of the 9th International Symposium on Heavy Vehicle Weights and Dimensions*, 2006.

R. M. Wood and S. XS. Bauer. Simple and low-cost aerodynamic drag reduction devices for tractor-trailer trucks. *SAE Transactions*, pages 143–160, 2003.

R. Woszidlo, T. Stumper, C. Nayeri, and C. O. Paschereit. Experimental study on bluff body drag reduction with fluidic oscillators. In *52nd Aerospace Sciences Meeting*, page 0403, 2014.

T. Y. T. Wu. Cavity and wake flows. *Annual Review of Fluid Mechanics*, 4(1):243–284, 1972. ISSN 0066-4189.